Development of a dual comb laser source toward atmospheric radical OH monitoring

Clément Pivard

▶ **To cite this version:**

Clément Pivard. Development of a dual comb laser source toward atmospheric radical OH monitoring. Physics [physics]. Université de Lyon, 2021. English. NNT : 2021LYSE1295 . tel-03729542

HAL Id: tel-03729542

https://theses.hal.science/tel-03729542v1

Submitted on 20 Jul 2022

HAL is a multi-disciplinary open access archive for the deposit and dissemination of scientific research documents, whether they are published or not. The documents may come from teaching and research institutions in France or abroad, or from public or private research centers.

L'archive ouverte pluridisciplinaire **HAL**, est destinée au dépôt et à la diffusion de documents scientifiques de niveau recherche, publiés ou non, émanant des établissements d'enseignement et de recherche français ou étrangers, des laboratoires publics ou privés.

N° d'ordre NNT: 2021LYSE1295

THÈSE DE DOCTORAT DE L'UNIVERSITÉ DE LYON

opérée au sein de

l'Université Claude Bernard Lyon 1

École Doctorale ED52

Physique et Astrophysique

Spécialité de doctorat : Physique des Lasers et Spectroscopie

Discipline : Physique

Soutenue publiquement le 15/12/2021, par:

Clément PIVARD

Development of a dual comb laser source toward atmospheric radical OH monitoring

---

Devant le jury composé de:

Nom, prénom, grade/qualité, établissement/entreprise	Président.e
PICQUE Nathalie, Chargée de Recherche, Max Planck Institute of Quantum Optics, Munich	Rapporteure
PLATT Ulrich, Professeur, Université d'Heidelberg, Institute for Environmental Physics	Rapporteur
BREVET Pierre-François, Professeur, Université Lyon 1	Examinateur
RAYBAUT Myriam, Ingénieure de recherche, ONERA Palaiseau	Examinatrice
RAIROUX Patrick, Professeur, Université Lyon 1	Directeur de thèse
GALTIER Sandrine, Maître de conférences, Université Lyon 1 ILM	Co-encadrante de thèse
HEBERT Philippe-Jean, Ingénieur de Recherche, CNES	Invité

Université Claude Bernard – LYON 1

Président de l'Université	M. Frédéric FLEURY
Président du Conseil Académique	M. Hamda BEN HADID
Vice-Président du Conseil d'Administration	M. Didier REVEL
Vice-Président du Conseil des Etudes et de la Vie Universitaire	Mme Céline BROCHIER
Vice-Président de la Commission de Recherche	M. Petru MIRONESCU
Directeur Général des Services	M. Pierre ROLLAND

COMPOSANTES SANTE

Département de Formation et Centre de Recherche en Biologie Humaine	Directrice : Mme Anne-Marie SCHOTT
Faculté d'Odontologie	Doyenne : Mme Dominique SEUX
Faculté de Médecine et Maïeutique Lyon Sud - Charles Mérieux	Doyenne : Mme Carole BURILLON
Faculté de Médecine Lyon-Est	Doyen : M. Gilles RODE
Institut des Sciences et Techniques de la Réadaptation (ISTR)	Directeur : M. Xavier PERROT
Institut des Sciences Pharmaceutiques et Biologiques (ISBP)	Directrice : Mme Christine VINCIGUERRA

COMPOSANTES & DEPARTEMENTS DE SCIENCES & TECHNOLOGIE

Département Génie Electrique et des Procédés (GEP)	Directrice : Mme Rosaria FERRIGNO
Département Informatique	Directeur : M. Behzad SHARIAT
Département Mécanique	Directeur M. Marc BUFFAT
Ecole Supérieure de Chimie, Physique, Electronique (CPE Lyon)	Directeur : Gérard PIGNAULT
Institut de Science Financière et d'Assurances (ISFA)	Directeur : M. Nicolas LEBOISNE
Institut National du Professorat et de l'Education	Directeur : M. Pierre CHAREYRON
Institut Universitaire de Technologie de Lyon 1	Directeur : M. Christophe VITON
Observatoire de Lyon	Directrice : Mme Isabelle DANIEL
Polytechnique Lyon	Directeur : Emmanuel PERRIN
UFR Biosciences	Administratrice provisoire : Mme Kathrin GIESELER
UFR des Sciences et Techniques des Activités Physiques et Sportives (STAPS)	Directeur : M. Yannick VANPOULLE
UFR Faculté des Sciences	Directeur : M. Bruno ANDRIOLETTI

Abstract

The atmospheric gas phase evolution is of main concern for air quality and climate evolution, as indicated in the recent IPPC Report [1]. In this context, the radical OH has been recognized as one of the key molecule in the atmosphere. The radical OH interactions in the atmosphere remain not fully understood, as it is very challenging to measure. To improve the understanding of the role of OH in the atmosphere, there is a need for instruments that should be sensitive, accurate, and have a fast acquisition time in the timeframe of the OH lifetime (ms). We propose to extend the already existing dual comb spectroscopy (DCS) methodology instrument from the IR [2,3] to the near UV region to take advantage of the strong absorption cross-section of OH at 308 nm. Numerical and theoretical work [4] effectively assess the feasibility of the DCS method in the UV range. This study concludes that the Ti:sa Kerr lens mode-locked laser source appears to be the most adapted laser source to realize DCS in the UV. The advantages of the remote sensing DCS method are multiple: it is a fast acquisition rate with similar sensitivity than the existing spectroscopic methods, it is an in-situ method, free of sampling retrieval and free of atmospheric fluctuations. A homemade DCS laser source has been fully realized in the laboratory with an original geometry. It consists in a single ring cavity laser generating two pulses trains of 100 fs. This geometry is advantageous for DCS as it allows a common noise sharing (amplitude and phase).

The total mode-locked emitted output power reaches 700 mW with 5.5 W pump power, which would provide enough power to probe atmospheric molecules with UV-DCS via third harmonic generation. The first tests of the DCS experiment using our homemade laser source have been realized on Fabry-Perot (FP) and O_2 molecules. We retrieved accurately the free spectral range of the FP and obtained, with high accuracy, the ro-vibrational transitions position of O_2 at 760 nm. We demonstrated that the here developed single cavity laser source provides high enough relative phase stability (at least 330 ms) between the two laser emissions. These first results represent an important milestone towards atmospheric trace gases remote sensing using UV-DCS.

Key words : Dual Comb Spectroscopy, ultrafast laser, single bidirectional laser cavity, Kerr lens mode-locking, OH remote sensing, climate change, air quality monitoring.

Résumé de thèse

L'évolution de la phase gazeuse atmosphérique est une préoccupation majeure pour la qualité de l'air et l'évolution du climat, comme indiqué dans le récent rapport du GIEC [1]. Dans ce contexte, le radical OH a été reconnu comme l'une des molécules clés de l'atmosphère, participant par exemple à 90 % de la réduction de méthane atmosphérique. Les interactions radicalaires OH dans l'atmosphère ne sont pas encore entièrement comprises car elles sont très difficiles à mesurer. Pour améliorer la compréhension du rôle de l'OH dans l'atmosphère, il existe un besoin d'instruments qui doivent être sensibles, précis et avoir un temps d'acquisition rapide dans la durée de vie de l'OH (ms). Nous proposons d'étendre la méthode de spectroscopie à double peigne de fréquence (DCS) déjà existant dans l'IR [2, 3] à la région proche UV afin de tirer parti de la forte section efficace d'absorption de OH à 308 nm. Une étude numérique et théorique [4] a évalué efficacement la faisabilité de la méthode DCS dans le domaine UV. Cette étude conclut que la source laser Ti:sa à verrouillage de modes par effet Kerr semble être la source laser la plus adaptée pour réaliser le DCS dans l'UV. Les avantages de la méthode DCS pour la télédétection sont multiples : vitesse d'acquisition rapide avec une sensibilité similaire aux méthodes spectroscopiques existantes, c'est une méthode in-situ, sans prélèvement d'échantillons et indépendante des fluctuations atmosphériques. Une source laser DCS a été entièrement réalisée en laboratoire avec une géométrie originale. Il consiste en un laser à cavité en anneau unique générant deux trains d'impulsions de 100 fs. Cette géométrie est avantageuse pour la méthode DCS car elle permet un partage des bruits commun (amplitude et phase) aux deux impulsions.

La puissance totale émise du laser à modes verrouillé atteint 700 mW avec une puissance de pompe de 5,5 W, ce qui fournit suffisamment de puissance pour sonder les molécules atmosphériques par UV-DCS via la génération de troisième harmonique. Les premiers tests de l'expérience DCS utilisant notre source laser ont été réalisés sur un étalon Fabry-Pérot (FP) et sur la molécule O_2. Nous avons récupéré avec précision l'intervalle spectrale libre du FP et obtenu, avec une grande précision, la position des transitions ro-vibrationnelles de l'O_2 à 760 nm. Nous avons démontré que la source laser à cavité unique développée ici offre une stabilité de phase relative suffisamment élevée (au moins 330 ms) entre les deux émissions laser. Ces premiers résultats représentent une étape importante vers la télédétection des gaz traces atmosphériques par UV-DCS.

Mots clés : Spectroscopie à double peigne de fréquence, laser ultra-bref, cavité laser bidirectionnelle, vérouillage des modes en phase par effet Kerr, télédétection OH, changement climatique.

Acknowledgements

Ce travail de thèse s'est déroulé à l'Institut Lumière Matière (ILM) au sein de l'équipe Atmosphères, Optique et Spectroscopie (ATMOS). Je voudrais tout d'abord remercier mon directeur de thèse et professeur Patrick Rairoux pour m'avoir accepté au sein de l'équipe, de m'avoir attribué sa confiance, de m'avoir encadré et formé. Je remercie également Sandrine Galtier, maître de conférence et encadrante pour m'avoir guidé et aidé pendant ces trois années de thèse et pour toutes les discussions scientifiques intéressantes que l'on a pu avoir.

Je remercie le professeur Pierre-François Brevet d'avoir présidé mon jury de thèse et de nous avoir prêtés en tant que chef de l'équipe ONLI de l'équipement optique. J'adresse mes remerciements au professeur Ulrich Platt et à Nathalie Picqué pour avoir rapporté mon manuscrit de thèse et pour avoir participé à mon jury de thèse. Je remercie également Myriam Raybaut et Philippe-Jean Hébert qui ont accepté d'être membre de ce jury.

Merci à Jérôme Morville de son aide, de m'avoir présenté son expérience CRDS et de m'avoir laissé travaillé dans sa salle d'expérience. C'est grâce à lui et à Guillaume Méjean du laboratoire interdisciplinaire de physique (LiPhy) que je remercie également, que j'ai eu l'opportunité de récupérer une cavité laser Ti:sa linéaire "faite-maison" sur laquelle j'ai pu m'éxercer et acquérir de l'expérience et de la compétence. Je remercie bien sûr Amanda Ross pour toutes les discussions scientifiques intéressantes, sa gentillesse et pour avoir corrigé mes expressions parfois trop "frenchi" dans mon manuscrit de thèse et dans ma présentation de soutenance de thèse. Je remercie Alain Miffre pour toutes les discussions scientifiques intéressantes, sa bonne humeur et d'avoir partagé son humour pendant les déjeuners. Merci à Patrick Crozet pour le prêt de matériel et également pour m'avoir présenté sa manip.

La partie la plus difficile de ma thèse a été de démarrer le blocage des modes en phase de façon passive, ce qui résulte au fonctionnement en régime impulsionnel de la cavité laser. Il est décrit dans la littérature que ce régime peut être obtenu lorsque toutes les conditions sont réunies (position des miroirs, longueur de la cavité optique, compensation de la dispersion positive de la vitesse de groupe, compensation de l'astigmatisme, alignement du faisceau laser intra-cavité, stabilité méca-

nique ...). Une fois ces conditions optimisées, il est possible de déclencher le régime "Mode-Lock" par induction d'une perturbation stochastique sur l'un des éléments de la cavité. En clair : en tapant sur la table. D'où le terme "Magic Mode-locking". J'ai donc passé un temps non-négligeable de ma thèse à essayer d'obtenir ces conditions nécessaires au déclenchement du régime impulsionnel. Je voudrais donc remercier vivement tous les chercheurs qui nous ont aidé de par leurs conseils à trouver des solutions pour optimiser ces conditions. Mes remerciements vont donc à Frédéric Druon de l'institut optique Graduate school (IOGS), à Marcel Krenz du Fritz-Haber-Institut ainsi qu'au professeur Jesus Garduno Mejia et à Catalina Ramirez de l'instituto de ciencias de applicadas y technologia pour tous leurs conseils qui se sont avérés payants.

Je remercie les services mécaniques, électroniques, informatique, infrastructures et administratif de l'ILM pour leur compétence, leur disponibilité et pour tous le travail fourni qui m'a permis de réaliser ma thèse dans de bonnes conditions.

Je remercie l'école doctorale PHAST et plus particulièrement Sylvie Flores et Anella Naizot pour leur jovialité, leurs conseils et pour toutes les discussions que l'on a eues pendant les pauses-cafés et pauses-déjeuners.

Merci à Gérard qui m'a soutenu et aiguillé dans mon projet professionnel.

Je remercie Danaël pour avoir partagé cette aventure de thèse qui s'est étendue du début de stage à la soutenance. Malgré les nombreuses boutades, chambrages et les très nombreuses défaites à Geoguessr Danaël reste tout de même un bon co-bureau et un co-bureau de qualité :).

Je remercie les nombreux(ses) doctorant(e)s que j'ai fréquenté(e)s durant ma thèse pour toutes les discussions scientifiques, pauses café, déjeuners, soutiens, randonnées, ski ... Côtoyer cette communauté internationale quotidiennement a été pour moi très enrichissant. Une pensée particulière pour Akash, Lysandra, Leonel, Cassandre, Lionel, Ong, Martina ainsi qu'aux membres de la Teamdoc.

Je remercie Philippe et les membres du "Body Gym" pour leurs encouragements sportifs et pour leur bonne humeur perpétuelle. Entre une séance de squat et de développé couché, j'ai apprécié répondre à la question qui revenait sans cesse : "Alors, le chercheur, as tu trouvé ?"

Je remercie mes amis proches qui ont toujours été curieux de mes travaux scientifiques pour leur soutien et leur amitié qui dure depuis des années malgré la distance : Charles, Alexis, Thomas,

Simon, Maxence, Kevin, Baptiste.

Je remercie ma famille, mes parents et mon frère pour m'avoir soutenu, encouragé, pour leur curiosité et également pour m'avoir toujours donné des conditions favorables à mon épanouissement intellectuel.

Enfin, je voudrais remercier ma Azizam pour m'avoir accompagné, supporté et soutenu durant cette aventure. Que ce soit pendant la période de confinement, ou durant les moments difficiles de la thèse, tu as toujours été présente sans aucune hésitation. Nini azizam, bazam az hemayat, eshgh va hozoore zibayat mamnoonam mo.

Nomenclature

ASE Amplified Spontaneous Emission
BBO Beta Barium Borate
BDCS Bidirectional dual comb spectroscopy
BS Beam-Splitter
CEAS Cavity Enhanced Absorption Spectroscopy
CEO Carrier Envelope Offset
CRDS Cavity Ring-Down Spectroscopy
CIMS Chemical Ionisation of Mass Spectrometry
CW Continuous Wave
DCS Dual comb Spectroscopy
DIAL Differential absorption Lidar
DM Dichroic Mirror
DOAS Differential Optical Absorption Spectroscopy
FAGE Fluorescence Assay by Gas Expansion
FID Free Induction Decay
FFT Fast Fourier Transform
FP Fabry-Perot
FSR Free Spectral Range
FTS Fourier transform Spectroscopy
FWHM Full Width Half Maximum
GDD Group Delay Dispersion
GVD Group Velocity Dispersion
HHG High Harmonic Generation
IGM Interferogram
KLM Kerr-Lens Mode-locking
LIF Laser Induced Fluorescence
LP-DOAS Long-Path Differential Optical Absorption Spectroscopy
LPF Low Pass Filter
MAS Minimum Absorption Sensitivity
ML Mode-Locking
MOAS Multipass Optical Absorption Spectroscopy
NEP Noise Equivalent Power
NIR Near Infra-Red
OP Output Coupler
PAH Polycyclic Aromatic Hydrocarbon
PD Photo-detector
PSD Power Spectral Density
RF Radio Frequency
RIN Relative Intensity Noise
RMS Root Mean Square
SAM Saturable Absorber Mirror
SFG Sum Frequency Generation
SHG Second Harmonic Generation
SNR Signal to Noise Ratio
SPM Self-Phase Modulation
TDL Thin Disk Laser
THG Third Harmonic Generation
Ti:sa Titanium:sapphire
UV-DCS Ultra-Violet Dual comb Spectroscop

List of Figures

List of Tables

Contents

Publications

Relevant Publications

- Galtier Sandrine, Clément Pivard, and Patrick Rairoux. "Towards DCS in the UV Spectral Range for Remote Sensing of Atmospheric Trace Gases." Remote Sensing 12.20 (2020): 3444.
- Pivard Clément, Sandrine Galtier, and Patrick Rairoux. "Towards Remote Sensing of Atmospheric Trace Gases in the UV spectral range using Dual-Comb spectroscopy." EGU General Assembly Conference Abstracts. 2021.

Summary

Atmospheric pollution and climate change are one of the main challenges of the 21st century for humankind. As indicated by the recent publication of the sixth report of the intercontinental Panel of Climate Change (IPCC) (first working group) [1], the retreat of the glaciers since 1990, the decrease in northern hemisphere spring snow, the global warm of upper ocean, the acidification of the ocean, the global mean sea level increase are many evidences of a current climate change. The comprehension of climate and atmospheric pollution needs a deep understanding of the atmospheric molecules dynamic, chemical reactions and evolution. The oxidising radical OH, considered as the "detergent" of the atmosphere, is in the center of the atmospheric chemistry reactions and still remains one of the most challenging atmospheric molecules to be measured in-situ because of its lifetime in Earth's atmosphere. The measurement of the radical OH dynamic is crucial to improve our understanding on the complexity of atmospheric processes [5] and improve the comprehension of the Earth's climate. The development of robust, sensitive and accurate instruments thus appears necessary [6]. The subject of my thesis falls in this framework, focusing on an experimental approach which is based on the fundamental interactions of light with the matter contained in the atmosphere and on new optical spectroscopy methods such as dual comb spectroscopy (DCS). This cutting edge approach [7, 8] is a relatively recent spectroscopic method that has attracted increasing interest in the last decade from the scientific community. The high resolution and fast acquisition inherent in this technique have been demonstrated to be beneficial for investigating the vibrational and rotational molecular transitions in laboratory and real atmospheric environment [2,3]. Its extension to the UV spectral range to probe the strong transition lines of some atmospheric molecules appears highly promising. The feasibility of assessing atmospheric molecules in the UV range using DCS, and the in-house construction of a dual-comb laser source are the core of this thesis. First, the purpose of this thesis was to answer the question : How to detect atmospheric radical OH in situ ? State of the art remote sensing optical methods have successfully detected this molecule [9, 10]. Thus, the interest to merge both approaches (DCS and remote sensing) has risen to monitor OH in-situ and without using air-sampling methodology [11, 12]. This has naturally raised questions such as how to improve our knowledge on the concentration dynamics of the radical OH ? Is the monitoring of atmospheric OH feasible in-situ by DCS in the UV range ? What will be the

sensitivity and the acquisition time to make the required measurements ? What laser source is best adapted for realising DCS in the UV ? This manuscript presents the results of three years' research work to answer these questions, leading to the development of a home-made laser source dedicated to UV-DCS, as the experimental part of this PhD work.

The manuscript is organized as follows. The first chapter presents the climate and pollution atmospheric current context, the atmospheric molecules of main interest, the main challenges in the detection of the atmospheric trace gas molecules and the state of the art of the OH radical detection methods. Dual comb spectroscopy, a new spectroscopic method, is introduced in the context of remote sensing of the OH radical.

The second chapter presents in detail the principles of dual comb spectroscopy. Maintaining a stable relative phase coherence between the two pulsed lasers over a given timescale is one of the main challenge of this method. The use of a single laser source has led to a simpler configuration of a low relative phase/amplitude noise laser emission of the two free-running pulse trains. In this context, the state of the art of DCS instruments using a single cavity laser source is presented.

Chapter 3 presents a numerical study on the feasibility on monitoring trace gas molecules in the ultra-violet range. The potential of DCS methodology to increase the knowledge on the dynamic of UV-absorbing atmospheric molecules' concentration through analysis of absorption spectra are presented. The numerical simulation results led to the experimental realisation of the laser source. Theoretical and numerical design development were necessary prerequisites for this project.

The chapter 4 presents the theory and design of the bidirectional mode-locked laser source. This study was necessary because we started the laser development from an empty table with the specific requirement of bidirectional laser emission from a titanium-sapphire (Ti:sa) oscillators.

The construction and development of the laser cavity is detailed in chapter 5. The optimisation of the laser environment, the laser alignment and the laser stability has led to the emission of two fs laser beams with high relative coherence for a period of time that has never been observed with free running Ti:sa single bidirectional laser cavity.

The chapter 6 presents the first dual comb spectroscopic measurements made in laboratory using the novel bidirectional laser source. The DCS method was applied to retrieve the free spectral range of a Fabry-Perot etalon and to record near IR absorption lines of ambient O_2. These measurements characterise the stability, relative coherence and spectral resolution of our DCS spectrometer based on the home-made bi-directional Ti:sa laser source.

Chapter 1

Introduction

1.1 Current challenges of atmospheric trace gases detection

The atmospheric gas phase evolution is of main concern for air quality, human health and climate evolution. As reported by the working group I of the sixth report of the IPCC, an increase in concentration of the greenhouse gases (GHG) such as CO_2, CH_4, N_2O has been observed in the atmosphere since 1750 [1]. Carbon dioxide levels have increased by more than 40 percent in the atmosphere since pre-industrial time [13]. Each of the last four decades global surface temperature has been successfully warmer than the previous one. Climate change may lead to some cases to extreme events such as floodings, tornados, heavy rains, exceptional droughts [14]. The assessment of the evolution of the future global earth surface temperatures were compared following the pioneer work of Manabe [15] using several Coupled Model Intercomparison Project (CMIP5, [16]) with different representative concentration pathways. An increase between 1.49 to 4.13 °C in 2100 compared to the period 1986-2005 [17] is expected. Some studies even demonstrated that a global warming by 2100 of 10 to 20 degrees is theoretically possible [18]. Such alarming forecasts have enourmous geopolotical impacts as a global warming of seven degrees would create local zones on earth where the metabolic heat dissipation of the human body would become impossible [19]. At 11-12 °of global warming, these local zones would expand and cover the main actual human living zones. Actions to reduce global warming should be taken now to avoid the worst potential consequences. Manzanedo et al. [20] showed by comparing with the COVID-19 situation that early actions and preventions are of great importance to cope with global crisis and this appear even more crucial as climate change has a much higher inertia. The 2018 report of the Intergovernmental Panel on Climate Change (IPCC) [21] concluded that the global greenhouse gas emission should be cut in half by 2030 and entirely by 2040 to avoid catastrophic events for humankind due to climate change.

Air quality depends on the complex interaction between the natural and the anthropogenic gas emitted in the atmosphere. It has become a major concern in the main cities as the air quality is decreasing and the population is growing [22]. According to the Union Nation, 55 % of the world population lives in urban areas. The World Health Organisation (WHO) and the United Nations Environment Programme (UNEP) created an air pollution monitoring network covering 50 cities in 35 developing and developed countries. It shows that developing countries are following the same pollution trend that did developed countries. With the population increase in their cities, a potential to follow the same pollution pattern or even worse exists [23]. Due to their fast economic growth, the atmospheric pollution of cities in developing countries has become a major problem. They suffer from NH_4^+, SO_2, O_3, NO_x and NH_3 pollution which can result in visibility deterioration, formation of acid rain and public health crises. As the population is growing, massive and systematic air quality measurements and multi-scale integrated models needs to be realised in cities [24]. The evolution of tropospheric ozone is of main concern for human health and the environment [25]. The observational-based review of Cooper et al. [26] shows a global ozone increase of 1 to 5 ppbv per decades which corresponds to an increase rate of more than 100 % of ozone since 1950. This is concerning as tropospheric ozone is toxic for the environment. Mauzerall and Wang [27] showed that tropospheric ozone was responsible for agricultural crops damages resulting in yields reduction. Several studies [28, 29] suggested a relation between ozone concentration and daily mortality in several US cities. Desqueyroux et al. [30] demonstrated that breathing ozone even at low concentration, is linked to pulmonary damages and asthma attacks.
Several studies show the danger of the air pollution (Particulate matters with diameter under 2.5 µm $PM_{2.5}$, NO_2/NO_x and CO) for the lungs [31], for the neuronal system [32–34], the cardiovascular system [35] and also for the cerebral development of children [36]. A study from 1980 to 1991 showed that the mortality rate in 11 cities, was increased due to ambient gaseous (NO_x,O_3, SO_2 and CO) air pollutants [37]. The gas-phase dynamics of our atmosphere is very complex and still not fully understood. For instance, the formation of secondary pollutants such as the formation of ozone, SO_4^{2-}, NO_3^- in urban area is not fully determined as unexpected results were observed [35].

The concentrations of many atmospheric trace gases in the atmosphere is controlled by Redox equilibre. Oxidation processes are a source of many molecules sink (CH_4, CO and volatile organic compounds (VOC)). They are responsible for the formation of the tropospheric ozone or secondary organic aerosols (SOA). The atmospheric oxidation system involves complex chemical processes with many reaction intermediates. Radicals OH and HO_2 are key molecules in the troposphere. HOx Radicals are molecules with one (or more) unpaired valence electrons which make them highly reactive. The OH radical is considered as the "detergent" of the troposphere. It is the primary oxidant in the troposphere, initiating the degradation of molecules including Volatile Organic Com-

pounds (VOC), CH_4, CO, CO_2, H_2, NO_2, isoprene and the monoterpenes [38, 39]. The oxidising capacity of the atmosphere is mainly driven by the radical OH concentration and in a smaller impact by NO_3, ozone, hydrogen peroxide H_2O_2 and halogen radicals. Radical OH is the major sink of atmospheric methane; 90 % of the loss of CH_4 is due to reaction with the hydroxyl OH radical in the troposphere [40].

The abundance of these radicals are highly dependant on the concentration of the primary molecule sources. The major sources of radical OH in the troposphere are the ozonolysis of VOC [41, 42] (see equation 1.1), the photo-dissociation of ozone followed by reaction with H_2O is the dominant source of OH [43] (see equation 1.2), photolysis of HONO [44] (see equation 1.3) and from the reaction of HO_2 with NO as represented in equation 1.4.

$$\mathrm{VOC} + \mathrm{O_3} \rightarrow \mathrm{OH} + \mathrm{products} \tag{1.1}$$

$$\mathrm{O_3} + \mathrm{h}\nu \rightarrow \mathrm{O(^1D)} + \mathrm{O_2}$$

$$\mathrm{O(^1D)} + \mathrm{H_2O} \rightarrow 2\mathrm{OH} \tag{1.2}$$

$\mathrm{O(^1D)}$ corresponds to the first electronic excited state of the oxygen atom.

$$\mathrm{HONO} + \mathrm{h}\nu \rightarrow \mathrm{OH} + \mathrm{NO} \tag{1.3}$$

$$\mathrm{HO_2} + \mathrm{NO} \rightarrow \mathrm{OH} + \mathrm{NO_2} \tag{1.4}$$

OH evolution in real atmospheric conditions is imperfectly understood due to its chemical reactions complexity [10]. Measurements of radical OH in real time realised by Martinez et al. [45] suggested that the reactions between ozone, NO_x and HO_x is still not fully understood in real outdoor conditions. In particular, they observed higher HO_2 concentrations than expected in high NO atmospheric concentration. Elshorbany et al. [46] demonstrated that the concentration of HOx radicals are highly correlated with NOx ambient concentrations. Ren et al. [47] found agreement with numerical simulations on the concentration of OH and HO_2 when HO_x production was high in the urban area of New-York City. However agreements with the numerical simulation dropped when the NO concentration was high, or when [HO_x] levels were low. In this case also, the nighttime OH concentration could not be reproduced. A missing reaction mechanism might explain this discrepancy [48]. This study also observed large discrepancies between experimental results and theoretical models in low concentration of NOx. Significant discrepancies between the measured

OH concentration and atmospheric chemistry models have also been highlighted in urban areas [49], in remote forest environments [50], and in high VOC concentration environment [51]. The understanding of the complex dynamics of the atmospheric gas is challenging. Therefore, a better understanding of the OH radical chemistry will lead to a better comprehension on the physico-processes involved in the troposphere.
As presented in this section, the evolution and influence of atmospheric trace gas molecules are of main concern for the climate and atmospheric pollution. In the next subsection, are presented some atmospheric molecules of main interest for this study.

1.2 Atmospheric trace gases absorbing in the UV range

The aim of this thesis is to realise a dual-comb spectrometer dedicated to detection of the OH radical by taking advantage of its strong $A^2\Sigma \leftarrow X^2\Pi$ absorption in the UV. The purpose being to improve on current concentration sensitivity, and to reduce the acquisition time required by the existing instruments. Many other atmospheric molecules such as SO_2, NO_2, H_2CO, BrO, OClO, $C_{10}H_8$ also absorb in the same range of wavelength and could plausibly render more complex OH concentration retrieval. Their main differential absorption cross-section are represented in figure 1.1 and 1.2. The total coverage range of their absorption transition lines between 200 to 540 nm are represented in figure 1.3. An interesting perspective would be to determine if these molecules can be measured simultaneously using our detection method. The concentration detection limit of these molecules using the UV-DCS was assessed numerically and as presented in chapter 3. These molecules are of great interest for the physico-chemistry of the atmosphere and are presented in this section as well as the ongoing detection methods.

SO_2 : Sulphur dioxide is a toxic gas that occurs naturally in areas of volcanic activity. Sulphur dioxide can be responsible for acid rain [63]. Yang et al. [64] observed in Guangzhou that 81.5 % of the total rainfall were sulphate type acid rains with an average pH of 4.83. Yang et al. [65] found that the increase of SO_2 in China was closely related to the affluence, industrial development level, energy consumption, urbanization rate and the degree of marketization. Sulphur dioxide is also connected to stratospheric ozone loss [66].

NO_2 : Nitrogen dioxide is a reddish-brown gas considered as an indicator for traffic-related air pollutants. Patenden et al. [67] demonstrated that there was a link between long term exposure to NO_2 and childhood allergy. Neuberger et al. [68] demonstrated that the lethality caused by urban air pollution could be predicted from levels of fine particulate matters of 2.5 µm or less (PM2.5) and NO_2. The level of NO_2 concentration has been determined to be a valid indicator of air quality and can predict human health [69, 70].

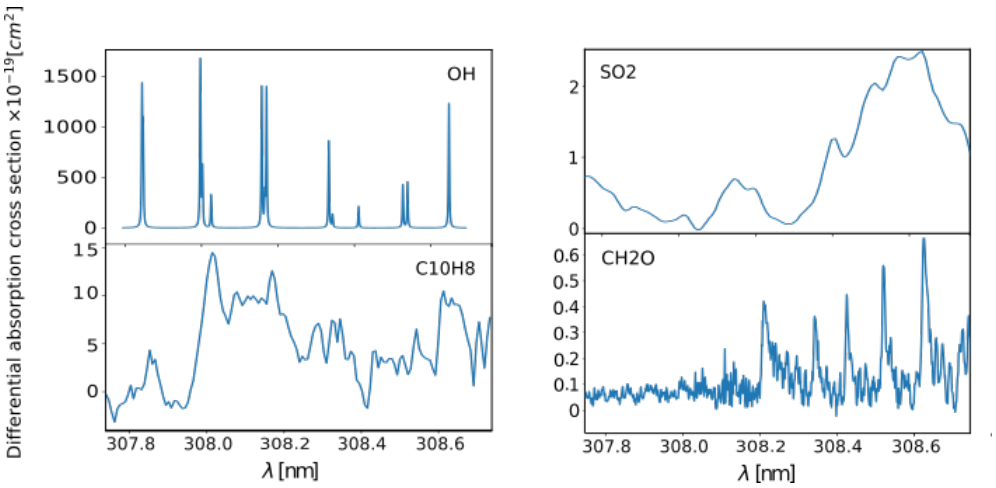

Figure 1.1: Differential absorption cross-section of atmospheric molecules of interest centred at 308 nm. These cross-section values were obtained from the Hitran database for T = 298 K and P = 1 bar (OH [52]) and Mainz (SO_2 [53, 54], naphtalene $C_{10}H_8$ [55], CH_2O [56]).

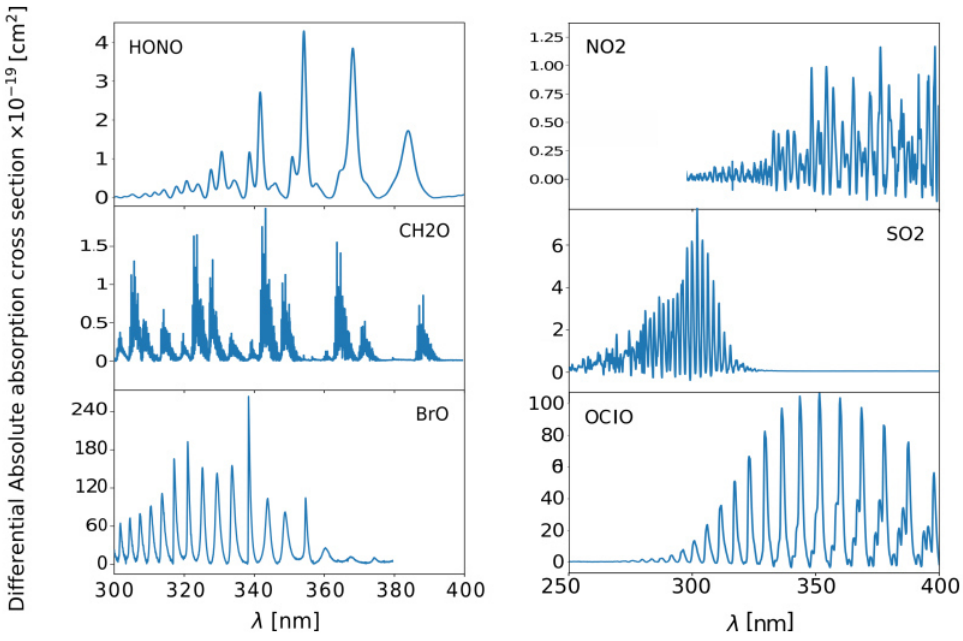

Figure 1.2: Absorption cross-section of atmospheric molecules of interests centred at 350 nm. These cross-section values were obtained from the Mainz database (SO_2 [54, 57], CH2O [58], HONO [59], NO_2 [60], BrO [61], OClO [62]).

OClO : Chlorine dioxide is a halogen yellowish gas that, along with BrO, is among the most important radicals involved in the ozone destruction [71, 72] in the Arctic and Antarctic poles.

$C_{10}H_8$: Naphtalene is the simplest polycyclic aromatic hydrocarbon (PAH). As other PAH, it is

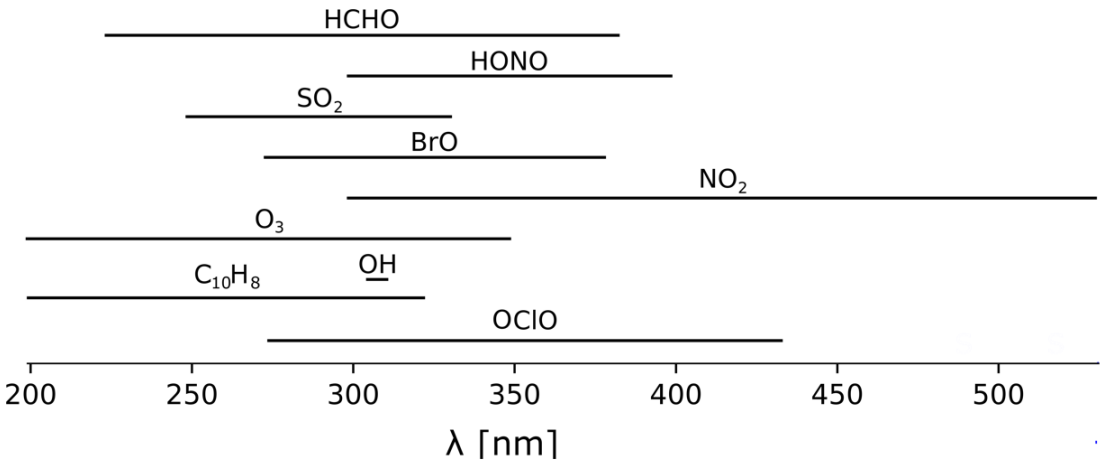

Figure 1.3: Absorption spectral range of atmospheric molecules of interests from 200 to 550 nm. Values were obtained from the Hitran and Mainz database.

emitted to the atmosphere from the incomplete combustion of organic materials such as domestic wood burning or motor fuel. Significant atmospheric naphthalene concentrations have been measured among other PAH in busy traffic areas such as Toulouse [73], Paris [74] or Taiwan [75]. The exposition to this substance was demonstrated to present a risk in developing cancer [76, 77].

CH_2O : Formaldehyde is a colorless gas that was first originally found indoors [78], but due to photochemical processes and the combustion of biofuels [79], formaldehyde is also detected in polluted urban areas [80]. A deterioration of the respiratory system due to an amount of 50 ppb in the ambient air was observed by Krzyzanowski et al. [81]. A lifetime exposition to formaldehyde results in a reduction of the pulmonary function level of people of 50 years old [82]. Some study suggests that formaldehyde in ambient air may cause asthma [83].

HONO : Nitrous acid plays a key role in the troposphere. HONO photolysis is an important source of hydroxyl radicals. OH production rate due to the photolysis of nitrous acid was estimated at $(0.1 - 3) \times 10^7 \text{molecules.cm}^{-3}\text{s}^{-1}$ [84,85]. Also, measurements showed a strong correlation between nitrous acid and nitrogen dioxide levels in heavy traffic circulation [86]. Still some source and formation pathways processes of HONO are still unknown [87].

BrO : Bromine monoxide contributes to the destruction of the stratospheric ozone in the polar region [88]. Ozone depletion during springtime is associated with an increase of BrO concentration [89]. The reactions processes and the origin of its abundance are not fully understood [90]. However, a recent study explained quantitatively the removal of ozone and mercury from the troposphere in Arctic, and bromine atoms are believed to dominate the oxidation of mercury [91].

Monitoring air composition becomes challenging for the air quality, climate survey and long term monitoring [6]. Instruments should be able to evaluate trace gases concentrations on very short time and this over several decades. Different instruments have been developed to monitor the atmospheric trace-gases, running as ground based, balloon-borne, aircraft-borne to satellite measurements. Basically, two types of instrument exist for measuring the atmospheric trace-gas: Spectroscopic and chemical methods. The main methods currently used are listed below with some atmospheric measurement examples : several spectroscopic methods take advantage of the absorption transitions of the atmospheric molecules to retrieve their concentration. This is the case for the Fourier transform Spectroscopy (FTS) that is widely used for atmospheric trace gas monitoring [92, 93]. The method principle is detailed in section 1.4.

Differential Optical Absorption Spectroscopy (DOAS) is one of the main common remote sensing techniques used to monitor atmospheric trace gases [94], from ground-based passing, airborne measurements [95], to embarked satellites such as Sciamachy [96]. The method is presented in section 1.3.

Differential absorption Lidar (DIAL) was used for detecting many trace gas molecules such as NO_2 [97, 98] H_2O, NH_3 [99] O_3 [100] SO_2 [101] and aerosols in the troposphere . The book by Megie [102] details this method.

The following methods analyse the concentration of atmospheric molecules from air samples. Laser Induced Fluorescence (LIF) technique has been used to retrieve several atmospheric trace gases such as SO2 [103], in-situ NO_2 [104] and OH from the enhanced Fluorescence Assay by Gas Expansion (FAGE) method (see section 1.3).

Cavity Ring-Down Spectroscopy (CRDS) allows very sensitive concentration retrievals of the target gases. It has been used for investigating trace gas molecules such as methane ([105]), formaldehyde in ambient air [106], nitrogen dioxide [107–109] or HONO [109].

Cavity Enhanced Absorption Spectroscopy (CEAS). Engeln et al. [110] provides a detailed description of the method. In situ measurements were realised on dinitrogen pentoxide (N_2O_5) [111], HONO, NO2 [112], NO_2 and I_2 [113].

Non optical spectroscopic methods have also been developed to assess the concentration of atmospheric gaseous compounds and they are presented here below:

Chemical Ionisation of Mass Spectrometry (CIMS) is a non optical spectrometric in-situ method. Measurements of atmospheric trace gas such as OH or gas phase sulphuric acid H_2SO_4 [114], nitric acid HNO_3 [115] or ground base measure of radical HO2 [116] were realised from the troposphere to the stratosphere [117]. The review of Huey [118] is detailing this method.

Chemiluminescence was successfully used for O_3, NOx [119] in laboratory and ambient atmospheric conditions. Ridley et al. [120] realised in situ measurements of NOx in the stratosphere. The book

of Heard [121] provides details on this method.
Chromatography was used to perform in-situ ground based or aircraft measurements [122, 123]. The review of Helmig et al. [124] details the atmospheric measurement using this technique.
Mass spectrometric (MS) methods are routinely used to measure ambient concentration of trace gases. It is operated in situ on the ground, ships, aircraft and balloons or rockets. Huey et al. [125] assessed the concentration of HNO_3, NO_2, O_3, $HOCl, CF_2O$ and SO_2 in outdoor conditions using MS.
To improve the knowledge on these chemical reaction mechanisms, instruments sensitivity, accuracy and rapidity must be improved (time-scale of the lifetime of these molecules in atmospheric conditions). The next section presents the actual OH detection instruments.

1.3 OH detection

OH radicals have a short lifetime (1ms to 1s), and are present in a very low concentration (10^6 molecules.cm^{-3}) ; < ppt) [126] at ground level. As a result, OH radical is very challenging to measure.
Despite its fundamental tropospheric importance, the dynamics of radical OH and its abundance remain inaccurately known. The main techniques used for detecting OH radical are presented in this section. The review of Heard et al. [9] provides a detailed description of the existing method measuring the concentration of radical OH and HO_2. Three main spectroscopic methods are used to detect the tropospheric radical OH (see Table 1.1) : The Fluorescence Assay by Gas Expansion (FAGE), the chemical ionization mass spectrometry (CIMS) and the differential Optical Absorption Spectroscopy (DOAS). The first two methods are using air-sampling retrieval instruments and the third offers direct, remote measurement of [OH].

The fluorescence Assay by Gas Expansion (FAGE) method principle is presented in figure 1.4. The first measurement of radical OH using this method was made by Hard et al. [128] in the laboratory. The method is similar to the Laser Induced Fluorescence (LIF) spectroscopy method. A frequency doubled ns pulsed laser at 308 nm promotes the radicals to an excited state using the most intense absorption transition of OH corresponding to $A^2\Sigma \leftarrow X^2\Pi$ electronic transition. 308 nm corresponds to the transition with the greatest absorption cross-section of the molecule. The concerned vibrational and electronic levels are represented in figure 1.5. At 308 nm, Stevens et al. [129] demonstrated that the formed OH radical from the photo-dissociation of ozone was negligible using a frequency doubled dye laser of 50 mW average power (20 ns pulsed length). As the molecule spontaneously releases energy by fluorescence, its concentration can be obtained from the quantitative analysis of the emitted light fluorescence.

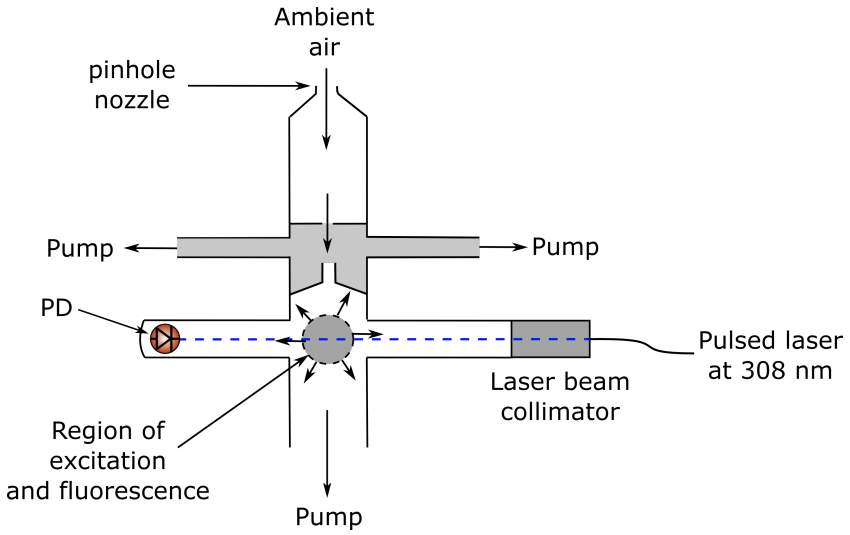

Figure 1.4: Fluorescence Assay by Gas Expansion (FAGE) experiment principle setup. An air sample enters the system from a pinhole nozzle and is directed towards the region of excitation. Low pressure environment is made in a cell to reduce the quenching of radical OH and thus increase the fluorescence lifetime and thus its detection. The sample is excited by a ns pulsed laser at 308 nm. The fluorescence is then detected by a photo-detector. The concentration of OH contained in the sample can be determined from the recorded fluorescence intensity. This figure was inspired by the publication of Chen et al. [127].

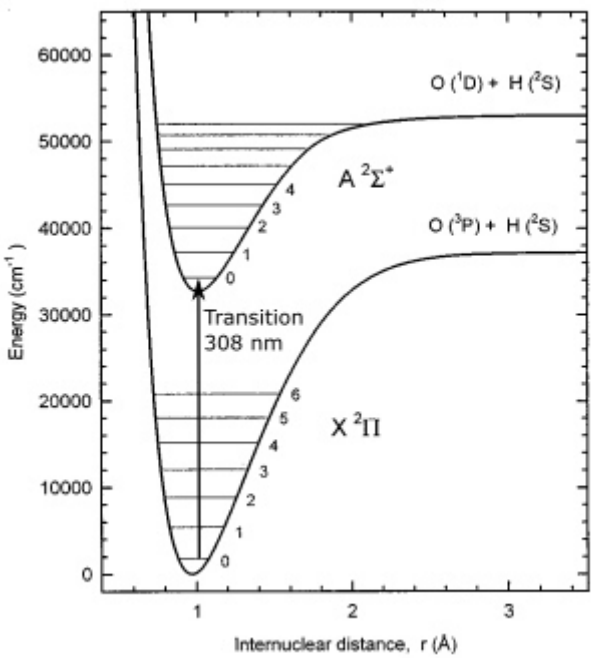

Figure 1.5: Simplified schema of the X (ground state) and A (first excited state) electronic energy states of OH and their vibrational energy levels. This figure is from the article of Luque and Crosley [130]. The electronic transition arrow at 308 nm was added.

The LIF method was first used in the stratosphere where conditions were more advantageous for detecting the fluorescence signal. At more than 10 km altitude, the detected fluorescence signal is higher due to higher OH mole fraction. First measurements were realised using hot air balloon by Stimpfle et al. [131, 132] and a few years later on ER-2 NASA aircraft (Wennberg et al. [133]). In the FAGE method, a gas sample is extended in a supersonic jet through a small nozzle into a low pressure chamber which reduces the quenching of radical OH by collision and thereby enhances the detection of the radical OH due to a longer fluorescence lifetime. The lifetime extension enhances the discrimination between the pulsed laser and the fluorescence signal [134]. This method has demonstrated a good sensitivity for the retrieval of the radical OH in the troposphere. $5,4.10^5$molecules/cm^3 were retrieved in 2.5 minutes of acquisition by Creasey et al. (Leeds University) [135] and less than 1×10^5 molecules.cm^{-3} in 30 integrated seconds from Stevens et al. [136] (Pennsylvannia State University USA). The main advantage of this instrument lies in the high sensitivity of the method. The drawbacks are mainly the cost, size, weight and the need of complex calibration of the instrument. This technique may suffer from the interference of other molecules such as the production of OH from ozone [129, 137, 138]. Also, the instrument has not been standardized for field use although design development is complete [139] commissioning a still in progress [140].

Chemical ionization mass spectrometry (CIMS) has demonstrated the highest sensitivity on the concentration of OH ($< 1.10^5$molecules/cm^3) in 300 s of acquisition time [141]. It is an indirect technique as it measures the product H_2SO_2 from the reaction of OH with SO_2. The high sensitivity of the method comes from the use of a mass spectrometer which is capable of identifying the molecules at concentration as low as 1 ion/cm^3.

The radical OH was measured with 10^6molecule.cm^{-3} precision in different locations of the Pacific using a CIMS instrument on-board an aircraft by Mauldin et al. [142–144]. A comparison from FAGE and CIMS instruments set on two different aircrafts was published by Eisele et al. [145]. The accuracy of the two methods was found to be in agreement with both results as the observed concentration was similar and the difference between the OH measurements from each instruments were within the uncertainties. The main drawbacks of the two sampling methods is the use of a nozzle and a pump vacuum system that may induce wall losses and interferences with other chemical components which are not all known [146].

The Differential Absorption Optical Spectroscopy (DOAS) is a method based on the absorption spectroscopy. The advantage of this spectroscopic method is that it does not require air sampling for measuring the air concentration of the molecules of interest. The first DOAS experiment for

retrieving tropospheric radical OH in outdoor condition was performed by Perner et al. in 1976 [147] with an averaged detection limit of 4.10^6 cm^{-3}. A frequency doubled dye pulsed laser source was emitted along 7.8 km, at 308 nm to take advantage of the strong absorption lines of OH.
The analytical method used for determining the concentration of the molecule from the retrieved spectrum is presented in figure 1.6. This robust method has been applied in this work and will be detailed in chapter 6. It consists in the separation of the "smooth" extinction component corresponding to the slow intensity variation with the wavelength of the spectrum that is due to atmospheric scattering of molecules, aerosols or instrumental effects. Thus, the so called differential spectrum contains only the sharper absorption molecular features of molecules. The simultaneous detection of the transition lines of the targeted molecules are usually obtained using either a laser, the direct or scattered light of the sun as light source and a grating system coupled with a CCD camera.

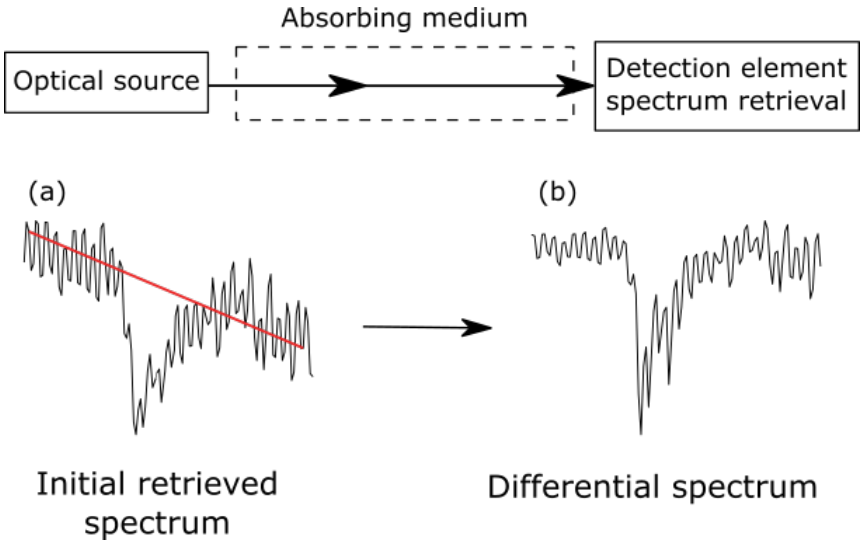

Figure 1.6: Differential Optical Absorption Spectroscopy principle. The light from an optical source is retrieved after it has propagated through an absorbing medium. The spectrum of this light is then recorded either using a grating spectrometer or by FTS. (a) Initial spectrum retrieved from the detection system. The linear red trace corresponds to the slow variation part of the spectrum. (b) Differential spectrum (slow variation part removed). A fit function can be used on the differential spectrum for retrieving the concentration of the molecule along the optical pathway using the Beer Lambert law (equation 1.5). Figure was inspired from the book dedicated to DOAS written by Platt and Stutz [10].

One of the main advantage of DOAS is that the method is self-calibrated from the Beer Lambert law given in equation 1.5. The concentration of the molecule can be determined from the initial laser intensity I_0, the optical path L, the absorption cross-section of the molecule $\sigma_{OH,\lambda}$ and the detected laser intensity after propagation I.

$$[OH] = ln\left(\frac{I_0}{I}\right)/(\sigma_{OH,\lambda}L) \tag{1.5}$$

The variations of $\sigma_{OH,\lambda}$ due to pressure and temperature fluctuations must be taken into account. Details can be found in the book of Platt and Stutz [10].

Different configurations of DOAS instrument exist. These configurations are presented in figure 1.7.

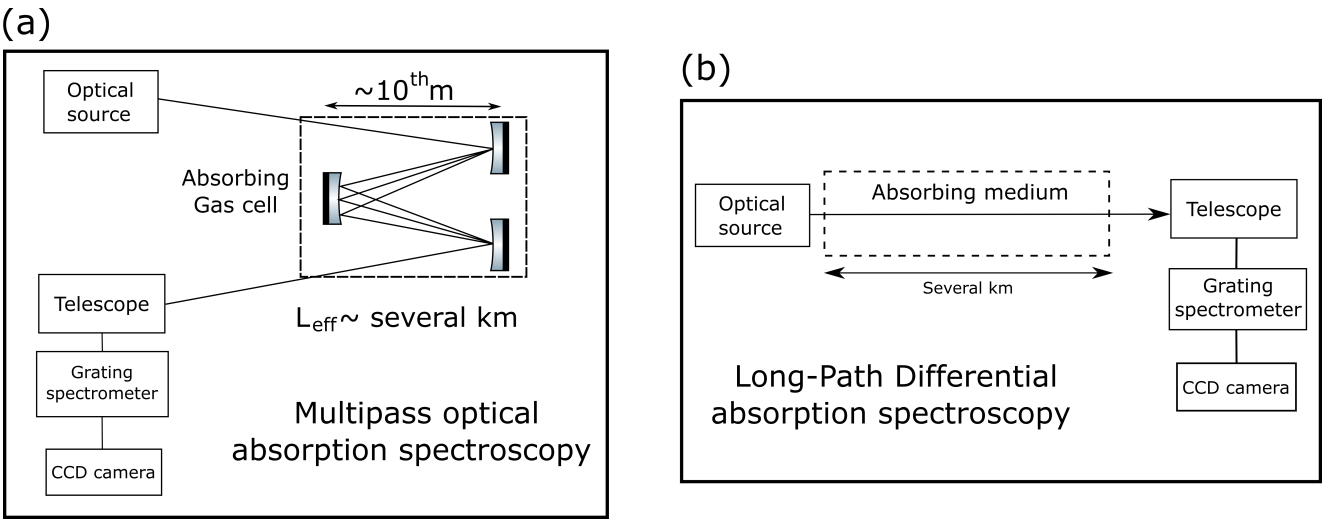

Figure 1.7: (a) Multipass Optical Absorption Spectroscopy principle. (b) Long-Path Differential Optical Absportion Spectroscopy.

The MOAS that stands for Multipass Optical Absorption Spectroscopy, is an in-situ spatially and temporally resolved instrument using an open and multi-folded absorption path. The length of the linear multi-pass absorption cell is more compact than for the Long-Path DOAS (LP-DOAS) and DOAS experiment. The effective path length obtained by Armerding et al. [148] attained of 1.2 km effective path length with 200 reflections in the cell that is only a few meters in length. The relatively compact cell allows to have a stable tropospheric chemistry environment. The measurement of $2 - 5.10^5$molecules.cm^{-3} was obtained in 1 minute monitoring time. This instrument has demonstrated to be able to simultaneously measure the concentration of $SO_2, CH_2O, C_{10}H_8$ and radical OH at 308 nm in a local outdoor tropospheric environment [149]. LP-DOAS takes DOAS data over several kilometres of optical path to increase the sensitivity [150–152]. For instance Dorn et al. [153] used 3 km of optical path using a folded optical multiple reflection cell of 20 m between the curved mirrors to retrieve the concentration of radical OH in 15 minutes of acquisition time.

Monitoring on a global scale using DOAS instrument embarked on satellites has been realised by the Global Ozone Monitoring Experiment instrument (GOME) for NO_2 [154], ozone [155] and for bromine monoxide [156]. The advantage of this method is the absence of complex calibration as well as the absence of complex system for retrieving an air sample which is a source of molecule

losses. The limitations are the lower sensitivity attained compare to the two other methods, a poor spatial resolution for the DOAS and LP-DOAS cases and a sensitivity to air turbulences that introduce optical noise [151]. However, scanning DOAS system (MAX-DOAS) overcomes this limitation [157]. Better assess the concentration dynamic of atmospheric molecules would improve the common understanding of many chemical reactions that are crucial in atmospheric pollution and climate processes.

The state of the art performance of some of the currently-employed methods for monitoring atmospheric OH radical in terms of sensitivity limit and acquisition time are summarized in table 1.1.

Table 1.1: State of the art experiment of the radical OH detection methods.

Detection method	Sampling or remote-sensing	Detection limit [molec.cm^{-3}]	Acquisition time	References
FAGE	Sampling method	1.10^5	30 s	[129]
CIMS	Sampling method	$< 1.10^5$	300 s	[141]
LP-DOAS	Remote-sensing method	$1,5.10^6$	300 s	[158]
LP-DOAS (chamber)		$1,5.10^6$	200 s	[152]
MOAS		5.10^5	300 s	[159]

Despite the high sensitivity of the air sampling methods CIMS and FAGE, these methods suffer from biais or artefacts linked to the air sampling method. Nowadays, all the DOAS measurements on radical OH are realised in atmospheric chambers [160,161] . As a consequence, there is currently a lack of direct in-situ and remote measurement of radical OH. This remark has initiated reflection on the sensitivity and precision attainable from DCS to detect this molecule in-situ. Our investigation with dual comb spectroscopy aimed to evaluate its capacity to detect atmospheric ambient radical OH without air sampling and in-situ measurement from a remote location.

Dual-comb spectroscopy is a Fourier transform spectroscopy technique, that uses the beat interferences between two coherent pulse trains to retrieve a broad optical spectrum. The advantage of the dual comb spectroscopy method is its capacity to retrieve a highly resolved broad spectrum in a short acquisition time as it was demonstrated by several teams presented in section 1.4. The spectral accuracy, resolution and acquisition time are set and controlled by the laser radiation rather than the instrument. The spectral resolution is thus limited by the spacing laser comb modes. As a comparison in the IR, DCS method can have a spectral resolution of 100 MHz which is at least ten times better than the spectral resolution reachable by DOAS instrumentation limited by a grating spectrometer (GHz range of spectral resolution). The dual comb spectroscopy has been demonstrated to be very well adapted for monitoring trace gas molecules in the atmosphere [2,162]. It has been demonstrated that the DCS is immune to atmospheric turbulences due to its very short sampling rate $<$ ms [163] which is a major asset for outdoor measurements. It has already been used to monitor the radical OH in a controlled combustion environment in the IR region [164]. A

comparison of the DCS methodology with the existential methodologies presented in this section in terms of sensitivity, rapidity and accuracy in the UV range was performed and is presented in chapter 3.
The DCS method needs a low phase noise laser source to keep a relative coherence between the two lasers and therefore to be able to retrieve a spectrum with sufficient frequency accuracy, resolution and signal to noise ratio. Having two laser sources with high mutual coherence is challenging and usually encountered in the context of a metrology lab environment where skill-set are required. In this thesis, is presented the development of a single bidirectional cavity laser source emitting two pulsed lasers that could be more easily used outdoor to detect in-situ atmospheric trace gas. The laser source of this DCS method is made to assess the concentration of these molecules remotely in real atmospheric condition. The state of the art of the DCS measurements and experiments is presented in next section.

1.4 Dual comb spectroscopy

Dual comb spectroscopy (DCS) takes its origin from Michelson Fourier transform spectroscopy. The two spectroscopic methods principles are represented in figure 1.8.

A conventional Fourier transform spectroscopy instrument is based on the interferometer originally developed by Michelson [165]. The instrument is represented in panel (a) of figure 1.8. In its simplest form, it is composed of two perpendicular mirrors and a beam splitter. The instrument is designed to split a collimated light source that can be coherent or incoherent, towards a stationary and a moving mirror. As the moving mirror is continuously displaced, a phase difference between the two propagating radiations is created. The two light beams are then re-combined together and are directed through an absorbing medium before being detected. Due to their phase difference, an interference figure corresponding to the intensity as a function of the path difference is recorded by a detector. A Fourier transform is applied to this interferogram to reveal the spectrum and highlights the transition lines of the absorbing molecules. More details on the FTS experiments can be found in the book of FTIR by Griffith and Haseth [166].
In dual-comb spectroscopy methodology, the path difference is not created by an arm length difference but is created by the use of two femtosecond pulsed lasers, where the repetition rate of the first laser is slightly shifted with respect to the second one. Dual-comb refers to the spectral nature of the pulse trains that are composed of a broad spectrum with equally spaced frequencies occuring at intervals determined by the frequency repetition of the laser. A difference in frequency repetition between the two trains of pulses gives rise to an interference pattern that is recorded on a photo-diode sensor. Each pair of pulses that overlap each other with a different phase shift, build the interferogram. The Fourier transform of this interferogram allows the retrieval of a spectrum

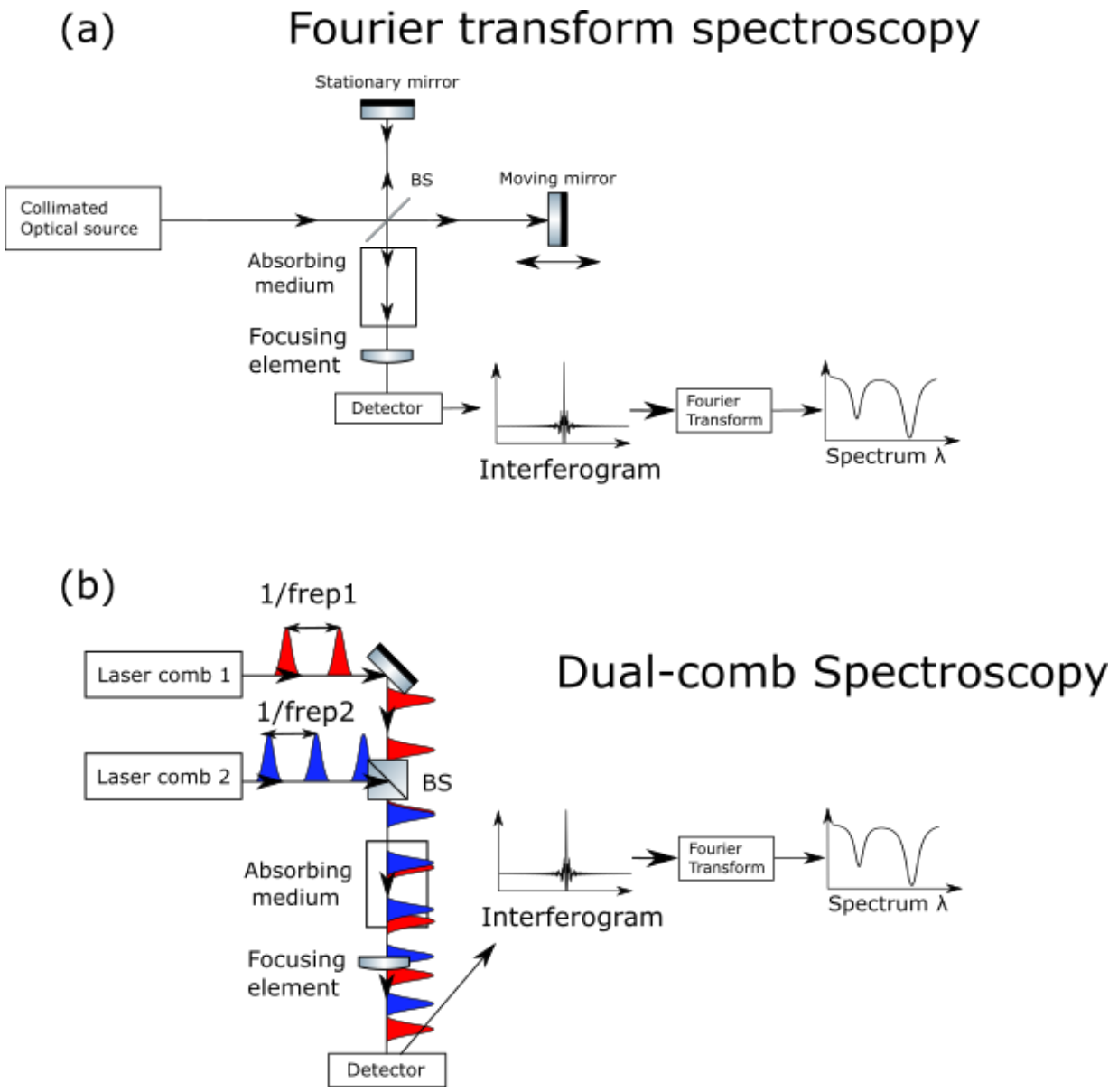

Figure 1.8: (a) Presentation of a conventional Michelson Fourier transform Spectrometer (FTS) method and (b) the Dual Comb Spectroscopy (DCS) method. BS stands for Beam-Splitter. The phase difference is created by a physical displacement of one mirror in the FTS method and by the frequency repetition difference between the two lasers in the DCS method. The interference between these two sources is then recorded and a Fourier transform is applied to retrieve the corresponding spectrum.

similar to the one contained in the emitted pulses, but down-scaled to the radio frequency domain. The spectrum is thus recordable by means of a fast photo-detector. The principles of dual comb spectroscopy are detailed in chapter 2. The force of the method lies in the fact that it is has no moving mechanical parts which removes mechanics noise and the limitations linked to acquisition time due to the velocity of the moving mirror in classic Michelson interferometry. Also, it is capable

of retrieving a broad spectrum (up to 140 THz was obtained with an averaged time of 22 minutes by Okubo et al. in 2015 [167]) and potentially in a very short time (13 µs to retrieve successive 60 GHz spectra by Millot et al. [168]), with a resolution that reached the spectral comb spacing (typically 100 MHz).

The first experiment using the heterodyne signal from two comb lasers was realised for optical coherence tomography by Lee et al. in 2001 [169]. This new method had a high scanning speed of 12.5 km/s, a repetition rate of 500 kHz and a spatial resolution of 100 µm. This was several tens to several hundreds times faster than conventional existing methods (pulsed laser repetition rate of 2 kHz and scanning speed of 20 m/s for the fastest conventional methods). Keilmann et al. [170] established the proof of principle of the DCS method in the mid-IR (8-13µm) and retrieved the transition lines of uncontrolled evaporating trichloroethylene gas. A spectrum of more than 5 µm width could be retrieved in 100 µs. In these pioneer studies, the absence of mechanical parts allows the experiment to be ten to hundred times faster than usual Fourier transform methods. One year after, DCS was used to monitor the concentration of NH_3 in a gas cell over several seconds of continuous measurement (Schliesser et al. [171]).

More recently, it has been demonstrated in laboratory that molecules such as CO_2, CH_4, C_2H_2 and vapour H_2O in multi-pass gas cell could be simultaneously measured by DCS in the mid IR using an ultra broad spectrum (40 THz by Zolot et al. in 2012 [172]). A representation of the retrieved spectrum is given in figure 1.9. Okubo et al. [167] recorded a broadband spectrum of 140 THz width at 1.5µm with a sub-Doppler resolution of 43 MHz. Several laboratory experiments have been performed using DCS in different wavelengths, covering the electromagnetic spectrum from 300 nm to 6 mm (THz region) [7, 8]. The sub-THz region was investigated by Yasui et al. [173] and demonstrated the retrieval by DCS of a detailed spectral structure with a resolution of 81.8 MHz and a spectral range of up to 1 THz. At shorter wavelengths, passing by the Mid-IR range (between 3.27 and 3.4 µm by Zhang et al. [174]) the transition lines of Rubidium 87 were recorded by means of Doppler-free two-photon excitation dual comb spectroscopy at 388 nm by Meek et al. [175].

DCS has also been applied to short-lived species such as highly reactive oxidant radicals. Recently, Hayden et al. [164] monitored in situ OH radical at 1491 nm using DCS in a combustion environment at 1700 K in real time and with high accuracy ($1.6.10^{-5}$ mole fraction).

DCS measurement in outdoor turbulent air path using reflective mirrors to have an absorption pathlength over 2 km was demonstrated by Rieker et al. in 2014 [2]. A spectrum over 70 nm centred at 1635 nm contained spectral information on CO_2, $C^{13}O_2$, CH_4, HDO and H_2O; the authors obtained their 2 km long path-integrated concentration with high accuracy (respectively 0.7 ppm, 1.7 ppm, 3 ppb, 130 ppb and 22 pm). They experimentally demonstrated that over several kilometres, the relative noise between the two combs were immune to the amplitude and phase

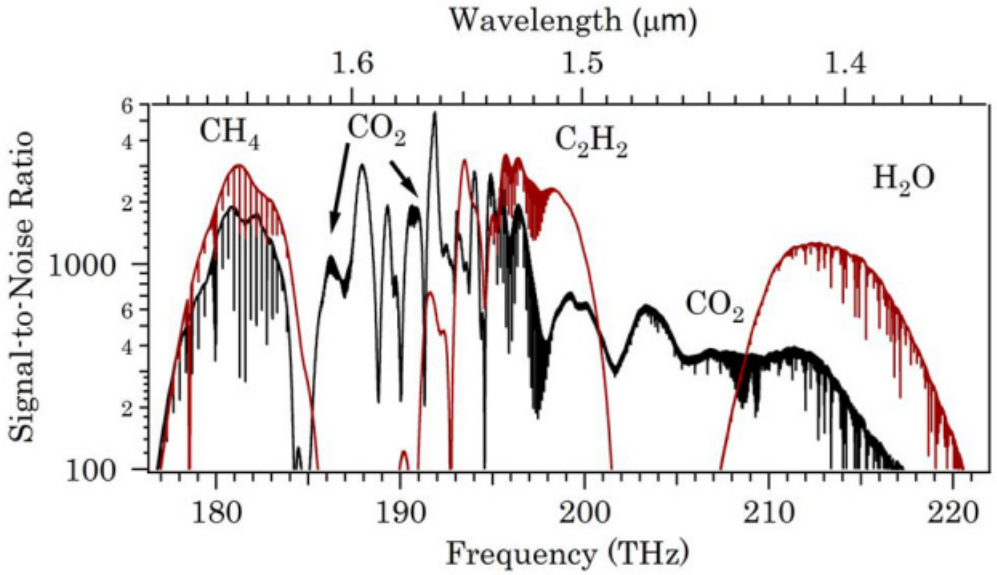

Figure 1.9: Spectral signal to noise ratio retrieved measured over the full spectrum (black line) and for a filtered spectrum (red line). The 180-220 THz spectral domain (1.36 µm-1.66 µm) is 40 THz (300 nm) large and contain 4.10^5 spectral elements. This figure was obtained from the results presented in the article of Zolot et al. [172] and displayed here.

fluctuations created by the atmospheric turbulence. This is an important aspect that differentiates the DCS from other remote sensing detection methods. Waxman et al. [176], monitored the path-integrated concentration of CO_2, CH_4, H_2O and HDO for several weeks over the city of Boulder. From these measurements, they were able to put a figure on the yearly CO_2 emission ($6.2 \pm 2.2.10^5$ metric tons) of the city. Dual comb spectroscopy have also been used at 3.4 µm to monitor daytime outdoor organic compounds such as acetone, isopropanol, ethane and methane [177]. The average concentration over the optical pathway was obtained with a sensitivity of respectively 5.7 ppm, 2.4 ppm, 0.4 ppb and 4 ppb through 1 km, and with 1 minute recording times.

Several studies showed that the method can be used for mapping trace gas molecules locally and in large open air areas. Cossel et al. [162] produced a horizontal and vertical mapping of multiple trace gas molecules simultaneously, using a flying helicopter reflector (unmanned aircraft system). The spatial mapping in real time of trace gas at a given location has industrial applications, for example to monitor methane leakage which is of main concern for safety, air pollution, climate change and costs reasons [178]. Coburn et al. [3] realised field deployment of DCS in industrial environment. They demonstrated that the DCS method was able to continuously and autonomously monitor the fluxes of trace gas molecules across km range of optical path. DCS was also continuously performed in a moving environment. Sinclair et al. [179] demonstrated that the optical coherence could be maintained with a portable all-fiber frequency comb device in a moving vehicle (up to 0.5g) and noisy environment.

It can be noted that the molecular phase information can be obtained with an asymmetrical geometry configuration. An asymmetrical configuration has one laser comb emitted through the gas cell and one emitted directly to the detector (local oscillator). The corresponding heterodyne signal is then recorded on the photo-diode. Giorgetta et al. [180] showed that the phase spectrum retrieval had a similar SNR, and sensitivity as the study of Rieker et al. of 2014 [2].

To our knowledge, no DCS experiment measuring radical OH on ambient real atmospheric condition has been realised in the UV range. Taking this challenge was part of my PhD work where I could develop and realize an home made bidirectional laser cavity. Several reasons support the development of our own laser sources in the UV range :
Several spectroscopic studies used the absorption cross-section of radical OH in the near infrared region (NIR) in combustion environment at 1491 nm [164], at 1515 nm [181] and at 1560 nm [182]. The advantage of undertaking an experiment in the NIR is the easy availability low cost of laser sources and optical components. The main drawback is the lower ro-vibrational cross-section intensity of OH (max of 10^{-20} cm^2 between 1400 and 1500 nm) compared with the electronic transitions $A^2\Sigma^+ \leftarrow X^2\Pi$ at 308 nm (max of $2.10^{-16}cm^2$) presented in figure 1.5. Also, the presence of water vapour transition lines in the NIR interfere with the OH absorption lines which reduces the sensitivity of the experiment. Because OH radical concentration in a combustion environment is several order of magnitude higher than in ambient air, its detection in the NIR becomes feasible. For comparison, atmospheric concentration of OH is typically 10^6molecules.cm^{-3}, and superior to 10^{16}molecules.cm^{-3} from a combustion process.
The development of a Ti:sa mode-locked laser coupled with a harmonic generator was chosen in this thesis to assess OH transition lines in the UV range. It has been chosen for its high laser output power at 800 nm which allows access to the UV by second or third harmonic generation. Also, this laser source is able to emit a highly resolved broad spectrum with a low phase/amplitude noise. This aspect is detailed in chapter 3. The dual comb laser can be emitted from a single laser cavity (see chapter 2). As the two laser beams are emitted from the same laser cavity, they experience similar amplitude and phase noise which results in a low relative noise and a high mutual coherence between the two trains of pulses. This has the advantage of avoiding the need for complex stabilizing electronic systems. The development of a compact, robust and transportable UV spectrometer can therefore be considered using UV-DCS.

Bidirectional Ti:sa laser cavities are currently not commercially available. Therefore, there are two solutions. Either the laser is custom-made in industry or the laser is developed in the laboratory. Building a home-made laser presents some advantages. The knowledge of the laser cavity details allows for versatility. Any dysfunction is also easier to fix. The laser source can thus be made compact, robust and adaptable to outdoor environment. Its characterisation will allow the control

of the laser source. Also, it is scientifically interesting as to the best of our knowledge, a Ti:sa UV-DCS laser source has never been produced yet.

1.5 Conclusion

The influence of the trace gas molecules on climate, air quality and human health was presented in the first section. The importance of several atmospheric molecules of interests having strong absorption transition lines in the UV range such as SO_2, NO_2, H_2CO, BrO, OClO, $C_{10}H_8$ and OH were presented. A focus was made for radical OH that is considered as a key compound of the atmosphere composition. The principle of the main detection methods monitoring atmospheric radical OH such as FAGE, CIMS and DOAS were presented as well as their sensitivity and acquisition time. The dual comb spectroscopy state of the art was presented highlighting that DCS appears highly relevant for measuring trace gas molecules in outdoor in situ condition. The DCS offers the immunity to atmospheric turbulences, with comparable sensitivity with the current methods.
In the next chapter, a description of the dual comb spectroscopy method principle is detailed.

Chapter 2

Dual Comb Spectroscopy

2.1 Introduction

Dual comb spectroscopy is a recent spectroscopy instrumental development. The pioneering work published by Schiller in 2002 [183] demonstrated for the first time a new approach for spectroscopic measurements and presented the fundamental concepts of the DCS method. The DCS method takes advantage of the femtosecond laser comb development that began in the late 1990s and which revolutionized optical metrology [184–186]. Many applications have risen from this new instrument : the femtosecond laser controlled by stable atomic clocks appears ideal for long term calibration of astronomical spectrographs [187]. In the ultra-broadband coherent communication field, the optical frequency comb laser has appeared advantageous because of its simplicity to be assembled, its robustness, and its available repetition rate [188]. In the molecular spectroscopic domain, the use of its broad spectrum with equally spaced modes that can be viewed as a "ruler", has brought a new instrument for monitoring with accuracy atomic and molecular transition. The easiest approach is given by direct frequency comb spectroscopy which consists of exciting simultaneously several transition levels of an atom or a molecule using a comb laser in a one or two photons absorption process. The fluorescence is then recorded with a photo-detector [189]. Other methods using frequency combs such as comb spectroscopy using a dispersive grating [190], external optical cavity [191], Ramsey-comb spectroscopy [192] or Michelson based frequency comb Fourier transform spectroscopy [193] have been developed for molecular spectroscopy.
DCS methodology, exploits the very fine spectral resolution of the frequency combs emitted by a laser. The laser emission assures an extraordinary stability of the resonant spectral spacing and of the spectral width of each modes of the comb. These optical frequencies are currently non-measurable with the photonic detectors available. The idea is to take advantage of the beating of the two frequency comb sources emitting at different repetition rate produced by Vernier or Moiré

interferences to retrieve the spectral information of absorbing molecules present in the pathway of the laser beam as it is presented below.
DCS methodology formalism is presented in this chapter where three essential parameters of DCS will be defined, namely f_{rep}, Δf_{rep} and in fine the spectral resolution ν_{res}. Given these quantities, it is possible to extract from this interference phenomenon the spectroscopic data of the molecules absorbing along the optical path of the two comb lasers. The retrieval procedures will be presented later in chapter 6, where laboratory measurements are analysed. Furthermore the DCS description in the different frequency domains (optical, RF) will help to discuss the mapping between both frequency domains. First, a brief description of the emission of one femtosecond pulse is presented in the temporal and frequency domain. Then, section 2.3 discusses the importance of f_{rep} and Δf_{rep} for DCS. The state of the art of the approaches for maintaining a relative coherence between the two combs of the methodology is given in the last section.

2.2 Dual Comb Methodology principle

DCS is based on the interference of two laser combs. The Ti:sa laser is considered in this chapter for the description of the dual comb spectroscopy principle. Each of the frequency comb laser source emits pulses at a specific rate given by the length of the cavity : $f_{rep} = \frac{v_g}{L}$, with v_g the group velocity of the pulse laser in air and L the length of the cavity for one pulse round trip. A mode-locked Ti:sa laser emits pulses of typically hundreds of femtoseconds. This results from the broad gain bandwidth phase-locked emission of the Titanium-sapphire. From pulse to pulse, a phase shift $\Delta\phi$ is created by a group and carrier velocity difference. This phase shift induces the "carrier-offset frequency" f_0 (or f_{CEO}; CEO for Carrier Envelope Offset) which corresponds to a global shift of the spectrum in the spectral domain. $\Delta\phi$ and f_0 are linked by the mathematical relationship given in equation 2.1.

$$f_0 = f_{rep}\Delta\phi/2\pi \tag{2.1}$$

Figure 2.1 represents the pulse train emitted from a mode-locked laser and its respective spectrum. The theoretical formalism of the spectrum of a fs mode-locked laser combs source is extensively described by Ye et al. [194]. The spectrum associated with the pulse train is composed of equally spaced frequencies that are created from the longitudinal modes of the laser cavity. These frequencies are commonly called "teeth" of the "comb". The spectrum of a train of femtosecond pulses can therefore be considered as a "rule" in the spectral domain. The frequency of mode number n is fully determined by the so-called "comb equation" given in equation 2.2 :

$$\nu_n = f_0 + n \times f_{rep} \tag{2.2}$$

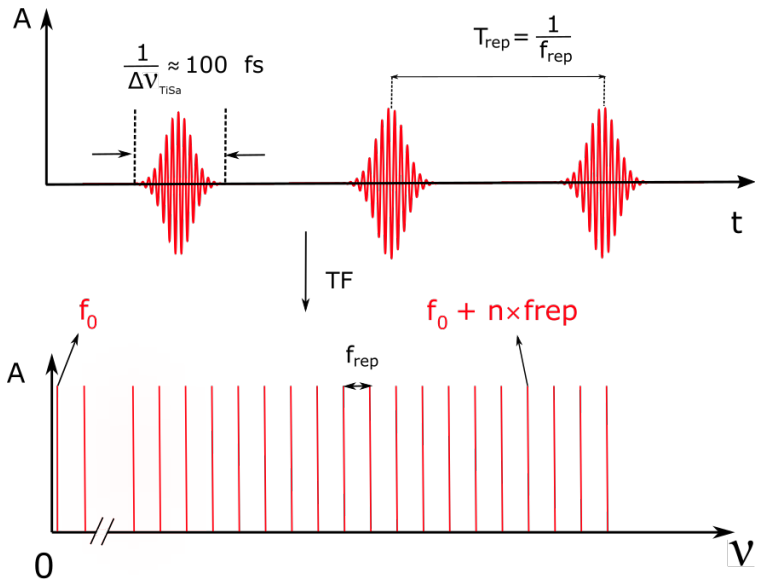

Figure 2.1: Description of the pulse-train emitted by a mode-locked laser in the temporal and frequency domains. A is the amplitude of the pulses train. $\Delta\nu_{Ti:sa}$ is the Gaussian FWHM of the laser spectrum. The emitted frequencies are discrete and evenly spaced, separated by f_{rep} the pulse repetition rate. T_{rep} is the time delay between successive pulses.

The DCS methodology uses both the time and the frequency domains of two laser combs. These two domains are described in the next two sections.

2.2.1 Time Domain description

The principle of the DCS method is summarized in figure 2.2. Two femtosecond laser pulse trains are propagated toward a beam-splitter that combines the two radiations.

The first laser emits femtosecond pulses at a rate of f_{rep1}. The second comb has a pulse rate f_{rep2}, slightly shifted by Δf_{rep} such that $f_{rep2} = f_{rep1} + \Delta f_{rep}$. The two laser beams are co-propagated toward an absorbing medium. The interaction with the absorbing medium is imprinted in the pulse. During the propagation of the pulse train, the absorbing medium induces a coherent reemission of the initial electric field of the pulse in the ps range due to the resonance with the ro-vibrational states of the absorbing molecules. Because all the molecules are absorbing at the same time, they initially rotate in phase and radiate at the same mode as the laser source. As the Ti:sa laser source is spectrally broadband, the molecule can be excited at different energies. This creates a molecular population in several rotational/vibrational/electronic states, from which

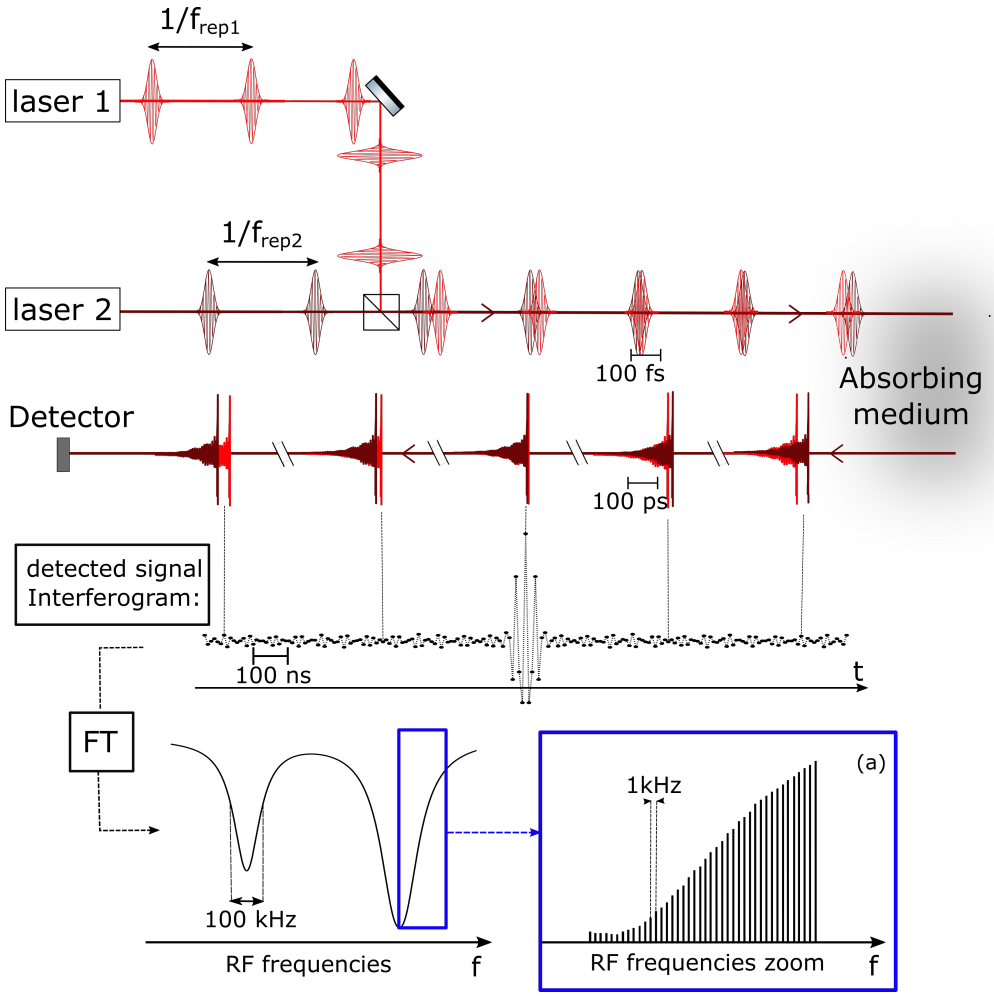

Figure 2.2: Schematic representation of the Dual Comb Spectroscopic method. Two pulse trains are generated with slightly different repetition rate. The two pulses trains are then combined to propagate through an absorbing medium. A beat signal is obtained from the successive intensity detection of thousands of relative phase-shifted pulses. The spectrum in the radio frequency domain is retrieved by a Fourier transform applied to the interferogram (square a)).

spontaneous emission is out of phase. As the absorption frequencies are quantified, the reemission of the molecule is incrementally re-phased a time later and so on. This creates the echoes in the pulse decay propagating through the absorbing medium that is represented in the figure 2.2. This time decay is called the Free Induction Decay (FID) [195, 196].

The interference pattern generated by the successive frequency combs of both lasers is created on the detector. The frequency beats are in the radio-frequency (RF) domain which is several orders of magnitude lower than the optical frequencies. By applying numerically a Fourier transformation to this interferogram, a spectrum in the RF domain is obtained. The beat notes are equally separated by Δf_{rep}. This spectrum is referred to as the RF-comb. Any absorption lines located in the frequency range of the laser spectrum can be observed as depicted in the figure 2.2.

The description of the dual comb methodology should be made in two time frames : the laboratory time frame and the optical frame. The interferogram (see figure 2.3) is described in the laboratory time frame. Each point of the interferogram corresponds to the total intensity of two superposed pulses from laser 1 and 2. Thousands to millions of pulses are necessary to measure a full interferogram. A modulation of the measured interferogram intensity is observed as the phase delay between the two pulses is continuously shifted from one couple of pulses to another. The time gap between each pulses couple is given by the inverse of the pulse rate : $\frac{1}{f_{rep1}} \approx \frac{1}{f_{rep2}} \approx \frac{1}{f_{rep}}$. In the optical time frame we should consider that the pulses of laser 1 and laser 2 are successively time delayed by a time increment given by $\frac{1}{f_{rep1}} - \frac{1}{frep2} \approx \frac{\Delta f_{rep}}{f_{rep}^2}$. It is induced by the repetition rate difference Δf_{rep}. The scaling factor $a = \frac{f_{rep}}{\Delta f_{rep}}$ can be used to rescale one time frame to another.

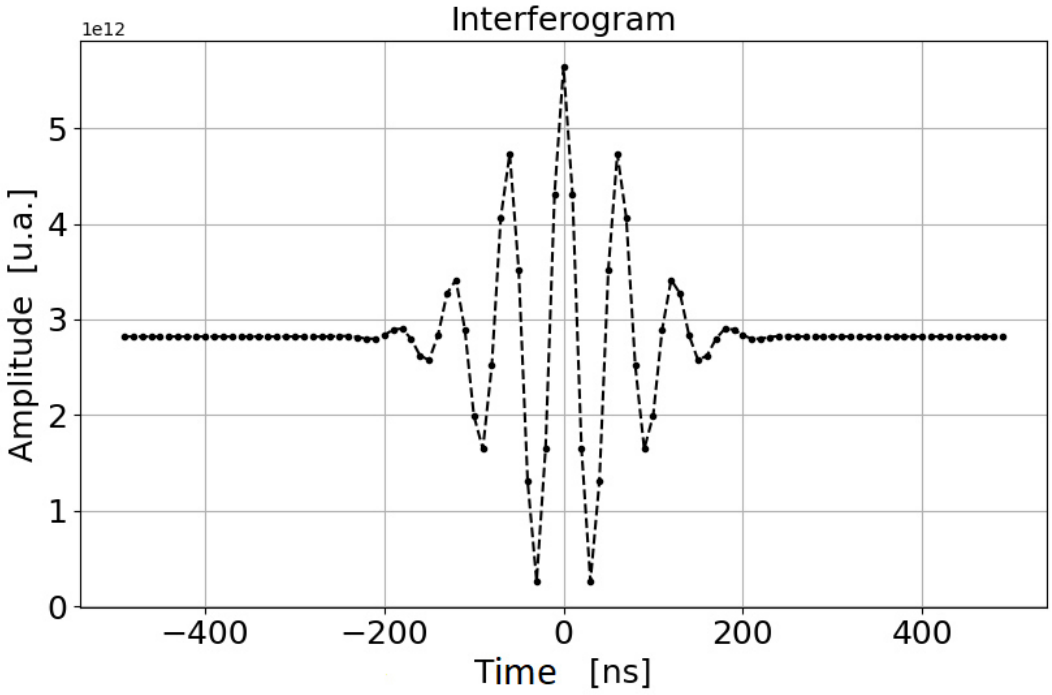

Figure 2.3: Simulation of one interferogram in the laboratory time scale. Each points represents the result from the superposition of two combs. The parameters used are the following : frequency repetition f_{rep} = 100MHz, difference in frequency repetition Δf_{rep}=200Hz, duration of the pulse : τ = 200 fs.

To describe the resulting interferometric electric field recorded by the detector, the description has to start from the description of the electric field propagating through the atmosphere. The mathematical expression of the electric field of the train of pulses of laser 1 is phase shifted and absorbed as it passes through an absorbing medium is given in equation 2.3.

$$E_1 = \sum_n E_{01} e^{2\pi i (f_{01} + n f_{rep}) \times t} e^{-\delta(\nu_n) - i\phi(\nu_n)} \tag{2.3}$$

E_{01} is the amplitude of the electric field emitted. f_{01} is the frequency offset of the comb and ν_n is the frequency mode of number n. The phase shift and the optical extinction at the n mode induced by the absorbing medium are given respectively by $\phi(\nu_n)$ and $\delta(\nu_n)$ and are expressed in equation 2.4 and 2.5.

$$\phi(\nu_n) = \kappa \times (-n\prime z) \tag{2.4}$$

$n\prime$ represents the real part of the atmospheric refractive index. z is the distance from an origin. κ is the wavenumber of the carrier-frequency. $\phi(\nu_n)$ is the dispersion part of the wave (i.e the spectral dependence of the phase velocity).

$$\delta(\nu_n) = \int_0^L \sigma(\nu) \times C dl \tag{2.5}$$

$\sigma(\nu)$ is the absorption cross-section of the molecule at the frequency ν, C is its concentration and L is the optical path length.

The mathematical expression of the superposition of two electrical trains of pulse E_1 and E_2 with slight relative Δf_{rep} frequency difference is given in equation 2.6. In the following, we consider only beating notes involving laser modes of the closest mode number n.

$$E_1(t) + E_2(t) = \sum_{n=0}^{\infty} E_{01} e^{2\pi i (f_{01} + n f_{rep1}) \times t} e^{-\delta(\nu_{1n}) - i\phi(\nu_{1n})} + E_{02} e^{2\pi i (f_{02} + n f_{rep2}) \times t} e^{-\delta(\nu_2 n) - i\phi(\nu_2 n)} \tag{2.6}$$

A photo-diode is required to observe interference between the two pulses trains. The electric current emitted by the photodiode is proportional to the intensity of the light. The resulting detected signal observed by the photo-diode can be expressed as follow :

$$I \propto (E_1 + E_2) \times (\overline{E_1 + E_2})$$

$$I(t) \propto \sum_{n=0}^{\infty} A_{1,n}^2 \times e^{-\delta(\nu_{1n})} + A_{2,n}^2 \times e^{-\delta(\nu_{2n})} \tag{2.7}$$

$$+ \ 2A_{1,n}A_{2,n}e^{-\delta(\nu_{1n})-\delta(\nu_{2n})}cos\Big(2\pi(\Delta f_0 + n\Delta f_{rep}) \times t - \Big(\phi(\nu_{1n}) - \phi(\nu_{2n})\Big)\Big) \tag{2.8}$$

$$+ \ 2A_{1,n}A_{2,n+1}e^{-\delta(\nu_{1n})-\delta(\nu_{2n})}cos\Big(2\pi\Big(-\Delta f_0 - n\Delta f_{rep} + f_{rep2}\Big) \times t - \Big(\phi(\nu_{1n}) - \phi(\nu_{2n})\Big)\Big) \tag{2.9}$$

$$+ \ 2A_{1,n}A_{2,n-1}e^{-\delta(\nu_{1n})-\delta(\nu_{2n})}cos\Big(2\pi(\Delta f_0 + n\Delta f_{rep} + f_{rep2}) \times t + \Big(\phi(\nu_{1n}) - \phi(\nu_{2n})\Big)\Big) \tag{2.10}$$

$$+ \text{ Higher frequency Modulation terms}$$

The measured intensity is composed of a constant part (2.7) and modulation components. In the expression of I(t), the spectral terms are expressed as a function of the frequency repetition difference Δf_0 and Δf_{rep} and not in terms of absolute frequencies (f_0 and f_{rep}). Thereby, the intensity variations I(t) are measurable with a fast detector. The first order interference is given by the equation (2.8), whereas equations (2.9) and (2.10) are modulation components created by interferences between modes of different number n for the two lasers. These terms must be later on filtered out as they contain no additional spectral information. As the higher terms are filtered, the time dependant and varying signal is given by the equation 2.11.

$$I(t) \propto 2A_{1,n}A_{2,n}e^{-\delta(\nu_{1n})-\delta(\nu_{2n})}cos\Big(2\pi(\Delta f_0 + n\Delta f_{rep}) \times t - \Big(\phi(\nu_{1n}) - \phi(\nu_{2n})\Big)\Big) \tag{2.11}$$

In the context of a symmetric set-up as depicted in Figure 2.2, and considering only the modes of the same order (beat created by the modes number of laser 1 and 2 = n), the following hypothesis is made : The absorption $\delta(\nu_{1,n})$ and phase shift $\phi(\nu_{1,n})$ on the mode n of laser 1 are equal to the absorption and phase shift of the mode n of laser 2. This is fair assumption as the two trains of pulses go along the same optical path in the symmetric geometry and because the molecular absorption linewidth are much wider than the relative comb tooth spacing ($<< f_{rep}/2$). Therefore, the equation 2.11 can be simplified into the equation 2.12

$$I(t) \propto 2A_{1,n}A_{2,n}e^{-2\delta(\nu_n)}cos\Big(2\pi(\Delta f_0 + n\Delta f_{rep}) \times t\Big) \tag{2.12}$$

It follows that the spectral sensitivity is doubled in this symmetric configuration. However, the information on the phase $\phi(\nu_n)$ is lost. An asymmetric setup would provide this information as

only one train of pulse passes through the absorbing medium and therefore the phase term would not cancel out in the modulation term.

This mathematical demonstration is correct in the case where the spectral bandwidth of the laser is in a spectral range where the two beating laser modes of number n (of laser 1 and 2) are the closest. As it will be detailed in the next section, a mode n of higher order of laser 1 can be the closest to the mode m of a lower order of laser 2. In these cases, the expression given in 2.12 would be modified into the equations 2.13 and 2.14.

$$I(t) \propto 2A_{1,n}A_{2,n}e^{-2\delta(\nu_n)}cos\Big(2\pi((k+1)f_{rep1} - m\Delta f_{rep} + \Delta f_0) \times t\Big) \tag{2.13}$$

$$I(t) \propto 2A_{1,n}A_{2,n}e^{-2\delta(\nu_n)}cos\Big(2\pi(m\Delta f_{rep} - kf_{rep1} + \Delta f_0) \times t\Big) \tag{2.14}$$

Where $k = n - m$, $k > 0$, the m mode is thus beating with the $n + k^{th}$ mode in the case 2.13 and $n + (k^{th} + 1)$ in the case 2.14. This formalism is explained and detailed in the next section.

2.2.2 Frequency Domain description

In this section, we consider the general case where modes from the two lasers of different number can interfere. The teeth frequencies of the two combs can be identified using the equations 2.15 and 2.16 in the frequency domain.

$$\nu_1 = f_{01} + nf_{rep1} \tag{2.15}$$

$$\nu_2 = f_{02} + mf_{rep2} \tag{2.16}$$

f_{01}, f_{02}, f_{rep1} and f_{rep2} are respectively the carrier-envelope offset frequency and the repetition frequency of laser 1 and 2. n and m are integer values and correspond to the n^{th} and m^{th} tooth of respectively the comb 1 and 2. The RF domain is in the electronic frequency range (less than 1 GHz). The principle of the heterodyne DCS method in the frequency domain is schematized in figure 2.4.

The beat frequencies are obtained from the successive spectral spacing between the two nearest modes of laser 1 with laser 2 (first order beating). This spectral spacing is proportional to Δf_{rep}. Therefore, in the RF domain, the frequency beat notes are equally spaced of Δf_{rep}. The RF domain is associated to the electronic signal of the photo-detector whereas the electromagnetic

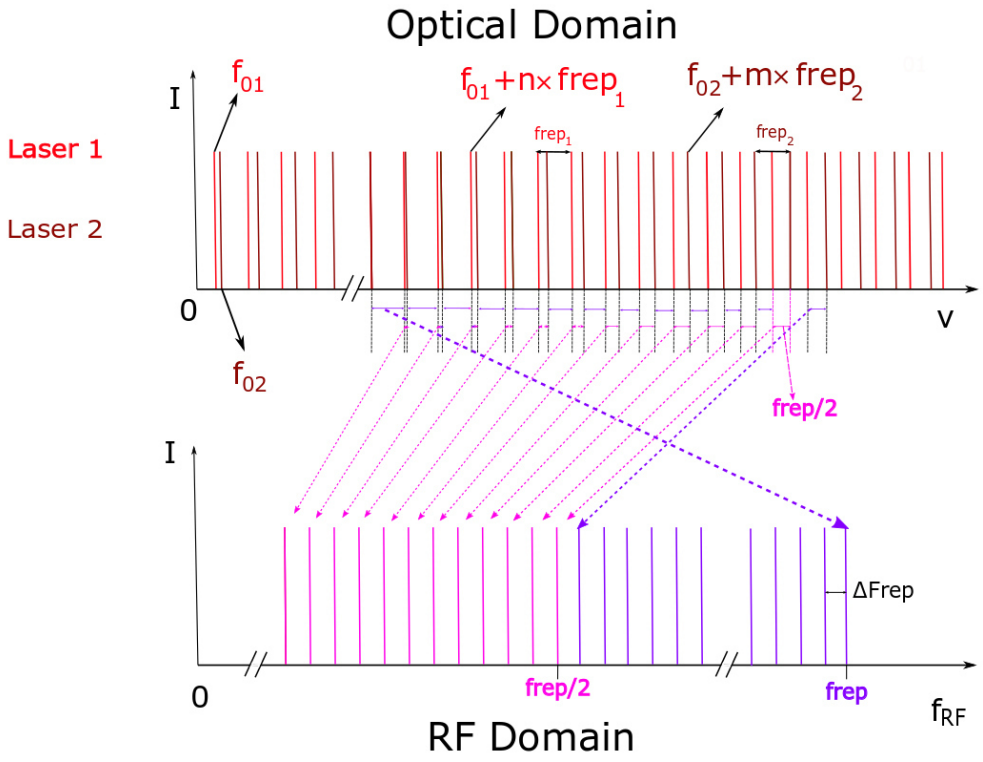

Figure 2.4: Representation of the beat frequencies of the heterodyne dual comb method. I is the spectral intensity of the laser comb. In the upper panel, is represented the emission of the two laser combs in the optical domain. The optical domain refers to frequencies contained in the fs pulses trains. The beats between two laser beams can be observed in the radio-frequency domain (RF domain). The first order beating corresponds to the pink modes up to $f_{rep}/2$. The purple modes correspond to the second order beating.

wave is associated to the optical frequency contained in the pulses trains. As it is showed in figure 2.4, the frequencies contained in the RF domain from 0 to $f_{rep}/2$ are created from the beats of the closest modes n^{th} and m^{th} of laser 1 and 2. The n^{th} modes are also beating with the $m+1$ modes, and the $m+2$ modes, $m+3$ and so on. An electronic filter at the photo-diode circuit must be used to remove the frequencies that are higher than $f_{rep}/2$ to avoid added frequencies between 0 and $f_{rep}/2$ from under-sampling of these higher RF frequencies (aliasing effect). Also, as explained in section 2.2.1 all the transition spectral information of the absorbing molecule is contained in the first order interference.

The values of Δf_{rep} and f_{rep} set the spectral spacing between the modes in the RF and optical domain. The superposition of the gain bandwidth (blue curve) with the two resonator combs in the frequency domain are represented in figure 2.5. The repeating frequency pattern between the modes that is shown in the figure 2.5 is detailed below. Only the frequency beats f_{RF} below $f_{rep}/2$ are kept for analysis to avoid aliasing effects. The description of the spectral schema is given below :

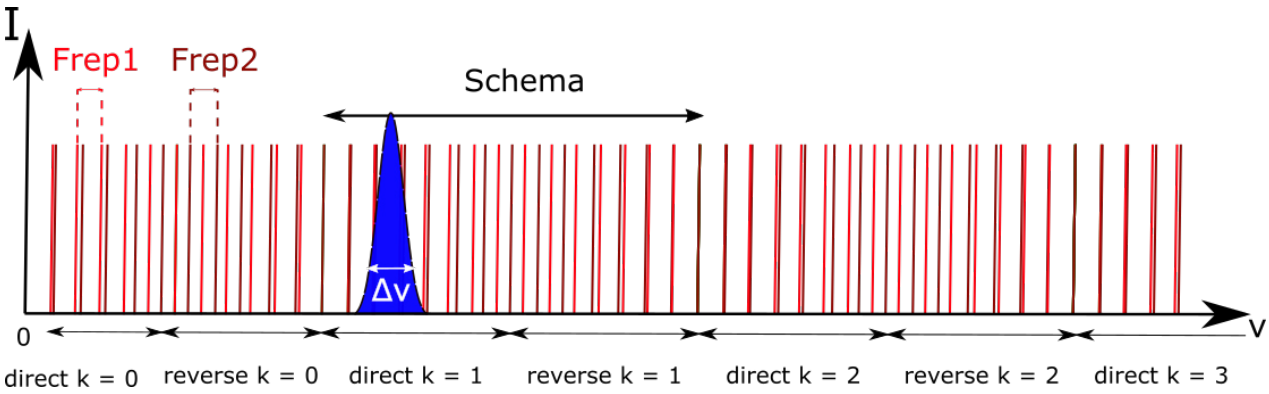

Figure 2.5: Representation of the modes of laser 1 (red modes lines) and 2 (dark red lines) in the optical frequency domain. The blue curve represents the emitted spectrum of the dual-comb laser. A "schema" represents the spectral pattern that is repeating k times over all the spectrum. The direct and reverse terms refer to the construction of the beat notes in the RF domain. For sake of clarity, this figure shows a dozen of modes for one "schema", whereas in reality one "schema" can contain tens of thousands to tens of millions modes.

- Starting from the frequencies at f_{01} and f_{02}, as n number increases the spectral spacing between the modes n and m increases such as $n \times \Delta f_{rep}$. The construction of the RF spectrum is direct.
- At $f_{rep}/2$ the mode m of laser 2 is spectrally equally distant from the mode n and the mode $n+1$ of laser 1. After this frequency, if the laser bandwidth is overlapping simultaneously the previous scheme and this scheme frequency, spectral mixing may occur (see section 2.3.1).
- After $f_{rep}/2$ the mode m of the laser 2 is getting closer to the mode $n+1$. In that case, the recorded RF beating note corresponds to the beating between mode m and mode n+1. The construction of the RF spectrum is reversed.
- The mode m and the mode $n+1$ are superposed. This frequency corresponds to the end of one full schema. The number of schemas is given by k.
- This schema is then repeated indefinitely such as the recorded RF beat notes correspond to the beating with the mode m and the mode n+k, as the frequency increases.

For one "schema", two cases can be distinguished in the RF spectrum reconstruction: the direct case and the reverse case. In the direct case the retrieved RF frequencies are proportional to the optical frequencies whereas in the reverse case the RF frequencies are increasing with decreasing values of the optical frequencies.

For the direct case :

$$f_{RF} = \nu_2 - \nu_1$$

$$f_{RF} = m f_{rep2} - n f_{rep1} + (f_{02} - f_{01})$$

When m = n it the expression can becomes the equation 2.17 :

$$f_{RF} = m\Delta f_{rep} + \Delta f_0 \tag{2.17}$$

with $m > 0$.

if m $\neq$ n, the expression can be written as the equation 2.18 :

$$f_{RF} = m\Delta f_{rep} - k f_{rep1} + \Delta f_0 \tag{2.18}$$

With $k = (n - m)$ and the n + k$^{\text{th}}$ mode beating with the m$^{\text{th}}$ mode.

In the reverse case :

$$f_{RF} = \nu_2 - \nu_1$$

$$f_{RF} = (n+1) f_{rep1} - m f_{rep2} + (f_{01} - f_{02})$$

If m = n, the expression can be written as the equation 2.19 :

$$f_{RF} = f_{rep1} - m\Delta f_{rep} - \Delta f_0 \tag{2.19}$$

if m $\neq$ n , the expression can be written as the equation 2.20 :

$$f_{RF} = (k+1) f_{rep1} - m\Delta f_{rep} + \Delta f_0 \tag{2.20}$$

The n + (k + 1) mode is beating with the m$^{\text{th}}$ mode. It has to be noted that these equations only describe the frequency beat of two modes from laser 1 and laser 2 that are the closest spectrally as the frequencies higher than $f_{rep}/2$ are filtered.

As it has been seen in this section, the f_{rep} and Δf_{rep} parameters are very important as they shape the RF spectrum. As described in the next section, these parameters have to be wisely chosen. They govern the spectral resolution and can be responsible for spectral mixing.

2.3 Determination of f_{rep} and Δf_{rep}

2.3.1 The spectral mixing problem

An optimization of the central position of the laser bandwidth ν should coincide at $k \times \frac{f_{rep}}{4}$ for optimization of this free-spectral-mixing bandwidth. Therefore the choice of f_{rep} and Δf_{rep} is critical. In this section, we describe their determination. For sake of clarity the frequency domain point of view is used in this section.

After determination of the RF bandwidth of the laser, using the scaling factor a, the risk of spectral mixing can be assessed by adjusting f_{rep} or Δf_{rep} to have the RF central position of the laser bandwidth at $f_{RF} = \frac{f_{rep}}{4}$. It can be seen from figure 2.5 that by modifying Δf_{rep} or f_{rep} we shift the position of the two combs in the optical frequency domain as well as their relative position. Thereby, it is possible to shift the position of the combs, and the position of one schema of width f_{rep} in such a way that the centre of the laser spectral bandwidth ν (blue curve in Figure 2.5) falls in the middle of a free spectral mixing bandwidth structure of width $f_{rep}/2$.

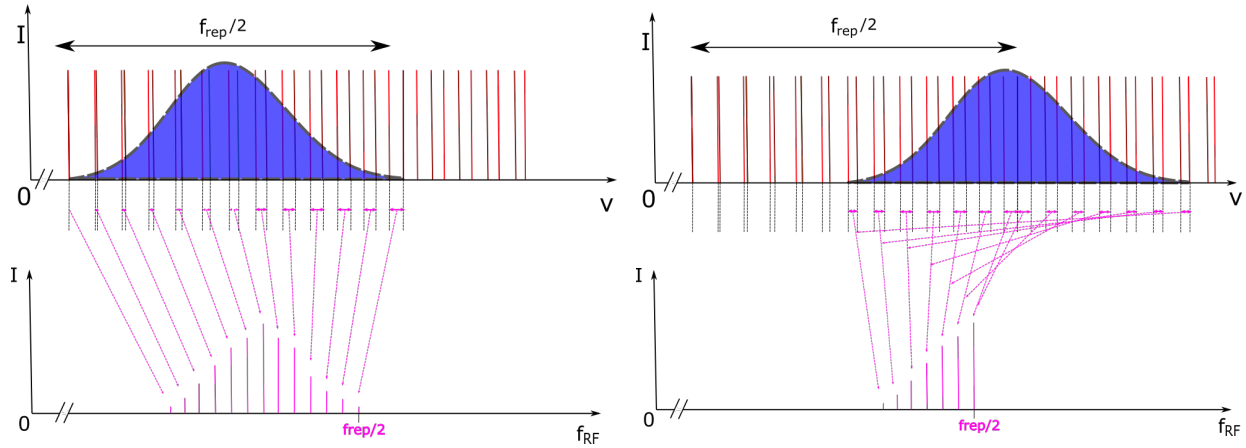

(a) Non aliasing case

(b) Aliasing case

Figure 2.6: Spectral mixing principle. The blue curve represent the spectral width emission of the dual comb laser source. f_{RF} represents the frequency in the radio frequency domain. $f_{rep}/2$ is the largest free spectral mixing bandwidth. In the free spectral mixing case (a), the spectral width of the laser is located away from the edge of the free-spectral-mixing spectral width $f_{rep}/2$. (b) Spectral mixing case.

The maximal spectral interval in the optical domain $\Delta\nu_{opt}$ is given by $\Delta\nu_{opt} = \frac{f_{rep}^2}{2\Delta f_{rep}}$. The corresponding value in the radio frequency domain (RF) $\Delta\nu_{RF}$ is obtained by dividing $\Delta\nu_{opt}$ with the scaling factor a ($\frac{f_{rep}}{\Delta f_{rep}}$) : $\Delta\nu_{RF} = \frac{f_{rep}}{2}$. If a part of the laser spectral bandwidth overlaps the edge of the spectral interval $f_{rep}/2$ (see b) of figure 2.6), spectral mixing occurs : Several similar frequency beats from two different spectral positions in the optical domain are summed twice in

the RF domain. This phenomenon is represented in Figure 2.6b, where the laser bandwidth (blue curve) overlaps the edge of the spectral interval ($f_{rep}/2$). This creates an unusable folded spectrum in the RF domain.
Appropriate values of Δf_{rep} and f_{rep} must therefore be imposed to avoid this spectral mixing effect. Two criteria must be met : the spectral bandwidth of the laser, in the radio frequency domain, must be lower or equal to $f_{rep}/2$ and its spectral position must be carefully set.

2.3.2 Spectral resolution

In determining the values of Δf_{rep} and f_{rep}, one has to consider their impact on the spectral resolution ν_{res} and on $\Delta\nu$. An ideal situation in spectroscopy is to have the broadest measurable spectral width and the lowest value of spectral resolution. We will see that some compromise has to be made between these two values.
The spectral resolution limit is obtained from equation 2.21 when the acquisition time window is inferior to the full interferogram (IGM) duration : $T = \tau_{IGM} < \frac{1}{\Delta f_{rep}}$. It depends on Δf_{rep}, f_{rep} and τ_{IGM} which is the time duration of one truncated interferogram. In that case, the resolution is equal to the spectral increment (equal to the inverse of the acquisition time). The resolution limit in the optical domain is thus given by the inverse of the acquisition time multiplied by the scaling factor a [7].

$$\nu_{res} = \frac{f_{rep}}{2\tau_{IGM} \times \Delta f_{rep}} \tag{2.21}$$

In the RF domain, the spectral resolution limit is equal to $1/2\tau_{IGM}$. In the case of $T > \frac{1}{\Delta f_{rep}}$, the teeth of the comb start to be resolved as the spectral increment becomes smaller than Δf_{rep}. This means that even if the spectral increment is lower than the spectral point spacing between two modes, the resolution is limited by the spectral spacing Δf_{rep} and f_{rep} in the optical domain : $\nu_{res,lim} = f_{rep}$. When the temporal window is longer than two full interferograms, the beat notes are fully resolved as at least two points per beat note are retrieved. The RF beat note spacing and the spectral increment are represented in figure 2.7.

When the RF comb structure is resolved with high SNR, the DCS spectrometer is free from the distortion of the line shape that is due to the instrumental function (no apodization). This aspect is unique to the DCS broadband spectrometer.
It should be kept in mind that for better resolution and high signal to noise ratio, it is interesting to increase Δf_{rep} as the interferograms apparition rate is faster and thus more interferograms can be measured during the coherence time of the laser.
A trade-off must be made between the values of Δf_{rep} and f_{rep}, depending on the chosen spec-

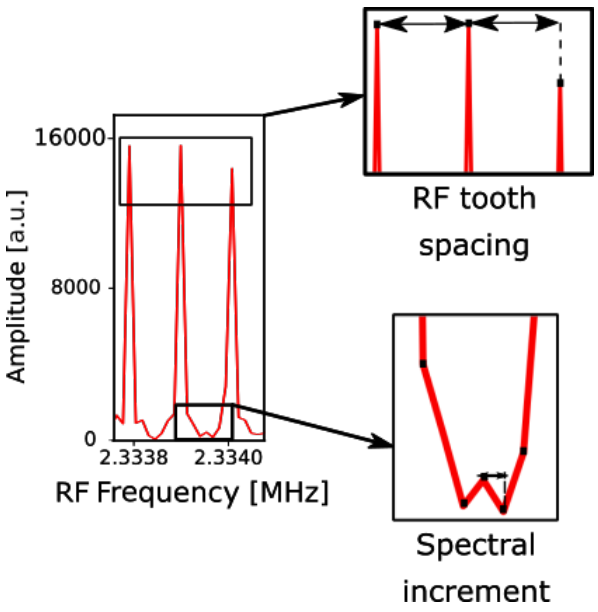

Figure 2.7: Representation of the spectral RF point spacing and the spectral increment from a RF spectrum. The spectral increment is equal to the inverse of the temporal trace window where the Fourier transform was applied.

troscopic strategy. A very broad $\Delta\nu$ bandwidth can be needed for molecules that have a wide absorption cross-section structure, with slow variation (according to the wavelength) such as O_3 or NO_2. In such a case a lower value of Δf_{rep} coupled with a high f_{rep} is an interesting strategy to apply. On the contrary OH or $C_{10}H_8$ are molecules with fast absorption cross-section variation. In that second case, a high value of Δf_{rep} and low f_{rep} is preferred to provide a high resolution. This aspect is further discussed in chapter 3.

Potentially, if the Δf_{rep} and f_{rep} parameters are wisely chosen, the dual comb spectroscopy method can have a high resolution, broad spectrum and a very fast acquisition time. In the next subsection is summarized the state of the art of the existing experiments using dual comb spectroscopy with a purpose to improve our knowledge on the concentration dynamic of the atmospheric molecules.

2.4 Dual Comb laser sources

2.4.1 Strategy for high mutual coherence

As Ideguchi et al explained [197], DCS experiments using two distinct laser sources requires effort to reach high relative coherence between the two combs. Two methods have been used : active stabilisation correction using feedback loops and continuous monitoring with a posteriori correction. The active stabilisation correction was composed of a phase/time feedback loop corresponding to a system where an error signal was sent to an actuator that actively stabilizes the four free-parameters

of the two frequency combs (f_{01}, f_{02}, f_{rep1} and f_{rep2}) to assure their mutual coherence. Coddington et al. [198] used a piezo-electric fiber stretcher and an external acousto-optic modulator (AOM) to adapt the frequency repetition of the cavity up to 100 kHz. The combs were locked on CW lasers references at 1550 nm and 1535 nm. The ro-vibrational transition lines of HCN could be obtained with 3 seconds of coherent averaging time by active stabilization [199].
Among the aposteriori strategies, several methods exists such as real-time adaptative sampling method [200] or coherent averaging protocols [198]. Real-time adaptative sampling consists in continuously monitoring the relative fluctuations between the free running comb lasers. The carrier phase noise as well as the frequency repetition were corrected in real time by re-sampling the interferograms. The error signals are taken as input parameters that are used for a correction of the digitizer sampling clock to match the difference in frequency repetition. The adaptive clock has been demonstrated to be able to recover the mutual the coherence between the two combs. Roy et al. [201] retrieved the HCN and H_2C_2 spectrum with high resolution (0.75 pm) during a 24 hours real time averaging of real interferograms. The transition lines at 1.55 µm of acetylene were retrieved with 2.6 GHz spectral resolution in 1 s of acquisition time [202]. The recovery of 2 seconds of full mutual coherence between the two combs was demonstrated by Deschênes et al. [203]. 120000 comb lines could be recovered in 2.7 s with 268 millions samples by continuous post-processing adaptive reconstruction of the coherence between two free running combs in real time by Ideguchi et al. in 2014 [197]. The drawbacks of these techniques is the use complex setup. Two CW stabilizing lasers and post-analysis material such as Digital Signal Processor or Field-Programmable Gate Array (FGPA) for high amount of memory and acquiring may be needed.
Coherent averaging protocols consists in forcing each recorded interferogram to have identical phase. The advantage of this method is to reduce the memory size of the recording. Coddington et al. [199] detail this coherent averaging procedure. The complexity of these experiment is to use an auxiliary stable laser system and a fast electronic chain. In the next subsections, the state of the art of laser systems that bypass these problems by using the same laser source to generate the two combs is detailed.

2.4.2 Dual comb generation using a single cavity laser source

The main advantage using a single cavity is that both lasers share common fluctuations and noises. This leads to common mode noise cancellation and intrinsically strong mutual coherence between the two train of pulses. Active stabilization and phase-lock electronics are therefore not needed. All the literature work presented in this section was performed without active stabilisation. This opens the path to compact, robust, transportable and easy operated instruments. Several single-cavity dual comb spectroscopy sources exist today : Fiber laser comb, electro-optic-modulator combs, micro-comb, solid-state laser comb and thin-disk laser oscillators. In this section is listed a quite

exhaustive state of the art of the methods that uses single cavity configuration for atmospheric spectroscopy purpose.

Fiber laser combs :

Several fiber based laser combs have used erbium-doped fiber as the gain medium. The advantage is the emitted range of wavelength (1.5 µm) where Telecom devices are readily and cheaply available in the optical market. The pump laser is also very accessible and the laser emission can be easily modulated with widely available drive electronics. An all-fiber bidirectional ring laser, passively mode-locked with slight frequency repetition shift was first demonstrated by Kieu and Mansuripur [204]. The design is composed of an erbium-doped fiber that plays the role of the gain medium. It is pumped with a 980 nm monomode laser. A fiber taper embedded in carbon nanotubes/polymer composite (FTECntPC) plays the role of the saturable absorber. A saturable absorber consists of an element that favors the mode-locking regime by applying losses to the low intensity lasing. The same laser source configuration has been used for monitoring the HCN narrow absorption lines in real time by Mehravar et al. [205]. They retrieved a 40 nm spectrum with 1 GHz resolution at 1550 nm in 1.28 ms of acquisition time.
This single ring cavity has shown very good relative stability, a shift in Δf_{rep} of maximum 0.1 % was observed over 60 s. At the same range of wavelength, another study showed that the Δf_{rep} of a free-running fiber laser could be very stable over time. The measured standard deviation of Δf_{rep} was 16 mHz for $\Delta f_{rep} = 52.74$ MHz while f_{rep} standard deviation was 10 Hz [206]. Thereby, they were able to retrieve 1990 interferograms in 1.6 s that allowed them to obtain the acetylene transition lines with a spectral resolution close to 1 pm.
A high coherence ultra-broadband dual comb fiber laser was achieved by Nakajima et al. [207]. They demonstrated a novel concept in the laser cavity geometry. They used two saturable absorber mirrors (SAMs) and nonlinear polarization rotation (NPR) to trigger the mode lock regime. They were able to generate 56 nm full width at half maximum bandwidth centred at 1055 nm. This technology could use the ultra broad-band width spectral emission and the high relative coherence of the laser for spectroscopic application.
The near infra-red region around 1060 nm was explored by Qin et al. [208] with an all fiber free-running bidirectional dual comb laser system for coherent anti-Stokes Raman scattering. They generated a laser beam from 1560 to 1060 nm with 9.6 THz of spectral bandwidth by means of a supercontinuum generation. The wavelength region in the vicinity of 2µm was explored using Thulium-doped fiber laser pumped with 790 nm monomode Ti:sa laser [209, 210]. In this configuration a semi-conductor saturable Bragg reflector (SBR) is present for facilitating the modelock (ML) regime triggering. The frequency repetition difference is caused by the fiber birefringence

which lead to the emission of two orthogonally polarized laser beam are superposed.

Recently the generation of Mid infrared dual comb all fiber bidirectional lasers in the range of 3.2 to 4.4 µm was demonstrated by Nakajima et al. [211].
Fellinger et al. [212] recently demonstrated a novel setup at 1030 and 1060 nm where the dual comb is generated from a Yb: mode locked fiber laser, and where f_{rep} and Δf_{rep} are controlled by a mechanic filter. This allows a full control of the repetition rate and their difference and thereby a full control of the spectral down-converting. The bidirectional dual comb fiber ring has appeared robust, low-cost and presented a high flexibility. However, these methods are emitting relatively low output power (less than 100 mW) and present higher phase noise level compared to bulk lasers even though this can be compensated using actuators. A high power (400 mW) 1060 nm dual comb source has been reported by Willenberg et al. [213] using the two polarization state of the cavity. A proof of principle spectroscopy has been performed on a semiconductor thin-film structure.
Overall, the fiber frequency dual comb has shown great flexibility in design. This instrumentation has demonstrated that it is adapted for spectroscopic measurement between 1064 nm to 4 µm with a high resolution and stability. The setup tools take advantage of a wide availability of electronic devices at 1500 µm due to the large development of Telecom devices.

Electro − optic − modulator combs :

An electro-optics-modulators combs is a non mode-locked laser technique. The two combs are generated from one monomode CW laser that is externally modulated in intensity or phase. This allows a control of the repetition frequency and the difference of frequency repetition of both arms with full control. Millot et al. [168] demonstrated spectroscopic measurement in laboratory of CO_2 isotopic ratio using intensity modulation for generating the combs. They were able to retrieve 0.13 nm spectral bandwidth with 300 MHz resolution within 550 µs (100 spectra averaged) at 1.55 µm. The available wavelength using this method was extended from 2 [214] to 20 µm [215]. Parriaux et al. [216] gives an up-to-date review of electro-optic modulator frequency comb performance.

Micro − comb :

Mode-locked lasers have been integrated to micro-resonator chip-based for spectroscopic measurements. Micro-chip lasers are monolithic solid-state lasers, where the laser crystal is in contact with the output coupler. This technology benefits from its compactness, robustness and small electricity consumption. As they have a large comb spacing, such systems are particularly suited to the mid-infrared region for monitoring condensed matter. The mid-IR region above 2 µm is really

interesting because most of rotational and vibrational induced absorption transitions are located in this spectral region [217]. Even though the average power is relatively low (tens of milliwatt [218]), this setup exhibits large line spacing (due to very short cavity) and higher comb energy, which results in high SNR and fast acquisition time. This makes chip-based micro-combs suitable for many spectroscopic applications. Dual comb spectroscopy was realised in the mid-IR region. Yu et al. demonstrated the detection of liquid acetone with a spectral coverage from 2.9 to 3.1 µm (wavelength could be spanned from 2.6 to 4.1 µm) with 127 GHz resolution. The first chip-based passively mode-locked waveguides (WGL) sharing the same cavity, was realized in 2017 by Hebert et al. [219]. One second of mutual coherence was obtained with free running experiment from this setup [220]. They retrieved 24 absorption lines of HCN with a spectral line spacing of 822.4 MHz centred at 1550 nm [221]. Other molecules such as methane were studied using a single cavity chip-based free running erbium doped laser [222]. They were able to retrieve the CH_4 spectrum in 1.28 s at 1650 nm, with a resolution corresponding of the line comb spacing of 968 MHz.
The development of a single source free running dual-comb MIXSEL setup has recently emerged for dual comb spectroscopy. The MIXSEL chip is a semi-conductor disk lasers (SDLs). This instrument is composed of a simple linear cavity where the MIXSEL chip plays the role of saturable absorber and gain medium. Two intracavity elements are used : an etalon that adjusts the center wavelength and a birefringent crystal for polarization splitting and dual comb generation. It generates two collinear laser beam polarized perpendicularly to each other. Δf_{rep} is created by the difference optical path in the birefringent crystal. Its use is well suited for 1 to 10 GHz repetition frequency. Its proof of principle has been realised on water vapor at 968 nm by Link et al. [223]. Acetylene gas transmittance was measured with a resolution of 2.7 GHz in 100 ms with residual errors of less than 3% [224] at 1.03µm. The 2 µm has appeared to be accessible as the first successful mode-locking laser at 2 µm has been demonstrated using a Tm:YAG ceramic laser [225].

The advantages of chip based single dual comb lasers relies in the fact that they induce less dispersion that fiber lasers facilitating the mode-locking regime, they have low electricity consumption, they are compact and robust.

Thin-disk laser TDL :

Recent promising work using thin disk laser (TDL) oscillators has emerged. It is a bidirectional laser cavity is composed of a 100 µm thin disk module that plays the role of the gain medium of the two laser beams. The two beams are focused in a titanium-doped sapphire crystal that plays the role of Kerr medium. The two laser beams have different optical path-ways as they have different end mirrors and different output couplers. Thereby the difference in frequency repetition can be easily tuned by translating one of the end mirrors. Fritsch et al. [226] demonstrated the first TDL

free running dual comb laser. They generated an average power of up to 14 W, at 1.03 µm with pulse durations of 300 fs. However, this system has a high noise level compared to other laser sources, that is caused by the cooling system in the thin disk. Very recently a reduction of the noise was developed by reducing the number of unshared components and thereby reducing the comb noise [227]. The dominant noise term in the cavity was determined to be on f_{rep}. Due to the high emitted power, this recent methodology seems promising for investigating the VUV, UV, mid-infrared region by frequency harmonic generation.
The state of the art of the dual comb instruments using a single laser source is summarized in the table 2.1.

Solid-state laser cavity :

Single cavity bidirectional passively mode-locked lasers, exists since 1998 when Wang et al. [228] accidentally generated two pulsed beams from a Ti:sa laser cavity. The first proof of principle of dual comb spectroscopy using a Ti:sa passively mode-locked bidirectional laser was realised by Ideguchi et al. [229] in 2016. The mode-lock is started by the nonlinear Kerr effect that plays the role of saturable absorber. They demonstrated a proof of principle of the method with a power emission of 340 mW in each arm and 61 nm bandwidth retrieval in the near IR (780-890 nm) with a fast scan rate (1ms). They obtained a relative-coherence between the two combs for 77 µs in free running experiment. A sealed enclosure of the cavity could improve the standard deviation of Δf_{rep} through time. As the emission in the near IR has a relatively high power emission, UV and XUV region are accessible by non-linear frequency generation. The advantages of these cavity are high stability and high relative coherence and a relatively high power that allow to generate UV or XUV with frequency harmonic generation.
As the Ti:sa emission is around 800 nm, fewer harmonic generations are needed to reach the UV range compared to the other strategies. Ti:sa show high average power (1W) with very high intrinsic coherence at short time scale, which make this technology very promising for UV-DCS (see section 3.3 for details). This thesis manuscript presents the development of the bidirectional ring cavity in a Ti:sa laser. The next subsection examines the origin of the difference in frequency repetition of a single cavity bidirectional Ti:sa mode-locked laser.

Table 2.1: Overview of single laser cavity for dual comb spectroscopy. When no molecules are indicated in the last column, it refers to laser cavity development only

Work reference	f_{rep}[MHz]	Δf_{rep}	P_{avg}[mW]	λ_0[nm]	$\Delta\lambda$[nm]	Targeted molecule
Fiber lasers						
Akosman et al. 2017 [230]	67.6	510 Hz	6	1975	9.8	
Zhao et al. 2016 [206]	52.7	1.3 kHz	16 25	1533 1544	33 22	C_2H_2
Nakajima et al. 2020 [207]	37.9	1.5 Hz	1.8 1.2	1550	56	
Mehravar et al. 2016 [205]	72.4	82 Hz	5.1	1555	9.6	HCN
Olson et al. 2018 [231]	60.8	229 Hz	0.9	1865	20	H_2O vapour
Fellinger et al. 2019 [212]	77	Up to 10 kHz	9.2 mW (total)	1030 1060	15 7	
Electro-optic combs						
Millot et al. 2015 [168]	300	100 kHz	50 250	1530 1625	2 3	$^{12}CO_2$ $^{13}CO_2$ $H^{13}CN$
Parriaux et al. 2019 [232]	300	57 kHz	25	1970	2.6	CO_2
Micro-combs						
Liao et al. 2018 [209]	71.9	3.2 kHz	3	1917 1981	35 20	H_2O
Yu et al. 2018	127 GHz	12.8	80 50	3000	400	C_3H_6O (liquid)
Hébert et al. 2017 [221]	822.4	10.5 kHz	2	1550	20	$H^{13}C^{14}N$
Guay et al. 2019 [222]				1.65 µm		CH_4
Link et al. 2017 [223]	1.7 GHz	4 MHz	>60	968	0.3	H_2O vapour
Nurnberg et al. 2019 [224]	2.7 GHz	51.9 kHz	28 24	1030	>10	C_2H_2
Solid state lasers						
Ideguchi et al. 2016 [229]	932	325 Hz	340 310	837	61	$Nd:YVO_4$ crystal
Thin disk lasers						
Fritsch et al. 2020 [226]	61.1	Up to kHz	12W 14W	1030	3.7	
Modsching et al. 2021 [233]	97	Hundreds of kHz	6W 8W	1030	5.5	

2.4.3 Bidirectional single cavity mode-locking

The ring cavity geometry is a configuration where two pulse trains laser beams can be emitted in two directions simultaneously. Even though the two counter propagating waves are circulating along the same cavity pathway, it is possible to induce a frequency rate difference between the two directions. The origin of this difference is a direction dependency of the non-linear Kerr effect occurring in the crystal. The self-steepening effect is different in shape in the two propagating directions. This is due to the non homogeneous pump beam intensity distribution in the crystal and the non-exact centred crystal position between the two curved mirrors (M1, M2). As the intensity is different in the two directions, the Kerr effect is modified and so is the group velocity (and so the repetition rate) [234, 235]. The frequency difference caused by the self-steepening effect in a KLM Ti:sa laser was characterized by numerical simulation by Sanders et al. [235]. The numerical model is based on a one dimensional dispersion-managed laser model and the interplay between the non-linear and dispersion effect via the non-linear Schrödinger equation presented in the subsection 4.1.2. A term taking into account the self-steepening effect was added. Ideguchi et al. [229] demonstrated that an estimated value using this numerical simulation was in agreement with the frequency difference that they obtained experimentally. They also demonstrated experimentally that the frequency difference repetition could be tuned by displacing the crystal, the cavity mirror M2 or the focusing lens. The value of the experimental repetition difference they obtained were in agreement with the numerical simulation formalism developed by Sanders et al. [235].

2.5 Conclusion

In this chapter was described the principle of the Dual comb spectroscopy methodology in the time and frequency domain. The main parameters f_{rep} and Δf_{rep} were presented pointing out they roles in a DCS experiment. They control the spectral resolution in the case where the beat notes are not resolved and only f_{rep} is responsible of the limit spectral resolution when the beat notes are resolved. If not well chosen, these two parameters can lead to the spectral mixing. Considering the spectral analyses of I(t), a low pass filter is used to remove the potentially under-sampled higher frequencies. The literature shows that one of the main difficulty of the DCS method is maintaining a relative coherence for a long period of time between the two laser pulse trains. The state of the art of the active stabilisation strategies used for maintaining this coherence was presented. Several laser configurations bypass the complex setup of active stabilisation by generating the two laser combs from one laser source. A selection of lasers generating two laser pulses train using a single laser source was presented. It is this strategy that has been adopted in this present work.

Chapter 3

Feasibility of UV-DCS for Remote Sensing of Atmospheric Trace Gases

3.1 Introduction

To our knowledge, spectroscopic measurement for detecting radical OH in the UV range in an open-air path are not currently deployed. Having established our goal of probing OH concentration at 308 nm radiation, using dual comb spectroscopy, we now examine constraints and challenges associated with remote sensing in this wavelength region. In the UV range, the phase noise of laser sources is higher than in the IR. Thus, this chapter aims at answering the following questions : Is DCS realisable in the UV range in atmospheric condition ? What laser source should be used and what performance in terms of signal to noise ratio and minimal concentration detection can be reached using UV-DCS ? Based on the previous considerations, a theoretical and numerical work has been realized to assess the feasibility of the DCS method in the UV range in real atmospheric condition. We show in this chapter that the most adapted laser source is based on the Ti:sa laser comb technology. The results on the expected signal to noise ratio (SNR) and minimum concentration detectable (sensitivity) are presented in this chapter for the following atmospheric molecules of interest OH, BrO, NO_2, OClO, HONO, CH_2O, SO_2. In all this chapter, these sets of atmospheric molecules are studied following two spectroscopic strategies. Case 1 is a high spectral resolution (2.5 GHz) in a narrow spectral range (1 THz) experiment centered at 308 nm. The Case 2 is centered at 350 nm, with 5 GHz spectral resolution and 50 THz spectral width. As seen in chapter 2, f_{rep} and Δf_{rep} are key parameters as they act on the spectral resolution, acquisition time and free aliasing spectral width of the UV-DCS. Our two case-studies use two different (f_{rep},Δf_{rep}) combinations considering the cross section structure of the atmospheric molecules absorbing in the

UV range. The molecule's absorption cross-section structures are presented in figure 5.17a for Case 1 and in figure 3.2 for Case 2. They correspond to the differential absorption cross-section of each atmospheric molecule of interest. The differential absorption cross-section structures corresponds to the fast varying (with the wavelength) absorption cross section structure of the molecule [236].

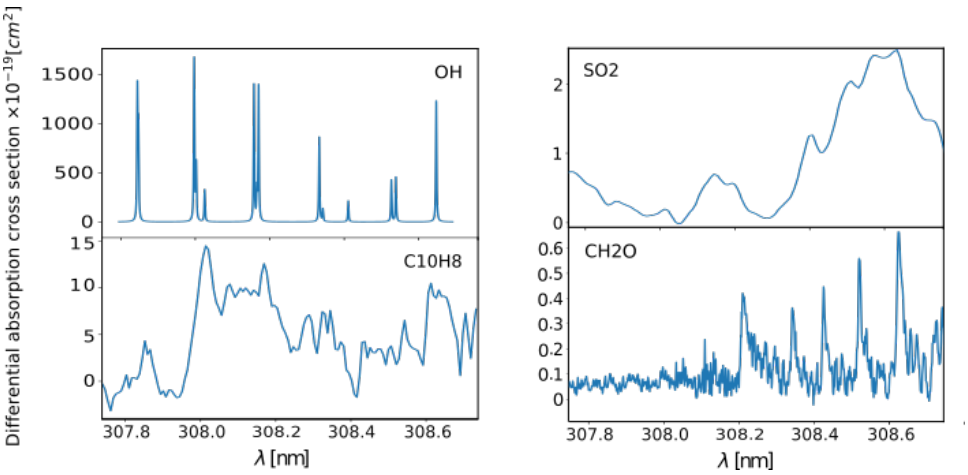

Figure 3.1: Case 1, differential absorption cross-section of atmospheric molecules of interest. Molecules of interests for Case 1 centered at 308 nm. From top left to bottom right : hydroxide radical OH, sulfur dioxide SO_2, naphtalene $C_{10}H_8$, formaldehyde, CH_2O

.

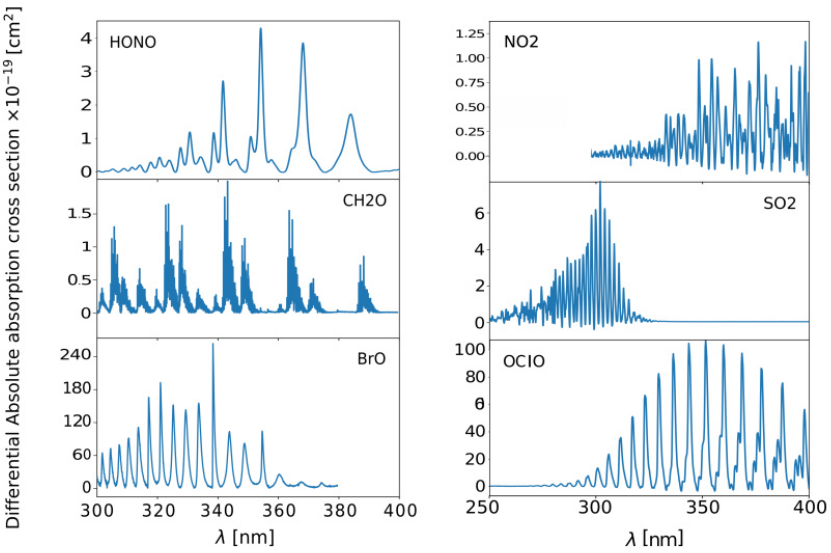

Figure 3.2: Differential absorption cross-section of atmospheric molecules of interest. Molecules of interest for Case 2, spectrum ranging from 300 nm to 400 nm range and 250 nm to 400 nm. From top left to bottom right : nitrous acid HONO, nitrogen dioxide NO_2, formaldehyde CH_2O, sulfur dioxide SO_2, bromine monoxide BrO, chloride oxide OClO.

It can be noted that the concentration of some molecules can be retrieved using the two cases. For example, SO_2 and formaldehyde present fast varying structures at 308 nm and also absorption lines of 1 nm width in the spectral range between 300 and 400 nm.

This chapter is divided in 5 sections. First, the sources of noises of the UV-DCS are highlighted. The choice of the laser source is investigated in section 3.3. The impact of the UV laser atmospheric propagation on the detected signal is assessed in section 3.4. Section 3.5, presents the expected signal to noise ratio of the UV-DCS for the two case-studies in the UV range. Section 3.6 presents the minimum sensitivity attainable by UV-DCS on trace gas molecules and radicals such as OH. In the last section, we verify that the UV radiations used for UV-DCS will not generate OH radical along their propagation.

3.2 UV-DCS Spectrometer signal fluctuations

3.2.1 Source of Noise

The signal to noise ratio (SNR) of the UV-DCS method can be defined in the temporal and spectral domains. The temporal SNR_t is defined as the ratio between the amplitude of the centerburst of the interferogram, and the standard deviation of the signal far away from the centerburst. The spectral signal to Noise Ratio SNR_f is defined as the ratio between the amplitude of the intensity spectral density and its standard deviation. Let us also introduce σ_f the noise standard deviation that corresponds to the inverse of SNR_f for normalized amplitude. This chapter refers also to the quality factor $Q = M/\sigma_f$ to compare the performance of the UV-DCS with state of the art remote sensing methods, where M corresponds to the number of spectral elements. Q was first introduced by Newbury et al. [237], it is defined as the signal to noise ratio per spectral element for 1 s of acquisition time. Here are listed the sources of noise of the sources of noise that influence the DCS signals :

- The Relative Intensity Noise (RIN) of the laser sources corresponds to the intensity fluctuation emitted by the laser. It is determined by the value of the power noise normalized with the average power emitted. It can be expressed as a Root Mean Square (RMS) value :

$$\frac{\delta P}{P_{average}} = \sqrt{\int_{f_1}^{f_2} S_I(f) df}$$

expressed in percentage, $S_I(f)$ is the power spectral density (PSD) in Hz^{-1}, δP is the root mean square of the amplitude fluctuations of the laser power, $P_{average}$ is the average power of

the laser. The amplitude fluctuation can be caused by the photons emitted spontaneously and amplified accidentally. As they do not have the same properties in terms of polarisation or phase compared to the stimulated emission, they induce noise in the recorded laser beam. This amplification in the cavity is called Amplified Spontaneous Emission or ASE. The amplitude noise of the pump laser is converted into amplitude and phase noise in the overall emission of the laser.

- Noise due to Residual Relative Optical Phase Noise of the laser source. The detail of the determination of the optical phase noise of the laser source is given in section 3.3. The main results are reminded here : For Case 1, the slow part of the phase noise $\sigma_{\phi,slow}$, has been estimated to be 0.33 rad. which results in a reduction of the SNR by 6.5 %. For Case 2, as the laser is generated only from one harmonic generation process, the phase noise is reduced by 2.4 %. These reductions factors are taken into account in all the calculation.

- The influence of atmospheric turbulence is developed in section 3.4. We show that the atmospheric turbulences are negligible for an acquisition time under 100 µs and $\Delta f_{rep} > 130Hz$ as the atmospheric fluctuation is "frozen".

- The noise equivalent power (NEP) is defined as the minimum radiation power detectable by the photodetector, which corresponds to the power that is needed to reach a SNR of 1. It takes into account two sources of noise: the dark-current which is the electric current present in the detector without light input, and the Johnson noise or thermal noise that represents the electric noise caused by the thermal agitation (this induce an added electron vibration and thus induces a noise).

- The shot noise is a fundamental quantum limit on the measure of power by a photo-detector. It is a noise that is caused by the variation of the photo-electrons emission created by the photo-cathode arriving at the first dynode.

- The dynamic range limit corresponds to a limit of the SNR and is imposed by the digitizer, the amplifier and the detector. It is the limit given by the acquisition setup. The detector has a limitation given by the dynamic range limit D. It is determined by the ratio between the maximal power that can measure the detector without saturation (before that the detector response is non-linear) with the input and the minimal power detectable which is the NEP. In the case where the digitizer is limiting the SNR, one can express $D = \sqrt{3} \times 2^N$. N is the number of effective bits of the digitizer.

- Multiplicative source of noise can have an important contribution in Fourier spectroscopy. As discussed in the paper of Newbury et al. [237], the main source of multiplicative noise comes

from the carrier phase noise of the laser sources. They demonstrate that the multiplicative noise can be suppressed in DCS to a level where it is unimportant, as soon as the spectral coverage of the experiment is orders of magnitude larger than the molecular absorption line width. Nevertheless we verified this assumption in all the case studies (see Table 3.8).

The formalism of UV-DCS global SNR noise is detailed in the next subsection.

3.2.2 Formalism SNR of a UV-DCS

The global spectral noise standard deviation σ_f of dual comb spectroscopy is expressed by the equation 3.1. This equation was introduced in the IR by Newbury [237].

$$\sigma_f = \frac{M}{0.8}\sqrt{\frac{\epsilon}{T}} \times \left(\frac{NEP^2}{P_c^2} + \frac{4h\nu}{\eta P_c} + 4bRIN + \frac{8}{D^2 f_{rep}} \right)^{1/2} \tag{3.1}$$

The global noise standard deviation is proportional to the number of spectral elements $M = \frac{\Delta\nu}{\nu_{res}}$. The dead time of the measurement is taken into account by $\epsilon = \frac{\nu_{res}}{f_{rep}}$. It corresponds to the percentage of time that is taken into account in the acquisition time for one interferogram. The unused part of the interferogram is called dead time because this time is still taken into account in the total acquisition time, but does not contribute to improvement in the SNR.
The four terms contained in the bracket of equation 3.1 are detailed below :

- The detector contribution is taken into account by the term $\frac{NEP^2}{P_c^2}$. P_c is the average laser power of the laser at the detector.
- The term $\frac{4h\nu}{\eta P_c}$ takes into account the detector shot noise contribution. h is the Planck constant. η is the quantum efficiency of the detector. ν is the optical center frequency of the laser dual comb.
- The term $4bRIN$ takes into account the fluctuations in the laser power. b is 1 for balanced detection and 2 for unbalanced detection. A balanced detection is a detection setup that uses the amplified current difference between two photo-diodes which reduces the statistical noises. From this signal, one can retrieve the spectrum of the molecule. Without the balanced detection, the RIN is doubled. However, it will be shown that the sensitivity is increased when the two laser beams follow the same optical path.
- The last term: $\frac{8}{D^2 f_{rep}}$ represents the limitation of the SNR due to the dynamic range of the digitizer.

The next subsection justifies our choice of a Ti:sa laser source to detect atmospheric trace molecules with UV-DCS.

3.3 UV-DCS laser source

3.3.1 Comparison of laser sources

The performance of a UV dual comb spectrometer depends directly on the intensity noise and the phase noise of the mode-locked lasers. The difficulty is to have a sufficiently high laser power in the UV range at 308 and 350 nm with a high enough relative coherence between the two combs. In this section, some options for the choice of the laser source are presented, followed by a study on the optical phase noise and the relative intensity noise (RIN) of a laser comb in the UV range.

According to figure 3.4 presented in section 3.6, 1 mW of detected power is sufficient to have a signal to noise ratio high enough to retrieve the concentration of a molecule. For a propagation through 5 km, 10 mW of initial UV emitted radiation is needed due to the atmospheric extinction. Several strategies to generate a UV comb do exist. One of them is the super-continuum broadening harmonic generation in micro-structures fibers in the UV range. However, due to the high level of phase noise obtained in the UV range, this strategy is not adapted for DCS purposes [238]. High harmonic generation (HHG) in noble gases can be used to generate UV phase coherent light, but the emitted power is not sufficient for detecting atmospheric trace gases. The third option is the use of the harmonic generation in bulk crystals which appears the most relevant strategy of atmospheric trac gases monitoring.

The *Erbium-fiber laser* is a potential laser source for UV-DCS. Based on the reported coherences in the IR (1.5 µm) [239], we estimated that the phase noise remains lower than 1 rad during one interferogram (100µs) in the UV. This was estimated using the following law : the power spectral density of the optical phase noise is quadratic in harmonic order p leading to a linear increase of the optical phase noise RMS with p. This was experimentally demonstrated in bulk crystal for second harmonic generation [240, 241]. For the experiment, the 4th (390nm) and 5th harmonic generation (312nm) are needed to obtain the targeted range of wavelength. For the 4th harmonic generation, 6 mW for 1 ps pulse duration has been reported [242]. 250 mW in the UV range has been generated by means of a poled crystal [243] but the reported spectral bandwidth is rather narrow (0.1 nm) and therefore not adapted for retrieving trace gas atmospheric concentration.

Ytterbium-fiber lasers can be a pertinent candidate for UVDCS. A proof of principle UV-DCS using Ytterbium laser has been reported at 350 nm (from high harmonic generation) in laboratory [244]. However the narrow spectral bandwidth of the emission that we can currently achieve is therefore not adapted for unambiguous retrieval of atmospheric trace gases concentration. Schuster et al. [245]

addressed the feasibility of UV-DCS using fiber lasers for laboratory studies.
Titanium-sapphire lasers (Ti:sa) generate a broadband spectrum from 600 to 1100 nm [246, 247]). The emitted power can reach more than 1 W for 5 W pump power from 532 nm [248] in the near infra-red. The conversion power ratio from doubling and tripling (frequency doubling plus frequency sum generation) of the fundamental laser can respectively reach 20 to 50 % and 3 to 10 %. These ratio would provide at least 30 mW after frequency tripling the fundamental Ti:sa laser which is enough for atmospheric trace gas detection in the atmosphere. Such UV sources have been generated via SHG of Ti:sa using intra or extra cavity schemes 10 fs pulses length (416 nm) [249], (438 nm) [250] and (390nm) [251]. Moreover, Rotermund et al. [252] have obtained 625 mW average power from SHG process and 150 mW from a frequency tripling (SHG+SFG).
The lowest optical phase noise reported in the litterature was obtained by phase-locking a Ti:sa frequency comb mode to an etalon source at 657 nm [253]. We estimated the relative accumulated phase noise integrated from 10 kHz to 50 MHz (Fourier frequency of the noise) to be lower than 0,5 rad from the work of Quraishi et al. [253]. From the work of Sutyrin et al. [254], we estimated an accumulated relative phase noise from 10 kHz to 50 MHz of 0.11 radiant. The harmonic generations from a Ti:sa laser appear to be the most adapted tool for monitoring trace gas molecules in the UV range. For determining the feasibility of the UV-DCS method, a study on the accumulated phase noise of the frequency doubled/tripled Ti:sa laser frequency needs to be made.

3.3.2 Influence of Ti:sa laser comb noise on the UV-DCS signals

The relative phase noise between two combs has not been studied in the literature. However, it has been shown that the relative phase noise can be similar to individual comb phase noise using a stabilization protocol [239]. In our case, some estimation of the phase noise power spectral density must be made to assess the stability of the laser source in the UV range. The optical phase noise $S_{\phi,n}$ of a mode n of the comb comes from the frequency repetition f_{rep} and from the frequency carrier-envelope f_0 fluctuation. This noise can be induced by local temperature fluctuations, by phonic or mechanic perturbation on the cavity components or by instability from the injected pump laser. As detailed in chapter 2, a comb is composed of spectral equally spaced frequencies such as the n$^{\text{th}}$ modes has the frequency $\nu_n = f_0 + n f_{rep}$. The frequency repetition f_{rep} can be easily locked contrary to f_0. The optical phase PSD of the mode n that is phased locked to an optical etalon n_{ref} is given by equation 3.2.

$$S_{\nu_n} = \left(\frac{n}{n_{ref}}\right)^2 S_{\nu_n Ref} + \left(1 - \frac{n}{n_{ref}}\right)^2 S_{CEO} \tag{3.2}$$

$S_{\nu_n Ref}$ and S_{CEO} are respectively the phase noise power spectral density of the optical phase of the

comb number n_{ref} and the carrier-envelope phase offset. The total accumulated RMS phase noise σ_ϕ^2, is obtained by integration of S_{ν_n} within the frequency range [f1,f2] as follow : $\sqrt{\int_{f_1}^{f_2} S_{\phi,n} df}$. The highest value corresponds to the Nyquist frequency : $f_{rep}/2$. The lowest frequency is given by the duration of one interferogram. The time coherence is defined as the duration in which the accumulated $\delta\phi_{RMS}$ is under 1 radian. We used the values indicated in Sutyrin et al. [254], and we verified that the contribution of the noise at Fourier frequencies higher than 1 MHz to the overall noise was negligible. The total phase noise RMS σ_ϕ^2 can be divided into two parts : the slow $\sigma_{\phi_{slow}}$ and the fast $\sigma_{\phi_{fast}}$ component :

- The slow component corresponds to an observation time of 130 ms which is the longest observation time for measuring the phase noise reported in the literature [254]. The coherence was stable for 130 ms ($\sigma_\phi < 1 rad$). Because of the existence of residual phase noise over time-scales longer than the duration of a single interferogram, $\sigma_{\phi,slow}$, the SNR of the averaged interferogram is reduced by the factor $\left(1 - \frac{\sigma_{\phi,slow}^2}{2}\right)$ [237]. This allows the averaging protocols to be applied to several interferograms.

- A multiplicative noise $\sigma_{multi,line}$ is contributing to the total noise across a molecular absorption spectral line of width $\Delta\nu_L$ due to the existence of residual phase noise over the duration of a single interferogram $\sigma_{\phi,fast}$ [237]. $\sigma_{multi,line}$ depends on the fast noise RMS $\sigma_{\phi,fast}$ that is calculated over an observation time of 100 µs (about one interferogram). The evaluation of $\sigma_{multi,line}$ is given in equation 3.4 and the results are given in equation 3.8.

We predict an accumulated phase noise of 0.33 rad from 10 kHz to 50 MHz after frequency tripling. This leads to a reduction of the SNR by 6.5 % in Case 1. In Case 2 this reduction is 2.4 % due to only one harmonic generation process. This allows UV-DCS measurement with limited reduction of SNR due to relative phase noise error. Such a level of accumulated phase noise is maintained during at least 130 ms. This is allowing averaging protocol that drastically reduces analysis time [239].
The relative intensity noise (RIN) of the laser source has also been estimated. A peak of noise that corresponds to the laser relaxation oscillation is usually seen at hundreds of kHz. Beyond 1 MHz, the RIN of the laser tends to follow the shot noise limit of the detection system. We decided to use a constant upper limit of the RIN value. IR Ti:sa comb RIN values were reported to be between -135 dBc/Hz and -140 dBc/Hz, from the litterature comparing different pump lasers [254–256]. The highest value was used for evaluating the laser RIN after SHG and frequency tripling. Then as said previously, the relative intensity fluctuation RMS of the p^{th} harmonic is expected to be p times higher leading to a RIN (PSD) p^2 higher than the RIN of the fundamental laser. Therefore, the laser RIN was estimated to be -129 dB/Hz for SHG and -125 dB/Hz for THG.

As a conclusion, the Titanium-sapphire laser seems highly relevant for dual comb spectroscopy measurement in the UV range. The Ti:sa laser needs low harmonic generation (second or third) to reach 308 and 350 nm as it generates enough power in the near IR region and has a low phase noise degradation. This results in a high signal to noise ratio of UV-DCS. Moreover its broad bandwidth is relevant for monitoring the atmospheric trace gases targeted.
In the next section, we examine the noise induced by the atmosphere on the laser source as it propagates.

3.4 UV pulse propagation in the atmosphere

The propagation of a laser beam in the atmosphere is subject to local variations in refractive index. This can be caused by temperature or pressure fluctuations. The impact on the electromagnetic wave pulse is twofold : it induces phase and amplitude fluctuations (or speckle) [257]. Phase fluctuation results in modification of timing delay (first-order $\frac{d\phi}{d\omega}$) and dispersion (second-order $\frac{d^2\phi}{d^2\omega}$), with ϕ the phase of the electromagnetic wave.
In the IR, Rieker et al. [2] have retrieved greenhouse gases concentration over two kilometres using an IR-DCS remote sensing instrument. The noise induced by atmospheric fluctuation appeared to be negligible as the duration of one interferogram was shorter than the characteristic fluctuation time of the atmosphere. One of the strengths of the method combining two laser pulses is the reduction of the noise in the RF beat signal. Since, both arms share the same optical path, they experience the same phase and amplitude noise. This relative immunity is a major advantage compared to usual Fourier Transform Spectroscopy or scanning laser spectroscopy.

In the UV range, turbulences induce greater phase and amplitude fluctuations. In the next two subsections, the level of noise induced by the propagation of the UV beam in the atmosphere on the UV-DCS method is assessed.

3.4.1 Atmosphere induced amplitude noise

Very few experiments have been performed to characterise the propagation of a light beam in the UV range. Armeding et al. [258] emitted a 308 nm light beam through the atmosphere. They observed a beam diameter variation that resulted in a maximum intensity fluctuation (RMS) due to atmospheric transmission of 2.10^{-3} for a single scan of 100 µs. A scan corresponds to the emission of a pulse laser over a range $\Delta\lambda$ within a time interval of Δt. Under the hypothesis of random noise, an averaging of up to 1s (10^4 scans) showed that the noise could be reduced to 10^{-5} where the atmospheric fluctuation can be "frozen". The time interval of 100 µs in the UV is low enough to guarantee that the fluctuation due to the atmosphere is under other source of noise. In our study

of UV-DCS method, 100 µs can correspond to the duration of one interferogram that leads to 1 GHz spectral resolution (using f_{rep} = 100 MHz and Δf_{rep} = 1kHz). It is in the proper spectral resolution to resolve the OH radical absoption line having a linewidth (FWHM) of 7.9 GHz (T = 293 K and P = 1 bar).

To confirm the veracity of this 100 µs value, a study has been conducted by considering fluid turbulence theory. Taylor's frozen hypothesis and the theoretical Kolmogorov spectrum are used for evaluating the power spectral density of the intensity noise due to atmospheric fluctuations. The Kolmogorov spectrum corresponds to the energy spectrum of turbulences motions. The Taylor's frozen hypothesis assumes that air parcels are moving at a constant speed experience constant deformations at the time scale considered. The cut-off frequency is the frequency where the atmospheric energy involved in turbulences starts decreasing strongly as $f^{-8/3}$. The same consideration was made by Rieker et al. [2]. They observed no additional amplitude noise over the cutoff atmospheric turbulence frequency. This frequency can be calculated from the following equation : $f_c = \frac{2.5U}{\sqrt{2\pi\lambda L}}$. U is the wind speed, λ the wavelength of the light beam, L the optical path length. For a typical wind speed of 5 m/s, a path length of 2 km at 308 nm, the cut-off frequency is 127 Hz. Moreover, in our experiment, the refresh rate of interferograms is given by Δf_{rep}. Therefore, over a Δf_{rep} value of 130 Hz the turbulence-induced intensity noise could be considered as frozen. A multiplicative noise due to atmospheric intensity noise can still occur during one interferogram. However, Rieker et al. showed experimentally that the multiplicative noise remains below the overall noise floor for IR-DCS [2]. An experimental assessment of this multiplicative noise would allow us to quantify its contribution in the UV-range.

3.4.2 Atmosphere induced phase noise

Phase noise implies timing jitter and dispersion in the pulse that decreases the coherence time of the experiment. The timing jitter S_{jitter} can be assessed by the following equation : $S_{jitter}(f) = (2\pi\nu_0)^{-2} S_\phi(f)$, where ν_0 is the carrier optical frequency, and S_ϕ the phase noise [257]. The intrinsic phase noise of one frequency comb is related to the fluctuation of the comb modes positions. The optical phase noise of the mode n of frequency f is given by $S_{\phi,n}(f) = S_{\nu,n}(f)/f^2$ with $S_{\nu,n}(f)$, the power spectral density (PSD) of the frequency fluctuations at frequency f. An atmospheric-induced phase noise of -70dBc was determined using the atmospheric parameters as in subsection 3.4.1. This leads to a timing jitter noise $<= 10^{-37} s^2$ at 10 kHz Fourier frequencies. The integration from 10kHz to 100 MHz is less than 1fs which is 10 times less than the increments of one interferogram $\Delta f_{rep}/f_{rep}^2$ = 10 fs considering Δf_{rep} at 1 kHz and f_{rep} at 100 MHz. In our experiment, the two beams propagate in the same optical path. As a result, they are both affected by similar atmosphere-induced phase noise. As a result, the phase noise induced by atmospheric

turbulences can be considered negligible compared to the intrinsic phase noise of the two UV combs.

It has been shown in these two subsections that the UV dual-comb laser should not be impacted by the atmospheric turbulence when Δf_{rep} >130Hz. However, the UV laser source may impact the atmosphere as the energy of the laser beam is high enough to ionize or dissociate molecules and therefore creates a bias in the concentration retrieval of UV-DCS method. This interrogation is assessed in section 3.7.
An evaluation of the signal to noise ratio attainable by UV-DCS is presented in the next section.

3.5 Numerical evaluation of UV-DCS SNR

3.5.1 Results

In this section, is presented the signal to noise ratio per spectral element Q of UV-DCS method with no dead-time ($\epsilon = 1$) for the two cases described previously.
The setup that is guiding the laser beam into the atmosphere and back to detectors has not been constructed yet. However, a typical UV Gaussian laser source of a 2 mrad divergence, would need a 50 times beam expander placed at the exit of the laser source and a 10 cm of diameter high-reflectivity mirror that direct the beam to the atmosphere. The collection of the laser will be done by a telescope off-axis system. A fast-steering mirror system will be used to correct the wandering beam fluctuation over the typical time of the interferograms refresh-time (correction rate slower than the refresh-rate of the interferograms Δf_{rep}). The parameters, on the laser source and the detection system, used for the theoretical simulation are summarized in table 3.2. The laser values given in this table correspond to existing Ti:sa laser sources. The value of f_{rep} corresponds to the most stable laser in terms of phase noise currently available.

Table 3.1: Parameters of UV-DCS method used of sensitivity and quality factor

Quantity	Variable	Value
Repetition frequency	f_{rep}	100 MHz
Relative Intensity Noise	RIN	$-125\ dBc/Hz^a$ or $-129\ dBc/Hz^b$
Noise Equivalent Power	NEP	$0.44.10^{-12}$.[c] $dB/\sqrt{Hz}$
Detection dynamic range	D	12 bits
Experimental geometry	F_{contra}	0.5[d]

[a] Estimated for the tripling frequency, [b] Estimated for second harmonic generation, [c] Biased photodiode detector, [d] Case of co-propagating pulses interfering in the absorption medium.

Figure 3.3, shows the quality factor as a function of the detected power for the two cases. Q was determined using equation 3.1. The laser RIN difference between Case 1 and Case 2 comes from the

frequency doubling and frequency tripling of a Titanium-sapphire laser emission. The frequency doubling and tripling generation are obtained using a non-linear Beta Barium Borate (BBO) or Bismuth borate BiB_3O_6 (BIBO) crystal. The doubling is obtained by secondary harmonic generation. It is a nonlinear process where two identical photons from the fundamental laser are generating a third photon that has a frequency twice higher than the initial photons. Mathematically the SHG depends on the nonlinear susceptibility tensor $\chi^{(2)}$. The SHG has a power efficiency of between 25 % to 50 % from the fundamental laser source. The tripling is obtained by sum frequency generation (SFG) from the SHG signal and the fundamental laser source. The sum frequency is also a non-linear frequency conversion in which the emitted photon frequency corresponds to the sum of the two initial photons frequencies. This phenomenon is also described by a non-linear tensor $\chi^{(2)}$. The tripling efficiency from the fundamental laser is between 3 to 15 %.

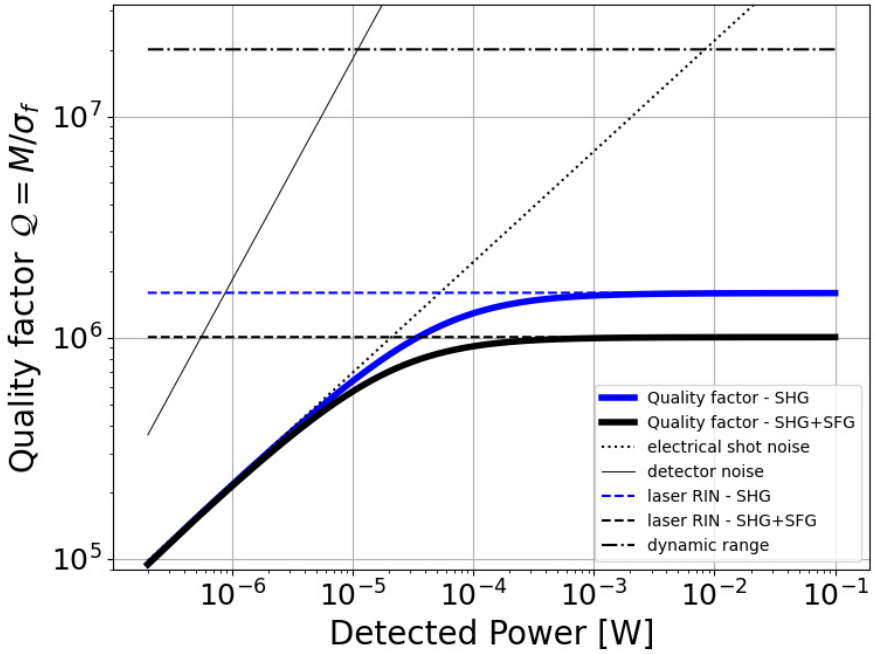

Figure 3.3: Quality factor $Q = M/\sigma_f$ as a function of the detected power. figure was plotted with $\epsilon = 1$ and acquisition time of 1s. The total second harmonic generation (SHG) quality factor at 350 nm is represented in black thick line and the frequency tripling quality factor at 308 nm is represented in blue thick line.

The UV quality factor is 6 times lower than the IR quality factor first introduced by Newbury [237]. The main reason is that the value of the RIN in the UV range is higher due to the harmonic generation that increases the noise. At low detected power, the quality factor is limited by the shot noise. From 1 mW, the noise induced by the laser limits the quality factor to 10^6 for the SHG+SFG and $1,8.10^6$ for the SHG. Several detectors were taken into account: avalanche, amplified, biased photodiode or Super Bilakali Photomultipliers. None of them was limiting the SNR value, either

through their NEP value or their dynamic range value. The best detector appeared to be the silicon photodiode because of its high saturation power capacity. The results on the sensitivity will be developed in section 3.6.

3.6 Minimum Absorption Sensitivity of UVDCS

Analysis of the absorption transition lines is similar to the one used in the DOAS method. the slowly varying component that is due to Rayleigh or the aerosol scattering is first removed. The remaining fast varying component corresponds to the absorption lines. The concentration of the molecules is then obtained by identifying, separating and fitting the absorbing lines structure from their established absorption cross-sections [236].
The sensitivity of the UV-DCS method is defined by the minimum absorption sensitivity (MAS) at a discrete line ($(\alpha_0 L)_{min}$). α_0 is the absorption coefficient for one absorption line of a target atmospheric molecule and L the optical path length. α_0 is defined as the concentration of the molecule multiplied by its absorption cross-section line. The MAS evaluation at a specific transition line is presented on equation 3.3 [237].

$$(\alpha_0 L)_{min} = 2\sigma_f \times F_{contra} \times \sqrt{\frac{4\nu_{res}}{\pi \sum_j \Delta\nu_{Lor,j}(\alpha_j/\alpha_0)^2}} \tag{3.3}$$

The sensitivity depends on the spectral noise standard deviation σ_f introduced in section 3.5. ν_{res} is the spectral resolution of the lines depending on the Δf_{rep} and f_{rep} parameters as explained in chapter 2. The sensitivity is improved by the number of absorption lines resolved $\Delta\nu_{Lor,j}(\alpha_j/\alpha_0)^2$, where $\Delta\nu_{Lor,j}$ is the width of the j^{th} absorption line fitted with a Lorentzian function. The sum of these lines, typically enhance the MAS by a factor from 0.1 to 1. F_{contra} takes into account the geometry of the spectrometer. As shown in chapter 2, in our experiment, the two laser combs traverse the absorbing medium, this results in enhancing the sensitivity by a factor of 2 $F_{contra} = 0.5$.

The SNR decrease discussed in subsection 3.3.2, is taken into account in the calculation. The MAS depends on the spectral coverage $\Delta\nu$ of the experiment (term present in σ_f, see equation 3.1) and the resolution ν_{res}. As a consequence, as it can be seen in figure 3.4, and in Table 3.3 the values of f_{rep} and Δf_{rep} have to be chosen wisely to optimize the MAS of the UV-DCS method.

In the following two subsections, is assessed the Minimum Absorption Sensitivity (MAS) value for the two cases Case 1 and Case 2. It can be noted that some atmospheric molecules such as sulphur dioxide or formaldehyde can be measured using the two cases strategies. The concentration of molecules is determined from the separation of the slow and fast-varying spectral structures.

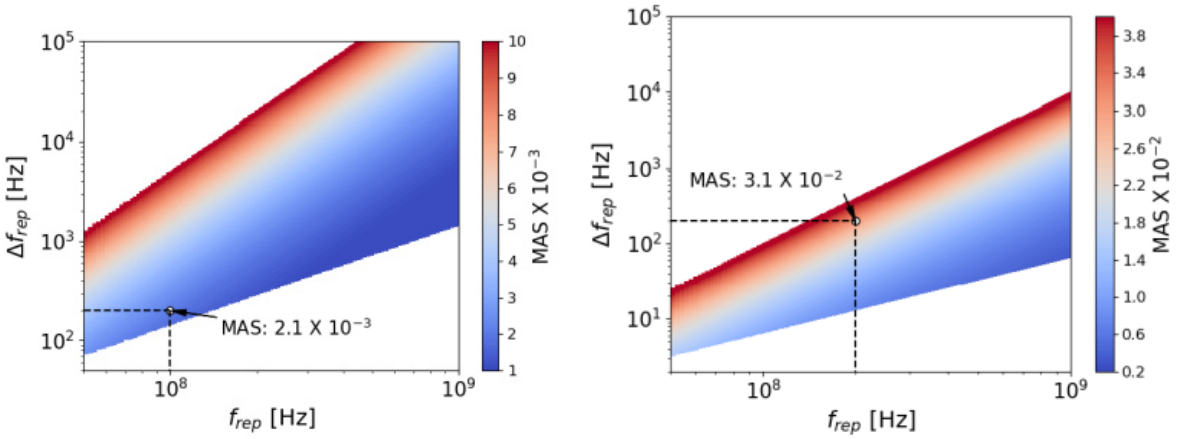

(a) Case 1

(b) Case 2

Figure 3.4: 2d plot of MAS determination for Case 1 and Case 2 as a function of f_{rep} and Δf_{rep}. The white excluded areas on the top left corner correspond to aliasing free spectral range $\Delta\nu$ values under 1 THz and 50 THz for respectively Case 1 and Case 2. Lower value of bandwidth correspond to a diminution of the number of lines measured resulting in a diminution of sensitivity. The white excluded areas on the bottom right corner correspond to resolution ν_{res} values higher than 3.5 GHz and 77 GHz for respectively Case 1 and Case 2. Higher resolution would results in a degradation of the absorption line shape. ϵ is approximatively 25 (2.5 GHz/100 MHz or 5GHz/200MHz) which decreases the SNR and then the MAS by 5 ($\sqrt{25}$).

Table 3.3: Result on the simulated MAS for the two case studies (f_{rep};Δf_{rep}) combination, illustrated in figure 3.4

Case study	Quality factor Q	f_{rep} ; Δf_{rep} ν_{res} ; M ; ϵ	MAS
$Case(1)$	10^6	100MHz ; 200Hz 2.5GHz ; 1200 ; 25	$2.1.10^{-3}$ $^*(OH : 1.10^{-3})$
$Case(2)$	$1,6.10^6$	200MHz ; 200Hz ; 5GHz ; 10000 ; 25	$3.1.10^{-2}$

3.6.1 Case 1 and OH detection

The first case-study Case 1 corresponds to the UV-DCS experiment where a narrow spectral bandwidth and a high spectral resolution is used. This experiment is made at 308 nm where some molecules of interests have their strongest absorption cross-section (see figure 5.17a). The relative intensity noise (RIN) of the laser used here is -125 dBc/Hz (see section 3.3). The MAS value as a function of a (f_{rep} and Δf_{rep}) combination is illustrated in figure 3.4a. This figure can be used for optimizing the UV-DCS sensitivity. There is a necessity of reaching a high resolution at 308 nm because of the narrow absorption lines of the atmospheric molecules (absorption lines width of 9 GHz (3 pm) such as OH to 150 GHz (50 pm)). The chosen parameters for the Case 1 are f_{rep} = 100 MHz, Δf_{rep} = 200 Hz for the following reasons : The resolution obtained is about 2.5 GHz

(0.8 pm; acquisition time of 100 µs) which is enough to retrieve the narrowest absorption lines of the molecules of figure 5.17a. The free-aliasing width is not a limiting parameter as its bandwidth is 25 times larger than the required 1 THz (see figure 5.17a). The free-aliasing spectral width could be narrowed to improve the resolution. However, as seen in figure 3.4, an increase in Δf_{rep} corresponds to a decrease in sensitivity.
One should keep in mind that as Δf_{rep} is increased, the time delay between the interferograms is reduced and so that allows more interferograms to be produced during the coherence time of the dual-comb resulting in averaging improvement.

Table 3.4: Results on the concentration detection limit of molecules of interest of the Case 1. The calculation used a 2 km light path with 200s of averaging time, a central wavelength of 308 nm, an optical spectral bandwidth of 1 THz and a MAS of $1.5.10^{-4}$.

Component	Differential Cross-Section $\times 10^{-19}$[cm^2/molec.]	Concentration Detection Limit [ppt]
SO_2	1.2	260
CH_2O	1.5	210
C_8H_{10}	15	20
OH	1670	0.08

The concentration detection limit corresponding to the MAS for Case 1 experiment is given in Table 3.4 for some atmospheric molecules of interest : SO_2, CH_2O, C_8H_{10} and OH. The concentration detection limit of OH is 0.08 ppt (corresponding to a MAS of 7.10^{-5}) at 200 seconds of acquisition time. In the literature, a MAS of 1.10^{-5} is obtained from active or passive DOAS (Differential Optical Absorption Spectroscopy) or MOAS (Multipass Optical Absorption Spectroscopy) with a similar acquisition time. The UV-DCS method would need 2.7 h of averaging time to reach such a sensitivity. This is not suitable for trace gas monitoring. However, one can reduce the averaging time and use the UV-DCS method for various environments from very clean air, in absence of quenching by NO_X for example, to an urban area where the concentration is typically 0.3 ppt [259]. As the UV-DCS can have a high sensitivity in a very short time (time of one interferogram) and it could be used for monitoring OH in an environment with a high concentration of OH environment. The monitoring of the combustion dynamics could be realized remotely using UV-DCS method.

The comparison of the UV-DCS method with state of the art remote methods is presented in Table 3.7. One can see that the sensitivity of UV-DCS is of the same order of magnitude as methods based on Differential Optical Absorption Spectroscopy (DOAS, LP-DOAS, MOAS) or standard UV Fourier Transform Spectroscopy.

3.6.2 Case 2 and other trace gas detection

For the second case the resolution is less restrictive. The bandwidth must be wider to include more absorbing lines. The resolution is not limiting the sensitivity in this case and can be reduced as the absorption lines are wider (> 1 nm; 3THz width; see figure 3.2). The chosen parameters of Case 2 are f_{rep} = 200 MHz and Δf_{rep} = 200 Hz for the following reasons : The resulting free-aliasing spectral bandwidth is 100 THz (30 nm) which is sufficient to retrieve most of the absorbing lines of molecules presented in figure 3.2. The resolution is 5 GHz (for an acquisition time of 100 µs) and allows to retrieve the absorption lines of Case 2 molecules. The parameters for both cases have been summarized in table 3.5. It can be noted that the resolution could even be reduced without any loss of spectral information. However, a decrease of Δf_{rep} will not provide a better sensitivity. A value of Δf_{rep} higher than 130 Hz allows to make the experiment immune to the induced atmospheric noise (see section 3.4). Moreover, the higher Δf_{rep}, the better the relative coherence between the two combs during one interferogram. It can be noted that a larger value of f_{rep} could relax the condition on Δf_{rep} and increase the free-aliasing spectral width. However, the state of the art low phase noise has been demonstrated for f_{rep} ranging from 100 MHz to 200 MHz. Hence, a f_{rep} values of 100 MHz and 200 MHz were chosen for respectively Case 1 and Case 2.

Table 3.5: Summarize of the characteristic parameters of Case 1 and Case 2. In both cases Δf_{rep} value is 200 Hz and the acquisition time is 100 µs.

	λ central [nm]	f_{rep} [MHz]	ν_{res} [GHz]
Case 1	308	100	2.5
Case 2	350	200	5

The RIN after second harmonic generation of a Ti:sa laser was estimated at -129 dBc/Hz (see section 3.3). The spectral resolution can be set up to the limit : 77 GHz (0.03 nm). The achievable MAS in Case 2 is showed in figure 3.2. The sensitivity is lower than in Case 1 which is explained by more spectral elements M to be measured.
The results of concentration detection limit for Case 2 is presented in Table 3.6 for SO_2, CH_2O, $BrO, OClO, HONO$ and NO_2.

The Case 2 strategy shows better sensitivity compare to UV-Fourier Transform Spectroscopy (UV-FTS) and a similar one compare to DOAS experiment. These results compared to state of the art spectroscopic remote method are summarized in Table 3.7.

Discussions on the multiplicative noise taken into account and on the correction of the interferograms for averaging are presented in the two next sections.

Table 3.6: Results on the concentration detection limit of molecules of interest of the Case 2. The calculation used a 2 km light path with 200s of averaging time, a central wavelength of 350 nm, an optical spectral bandwidth of 50 THz and a MAS of 2.10^{-3}.

Component	Differential Cross-Section $\times 10^{-19}$[cm^2/molec.]	Concentration Detection Limit [ppt]
SO_2	5.7	700
CH_2O	0.48	625
BrO	15	20
$OClO$	107	38
$HONO$	4	1000
NO_2	2.5	1600

Table 3.7: Comparison of MAS for 1 s acquisition time determined in this simulated study with state of the art sensitivity performances of open-path, remote and under tropospheric conditions. LP-DOAS : Long Path Differential Absorption Spectroscopy, MOAS : Multi-pass Optical Absorption Spectroscopy, UV-FTS : UV- Fourier Transform Spectroscopy.

	Experiment Type	MAS at 1 s
Case 1		
	LP-DOAS [259], [260], [158]	$[2-3]\times 10^{-4}$
	MOAS [258]	$[1-2]\times 10^{-4}$
	UV-FTS [261]	$[1-2]\times 10^{-4}$
	UVDCS (numerical study, this work)	$[1-6]\times 10^{-3}$
Case 2		
	LP-DOAS [260] [262] [263]	2×10^{-2}
	UV-FTS [261]	0.2
	UV-DCS(numerical study, this work)	$[1-3]\times 10^{-2}$

3.6.3 Discussion on the multiplicative noise

In all the results presented, the multiplicative phase noise (presented in section 3.2.1) were taken into account using the equation 3.4.

$$\sigma_{multilines} \approx \frac{3\Delta\nu_L}{\Delta\nu}\sqrt{\frac{\Delta\nu}{T f_{rep}^2}}\sigma_{\phi,fast} \tag{3.4}$$

$\Delta\nu_L$ is the absorption line width of the targeted molecule, $\Delta\nu$ is the optical spectral width of the Ti:sa comb, T is the acquisition time. In the table 3.8 is summarized the estimated multiplicative noise $\sigma_{multilines}$ induced by some trace gases of interest for our study. We show that the multiplicative noise is at least 4 times lower than the additive noise σ_f for the measure of the molecules studied in this work.

Table 3.8: Comparison between additive and multiplicative noise using with 1 s acquisition time. Case (1): $\sigma_{\phi,fast} = 0.33$ rad, $\Delta\nu = 1$ THz, $f_{rep} = 100$ MHz, Case (2): $\sigma_{\phi,fast} = 0.22$ rad, $\Delta\nu = 50$ THz, $f_{rep} = 200$ MHz. σ_f corresponds to the standard deviation of the noise considering only the additive sources of noise, as calculated via equation 3.1.

Case Study	Components	$\frac{\Delta\nu_L}{\Delta\nu}$	$\sigma_{multi,line}$	σ_f
Case (1)				
	OH	1 / 111	8.9×10^{-5}	1×10^{-3}
	Naphthalene	1/ 33	3×10^{-4}	2×10^{-3}
	Formaldehyde	1/ 33	3×10^{-4}	2×10^{-3}
	SO_2	1/ 22	5×10^{-4}	2×10^{-3}
Case (2)				
	BrO/Formaldehyde	1/25	9.3×10^{-4}	3×10^{-2}

3.6.4 Discussion on interferogram correction

For both case-studies, the simulated MAS results are achievable if the phase-corrected interferograms can be averaged. For UV-DCS the SNR at 100 μs is approximatively 5 for Case (1) and below 1 for Case (2) which prevents direct phase correction or summed FT spectra. However we estimated that the coherence is maintained during longer acquisition time, up to 130 ms. This allows the use of coherent averaging protocols as proposed by Coddington *et al.* [199] for approximatively ten interferograms. The summed interferograms can be then averaged out after usual phase correction [264]. The conditions of such a correction is either a high signal/noise ratio for the summed interferograms or a monitoring of f_{rep}, f_0 and of the slow optical frequency comb amplitude fluctuations. Real-time adaptative sampling can also be considered [197]. Longer acquisition time can be achievable using consecutive similar schemes. In practice, the averaging time is limited by buffer size considerations and acceptable processing times.

3.7 Capacity of a UV beam to create OH radicals

At 300 nm, the light beam has enough energy (4 eV) to break molecule bonds such as the O-O bond of ozone whose dissociation energy is 1.27 eV. The photo-dissociation of O_3 to excited photo-products is thus made possible and produces a ground state O_2 as well as an oxygen in an electronic excited state $O(^1D)$. The photo-dissociation of ozone is the main source of OH in the atmosphere [43]. The reaction is shown in 3.5 :

$$O_3 + h\nu = O(^1D) + O_2 \tag{3.5}$$

$O(^1D)$, plays an important role in the lower atmosphere since it is the dominant precursor of the formation of OH radicals. OH is mainly produced from the chemical reaction of $O(^1D)$ and H_2O showed in reaction 3.6 [265].

$$O(^1D) + H_2O \rightarrow 2OH^{\cdot} \tag{3.6}$$

At higher altitudes, this reaction is in competition with the quenching of $O(^1D)$ that produces its ground electronic state $O(^3P)$ from N_2 and O_2 [266]. $O(^3P)$ is the ground state of the oxygen atom and is 2 eV lower in energy than $O(^1D)$. $O(^3P)$ does not react rapidly with atmospheric molecules and thus it can be neglected in the production of OH [265].

To calculate the production of OH induced by the UV laser beam, one has to compute first the induced O_3 photolysis rate. This is equivalent to compute $J(O(^1D))$ the $O(^1D)$ production rate. The equation is expressed in 3.7.

$$J(O(^1D)) = \int^{\lambda} \sigma(O_3, \lambda) \times \phi(\lambda) \times F(\lambda) d\lambda \tag{3.7}$$

The temperature is considered constant as the laser beam is propagating horizontally. The formation rate of the excited oxygen depends on the absorption cross-section of O_3 : $\sigma(O_3, \lambda)$, on the quantum yield of $O(^1D)$: $\phi\ (\lambda_0, O^1D) = 0{,}79$ and on the photons flux $F(\lambda)$ for $\lambda_0 = 308$ nm contained in the laser radiation, in photons.cm^{-2}.nm^{-1}.s^{-1} expressed in equation 3.8. [265].

$$F = \frac{P}{h\nu \times \pi(d/2)^2} \tag{3.8}$$

With P the lasing power emitted, $h\nu$ the energy of the photons and d the diameter of the light beam. F was found to be $\approx 10^{14} photons.s^{-1}.cm^{-2}$ taking into account a light beam diameter of 10 cm and an emitted power of 10 mW.

The formation rate of $O(^1D)$ is found to be :

$$\mathbf{J(O(^1D)) = 10^{-5} s^{-1}}$$

The laser beam is absorbed by all the atmospheric interferent i in the UV range, presented in figures 5.17a and 3.2. The laser beam is also scattered by the atmospheric molecules and aerosols. These molecules reduce the photolysis of ozone as they interfere with the light beam. The laser beam attenuation is taken into account using Beer Lambert equation expressed in equation 3.9. The term α_i is the extinction coefficient of the molecule i and is equal to its atmospheric concentration C in molecules/cm^{-3} times its absorption cross-section $\sigma_i(\lambda_0)$.

$$J^L(\lambda_0, O(^1D)) = J(\lambda_0) \prod_i e^{-\alpha_i(\lambda_0)\times L} \tag{3.9}$$

The total atmospheric extinction is $\prod_i e^{\alpha_i(\lambda_0)\times L} = e^{-\tau(\lambda_0)} \approx 0.25$ for 2 km optical path. With τ the total atmospheric extinction at λ_0. Therefore, the formation rate of O^1D corrected by the atmospheric extinction worth approximately $\mathbf{J^L(\lambda_0, O^1D) = 2.5.10^{-6} s^{-1}}$, which is one order of magnitude lower than its first estimation from 3.7.

Let us calculate the production of OH using $J^L(\lambda_0, O^1D)$. The production of OH from the photodissociation of O_3 (reaction 3.5) is expressed by the equation 3.10 in molecules per cm^3.

$$P(OH) = 2f \times [O_3] \times J^L(\lambda_0, O(^1D)) \tag{3.10}$$

The factor f is given by the equation 3.11 [126].

$$f = \frac{k_{O^1D+H_2O}[H_2O]}{k_{O(^1D)+H_2O}[H_2O] + k_{O^1D+N_2}[N_2] + k_{O^1D+O_2}[O_2]} \tag{3.11}$$

Where $k_{O(^1D)+N_2}, k_{O(^1D)+H_2O}, k_{O(^1D)+O_2}$ are reactive or quenching $O(^1D)$ removal rates coefficient in s^{-1}. The factor f is evaluated at 0,057. The production of OH due to the interaction of the emitted UV light beam is computed from the equation 3.10 and is found to be $\mathbf{P(OH) = 10^5}$ $\mathbf{molecules(OH).cm^{-3}.s^{-1}}$. All the reaction rate coefficients have been obtained from Dunlea et al. [266].

The concentration of the produced OH can be estimated from its atmospheric lifetime τ_{OH} and its production by simple multiplication : $[OH] = P(OH) \times \tau_{OH}$. The lifetime of OH varies from ms to second timescales and is strongly sensitive to the concentration of NOx. In a polluted environment the reaction constant k' of OH range from 15 to 130 s^{-1} and about 1s in pristine environment (low concentration of Nox) [267]. In Lyon the concentration of NO_2 is around 50 ppb ($k' \approx 50 s^{-1}$) [268].

Typical concentration of OH are about 2.10^6 to 10^7 in pristine [269] and urban area [270]. In an environment such as Lyon the concentration of produced OH due to the UV laser beam reaches $\mathbf{10^3 molecules.cm^{-3}}$, for $\mathbf{k' = 50 s^{-1}}$, and it reaches $\mathbf{10^4 molecules.cm^{-3}}$ for a less polluted environment $\mathbf{k' = 15 s^{-1}}$. In a pristine environment the **k'** is around 1 or 2 s^{-1} and produced OH due to UV excitation would be $[OH] \approx \mathbf{10^5 molecules.cm^{-3}}$.

The state of the art remote sensing of the minimal concentration detection of OH measurement was up to 10^6molecules.cm^{-3} made by Multipass Optical Absorption Spectroscopy instrument (MOAS) or Fourier Transform Spectroscopy (UV-FTS) [258, 261]. The concentration of OH produced by laser photolysis at 308 nm is at least ten times lower than the sensitivity attainable by the current state of the art spectroscopic methods. One has to keep in mind that the results were obtained with an initial laser beam power of 10 mW. The production of OH is expected to be higher with an increase of the UV light power. It can be noticed that the light beam power is not constant during its propagation.

The laser beam has enough energy to photo-dissociate other molecules such as NO_2. As the formation rate of NO is the same order of magnitude as that of OH, a production of NO and a reduction of NO_2 is existing. However, the photon-induced variation estimation (following the same procedure as indicated above) in the concentration of NO produced and the concentration of NO_2 loss remain tiny compare to the average tropospheric concentration of NO and NO_2. Indeed the concentration of NO in an urban area like the city of Lyon is in range 10^{24} molecule.cm^{-3} while the production rate is in range of 10^4 molecule.cm^{-3}. Moreover, even though the quantity of NO_x influences the concentration of OH, it does not alter it at this order of magnitude of concentration fluctuation [271]. We can be confident that it is safe to neglect any production of OH or the loss/production of molecules through photolysis by a UV-dual comb radiation source.

3.8 Conclusion

This work has provided a first framework for future experimental demonstration of remote sensing spectroscopy in the UV range in an open-air atmosphere using Dual-Comb Spectroscopy. The evaluation of the method was investigated using two case-studies. The amplitude and phase noise induced by the atmosphere on the UV pulsed laser during its propagation were investigated. Δf_{rep} should have a higher value than 130 Hz to render the experiment immune to atmospheric phase and amplitude noises. In general a high value of Δf_{rep} is advantageous for the UV-DCS method. It allows more interferograms to be recorded during the coherence time of the two combs. Harmonic generation from a Titanium-sapphire laser was chosen as the source of the UV-DCS. Its high power emission, spectral broad range and its low noise makes it the best candidate for realistic UV-DCS measurement. A numerical evaluation of the signal to noise ratio of the UV-DCS method has permitted the identification of the main limiting element which is the RIN of the UV laser source. But we believe that with future laser power stability protocols improvements, the signal to noise ratio of UV-DCS method will be improved. Considerations of phase corrections of the interferograms were discussed. Then, attainable sensitivity using UV-DCS was assessed for the two

case-studies and compared with the state of the art UV remote sensing techniques. Based on our numerical work, and with the current laser sources, the UV-DCS method appears to not surpass current differential absorption spectroscopy in terms of sensitivity. However, it is competitive when a broader spectral range is needed. The detection of atmospheric molecules using UV-DCS methodology will allow inter-comparisons with other remote sensing detector. UV-DCS could therefore contribute to improving our knowledge on open-path and broadband experiments on highly reactive molecules in the UV range. This work is preliminary to experimental verification such as the impact of the multiplicative noise on one interferogram or the use of averaging strategies. The measurement of the propagation of a UV beam in the atmosphere should also confirm that the photo-dissociation of molecules in the optical path is negligible.

As the majority of the phase noise originates from the pump laser source, a high relative coherence between the two combs can be obtained using a single cavity [229]. This is the strategy applied in this thesis. In the next two chapters, is described the setting-up of a bi-directional mode-locked femtosecond laser and its experimental realization.

Chapter 4

Setting up a bidirectional passive mode-locked solid state laser cavity

The solid state titanium-sapphire mode-locked laser source combined with second or third harmonic generation appeared to be the most adapeapted laser source for monitoring remotely the atmospheric molecules of interest absorbing in the UV range. The advantages of this laser source is the possibility to retrieve a broad spectrum at high resolution in a very short time using a powerful low noise laser emission. According to our numerical simulation presented in chapter 3, the realisation of dual comb spectroscopy using a Ti:sa-based laser source in the UV is competitive with actual spectroscopic methods for trace gas detection. One of the difficulty using Ti:sa laser sources for DCS is to keep a relative coherence between the two pulses trains. As seen in chapter 2, this relative coherence can be improved without the need of complex stabilisation system using a single bidirectional cavity system. Before building the laser cavity, we investigated the influence of cavity design. In this chapter is presented the cavity design realisation of a single bidirectional cavity dual comb laser. The generation of fs pulses from a Ti:sa laser are obtained by a method called mode-locking. Initiating a bidirectional mode-lock regime can be difficult. Experimentally, it is easier to start the passive mode-locking regime using a linear cavity as the laser pulses are injected twice as often in the gain medium per round trip compare to a ring cavity. The linear cavity and the bidirectional cavity are presented in figure 4.1. The two setups are composed of two curved mirrors (M1-M2) focusing the laser inside the gain medium, one output coupler (OC) a Ti:sa crystal and one or several planes mirrors. The geometry of a linear configuration allows an unique laser emission direction, whereas the ring resonator can generate two laser emissions in two different directions (see b) of figure 4.1). The linear and ring cavity use the same curved mirrors, crystal and pump injection setup. Therefore the ring cavity can be made by adaptation of the linear cavity. All the numerical work presented in this chapter applies for both cavities. The development

and optimization studies on Kerr lens mode-locked laser cavities detailed in the review of Yefet et al. [272], the book Ultrashort Laser Pulse Phenomena of Diels and Rudolph [273] and the articles of Garduno et al. [274, 275] have provided a very good framework to optimise the cavity design.

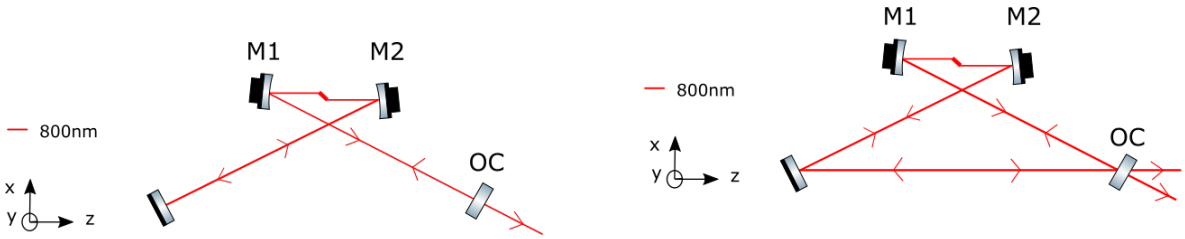

Figure 4.1: Schematic of a simplified linear cavity (a) and bidirectional laser cavity configuration (b). There are both composed of two curved mirrors that are called M1 and M2, a Ti:sa crystal and an output coupler.

In this chapter is first presented the theoretical background of passive mode-locked lasers. It contains the presentation of a common model that describes the passive mode-locked regime in a steady state. The generation of pulse trains which is due to the interplay between the non linear Kerr lens effect and the net dispersion in the laser cavity is presented in the next section. In section 3 are presented several methods to start the ML regime. A numerical study was performed to build a KLM laser cavity. The section 4 is presenting the different numerical simulations results obtained during this thesis. The optimization of the intra-cavity power through the Brewster angle optimisation of optical elements, the compensation of the astigmatism for the pump laser and intra-cavity laser, the net dispersion compensation and laser stability were investigated and are presented.

4.1 Laser mode-locked cavity theoretical background

4.1.1 The mode-locking formalism

The mode locking consists of a method that generates ultra-short pulses from a laser cavity. The term "mode-locked" refers to the simultaneous oscillations of thousands of modes in a resonator where all the modes have a constant phase relation. The mode locked laser is also called "phase-locked" laser. The electric field resulting from the sum of all these phase locked modes can be given by the equation 4.1 and 4.2. In this paragraph, the amplitude of each modes are considered equal to E_0.

$$E(t) = \sum_{n=0}^{n=N-1} E_0 e^{i\phi_n} e^{i\omega_n t} \tag{4.1}$$

E_0 is the amplitude of the electric field mode, ω_n the pulsation rate of the mode n, t the time and N the number of existing modes. In the case of a mode-locked laser, all the modes of phase ϕ_n present the same phase ϕ_0. Thereby the total electric field can be developed to the equation 4.2. The detail of the development can be found in the book of Diels et al. [273] or the book of Silvfast et al. [276].

$$E(t) \propto \frac{E_0}{2} e^{i\phi_0} \frac{sin(\pi N f_{rep} t)}{sin(\pi f_{rep} t)} \tag{4.2}$$

N is the total number of oscillating phase-locked modes. Δf_{rep} corresponds to the repetition frequency difference, E_0 is the initial electric field amplitude and f_0 is the carrier envelope offset frequency of the laser comb. From this equation it can be seen that for a large N value, strong peaks are created when $t = 1/frep$ which corresponds to the temporal separation between the pulses. The "mode locked" principle is represented in figure 4.2.

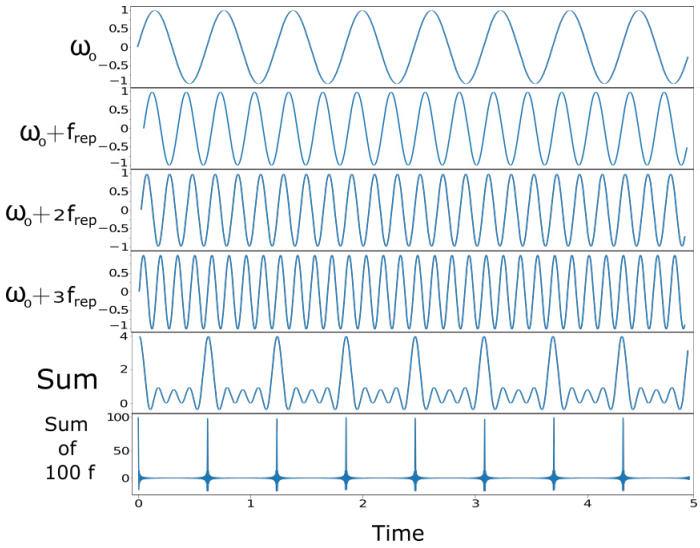

Figure 4.2: Representation of the mode-locked principle from equation 4.1. Each panel represents the electric field of cavity modes or the sum of these cavity modes evolving in time. Four cavity modes of frequencies separated by f_{rep} are represented in the four first panels. These modes share a constant phase relation. The sum of these 4 cavity modes is represented in the "Sum" panel. A representation of the sum of 100 phase locked cavity modes separated by f_{rep} is represented in the last panel. The units in time and intensity are arbitrary units given as indication.

When the modes have random phase no pulse is observed. The sum of a hundred of modes with random phase noise is presented in figure 4.3. It can be noted that the intensity of the laser is much higher when a phase relation is existing between the modes. The phase-locking of thousands of modes may create in the Ti:sa laser very short pulses in the femtosecond range with high intensity. Models have been developed to understand and describe the mode-locking origin. This is described in the next subsection.

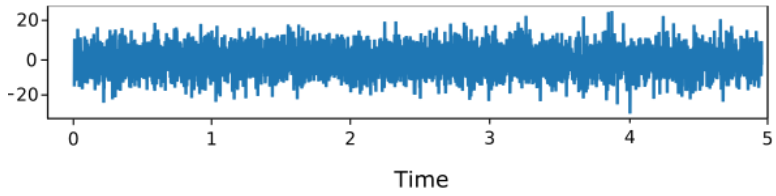

Figure 4.3: Representation of the sum of 100 modes with random phase value.

4.1.2 Circulating pulse model

A simple circulating general round trip model that describes a femtosecond pulse propagating in a mode-locked laser is presented in figure 4.4. It describes a circulation of the pulse inside the cavity where each block and connecting lines are shaping the pulse.

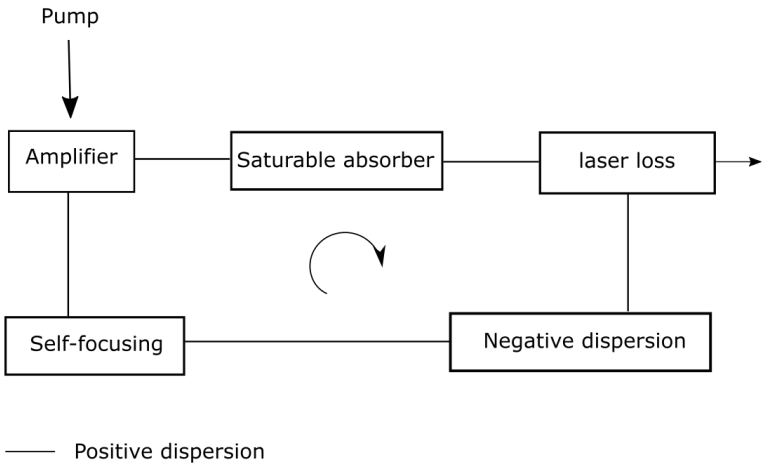

Figure 4.4: Schematic of a model describing the circulation of a fs pulse inside a laser cavity. The straight line corresponds to free propagation of the pulse in a positive dispersion medium (air or crystal for example).

A pumped amplifier is amplifying the intra-cavity laser power with each round trip. The saturable absorber is an element that advantages the mode-locking regime compare to the CW regime. It is detailed in section 4.3. The laser loss corresponds to the output emission of the laser which results in a source of loss of intra-cavity power. The dispersion is responsible for the temporal broadening (positive) or narrowing (negative) of the pulse. The self-focusing is a non-linear effect responsible for self phase modulation and initiation of the mode-lock regime. This system can be described as periodic. After one round trip, the pulse shape is returned to its original value. The amplifier, the self-focusing and the saturable absorber elements can be located in the same medium (crystal) as it will be seen in the section 4.3.

In stationary regime, the shape of the pulse is periodic along the cavity. The envelope of the pulse A(z) at a position z in the cavity is equal to itself after one cavity trip $\mathrm{A(L_{eff}+z)}$. Each block presented in figure 4.4 is applying an operator $\hat{\mathrm{U}}$ to the pulse envelope $A(z)$. The following equation can be written : $\mathrm{A(z+L_{eff})=\hat{U}_N\hat{U}_D\hat{U}_G\hat{U}_LA(z)}$. $\hat{U}_N$, $\hat{U}_D$, $\hat{U}_P$ and $\hat{U}_L$ are respectively the non-linear, the net dispersion, the gain and the loss operator. The net dispersion corresponds to the total contribution resulting from the negative and positive dispersion. The amplifier block is taken into account by the gain operator, the self-focusing by the non-linear operator and the positive and negative dispersion by the dispersion operator. As the cavity is in its stable stationary regime, $\hat{U}_N\hat{U}_D\hat{U}_G\hat{U}_L$ must be equal to the identity $\hat{I}$ operator. This means that the pulse shape returns to its original shape after one round trip.

In this context the continuous model consists in considering that all the induced processes of each block are distributed along the whole cavity. It is thus considered that the pulse is propagating through the same medium where all the pulse-shaping effects occur simultaneously. Thus it can be written that : $\mathrm{A(z+L_{eff})\approx A(z)+L_{eff}\frac{\partial A}{\partial z}}$. L_{eff} is the effective length of the cavity. This is mathematically valid if the evolution of the laser pulse shape remains small compare with the size of the cavity. In a stationary regime, the gain and loss compensate each other exactly. Therefore, the differential equation can be written as $\frac{\partial A}{\partial z}=\hat{D}A+\hat{N}A$. $\hat{D}$ and $\hat{N}$ are respectively the net dispersive and non-linear operators. The non-linear Schrödinger equation presented in equation 4.3 can be determined from this equation by developing the operators $\hat{D}$ and $\hat{N}$. More details on this analytical model can be found in the articles of Haus et al. [277], Martinez et al. [278] or in the chapter 5 of the book of Diels [273].

$$\frac{\partial A(z,t)}{\partial z}=-i\frac{1}{2}\frac{d^2k}{d^2\omega}\frac{\partial^2A(z,t)}{\partial t^2}+i\gamma|A(z,t)|^2A(z,t) \tag{4.3}$$

Where $\frac{d^2k}{d^2\omega}$ is the group velocity dispersion where k is the wavenumber and ω is the pulse ratio, γ is a nonlinear parameter (it is detailed in section 4.2). A solution of the non-linear Schrödinger equation is the soliton equation : $A(z,t)=A_0\frac{e^{i\phi(z)}}{cosh(t/\tau)}$. A_0 is the amplitude of the pulse envelope and τ is related to the pulse duration FWHM of a secant hyperbolic where $\tau=1.76\tau_{(FWHM)}$. A condition for this solution to exists is an over compensation of the global net cavity dispersion : $\frac{d^2k}{d^2\omega}=-\gamma A_0^2\tau^2<0$. This soliton effect was first experimentally highlighted by Salin et al. [279]. This model was in agreement with the results obtained by Curley et al. [280] who observed that the higher the value of $\frac{d^2k}{d^2\omega}$, the narrower was the spectrum.

This continuuous model is at the limit of applicability in the case of Ti:sa laser. This model main hypothesis is that the temporal and spectral evolution of the pulse remain relatively low along the cavity. However, for a Ti:sa laser, the spectrum can reach 200 nm width with pulses as short as a dozen fs [246, 280, 281]. As it is described in the subsection 4.2.2, the shorter is the pulse, the stronger is the dispersion impact on the pulse duration (figure 4.8). Curley et al. [280] observed

that in a Ti:sa laser cavity the spectrum and pulse duration on both end sides of the cavity were different (35 and 54 nm width). A more sophisticated model was developed by Brabec et al. [282]. This model consists of a solitary laser description where a passive amplitude modulation is added to the model. This new model provides a very useful analytical expression given in equation 4.4 that quantifies the amount of negative dispersion |GDD| to induce to the cavity to allow the mode-lock regime and the propagation of pulses of duration Δt. The global net group delay dispersion of the cavity must be lower or equal to this value for observing a stable soliton propagation in the cavity. More details on this equation can be found in Brabec et al. [283].

$$\Delta t = 3.53 \times \frac{|GDD|}{\psi \times E_p} \tag{4.4}$$

with $\psi = \frac{4\pi n_2}{\lambda_0^2}$. The global net round-trip dispersion $|GDD|$ can be determined from E_p the energy of one pulse in Joule, n_2 is the second order refractive index of the gain medium in m^2/W, λ_0 is the central wavelength of the pulse. The energy of one pulse can be found by knowing the average output power P_{out}, the OC transmission T_{OC} and the repetition frequency f_{rep}. This equation has been, used by Kasper and Witte [284] for estimating the net cavity GDD to compensate for realising experimentally a prismless Ti:sa solid state laser generating 10 femtosecondes pulses. Therefore, the equation 4.4 appears useful for determining the net dispersion value that must be induced to the laser cavity to generate fs pulses.
In the next section is detailed the non-linear Kerr lens mode-locking which is at the origin of the passive pulsing regime of the developed cavity.

4.2 Generation of femtosecond pulses theoretical background

4.2.1 Kerr-lens description

The generation of a fs pulse results from an interplay between the self phase modulation (SPM) initiated by the Kerr-lens mode locking (KLM) and the dispersion. The SPM produces new frequency components and broadens the pulse spectrum. The self-focusing is the consequence of the non linear dependence of the crystal refractive index with the laser intensity. As it is detailed in this section, at high laser beam intensity, the refractive index of the material is given by the equation 4.5

$$n(I) = n_0 + n_2 \times I(r) \tag{4.5}$$

n_0 and n_2 are the initial and the second order refractive index of the material, $n_2 = \gamma \times \frac{2}{cn_0\epsilon_0} = \frac{3\omega_0\chi^{(3)}}{4n_0\epsilon_0 c^2}$, $\gamma = \frac{3\omega_0\chi^{(3)}}{8n_0 c}$, where ω_0 is the central frequency of the pulse envelope, $\chi^{(3)}$ is the third non-linear order of the dielectric susceptibility and c the light celerity. I is the intensity of the laser that is dependant on the radial position r. The detail of this equation determination can be found in the appendix section 6.5. The second order refractive index value of Ti:sa crystal is $3.10^{-20}\text{m}^2.\text{W}^{-1}$. Hence, this phenomenon is only visible for high intensity laser beam. As the intensity of the laser beam is inhomogeneous and follows a Gaussian shape, the laser beam is more intense in the centre (r=0) than at its edges. This results in a higher refractive index in the center of the laser beam propagation. This can be viewed as a material that is thicker in the middle than at its wings which has the same effect than a spherical converging lens. The optical light pulse keeps shaping itself by self focusing, until it reaches its final state. This effect leads to a "self mode locking" by the effect of self phase modulation. This phenomenon is represented in figure 4.5.

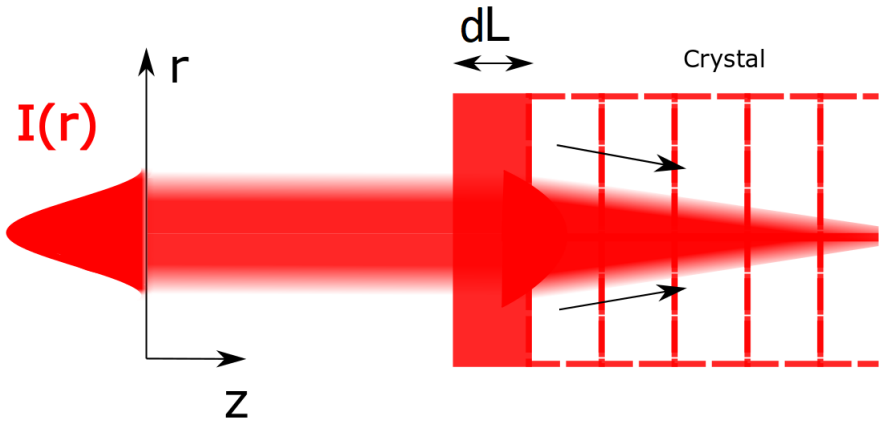

Figure 4.5: Schematic of a self-phase modulation Kerr effect. The refractive index is dependant on the laser beam intensity (see equation 4.5). As the laser beam has a spatial Gaussian distribution shape, the refractive index is higher in the center of the crystal compare to the edges. The diagram shows crystal portions of length dL. Each portion receives a more intense laser beam as the beam is more and more focused. Thereby, the laser is self-focused in the crystal.

As seen in this section, the optical pulses must be intense enough to start the self-phase mode-locking. If the pulses are too long in the temporal domain, the intensity of the pulse is thus reduced, and the non-linear refractive index might not be impacted enough for having a sustainable and efficient focusing. The duration of the pulses are increased by the positive dispersion induced by different medium where the laser beam is propagating such as the air, the crystal or the prisms. Thus, the duration of the eventual pulses circulating in the cavity, must be shortened. This part is detailed in the next subsections.

4.2.2 Group-velocity dispersion management

The global positive dispersion of the cavity induced by the propagation of the laser beam through the crystal or the air needs to be compensated. First a definition of the group velocity dispersion is given.

It is possible to develop the wave-number κ_0, using the Taylor expansion around a central pulsation ω_0 in a transparent material, that corresponds to a zone where the refractive index value is linear with the frequency. The development is given in equation 4.6.

$$\kappa(\omega) = \kappa_0 + (\omega - \omega_0)\frac{d\kappa_0}{d\omega} + \frac{1}{2}(\omega - \omega_0)^2\frac{d^2\kappa_0}{d^2\omega} + ... \tag{4.6}$$

- $\kappa_0 = n(\omega)\frac{\omega_0}{c}$
- $\tau = \frac{d\kappa_0}{d\omega}$
- $GVD = \frac{d^2\kappa_0}{d^2\omega}$

τ corresponds to a temporal delay induced to the pulse.
The GVD is the group velocity dispersion. The velocity of each wave contained in the pulse is called the phase velocity $v_\phi = \frac{c}{n(\omega)}$. The group velocity is given by v_g and $v_g^{-1} = \frac{d\kappa}{d\omega} = \frac{n_g}{c} = (n\omega + \omega\frac{dn}{d\omega})/c$. The difference of phase velocities for each wave (of different frequencies) contained in the pulse results in a temporal broadening of the pulse as shown from the evolution of an initial pulse (figure 4.6) that propagates through a material with a positive dispersion (figure 4.7). As illustrated on the figure 4.7, when the GVD is positive, the lower frequencies contained in the pulse have a higher velocity than the higher frequencies. When $\frac{d^2\kappa_0}{d^2\omega} < 0$ the opposite is observed, the higher frequencies travel faster than the lower frequencies. The sign of the GVD depends on the nature of the material.
It should be noted that several definitions are given for the dispersion of the pulse. The GVD, in fs^2/mm defined above, is the second derivative of the wavenumber with respect to the pulsation $\frac{d^2\kappa}{d^2\omega}$. The GDD, in fs^2, is the group delay dispersion and it corresponds to the GVD multiplied by the distance of propagation : $GDD = GVD \times z$, where z is the propagation distance from a reference origin taken as 0 of the pulse through the material.

Figures 4.6 and 4.7 show two simulated electric field of a pulse propagating through a material using the equation of the sum of thousands of electric fields of angular frequency ω separated by 100 MHz : $E = A\exp(\Phi)$ with Φ the phase of the pulse, which form a fs pulse. $\Phi = -(\omega + \omega_0)t + \kappa \times z + \phi_0$ and $\kappa = \kappa_0 + \frac{d\kappa_0}{d\omega} \times \omega + 1/2\frac{d^2\kappa_0}{d\omega} \times \omega^2 + 1/6\frac{d^3\kappa_0}{d\omega} \times w^3$. The width of the pulse as a function of the GVD in the temporal domain, is given by the equation 4.7. The pulse is said to be Fourier transform

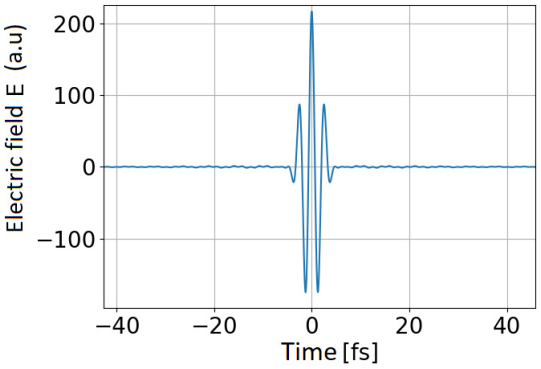

Figure 4.6: Original 4 fs impulsion at Fourier limits, before its propagation through the atmosphere.

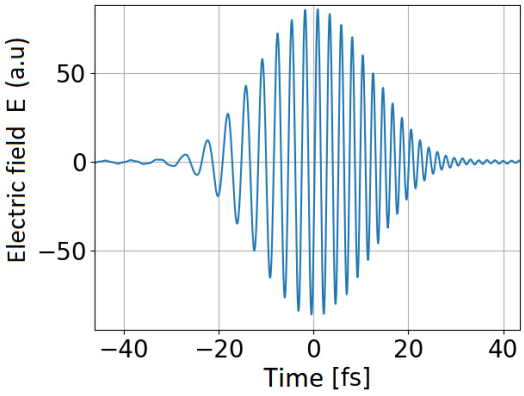

Figure 4.7: Same pulse after propagation through 10 meters of atmosphere.

limited when its temporal duration $\Delta t = \Delta t_0 = \frac{1}{2\Delta\omega}$. Δt_0 is the temporal limit duration of the pulse. On the contrary, when the pulse is "chirped", the pulse is broadened in the time domain and its duration follows the equation 4.7.

$$\Delta t = \sqrt{\Delta t_0^2 + (GVD \times z \times \Delta\omega)^2} \tag{4.7}$$

z is the distance propagation, $\Delta\omega$ is the spectral width of the pulse. The broader the pulse spectrum (which corresponds to a short Fourier limit duration Δt_0), the greater the dispersion impact on its duration, as shown on figure 4.8.

The non-linear and dispersion interplay formalism which is responsible for stable propagation of pulses in the laser cavity was presented in this section. Experimentally, it is necessary to induce negative dispersion to the laser cavity to have short enough pulses that can initiate the KLM. A prism compressor of several prisms is used to induce negative dispersion to the cavity. The theoretical principle and the main parameters of this optical system are presented in the next subsection.

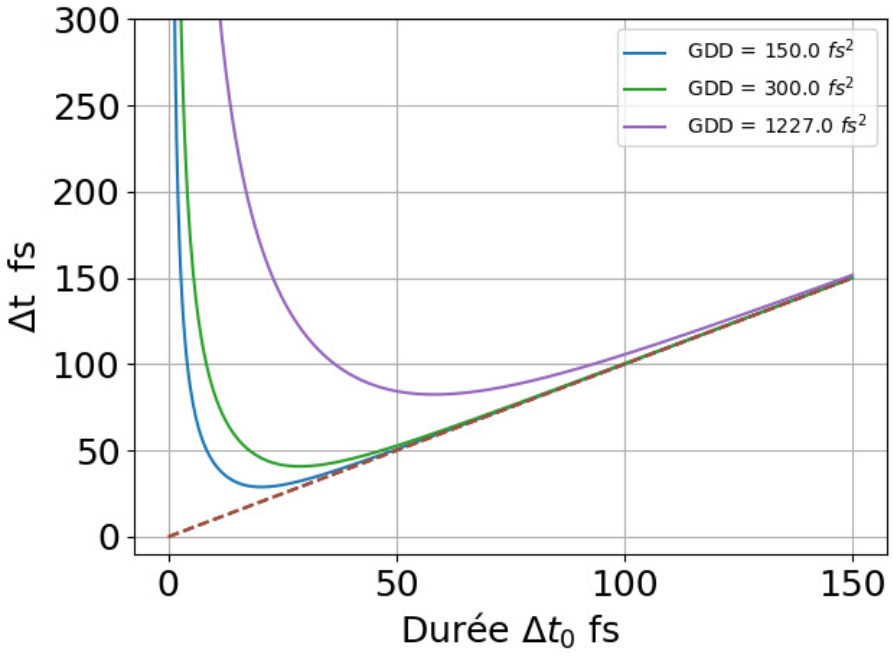

Figure 4.8: Duration of the pulse as a function of the Fourier limited duration Δt_0 for three different GDD values : 150, 300 and 1227 fs^2

4.2.3 Prism Compressor

The pulses are propagating through several dispersive elements (positive dispersion), that causes the lower frequencies to go at a higher speed than the higher frequencies. This results in a temporal broadening of the pulses. The purpose of the prism compressor is to separate spatially the high frequencies from the lower frequencies contained in the pulse. Then, in a second step, its aim is to increase the propagating distance of the faster frequencies to let the slower and faster frequencies to be temporally superposed. The propagation of the laser beam through a prism compressor system of four prisms is given in figure 4.9.

Note that the prism compressor represented in figure 4.9 is used in the ring cavity configuration. In the linear configuration, only two prisms are used because the laser beam is propagating twice in the prism compressor, given an equivalent negative dispersion value to the 4 prism compressor in the ring configuration. The prism is cut at a minimum deviation angle for 800 nm, which means that, when the incident laser beam θ_0 is at Brewster angle, then the prism exiting angle θ_3 beam is also at Brewster angle: $\theta_0 = \theta_3$. The Brewster angle has been determined at 59.7° (the determination of the Brewster angle will be presented in subsection 4.4.1). In this case, the advantage to set the incident angle at the Brewster is twofold : it minimizes the reflection loss and allows to have the exiting refracted angle at Brewster angle. Three factors are contributing to the total group velocity dispersion induced by the prism compressor.

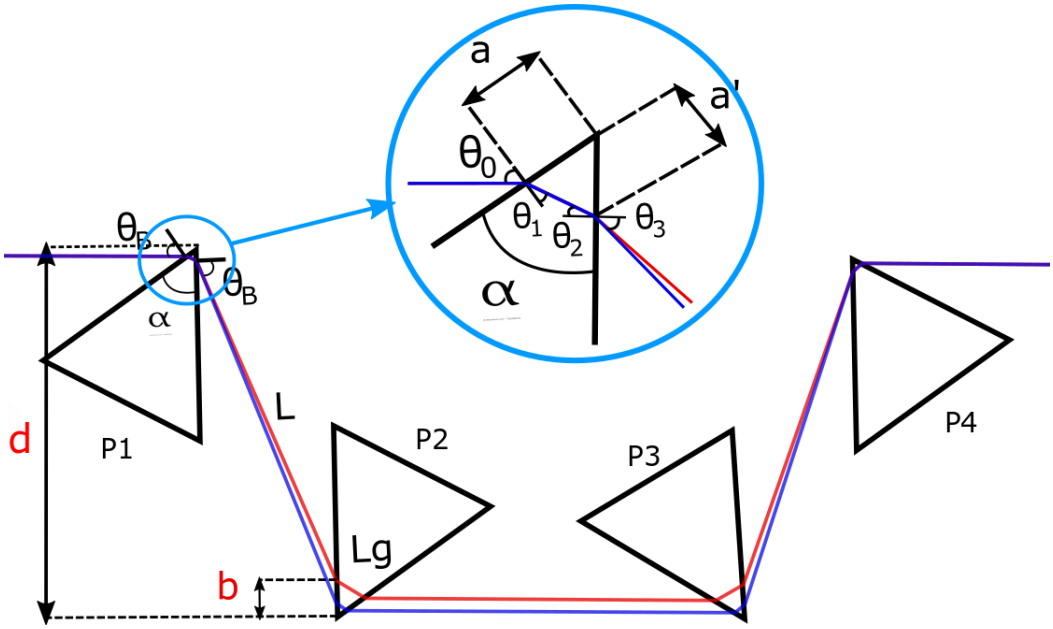

Figure 4.9: Prism compressor composed of 4 prisms numbered from P1 to P4. The parameters that can be changed experimentally are the distance between the two prism apexes : d, and the distance b. The distance b corresponds to the distance between the apex of the second prism and the entering location of the beam, on the prism surface. θ_0 is the incident angle of the beam, θ_1 and θ_2 are the refracted angles of the beam inside the prism, θ_3 is the exiting angle, or refracted angle at the exit of the prism. α is the angle of the summit of the prism, usually called apex. The distances L and L_g are, respectively, the distance of propagation of rays in the air and in the SF10 material. a and a' are respectively the distance from the apex of the first prism, to the location of the beam, on the surface prism, at the entry (a) and at the exit (a').

- A positive GVD, induced by the propagation of the pulse passing through the thickness of glass L_g.
- Negative GVD contribution is due to the angular dispersion $d\theta_3/d\omega$ over an air distance L . This cause the higher frequencies to propagates through less distance than the low frequencies, in the second prism. The difference of distance is increasing with the increase of the distance L.
- Negative GVD contribution due to the angular dispersion $d\theta_1/d\omega$ over a distance L_g in the glass of refractive index n. (The laser beam is at the minimum deviation angle, this term has only weak impact).

The dispersed frequencies induced by the two first prisms, are then spatially re-combined by a second set of prisms. The second prism couple (P3-P4) are set in a symmetrical way with the first set of prisms. They have the exact same dispersive effect than the first couple of prisms.
Considering the optical path, the angular dispersion, due to the first prism, the distance travelled

in the air L and in the prism L_g, it is possible to obtain the GDD of the compressor system, given by the equation 4.8 for a minimum deviation and Brewster incident beam. The detail of the determination of this equation can be found in the book of Ultrashort Laser Pulse Phenomena written by Diels and Rudolph [273].

$$GDD = \frac{d^2\Phi(z,\lambda) \times z}{d\lambda^2} = \frac{\lambda_0^3}{2\pi c^2}\left[L_g(b,d)\frac{d^2n}{d^2\lambda} - \left(4L(b,d) + \frac{L_g(b,d)}{n^3}\left(\frac{dn}{d\lambda}\right)^2\right)\right] \tag{4.8}$$

Φ is the phase of the electric pulse. λ_0 is the central wavelength, c the celerity of light in vacuum. n is the refractive index of the SF10 prism material. At 800 nm, the refractive index $n = 1.7113$ ([285]).

L_g and L are given in equation 4.9 and 4.10.

$$L_g = \frac{\left((d - n \times ((d - a') \times tan(\frac{\pi}{2} - \theta_3) + ds)\right) \times sin(\alpha)}{cos(\theta_l)} \tag{4.9}$$

$$L = \frac{tan(\frac{\pi}{2} - \theta_0)(d - a') - ds}{cos(\theta_0)} \tag{4.10}$$

a' is the distance from the apex of the first prism to the exit location of the light beam (see figure 4.9), and is given by equation 4.11. $ds = tan(\frac{\pi}{2} - \theta_0) \times b$

$$a' = a\left(cos(\alpha) + sin(\alpha) \times tan(\frac{\pi}{2} - \theta_l)\right) \tag{4.11}$$

This formalism was used to estimate the net negative dispersion induced by a prism compressor as a function of the parameters d and b. From a practical point of view, this estimation is useful and necessary to experimentally set the distances between the prisms. The mode-locked regime can be initiated, when the right net negative amount of dispersion is induced to the cavity. The experimental techniques used to commence mode-locking are presented in the next section.

4.3 Mode-locking techniques

4.3.1 Start of the passive ML

The techniques used for triggering the mode-locking regime are either active or passive. In the active case, an external amplitude (AM) or frequency (FM) modulation at a frequency corresponding to a multiple of the laser cavity repetition rate, launch the ML regime. A more detailed description

of active mode-locking operation can be found in the work of Kuizenga et al. [286, 287]. Passive mode-locking regime is usually achieved by the use an intra-cavity saturable absorber. A saturable absorber is an element that has a saturated level of absorption which results in the induction of more losses to the low intensity than to the high intensity light. As the fs pulses have a high intensity, this regime is preferred compare to the CW laser regime. Therefore, the repetitive fs pulses propagation in the gain medium produce a fast loss modulation. Usually, much shorter pulses are obtained with passive mode locking method because the recovery time is much faster for passive saturable absorber than for a sinusoidal AM or FM. Two passive mode-locking strategies are used : semiconductor saturable absorber mode-locking (SESAM) and Kerr lens mode locking. The SESAM method uses a semi-conductor element that is integrated into a mirror of the laser cavity. This device is more efficient for reflecting high intensity laser. The semi-conductor absorbs the photons with sufficient energy which results in the excitation of an electron from the valence to the conduction band. In a high intensity regime, electrons can accumulate in the conduction band and cause depletion of the absorbing transition : the absorption is saturated. More details on the mode-locking active and passive methods can be found in the review of Keller [288]. The Kerr-lens mode locking regime was presented in the beginning of this chapter. It is a third order non-linear effect where the intra-cavity laser is self-focused in the crystal.

Magni et al. and Cerullo et al. [289, 290], Shieh et al. [291] or Salin et al. [292] describe the experimental conditions for self-starting Kerr-lens. An efficient method for starting the ML regime is the retro-injection of the laser output beam back inside the cavity. A phase shift between the retro-injected beam and the intra-cavity beam creates a perturbation into the laser. The light radiation retro-injection method has been previously used by several teams such as Bartels et al. in 1999 [293], or Pelouch et al. [294]. Experimentally, a mirror is mounted on a frequency controlled piezo stack (up to 2V amplitude). It reflects back the output laser beam from one of the two directions back in to the cavity. The retro-injection is inserted at the negative arm (clockwise direction of beam : OC-M4-M2-crystal). This direction corresponds also to the shortest arm. Despite the high efficiency of the method, the mode-locked regime was observed only in one direction.

A perturbation can also be initiated by tapping one of the cavity mirrors or by quickly translating one of the cavity mirror or one of the prisms (dispersion change). The experimental observations of KLM means that the ML regime has been favoured compared to the CW regime. The physical processes involved are detailed in the following paragraphs.

4.3.2 Mode-lock methods

Triggering the Kerr lens mode-locking requires an external action, as it doesn't spontaneously start from the CW regime. The ease of onset of the mode-locked regime is closely related to the Kerr strength. The strength K of the Kerr effect can be defined by the equation 4.12. It represents the laser beam size modification due to a small variation of power. This equation was retrieved from the review article of Yefet et al. [272]. From the analytical expression for the Kerr effect, one can determine the locations in the stability map where the onset of the mode-lock regime should be the easiest to produce [295].

$$K = \frac{P}{w_{CW}} \times \left(\frac{dw_{CW}}{dP} \right) \tag{4.12}$$

P is the pulse peak power, w_{CW} is the laser beam radius in a continuous regime of the laser at one of the end mirror.

Three passive mode-locking techniques have been used to induce losses to the CW regime to initiate the fs-pulses : the hard ML, the soft ML and the Virtual hard ML. These techniques play a similar role to fast-saturable absorbers.

Hard Aperture

Hard aperture mode locking is a technique that uses a physical slit inside the cavity. It is aimed at spatially inducing loss to a part of a laser beam. Depending on the laser regime (ML or CW), the laser beam has different beam size, divergence along the cavity. The idea of hard mode locking is to find a position in the cavity where the CW laser beam has a higher size than in the ML regime. Then by inducing loss due to the closing of a physical aperture (typically a razor blade) loss of the CW laser beam is induced while the entire laser beam in the ML regime can pass through the aperture. Its size in both planes can be determined by using the Gaussian and ABCD formalism. Lin et al. [296] demonstrated that an analytical method using the q parameters of a Gaussian beam could be used to determine the size of the beam in both planes at each point of the cavity.
Cerullo et al. [290, 297] and Magni et al. [289, 298] used an equation similar to the equation 4.12 to map the size variation of a laser beam as a function of the distance between the two curved mirrors M1 and M2 and the position of the crystal. This has defined the optimum positions of the crystal and the slit where the Kerr effect was strong.

Soft Mode-Locking

The soft mode locking technique uses also a difference in the size of the laser beam between the two regimes. CW losses are induced in the crystal when the pump beam diameter does not match the CW intra-cavity laser beam size. For some positions of the crystal and the two curved mirrors, the CW beam size becomes larger than the ML beam size. In that situation, a small pump size can promote the ML regime due to the partial overlap of the pump beam with the CW laser beam. The soft mode locking technique is supposed to be more efficient at position where the hard mode locking is less efficient [272]. This comes from the fact that a large CW spot size at the end mirror corresponds to small spot size in the crystal and vice-versa.

Virtual Hard Mode-Locking

This methods consists in setting the position of M1-M2 slightly beyond the stability limits of the CW regime. As presented [272] and experimentally demonstrated by Yefet et al. [299], the ML stable operation can still exists beyond the CW stability zone. The CW laser beam is thus suffering from diffraction losses and therefore this method is equivalent to the use of an intra-cavity aperture.

Numerical simulations were performed to estimate important cavity parameters using the generation of fs pulses theoretical background. This is described in next section.

4.4 Numerical simulation results on the laser cavity

This section is summarizing the numerical simulation work realised to build the laser cavity. To start the ML regime, an intra-cavity laser power threshold must be crossed. The work of Kowalevicz et al. [300] demonstrated that the threshold could be reduced to as low as 200 mW of pump power by adapting the cavity design. In our work, the purpose is not to reduce the ML threshold but rather to optimize the ratio between the emitted output power and the pump power and to have at least 300 mW emitted in each arm to generate enough power in the UV range (See chapter 3). The ways to increase the optical power are the following :

- Reducing the loss in the laser cavity, this encompasses astigmatism compensation and the reflection loss minimisation at the intra-cavity solid elements.
- Optimizing the light intensity of the pump laser in the gain medium as well as the mode-matching

- The identification of the stable zones

We first describe how to reduce the loss by reflection on the crystal, secondly how to compensate the astigmatism of the intra-cavity laser and in the third subsection is described how to compensate the astigmatism of the pump laser.

As seen in subsection 4.1.2, the net cavity dispersion must be negative to generate a mode locked laser. A preliminary estimate of the amount of negative dispersion needed is investigated in the 4th subsection. A prism compressor was designed and a quantitative evaluation of the amount of associated negative dispersion was assessed from numerical simulation. This is presented in the 5th subsection. The knowledge of the cavity stability is experimentally necessary to generate CW and ML laser. This part was investigated and is presented in the last subsection.

4.4.1 Brewster angle optimization

Several solid intra-cavity optical elements are a source of power loss in the cavity due to the reflection of the laser beam on their surfaces. The crystal tilt might induce excessive loss on the pump and the intra-cavity laser beam power. Also, the prism compressor inserted inside the cavity which is composed of 2 (linear cavity) or 4 prisms (ring cavity) is also a source of power loss depending on their tilt. The purpose is to minimize the loss of power due to the reflection on the surface of these optical elements. The reflectivity ratio R, depends on the angle of incidence of the beam. It exists an angle for which the reflectivity ratio is near 0 for the parallel polarisation part of the laser beam. This angle is the wavelength dependant Brewster angle θ_B. In this work, the Brewster angle is estimated at 800 nm. 800 nm corresponds to the center of the titanium-sapphire emission gain coefficient. The expression for reflectivity ratios as a function of the angle of incidence θ are given in equations 4.13 and 4.14.

$$R_{perp}(\theta) = \left(\frac{1-\alpha(\theta)\beta)}{1+\alpha(\theta)\beta}\right)^2 \tag{4.13}$$

$$R_{par}(\theta) = \left(\frac{\alpha-\beta}{\alpha+\beta}\right)^2 \tag{4.14}$$

with $\alpha(\theta)$ given by the equation 4.15 and $\beta = n_2/n_1$. n_2 and n_1 are respectively the refractive index of the refractive and incident medium.

$$\alpha = \frac{\sqrt{1-(n_{air}/n_r)^2 \times sin(\theta)}}{cos(\theta)} \tag{4.15}$$

n_{air} and n_r are respectively the refractive index of air (1.00027 [301]) and the first order refractive index of the refracted medium (1.7601 [302] for the titanium-sapphire crystal and 1.7113 [285] for the SF10 glass). θ is the angle of incidence.

To minimize the reflection on the surface of the crystal, the light beam has to be polarized in the horizontal direction (parallel polarisation). At Brewster angle, the angle between the reflected and refracted rays is perpendicular. From the Snell Descartes law, one can determine the Brewster angle by the following relation : $tan(\theta_B) = n_r/n_{air}$, where n_r and n_{air} are the refractive index of a parallel polarized beam respectively, of the reflective material and the air. The pump laser beam must be p polarized to reach a near-zero reflection loss. The value of the Brewster angle at 800 nm has been determined to be $\theta_B = 60.39°$ for the Ti:sa crystal material and $\theta_B = 59.7°$ for the SF10 glass.
The crystal is Brewster cut which means that the angle between the entry or end surfaces with the side of the crystal are at Brewster angle. Hence, the incident laser beam that is entering the crystal at Brewster angle is thus parallel inside the crystal to its side. When exiting the crystal the laser beam is also parallel to the initial incident laser beam.
As the Brewster angle of the crystal for 532 nm and 800 nm is close (60.55° instead of 60.39°), the tilt of the crystal can minimize the loss due to the reflections of both the pump and the intra-cavity laser beam on the surfaces of the crystal. However, the drawback of the incident angle set at Brewster angle for the crystal is that it causes a spatial deformation, called astigmatism, in the beam which results in a reduction of the laser pump intensity. The next step consists in compensating this spatial deformation. The optimization of the shape of the light beam is described in the next subsection.

4.4.2 Intra-cavity astigmatism compensation

To minimize the reflection loss on the surface of the crystal, the intra-cavity laser beam has an angle of incidence of 60.39 degrees with the surface of the crystal in the tangential plane (xz plane). In the sagittal plane (xy plane), the laser beam is perpendicular to the surface. This difference in the two planes creates astigmatism in the laser beam and can reduce the laser performance and even in extreme case, can prevent laser propagation. The principle of astigmatism is presented in figure 4.10. When the light is propagating through an optical element (a lens, a curved mirror, a tilted crystal), depending on the orientation of the optical element, the focal points indicated as T_f and S_f in the tangential and sagittal planes are spatially shifted. This has the effect of elongating the laser beam which increases the transversal surface of the laser beam and thus reduce the laser intensity. Astigmatism is mathematically defined as the ratio between the size beam in the tangential plane

and the size beam in the sagittal plane (equation 4.16). An astigmatism of 1 corresponds to a perfect round laser beam.

$$A = \frac{w_x}{w_y} \tag{4.16}$$

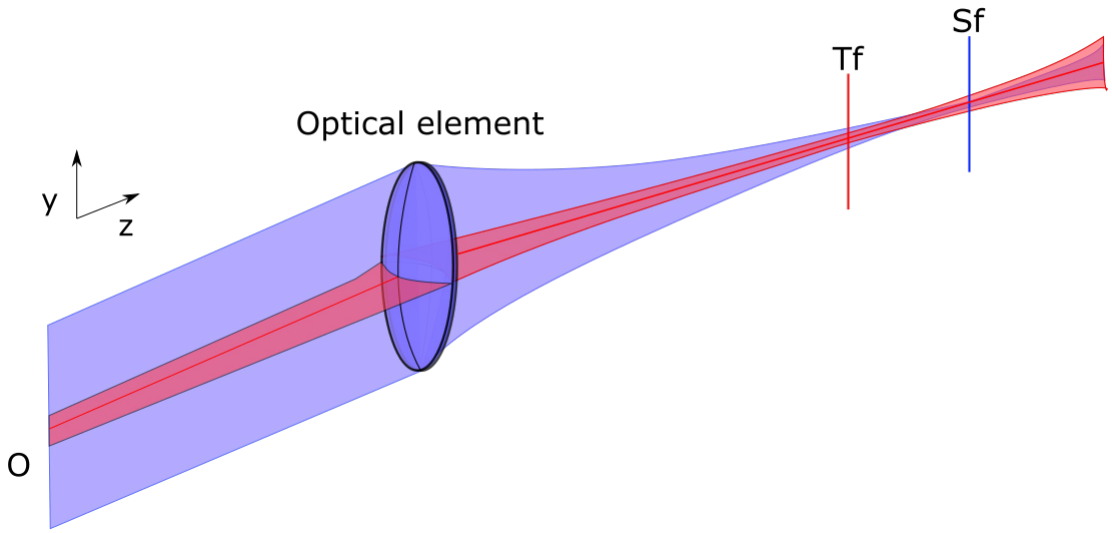

Figure 4.10: Principle of astigmatism. The astigmatism corresponds to an existing difference of position between the focal point T_f in the tangential plane and S_f in the sagittal planes.

During its propagation in the crystal, the focused laser beam is more stretched in the tangential plane than in the sagittal plane. The size of the laser beam in the tangential and sagittal plane are,respectively given by w_x and w_y. They are given by the equations 4.17 and 4.18 [273] according to a Gaussian laser beam propagation.

$$w_x = nw\sqrt{1 + \left(\frac{\lambda}{\pi w} \times \frac{L\sqrt{1+n^2}}{n^4}\right)^2} \tag{4.17}$$

$$w_y = nw\sqrt{1 + \left(\frac{\lambda}{\pi w} \times \frac{L\sqrt{1+n^2}}{n^2}\right)^2} \tag{4.18}$$

w is the beam waist size of the laser beam inside the crystal, n is the extraordinary refractive index of the crystal, L is the crystal length. The equations 4.17 and 4.18 comes from the reference [273].

At the exit of the crystal, the size of the laser beam in the tangential direction w_x is reduced because of the Brewster tilted surface. However as the waists sizes in both direction have evolved

in the crystal in a non linear way (see equation 4.17 and 4.18), they exit the crystal with different size in the x and y direction. The laser beam is thus astigmatic, at the exit of the gain medium. It is similar to consider in the tangential plane a crystal length $L_t = L/n^3$ and in the sagittal plane : $L_s = L/n$. L and n are the geometric length of the crystal and its refractive index. The crystal astigmatism is considered as $\Delta L = L_s - L_t$.
This effect can be compensated upstream, by setting up a specific angle ϕ (see equation 4.21) in the xz plane, to the two curved mirrors M1 and M2 with the propagation direction of the laser beam. This angle modifies the mirrors focus length in the tangential and sagittal planes. The modified focus length are given by the equation 4.19 and 4.20.

$$f_t = f \times cos(\phi) \tag{4.19}$$

$$f_s = \frac{f}{cos(\phi)} \tag{4.20}$$

The formalism has been introduced by Tache et al. [303]. f_t and f_s are the focal lengths in the tangential and sagittal planes. f is the paraxial focal length of the laser beam (incident angle of 0).

f is the paraxial focus length value of the curved mirrors. The angle ϕ in the xz plane given to the mirror with the laser beam adds an astigmatism that compensate the Brewster crystal astigmatism. The mirror astigmatism $\Delta f(f, \theta) = f_s - f_t$ can compensate the crystal astigmatism by solving $\Delta f(f_1, \phi_1) + \Delta f(f_2, \phi_2) = \Delta L$. The solution of this equality is given in equation 4.21 where $\phi_1 = \phi_2$. In our case the initial focal lengths of the curved mirrors M1 and M2, are respectively : $f_1 = f_2 = f = 50$ mm.

$$\phi = arccos\left(\sqrt{1 + N^2} - N\right) \tag{4.21}$$

with : $N = L/(4fn) \times (1 - 1/n^2)$ [304].

A tilt angle on the mirrors M1 and M2 in the tangential plane ϕ**=11.2°** is needed to compensate the astigmatism of a 10 mm Ti:sa crystal.

4.4.3 Pump laser astigmatism compensation

The pump laser beam injected in the crystal, is also impacted by the angle of the crystal with the laser beam direction. The pump laser, focused at the centre of the crystal, also suffers from an astigmatism that has to be compensated. The optimisation of the efficiency of the light focusing within the crystal is described below.
The laser pump beam (532 nm Nd-Yag laser), is initiating the population inversion in the gain medium. Before entering the gain medium, the laser beam is focused by one lens, it is going through one tilted curved mirror with 11.2 ° tilt and through the Brewster tilted face of the crystal. This is schematized in figure 4.11. Compensating the pump astigmatism allows to optimise the laser intensity deposited in the crystal. The pump energy has to be high enough to reach the lasing threshold of the crystal. To provide enough energy, the light beam is focused, using a lens, into the crystal .

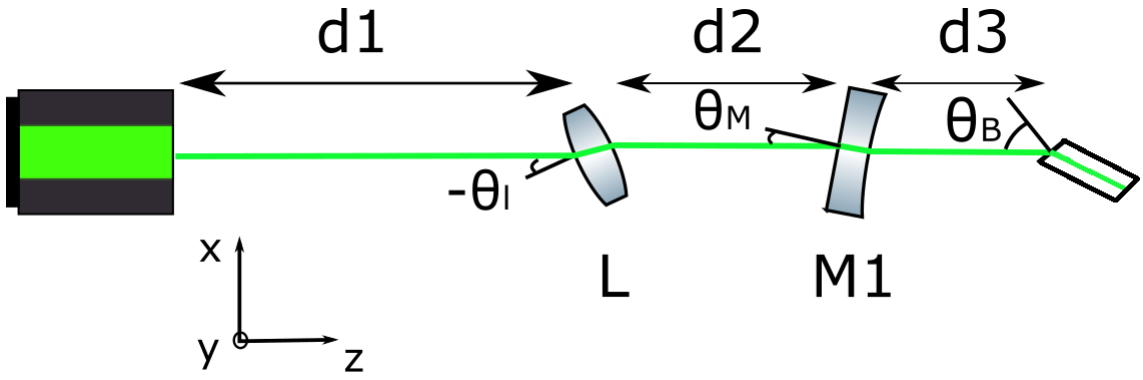

Figure 4.11: Pump laser focused inside the crystal. The light beam pass through the lens L tilted with the angle θ_l, the curved mirror M1 that is tilted by the angle θ_M, and the crystal. The distance d_1, d_2, d_3 are respectively the distance between the laser and the lens, the lens and the mirror and the curved mirror and the crystal.

One solution to compensate the astigmatism created by the tilt of the curved mirror and of the crystal, is to tilt the lens. We adapted the mathematical formalism presented by Ramirez et al. [305] to determine the tilt angle needed for the pump lens of our optical system. The ABCD matrix and Gaussian beam formalism is used. The description of a Gaussian beam propagating through a thin lens, a thin mirror and in the crystal in the tangential and sagittal plane is made. The ABCD matrix of the system is presented in equation 4.22 for the tangential plane and 4.23 for the sagittal plane. First, the distance between the lens and the curved mirror required to focus the light beam in the middle of the crystal, can be determined by solving the equation $A_T(d_2) = 0$ or $A_S(d_2) = 0$, where $A_{T/S}()$ corresponds to the first term of the total ABCD matrix of the lens-mirror-crystal system. A distance of $d_2 = 34.12$ mm has been determined. A focal length of 100 mm is used. The distance between the curved mirror M1 and the crystal of $d_3 = 49.5$ mm was selected for this

calculation. This distance corresponds to a stable position of the cavity and to a waist position of the intra-cavity laser beam in the middle of the crystal for a M1-M2 distance of 107.2 mm (See figure 4.14 in subsection 4.4.4).

Tangential plane :

$$\begin{pmatrix} A_T & B_T \\ C_T & D_T \end{pmatrix} = \begin{pmatrix} 1 & t/n_3 \\ 0 & 1 \end{pmatrix} \begin{pmatrix} \alpha_3 & 0 \\ 0 & 1/\alpha_3 \end{pmatrix} \begin{pmatrix} 1 & d_3 \\ 0 & 1 \end{pmatrix} \begin{pmatrix} 1/\alpha_2 & 0 \\ -\beta_2/R_4 & \alpha_2 \end{pmatrix} \times \begin{pmatrix} \alpha_2 & 0 \\ \beta_2/R_3 & 1/\alpha_2 \end{pmatrix} \begin{pmatrix} 1 & d_2 \\ 0 & 1 \end{pmatrix} \begin{pmatrix} 1/\alpha_1 & 0 \\ -\beta_1/R_2 & \alpha_1 \end{pmatrix} \begin{pmatrix} \alpha_1 & 0 \\ \beta_1/R_1 & 1/\alpha_1 \end{pmatrix} \begin{pmatrix} 1 & d_1 \\ 0 & 1 \end{pmatrix} \tag{4.22}$$

Sagittal plane :

$$\begin{pmatrix} A_S & B_T \\ C_T & D_T \end{pmatrix} = \begin{pmatrix} 1 & t/n_3 \\ 0 & 1 \end{pmatrix} \begin{pmatrix} 1 & 0 \\ 0 & 1 \end{pmatrix} \begin{pmatrix} 1 & d_3 \\ 0 & 1 \end{pmatrix} \begin{pmatrix} 1/\alpha_2 & 0 \\ -\mu_2/R_4 & 1 \end{pmatrix} \times \begin{pmatrix} 1 & 0 \\ \mu_2/R_3 & 1 \end{pmatrix} \begin{pmatrix} 1 & d_2 \\ 0 & 1 \end{pmatrix} \begin{pmatrix} 1 & 0 \\ -\mu_1/R_2 & 1 \end{pmatrix} \begin{pmatrix} 1 & 0 \\ \mu_1/R_1 & 1 \end{pmatrix} \begin{pmatrix} 1 & d_1 \\ 0 & 1 \end{pmatrix} \tag{4.23}$$

Where :

$$\alpha_i = \frac{\sqrt{n_i^2 - sin(\theta_i)^2}}{n_i cos(\theta_i)}$$

$$\beta_i = \frac{n_i}{cos(\theta_i)} - \frac{n_i}{\sqrt{n_i^2 - sin(\theta_i)^2}}$$

$$\mu_i = \sqrt{n_i^2 - sin(\theta_i)^2} - cos(\theta_i)$$

n_1, n_2, n_3 and θ_1, θ_2 and θ_3 are respectively the refractive index and incident angle of the lens, the curved mirror M1 and the crystal.

The purpose is to minimize the astigmatism of the pump laser beam induced by the curved mirror tilt and the incident angle on the crystal surface by tilting the lens. The tilt angle of the lens that is needed to minimize this astigmatism can be determined from the ABCD transfer matrix of the lens-curved mirror-Brewster angle crystal optical system. Then, the size of the beam in the tangential and sagittal planes can be determined after the system (i.e in the middle of the crystal) from the ABCD transfer matrix and the initial laser size beam (that is supposed to be perfectly round). The result is plotted in figure 4.12 where the astigmatism $\frac{w_T}{w_S}$ value is computed as a function of the incident angle θ_l °of the lens.

The astigmatism A is computed for different lens tilt as represented in figure 4.12. The curve obtained is symmetrical at $\theta_l = 0$. Therefore there is a negative and positive solution. The

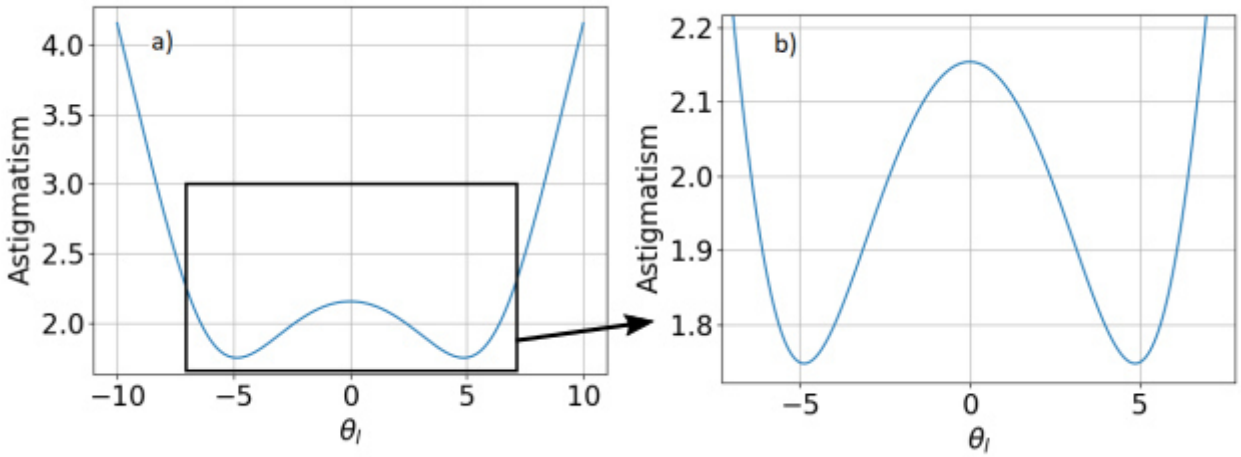

Figure 4.12: Calculation of the astigmatism as a function of the tilted angle of the lens. A vertical zoom corresponding to the black square of figure a) is represented on the figure b). Negative values correspond to inclination that is counter-clock-wise while positive figures correspond to clockwise angle (the mirror and the crystal have positive tilt).

negative solution corresponds to the case where the lens tilt is in the opposite direction from the mirror or crystal tilt. The positive solution is for a tilt in the same direction and requires a cavity alignment procedure. Experimentally, it is easier to induce a negative tilt to the lens to compensate the astigmatism. We can observe that the astigmatism is not fully compensated (which would correspond to A=1), but a minimum of astigmatism of 1,7 is determined for a lens tilt of ±4,4°.

The astigmatism difference in the crystal, that is induced by a ± 4.4 °tilt can be observed on figure 4.13 where the size beam was calculated for the tangential and sagittal plane as a function of the distance from the pump laser emission. In the middle of the crystal the tangential size beam of the pump is 1,76 times larger than the sagittal size beam in the lens-tilted case, the factor being 2.15 if no tilt is made.

The optimization of the intra-cavity optical power has been investigated. The position of the two curved mirrors M1 and M2 relative to the position of the crystal is crucial to generate a stable laser. The intra-cavity power is very dependant on the position of the intra-cavity waist in the gain medium. For some distances between M1 and M2, the laser is stable. These range of distance are called stability zones. Details are given in the next paragraph.

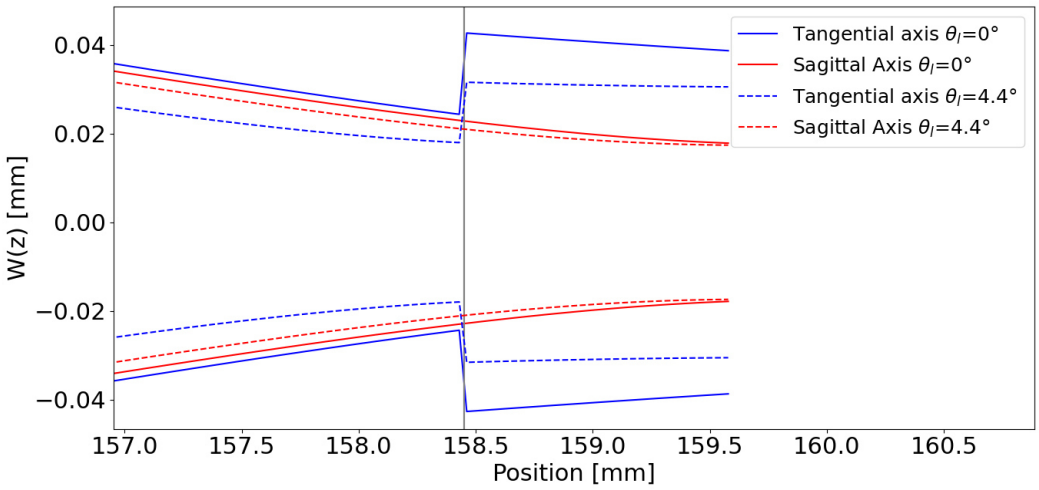

Figure 4.13: Caculation of the size beam in the crystal, for two lens tilts θ_l: 0 (lines) and 4,4° (dashed lines). The vertical gray line represents the delimitation between the air (lower values of distance) and the crystal material (higher values of distance). The broadening of the size of the beam in the tangential plane is creating an astigmatism. The 4.4° case correspond to a minimum astigmatism (see figure 4.12). The position represented in the x axis correspond to the distance from the laser pump.

4.4.4 Cavity laser beam stability

The stability of the optical resonator in the CW or ML regime is very dependant on the distance between the two curved mirrors M1 and M2. When stable, the TEM 00 laser transversal shape appears more or less round, with a constant high power. On the contrary, when the laser is unstable, the output power appears very sensitive to alignment or perturbations, a mix of higher transversal modes are emitted, the shape of the beam can appear highly astigmatic. For optimizing the output power and to determine the favourable zones to start the pulsing mode regime, it is important to know the stability zones of the laser. The stability zones are simulated for two cavity configurations : a linear cavity and a ring cavity. The astigmatism correction presented on section 4.4.2 is taken into account in the numerical calculation. As it will be described in chapter 5, a linear cavity was developed first. The passive mode-locking regime can be experimentally hard to obtain. In a linear configuration, the pulses propagate twice in the gain medium before being emitted from the cavity. As a result, the intra-cavity power is higher and therefore the mode-lock regime is more easily reached.

The stability of a resonant cavity depends on the distance between the two focusing mirrors, the length of the crystal and the length of the cavity. The Gaussian beam and ABDC matrix formalism inside a resonator are used to numerically evaluate the stability of the cavity as a function of the positions of the focusing mirrors. The compensation of the crystal astigmatism is taken into account for the two configurations using appropriate curved mirror tilt angles ϕ as calculated from equation

4.19 and 4.20. When oriented, the curved mirrors M1 and M2 are inducing a different focus distance that depends on the tilted angle of the curved mirror. As presented in section 4.4.2, the incident angle for compensating the crystal astigmatism is 11.2 °for the two configurations. To be stable an intra-cavity Transverse Electromagnetic Mode 00 (TEM00) laser beam must respect the condition given by the inequality 4.24.

$$-1 < 1/2 \times (A + D) < 1 \tag{4.24}$$

where A and D are the elements of the ABCD transfer matrix of the resonator. If the condition given in equation 4.24 is respected, it is then possible to determine the size of the laser beam at the output coupler as a function of the distance between M1 and M2 using the ABCD transfer matrix of the cavity.

Linear cavity

The linear cavity schema is represented in figure 4.14. The ABCD matrix transfer of the linear cavity resonator is given in equation 4.25.

$$\begin{aligned}\begin{pmatrix} A & B \\ C & D \end{pmatrix} = &\begin{pmatrix} 1 & 0 \\ 0 & L_1 \end{pmatrix} \begin{pmatrix} 1 & 0 \\ \frac{-1}{f_{M1}} & 1 \end{pmatrix} \begin{pmatrix} 1 & 0 \\ 0 & z \end{pmatrix} \begin{pmatrix} 1 & 0 \\ \frac{-1}{f_{M2}} & 1 \end{pmatrix} \begin{pmatrix} 1 & 0 \\ 0 & L_2 \end{pmatrix} \\ &\times \begin{pmatrix} 1 & 0 \\ 0 & L_2 \end{pmatrix} \begin{pmatrix} 1 & 0 \\ \frac{-1}{f_{M2}} & 1 \end{pmatrix} \begin{pmatrix} 1 & 0 \\ 0 & z \end{pmatrix} \begin{pmatrix} 1 & 0 \\ \frac{-1}{f_{M1}} & 1 \end{pmatrix} \begin{pmatrix} 1 & 0 \\ 0 & L_1 \end{pmatrix}\end{aligned} \tag{4.25}$$

The focal distance of the curved mirrors M1 and M2 take a different value in the sagittal and tangential planes to compensate the crystal astigmatism. A tilt is given to the two curved mirrors which modify the focal distance of M1 : f_{M1} and M2 : f_{M2}. For one plane, the foci of the two mirrors have the same value given by their tilt and given by equations 4.19 in the tangential plane or 4.20 in the sagittal case. z, L_1, L_2 are respectively the distance between M1 and M2, the distance between M1 and the output coupler and L_2 the distance M2 and the end mirror M4. If the condition given in equation 4.24 is verified, then the size of the laser beam at the output coupler can be obtained from the ABCD matrix of the resonator and from equation 4.26.

$$w = |B| \times \frac{\lambda}{\pi} \times \sqrt{\frac{1}{1 - \frac{(A+D)^2}{4}}} \tag{4.26}$$

λ is the wavelength of the laser beam. Note that adding the crystal matrix contribution in the transfer matrix appeared unnecessary as the impact on the stability plot was negligible. In this approximation, the plot of the size beam as a function of the distance z is sufficient to simulate the

cavity stability which was verified experimentally (this will be presented in section 5.5).
The linear cavity is composed of the same curved mirrors M1 and M2, same crystal, same lens as the ring cavity. This cavity has a length L_1 (M1 to OC) and L_2 (M2 to M4) of respectively 1,07 m and 1,48 m. The arm lengths were chosen to have a frequency repetition of around 100 MHz. The length of the crystal is 10 mm. The stability zone of the linear laser cavity represented in figure 4.14 is the size of the beam as a function of the distance between the two curve mirrors (distance z). The size of the beam has been obtained from the computation of the resonator matrix and the Gaussian beam formalism for each distance z. When the laser beam propagation in the cavity is unstable, the size beam is set to 0. For a linear cavity, two stable zones are present from 106,3 mm to 108,6 mm and from 110 to 112 mm. It can be seen that the intra-cavity astigmatism is only fully compensated for one distance z : (108,3 mm).

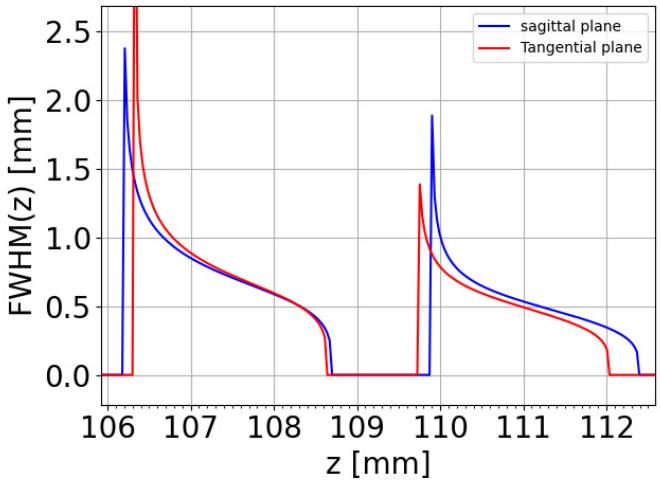

Figure 4.14: Calculation of the linear cavity laser stability zone. The FWHM size of the laser beam at the output coupler of the cavity is represented as a function of the distance between the two focusing mirrors M1, M2 : z.

Ring Cavity

In the ring cavity configuration the radiation runs only once through the crystal per round trip in the cavity. As a result instead of the propagation of a standing wave in the cavity, a travelling wave is created. The beam waist dimension is determined from the transfer matrix of the cavity given in equation 4.26 and the equation 4.27.

$$\begin{pmatrix} A & B \\ C & D \end{pmatrix} = \begin{pmatrix} 1 & 0 \\ 0 & L_{r2} \end{pmatrix} \begin{pmatrix} 1 & 0 \\ \frac{-1}{f_{M1}} & 1 \end{pmatrix} \begin{pmatrix} 1 & 0 \\ 0 & z \end{pmatrix} \begin{pmatrix} 1 & 0 \\ \frac{-1}{f_{M2}} & 1 \end{pmatrix} \begin{pmatrix} 1 & 0 \\ 0 & L_{r1} \end{pmatrix} \tag{4.27}$$

where L_{r1} and L_{r2} are respectively the distance between the OC and M2 and the distance between the OC and M1. As for the linear configuration, the matrix is used to calculate the stability zone in the tangential and sagittal planes using the same tilted angle ϕ for M1 and M2.

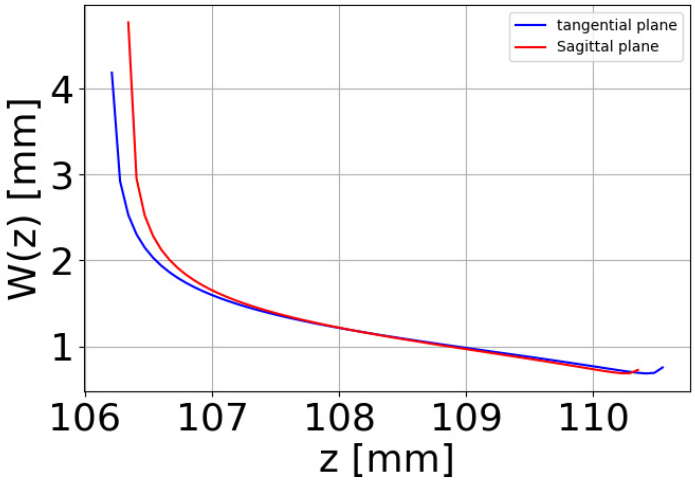

Figure 4.15: Calculation of the ring cavity stability zone. The size of the beam at the output coupler as a function of the distance z between the two curved mirrors M1 and M2.

The cavity length is 2,5 m. In this configuration only one stable zone is observable as shown in figure 4.15. As it can be seen on the figure, the laser beam astigmatism is perfectly compensated for a distance between M1 and M2 of 108,2 mm. The experimental determination of the output power was investigated and is presented in chapter 5. The maximum output power level is found in the middle of the stability zones.
The cavity design was optimized to produce the highest CW output power from the linear or ring laser cavity configuration. The next section considers how to obtain the Kerr lens mode-lock regime from these two cavity configurations with the aid of the cavity stability graphs.

To start the mode-locking regime, as presented in section 4.1 a net negative dispersion must be induced to the cavity. In the next subsection, the amount of net negative dispersion to induce to the cavity is investigated.

4.4.5 Net cavity dispersion compensation

As seen previously, the positive dispersion increases the duration of the pulses. That is why it is important to consider the impact of each element in the cavity. Therefore, to trigger the mode-locked regime, the pulse must be shortened. In this subsection, is presented the estimation of the positive dispersion induced by each intra-cavity elements and the estimation of the negative dispersion to induce to the cavity that is necessary to start the mode-locking regime.
In figure 4.16 and 4.17 are represented the dispersion induced by each optical elements as a function of the wavelength (4.16a and 4.17a) for respectively the linear and the ring cavities. Also, the

induced dispersion at 800 nm is represented for the two cases in figures 4.16b and 4.17b. In the linear case, the dispersion must be counted as twice for each elements as the laser pulses are propagating twice in each optical components before being emitted.

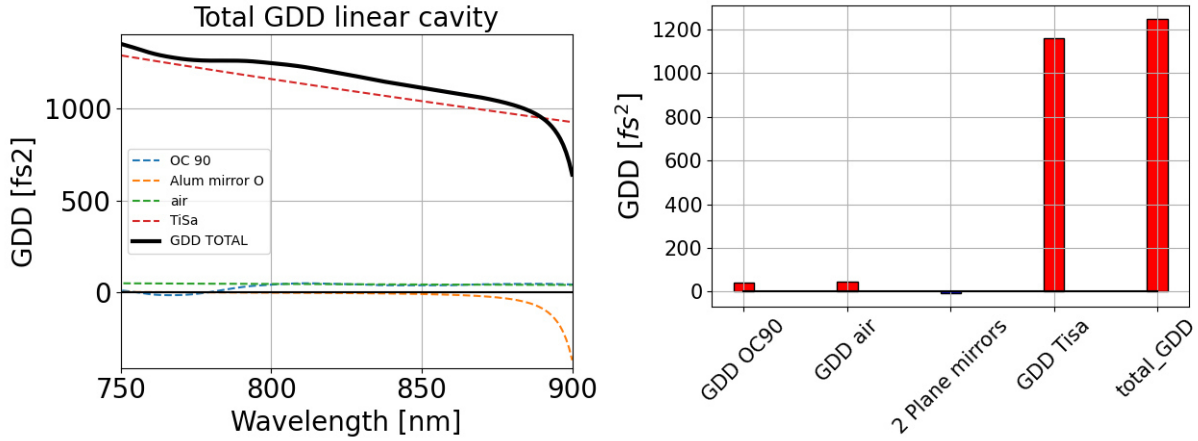

(a) (b)

Figure 4.16: Calculation of the GDD induced by each element of the cavity in the linear configuration. 4.16a GDD is represented as a function of the wavelength. In figure 4.16b, the dispersion of each element is represented at the maximum gain of the crystal Ti:Sa : at 800 nm. Red and blue bars correspond to respectively the induced positive and negative dispersion. At 800 nm the plane mirrors account for a very low negative dispersion (-3.5 fs^2). As the pulses are bouncing twice in the cavity before being emitted, their positive induced GDD must be counted twice for each element. The data were sourced from Layertech datasheets for the mirrors, from Ciddor et al. [306] for air, from Dodge et al. [307] for the Ti:sa crystal.

For both the ring and linear cavities, the repetition frequency was set close to 100 MHz, the duration of the pulse is 100 fs (this was experimentally verified, see chapter 5 for more details), the output power was chosen at 550 mW which corresponds to 10 % of the pump cavity power. It is expected to experimentally reach this amount of power. The output coupler transmission is 10 %.

As presented in the section 4.1, to see the propagation of a soliton-like femtosecond pulses in the cavity, the overall net dispersion of the cavity must be set negative. The total negative dispersion to be introduced in the cavity has been determined from equation 4.4. At 800 nm, an estimation of a negative dispersion of at least - 2250 fs^2 for the linear cavity configuration and - 1680 fs^2 for the bidirectional ring cavity configuration must be induced to generate stable mode-locked pulses. This difference of negative dispersion comes from the fact that the pulse is doing one round trip in the linear cavity to reach its original position while it is doing one cavity trip in the ring case. It has to be noted that depending on the precision of the parameters, the modification of the value can be non negligible. For instance, if the duration of the pulse is between 50 or 150 fs^2 the net negative GDD to compensate goes from -500 to -1500 fs^2. Therefore, this quantity is used as an experimental indicator, and not as an accurate value determination of the global net dispersion.

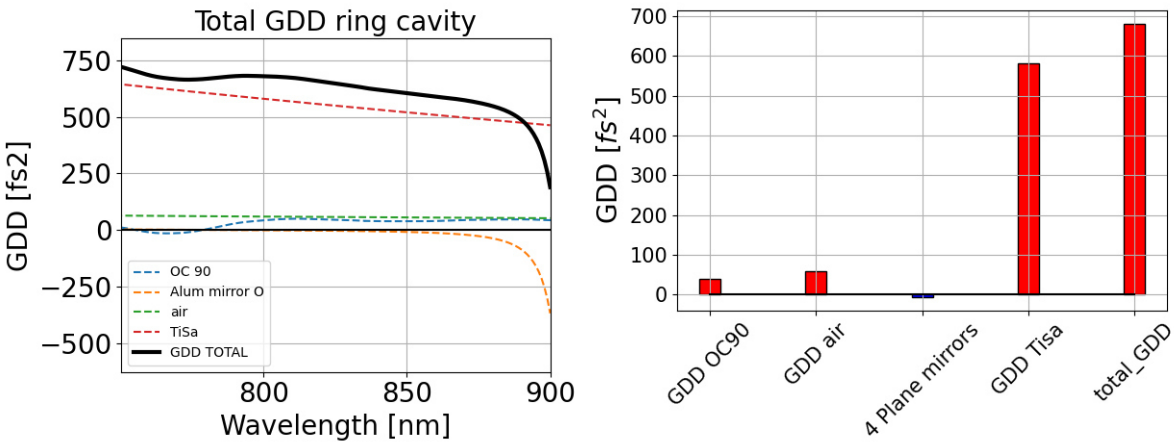

(a) (b)

Figure 4.17: Calculation of the GDD induced by each element of the cavity in the ring configuration. 4.17a GDD is represented as a function of the wavelength. In figure 4.17b, the dispersion of each element is represented at the maximum gain of the crystal Ti:Sa : at 800 nm. Red and blue bars correspond to respectively the induced positive and negative dispersion.

The insertion of a negative dispersion can be realised by using an intra-cavity prism compressor. The presentation of the prism compressor numerical simulation results is given in next subsection.

4.4.6 Prism compressor

The equation 4.8 was used to plot the GDD induced by the compressor prisms as a function of b and d given in figure 4.18. As presented in figure 4.9, the parameter d corresponds to the apex vertical distance between the two first prisms. b is the distance from the apex of P2 to the position of the entrance of the dispersed laser beam.

The figure 4.18 is a very useful map for setting up the prism compressor. To expect a stable mode-locking regime, the induced GDD must be at least lower than the represented dashed lines on the figure 4.18. A laser beam width of 1 mm is considered in the computation. This means that a distance of at least 16 cm between P1 and P2 must be respected to expect the propagation of an intra-cavity soliton. It can be seen that the range of distance where the ML regime propagation between the two prisms can go from 150 mm to more than 30 cm. However, a short distance is preferred experimentally because of the spatial limitations of the cavity. As previously seen, the determination of the total net negative dispersion to induce in the cavity remains an estimation as given by equation 4.4. Therefore a distance of more than 150 mm is preferred. SF10 glass (1.7113 [285]) was chosen because of its high refractive index value which leads to shorter distance d between the prisms and thereby optimize the size of the cavity. With fused silica prisms, the

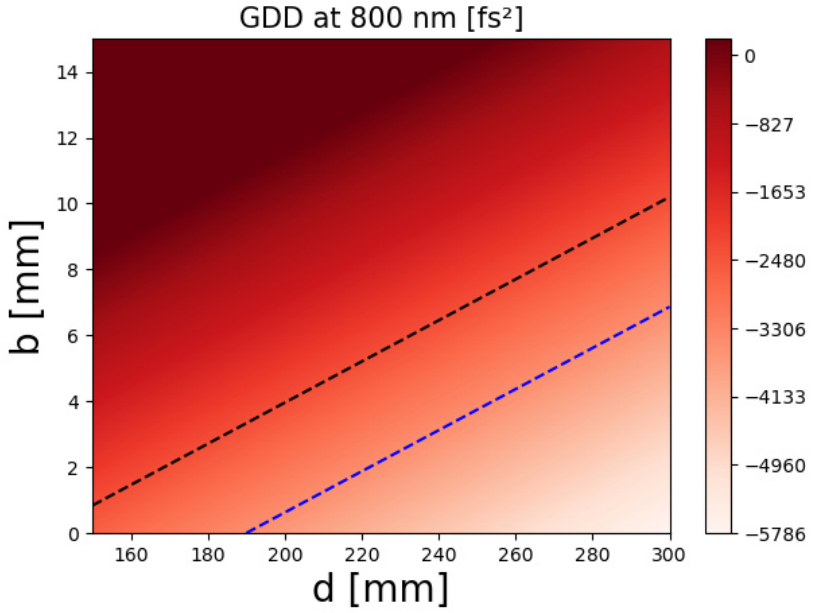

Figure 4.18: Calculation of the Group Delay Dispersion (GDD) of a SF10 prism compressor as a function of the parameters b and d presented in figure 4.9. The black and blue dashed lines correspond to the minimum GDD to induce to the cavity to obtain the ML regime, for respectively the ring and linear cavity : - 2360 and - 3480 fs².

distance between P1 and P2 would have been at least 75 cm in the ring case and 95 cm in the linear cavity case to compensate the total dispersion. These distances are not adapted to the size of the cavity.

We also checked that geometries quoted in the literature corresponded to our expectations. For instance, in the bidirectional ring cavity developed by Mejia et al. [275], the total net negative dispersion to induce has been estimated from our simulation at - 630 fs². The positive dispersion given by their cavity is about + 280 fs² (for the single fold cavity). This gives a total of 910 fs² negative compensation to induce to the cavity. A distance of 150 cm is separating P1 from P2 (and P3 from P4). A distance b of 5 cm using SF10 prisms is enough to induce a total of -1000 fs² of negative dispersion and generate fs pulses, which agrees with our simulations.

In the study of Lemoff et al. [308] we estimated a net compensation dispersion of -355 fs² to induce to the cavity. The cavity induces a positive dispersion of + 1225 fs². A distance of 22 cm between the P1-P2 (P3-P4) SF10 prisms was set. Depending on the position of the inserted laser beam in the second prism (b value), the compensated GDD can range from - 2600 fs² to -3700 fs² which appears in agreement with our estimation. Several published papers demonstrated prismless cavities that were able to run in a mode-locked regime using chirped mirrors. For Bartles et al. [309], the total net GDD to induce has been calculated at -30 fs². As the Ti:sa crystal used is 1.9 mm and the cavity length is 30 cm the positive dispersion to compensate is 120 fs². A total net negative dispersion

to induce to the cavity has been determined to be -150 fs^2. In this case the use of chirped mirror was enough to obtain -50 fs net total dispersion. According to the experimental parameters of Ideguchi [229], we estimate a net negative dispersion to induce to the cavity of -190 fs^2. We show a good agreement between our simulations and observations. Kasper et al. [284] developed a laser cavity composed of 5 chirped mirrors that each induce a negative dispersion of 40 fs^2 which results in a total of -200 fs^2. We estimated a net total dispersion to compensate of -30 fs^2. The positive total dispersion induced by the cavity elements is 145 fs^2. Therefore, the estimation of the total net dispersion using the equation 4.4 and the estimation of the negative GDD induced by the prism compressor were in good agreement with the results presented in several published work.

4.5 Conclusion

In this chapter, the elements to design the laser cavities have been presented. The start of the Kerr lens mode locking requires a compensation of the intra-cavity dispersion and a knowledge on the required conditions. Techniques were presented to experimentally start the mode-lock regime. To optimize the output power, the optical elements transmitting the laser beam must be set at Brewster angle. This can contribute to astigmatism of the laser beam that is in turn compensated by setting specific incident angles to the curved mirrors for the intra-cavity laser and a tilt on the lens for the pump laser beam. The laser stability plot indicates the distances between the focusing mirrors where the laser beam is the most stable and emits powerfully. In the next chapter is presented the experimental realisation of the linear and ring cavity laser as well as their characteristics.

Chapter 5

Dual Comb laser realisation

5.1 Introduction

The realisation of a home-made solid state bidirectional ring Kerr-lens mode-locked laser is presented in this chapter. As discussed in chapter 3, the reasons for developing this specific cavity was the potential high relative coherence between the two pulse trains and the ability to reach the UV spectral range by few harmonic generations as the Ti:sa laser emits a high output power in the near infrared region. A bidirectional laser cavity generates, from a single cavity, two fs pulse trains that will be used for DCS measurements as presented in chapter 3. We built a ring bidirectional cavity based on the numerical results obtained in chapter 4. The optimization of the output power, the determination of the laser cavity stability, the compensation of the dispersion, the Kerr-lens mode locking phenomenon were presented in chapter 4. The laser source was chosen to be home-made for several reasons : Ti:sa bidirectional mode-locked laser cavities are not commercially available. The realisation of a custom-made laser is possible but remains very costly. The creation of a home-made cavity laser is advantageous as the cavity can be easily adapted as a function of the spectroscopic needs.
Several teams have demonstrated the experimental realisation of a bidirectional Ti:sa mode-locked lasers such as Garduno et al. or Ideguchi et al. [229, 274].
Initiating of the Kerr lens mode locking regime was the main difficulty during the laser realisation. A non-negligible time of the thesis was spent on deep learning from the literature and from empirical experimental observations. The implementation of this ambitious project was made possible because of patience, accuracy, obstinacy and attention to details. In fine, this work led to the realisation of a pared-down experimental configuration where every detail of the cavity is controlled.
The KLM bidirectional ring cavity was built in a step by step procedure. The first step consists of the realisation of a linear cavity configuration. Indeed, the mode-lock regime is easier to achieve

in a linear cavity compared to a ring cavity because of the higher intra-cavity power in the former configuration. The second step consists in adapting the linear cavity to a ring cavity laser.
This chapter first describes a study on the spectral density noise of the optical table as well as the laboratory environment where the cavity laser was constructed. The characteristics and common elements of both the linear and ring cavities are also presented in the first section. In section 5.3, the laser setup is presented. Section 5.4, is presenting the stability zones (for CW and ML laser) in a linear cavity configuration. The home-made linear cavity is then extended to a ring bidirectional laser cavity where its stability zone is presented in the CW and ML regime. A procedure for obtaining experimentally the mode-locked laser regime is given in section 5.5. In section 5.6, a measure of the pulses duration and of the relative coherence of the emitted lasers.

5.2 Laboratory environment

5.2.1 Optical table

A stable and low noise environment is required to achieve a stable mode-locked laser emission. A study on the density spectral noise of three different optical tables located in three separated laboratory rooms was performed to determine the optimum location for optical table where the laser cavity would be produced. The experimental setup is composed of a Michelson interferometer presented in figure 5.1.

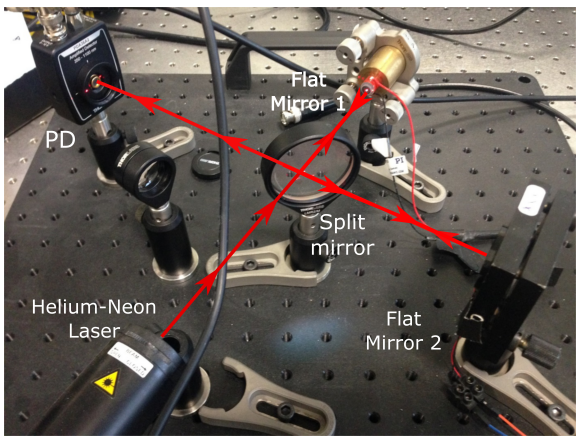

Figure 5.1: Michelson system used for measuring the mechanical and phonic stability of the room and optical table. It is composed of a CW helium laser laser emitting at 632.8 nm, one fixed mirrors, one mirror mounted on a piezoelectric device, a beamsplitter, and a photodiode. The laser beam is split and recombined towards the photo-detector. Interferometric fringes are created on the photodiode when one of the mirror is phase shifted with the second one.

Output from a continuous He-Ne laser emitting at 632.8 nm, is split towards two arms (to flat mirrors 1 and 2). The laser beam is recombined and hits a photo-detector that records the interference

fringes created by the phase difference between the two arms. The spectral density noise on the tension $S(f)$ is recorded from the temporal signal fluctuations δV such as $S(f) = \int_0^{+\infty} < \delta V > e^{-2i\pi ft} dt$. Here t is the acquisition time and $< \delta V >$ is the average fluctuation δV at frequency f. The root mean square (RMS) noise value V_{RMS} on the voltage can be determined by integrating the spectral density noise over all the spectrum : $V_{RMS} = \sqrt{\int S(f) df}$. The RMS of the vibration distance of the mirror δd_{RMS} can be determined from the following relation : $\delta d_{RMS} = \delta V \frac{\lambda_{He}}{2\pi\Delta V}$ where λ_{He} is the wavelength of the He-Ne laser (632.8nm), ΔV is the average voltage taken from the photo-diode signal.

The spectral density noise measurements are presented in figure 5.2.

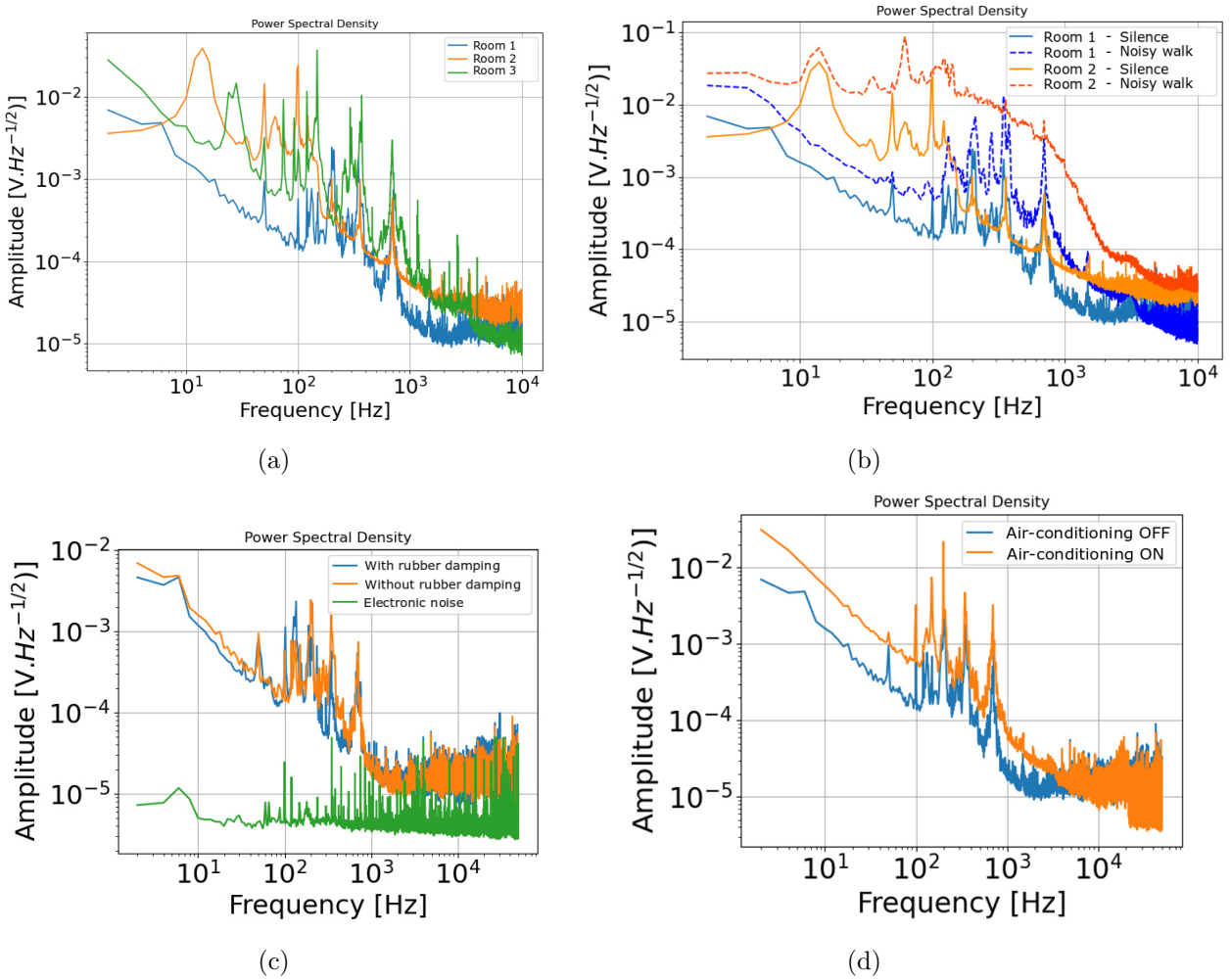

Figure 5.2: Spectral density noise obtained with a Michelson interferometer.5.2a Comparison of three different laboratory rooms, 5.2b Comparison of two rooms in a silent and a noisy environment (person walking loudly), 5.2c Comparison of two cases : presence of a rubber plate damping under the breadboard, the electronic noise was added, 5.2d Comparison of two cases : air-conditioning turned on and off.

First we compared the spectral density noise for three different rooms where the Michelson instrument was set on three different optical tables (figure 5.2a). It can be seen that for Room 1 the overall noise recorded is under the two other rooms apart from some spectral peaks between 110 and 130 Hz. Some typical noise peaks at 50 and 100 Hz can be observed in the three rooms as they correspond to the current frequency delivered by the national french electric network. A summary of the measured integrated RMS noise δd_{RMS} for the different experiments is given in the table 5.1. The integrated RMS noise δd_{RMS} has appeared to be much lower (0.9 (1) nm) than for the rooms 2 and 3 (respectively 4.7 (1) nm and 4.2 (1) nm). This result can be explained by two things : the room has a noisier environment or the optical table is less efficient for isolating the noise. Therefore, two situations were compared in the rooms 1 and 2. The first experiment consisted of a person walking in a noisy way around the table while the Michelson interferometer was recording. The second situation corresponds to a silent and calm environment (figure 5.2b). It can be clearly seen that the optical table of room 1 is absorbing the noise much more efficiently (δd = 3.4 (1) nm for room 1 and 19.4 (1) nm for room 2 during noisy walk). Therefore, room 1 and its optical table were chosen to host the dual comb spectroscopy laser source.
The questions of adding a damping between the breadboard and the optical table were studied and the result is presented in figure 5.2c. The instrument setup was set on the breadboard during the experiment. The presence of a rubber damping is slightly improving the stability (0.7 (1) nm compared to initial 0.9 (1) nm). The electronic noise of the recording instrument setup is also presented in the figure. The last experiment was consisting of measuring the noise induced by the functioning air-conditioning unit. It can be seen from the figure 5.2d that the overall spectral noise is higher when the air conditioning is running. The RMS noise δd is about 3.2 (1) nm when the air-conditioning is on. During the experiment, the air-conditioning box was isolated from the floor and partially from the wall which leads us to suppose that most of the induced noise was due to air turbulences. Therefore, the air flow from the air conditioning towards the cavity was deviated.

Experience	δd [nm]
Room 1	0.9
Room 2	4.7
Room 3	4.2
Room 1 Noisy walk	3.4
Room 2 Noisy walk	19.4
Room 1 with rubber damping	0.7
Room 1 air conditioning ON	3.2

Table 5.1: Summarize of the integrated RMS noise δd for each realised spectral density noise measurement.

5.2.2 Laser Environment

The laser cavity environment is composed of a 20 cm thick optical table with passive vertical vibration-isolating absorber feet. The cavity is set on an independent breadboard optical table of dimension 120×50 cm. Four rubber damping plates are sandwiched between the optical table and the breadboard for optimum noise insulation. The pump laser beam and the laser cavity are protected and isolated by means of a box covered with a phonic and thermal insulating rubber foam. The air expulsion trajectory of the air-conditioning is steered away from the laser cavity to decrease air turbulences. A picture of the laser environment set-up is given in figure 5.3.

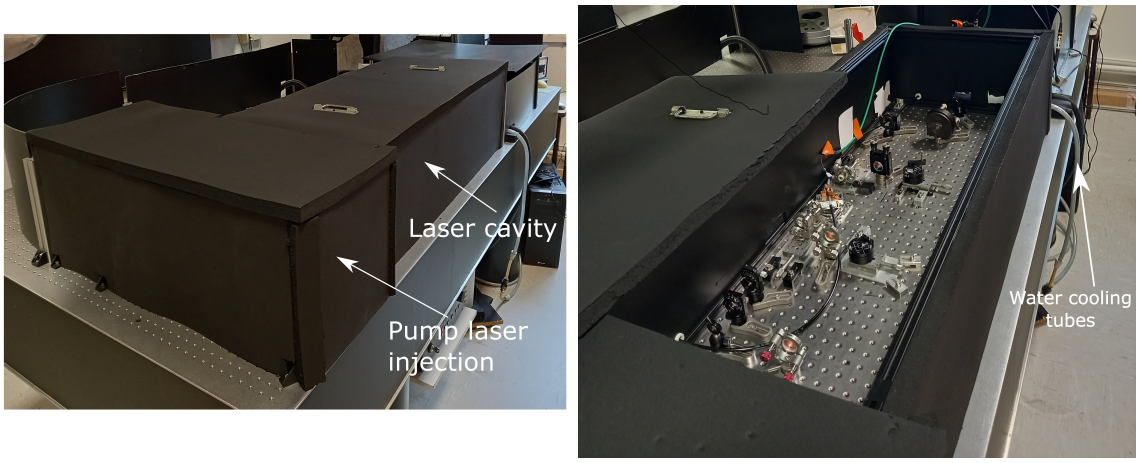

(a) (b)

Figure 5.3: Laser cavity environment. The laser pump injection and the laser cavity are isolated with a phonic and thermal insulating rubber foam. The breadboard is posed on rubber plates.

5.3 Laser setup

5.3.1 Optics

Diagrams illustrating the linear and ring cavity are given in figure 5.4.

The two cavity configurations share some common elements. The intra-cavity laser is focused in the crystal by two concave mirrors with radius of curvature of 10 cm. The two concave mirrors are called M1 and M2. M1 is anti-reflection coated ($< 1\%$ of total reflectivity) at 532 nm which allows the injection of the pump beam through M1 in the crystal. The two concave mirrors M1 and M2 are highly reflective mirrors (99.8 % of reflectivity from 700 to 900 nm). M1 and M2 are oriented with an incident angle of 11° that compensates the laser astigmatism caused by the Brewster angle of the crystal [273] (see chapter 4 in subsection 4.4.1 for details). Flat mirrors called M3, M4 and M5 are

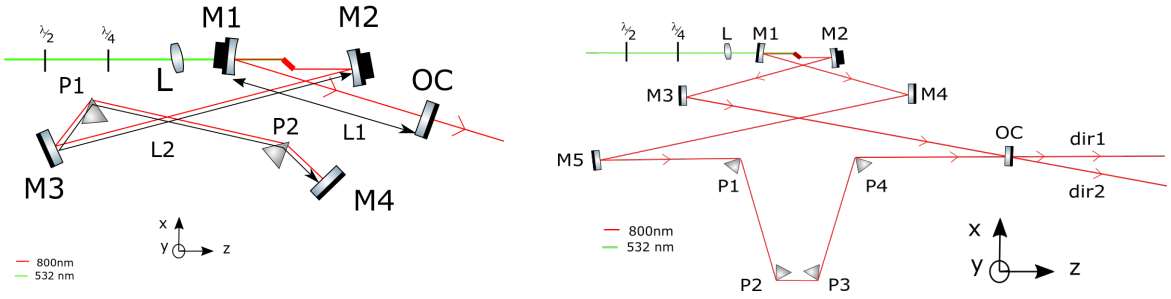

Figure 5.4: The linear and bidirectional ring cavity setups. There are both composed of a focusing pump lens of 100 mm, a half and quarter waveplates to control the pump laser polarisation, two curved mirrors of focal distance 50 mm M1 and M2, a crystal of 10 mm long, 2 (linear) and 4 (ring) SF10 prisms, a wedged 90 % reflection output coupler and high reflective flat mirrors M3, M4 (both cavities) and M5 (ring).

highly reflective from 700 to 900 nm (99.9 %). They are GVD optimized ($< 50 fs^2$). All the mirrors are set on stable mounts (Polaris®mounts Thorlabs). The output coupler is 90 % reflective. The exit face must be wedged to avoid any phase-shifted retro-reflection lasing into the crystal. This could create instability in the laser intensity and prevent from starting the mode-locking regime. As detailed in subsection 4.1.2, to allow the propagation of a soliton in the cavity, the overall group delay dispersion should be negative. In this cavity, the GDD must be in the range of - 2250 fs^2 in the linear cavity and - 1680 fs^2 in the ring cavity case. The difference between the two net GDD account for the fact that in a linear cavity the intracavity-wave propagates through the crystal twice instead of only once in a ring cavity. A prism compressor (2 prisms in the linear cavity and 4 prisms in the ring cavity) composed of SF10 flint glass prisms is used to induce a global negative dispersion which favors the conditions of propagation of a soliton. These prisms must be set up at Brewster angle to minimize the intra-cavity intensity loss due to the reflection.

The crystal is a Brewster-cut 10 mm length Ti-sapphire of composition $Al_2O_3 : Ti^{3+}$ (made by Roditi®). The Titanium doping of the crystal is 0.20 %, which gives it an absorption coefficient of $3.2 cm^{-1}$. It is pumped with a 5 W diode laser (Verdi V-5®), at 532 nm which was kindly loaned by Pierre-François Brevet from the team ONLI (Optique non linéaire et interfaces) in ILM (Lyon). To minimize the reflection on the crystal, the polarisation of the pump beam is controlled and set linearly parallel by means of a half wave plate and if necessary with a quarter wave polariser plate placed just before the pump lens. The pump beam is focused in the crystal by a 100 mm focal length lens (the pump lens). This creates a 24 µm beam diameter inside the crystal. To compensate for the pump beam astigmatism, the pump lens is tilted to an angle of 11° with the propagating beam. This geometry been calculated using the formalism developed by Ramirez-Guerra et al. [310]

and was detailed in subsection 4.4.3. The lens, the crystal and the curved mirror M2 are placed on micrometer translation stages to optimize the position of the intra-cavity laser beam in the crystal. The prisms are also set on translation stages to optimize the position of the intra-cavity laser beam on the surface of each prism and optimize the GDD. In the case of the linear cavity, the tilt of each prism is controlled by a circular kinematic mount which allow the optimization of the Brewster angle. For the ring configuration, only two prisms are set on circular kinematic mounts.

5.3.2 Mechanical and thermical considerations

5.3.2.1 Crystal mount conception

The crystal mount is made of copper-brass allay to ensure efficient evacuation of heat. It is presented in figure 5.5. The base of the mount is made in such a way that the whole system can rotate by some 10 degrees to be able to adjust the Brewster angle. The plate in contact with the breadboard and under the translation stage can also be translated perpendicularly to the pump beam direction to control injection of the pump beam into the crystal. The crystal surfaces are all in contact with the mount apart from the laser beam entry and exit surface faces. Water circulates inside the crystal mount to keep the temperature of the mount constant and evacuate the heat released by the crystal.

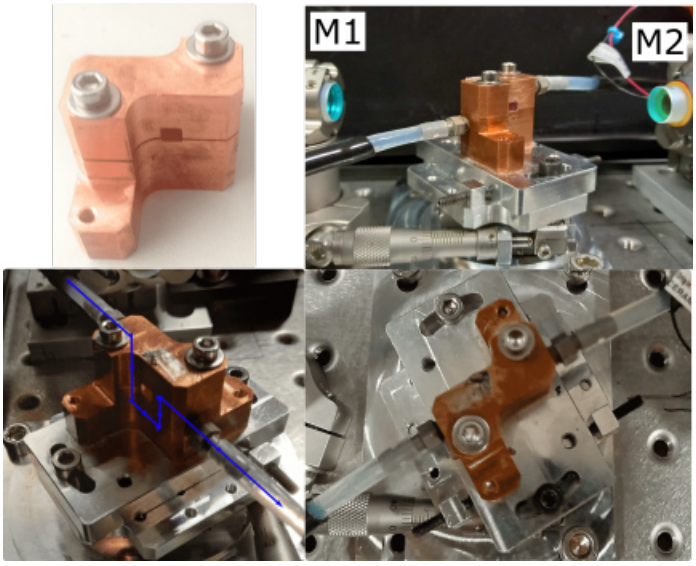

Figure 5.5: Several views of the Ti:sapphire crystal mechanical mount including the copper-brass mount, rotation and translation stages and the water cooling geometry (in blue arrays).

5.3.2.2 Prisms mount

The SF10 prisms (Thorlabs) are set on two types of mounts as showed in figure 5.6. P1 and P4 (or P1 and P2 in the linear case) are set on mounts that can be rotated for Brewster angle optimization while P2 and P3 (ring case) are set on the same home-made mount that can be linearly translated. P2 and P3 prisms are arranged symmetrically along the axis of the shared translation. The cavity and the compressor alignments are therefore maintained during the translation. The home-made mount is showed on the left and middle pictures in figure 5.6. The prism mount can even be translated by hand by applying a pressure on the side of the block. This can be used for applying a coarse dispersion change to initiate the mode lock regime for instance. The prisms are fixed with a homogeneous pressure applied on their top surface. This pressure homogeneity is important to avoid refractive index gradients inside the prism.

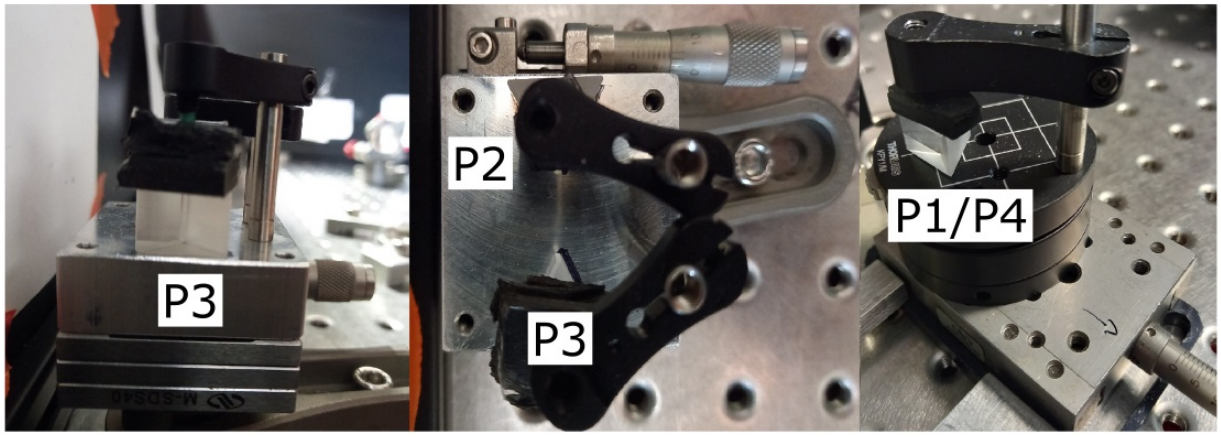

Figure 5.6: Prism mounts. The home-made mounts of P2 and P3 prisms is represented in the left and central picture. The metal block is set on a translation stage. This mount is used only in the ring configuration. The prisms P1 and P4 (P1 and P2 in the linear configuration) are set on similar mounts as presented in the right picture. These mounts can be manually rotated to allow fine adjustment of the Brewster angle of the prism. The rotative mounts are set on a translation stage.

5.3.2.3 Mirror mounts

Different mirror mounts are used in the laser cavity. The mirror M2 (see figure 5.6) is mounted on a home-made thick plate of dural metal.

Positioning holes were made on the dural plate to set the mirror mount exactly at a specific angle (11.2°) that compensates for the intra-cavity astigmatism. The mirror mount of M2 is a half inch ®Polaris mount similar to the one presented in the right picture of figure 5.7b. The output coupler was set on a heavy and stable mirror mount as presented in figure 5.7a. The flat mirrors (M3-M4-M5) are set on the same type of ®Polaris mounts as presented in figure 5.7b.

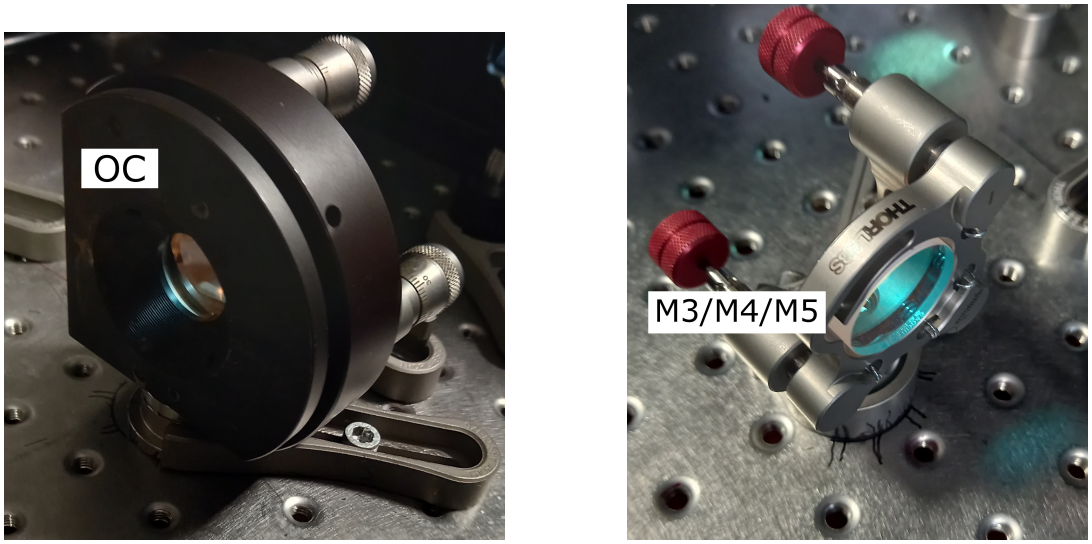

(a) (b)

Figure 5.7: Mirror mounts used for holding the flat mirrors and the output coupler. The mount mirror presented in figure 5.7a is a heavy mirror mount. The mirror mounts presented in figure 5.7b are one inch and adjustable in three directions, ®Polaris mount mirrors from Thorlabs.

The different optical, mechanical and thermal elements of the laser cavity have been presented, the cavity can now be set up. The alignment procedure used for aligning the pump laser inside the crystal and the intra-cavity alignment for obtaining the generation of the CW laser are detailed in the next subsection.

5.3.3 Pump beam alignment procedure

The alignment of the pump beam in the crystal follows a rigorous step by step procedure. At first the pump laser beam is turned on low power and set parallel with the laser cavity optical breadboard by means of two highly reflective flat mirrors at 532 nm. The alignment procedure is summarized in figure 5.8.

The laser beam is first directed through a slit S1 that is set after the crystal and mirrors positions. S1 is used as a position reference. The laser beam should remain in the centre of the slit S1, while the lens and the first curved mirror are added one by one. The crystal is roughly placed at Brewster angle. Optical geometry gives a transversal beam shift position of 8.7 mm from the centre of the slit S1. A new slit called S2, is centred at the shifted pump beam close to S1. The use of S2 allows a coarse alignment of the Brewster angle of the crystal. The position of the pump beam reflected on the surface of the crystal is also verified using an industrial drawing. To finish, the slit S2 is placed beyond the crystal. The beam alignment should remain in the centre of the slit S2. A half wave-plate is placed before the lens to set the polarisation of the pump beam horizontal. A

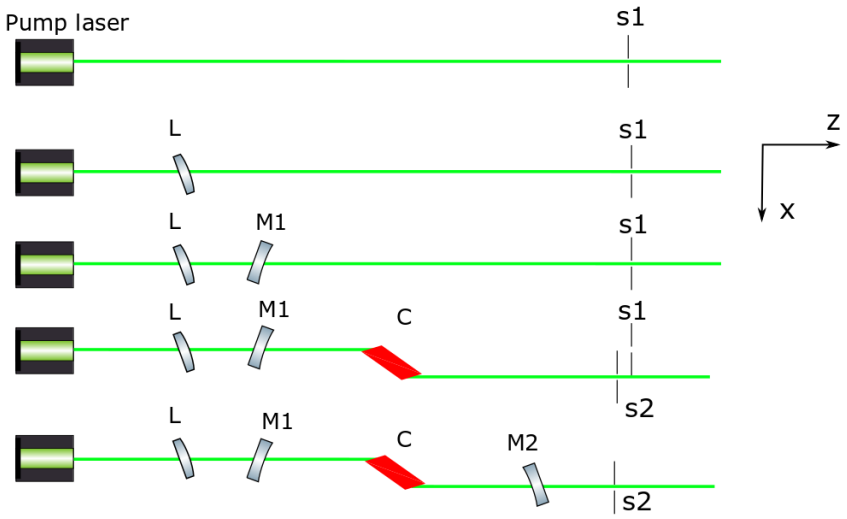

Figure 5.8: Procedure for pump beam alignment in the crystal. Each optical element is positioned in turn : the lens (L), the slits S1 and S2, the curved mirror M1 and M2 and the crystal C. This alignment procedure was adopted after helpful discussion with Garduno Mejia and Catalina Ramirez from the instituto de Ciencias Aplicadas y Tecnologia in Mexico.

minimization of the reflected beam power indicates an optimized polarisation direction.
Two beam blockers should be set at the trajectory of the beam reflected and transmitted by the crystal. After verification, the laser pump can be set to high power. As the crystal is at Brewster angle, the reflectivity of a parallel polarized laser beam, should be minimal. The Brewster angle of the crystal can be optimized to obtain a position where a minimum of reflectivity is observed. The horizontal polarisation of the pump beam should be verified beforehand. As the reflectivity was measured at less than 1 mW (the sensitivity limit of the power-meter), the beam blocker was removed.
Now, that the pump laser alignment inside the crystal has been optimized, the next step consists in the generation of the CW and ML Ti:sa laser.

5.4 The linear cavity

5.4.1 CW and ML regime : Generation procedure

The home-made linear cavity resonator is represented schematically in the figure 5.9. This linear laser has an X shape.

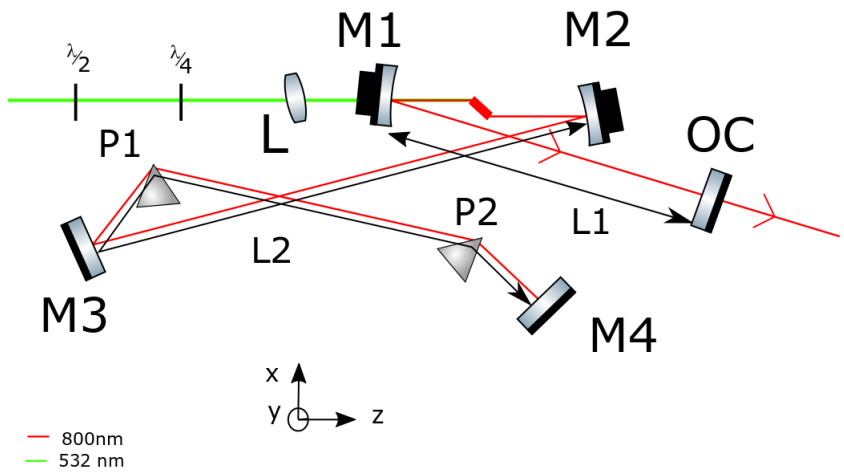

Figure 5.9: Schema of the linear X cavity. M1 and M2 are two curved mirrors with focused length of 50 mm. M3, M4 are high reflective flat mirrors. P1, P2 are SF10 prisms. L is the pump focus lens. The semi and quarter waveplates are represented by $\lambda/2$ and $\lambda/4$. The arm lengths of the cavity are given by L1 and L2. The OC represents the output coupler of the cavity.

The alignment procedure to obtain the CW laser regime consists in superposing on each mirror the spontaneous light emitted from the crystal. At this step, the cavity mirrors are not aligned for perfect superposition of the spontaneous light beam (which can be seen at the outset). As a results, two spots should be observed with an IR camera after the output coupler. The first spot is due to the direct emission from the crystal through the output coupler while the second spot, which is slightly weaker, is due to the transmission of light after one round-trip in the cavity. The CW laser regime should start when the two counter propagating fluorescent beam are superposed. If the CW laser regime does not start, this is likely to be because the cavity is in an unstable configuration. The stability of the cavity is strongly dependant on the position of the crystal, the position and tilt of mirrors M1, M2, their focal length and the length of the cavity. The stability zone can be easily calculated using the matrix ABCD and the Gaussian beam formalism (see section 4.4.4). It is easier to generate CW laser in the middle of a stability zone. After optimisation of the stability zone position, the CW regime should start. Adjustments to the vertical and horizontal positions of the laser beam on each mirror can then be done to optimize the IR output power. Then the mirrors M5 and the OC can be set up and the procedure is iterated. The output laser power should be in the range of 10 % of the laser pump power.

The mode-locking regime was obtained by means of a perturbation applied on the end mirror M4 of the cavity. The perturbation was induced by a vibration applied by a piezo-electric element glued to the back of the mirror. A sinusoidal signal was sent to the piezo-electric mirror at about 200

Hz. The output laser beam was monitored with a fast photo-diode (Biased Si Detector DET10A2, Thorlabs) and a spectrometer. The spectrometer is a grating AvaSpec-ULS3648 fiber-optic with a resolution of 1 nm from 200 to 1100 nm.

5.4.2 CW and ML stability zones : Output power optimisation

A way to determine the stability zones is to measure the output power of the laser beam for different distances between M1 and M2.
Experimentally, the mode-locked regime is present when pulses temporally separated by the inverse of the repetition frequency f_{rep} and a broadening of the spectrum are observed simultaneously on the fast photo-diode and the grating spectrometer respectively. At the beginning, to start the mode-locking, it is advised to set the cavity at a high CW output power position. From experience, it has been seen that it was easier to start the mode-lock regime in the middle of a CW stability zone regime. Once the CW output power is optimized, the mode-locking procedure can start. To start the passive mode-locking regime, a mechanical perturbation on one of the cavity mirrors must be applied. During the experiment a piezo-electric device glued to the back of the end mirror of the cavity (M5) was used to trigger perturbations on the mirror. The procedure used for mode-locking was the following :

- 1. CW operation. The cavity is aligned to optimize the CW output power in the middle of one of the CW stable zone (see next subsection in figure 5.11).
- 2. M4 mirror mechanical perturbation. A vibration is induced to the mirror M4 from a piezo-electric device glued to its back.
- 3. Mode-locking start. While the mirror is vibrating, the intra-cavity laser beam is manually misaligned (adjusting the end mirror of the cavity). A reduction of the output power of about 10-20 % should be observed. While modifying the alignment, the signal on the photo-diode or on the spectrometer is observed.
- If the mode-locking is not achieved at this stage, the second prism can be translated inward or backward to induce more or less propagation of the laser beam in the dispersive SF10 material. The curved mirror M2 can also be slightly translated. If no mode-locked regime is observed, the cavity mirrors probably need to be cleaned.

While the cavity was misaligned, we followed the evolution of the laser beam intensity with time was observed. Some combination of alignment, prism positions and output power led to easier triggering at the mode-lock regime. Usually, the optimization of the pulse apparitions or the apparition of

spectrum broadening led to stable mode-locking regime. After optimisation of the alignment of the pump power and of the position of the lens and crystal, the mode-lock regime could be triggered without the frequency generator but simply with only a flick on the mirror mount or a slight translation of the prism P2. The fs regime is unambiguous. The spectrum is obviously broader and intense pulses separated by $1/f_{rep}$ ns were clearly observed on the photodiode. An example of a spectrum that was obtained is shown in figure 5.10.

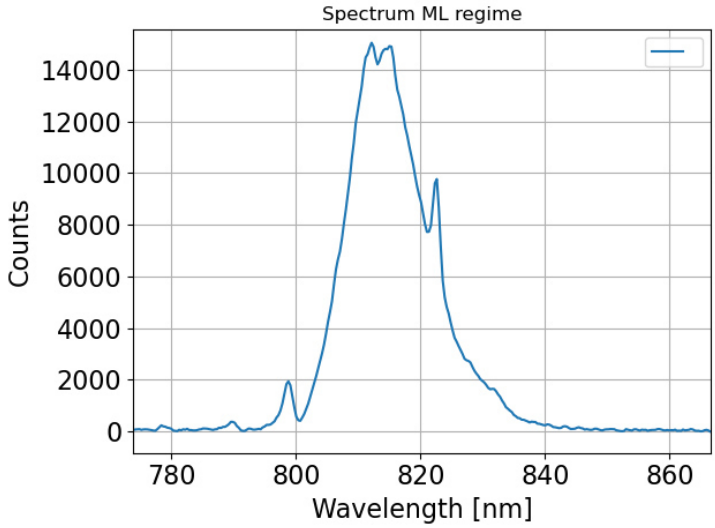

Figure 5.10: Spectrum of the comb laser obtained at a M1-M2 distance of 111,03 mm observed on a grating spectrometer with 1 nm resolution.

An identification of the stability zone in the CW regime is first realised as presented by the blue dots of figure 5.11. Then the procedure in three steps given above can be followed to mode-lock the laser. The stability zone is then measured in the ML regime as showed by the orange dots of figure 5.11. The laser output power are plotted as a function of the two curved mirrors M1-M2 distance for the CW and ML regime, showing the stability zones of both modes of operation.

The stability map can then be used to experimentally determine the location where the mode-locking regime is easier to start. The output power for both cases was recorded a few cm from the output coupler. For each point, the cavity alignment was optimized. For a linear cavity, two stable zones are observed. In the middle of each stability zone (z = 106.8 mm and 110.55 mm), the mode-locking regime was much easier to obtain. It can be observed that the mode-locked regime commenced in the areas where the CW output power was close to maximum. The horizontal error bar corresponding to the M1-M2 distance was estimated from the translation stage sensitivity.
For the same pump power and same configuration the mode-locked output power was very reproducible after realignment. This was leading to an intensity fluctuation on the optimized ML output power less than the power-metre RMS measurement uncertainty, which was about 0.1 % of the

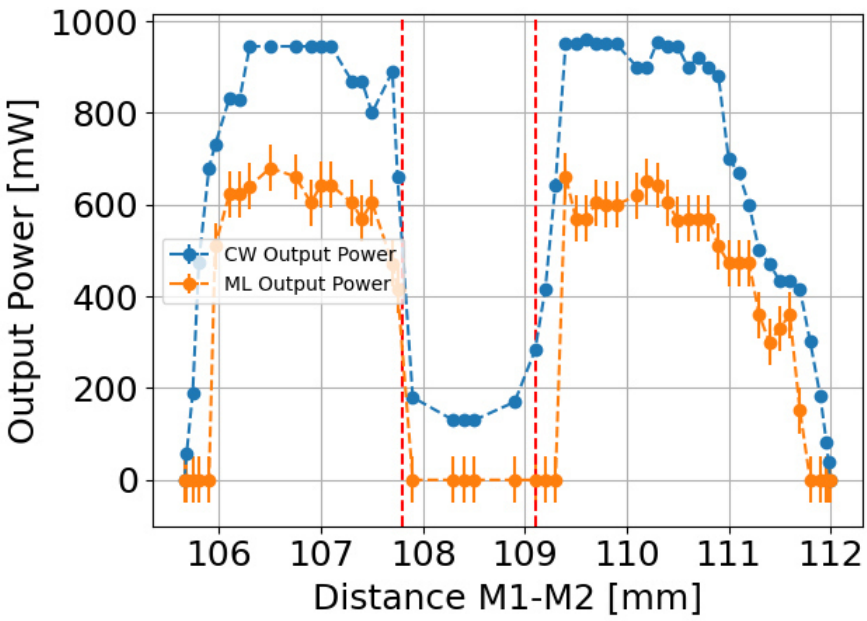

Figure 5.11: CW and ML stability zones of our home-made linear cavity laser. The two vertical dashed red lines distinguish between the stable and the unstable zone, the unstable zone being in the middle of the stable zone. The measured output power in the middle unstable zone is not zero due to the existence of superposed transverse modes. The measurement error on the CW output power is smaller than the dot.

measured laser power. For assessing the output power repeatability, several scan from 106 to 112.5 mm with one output power optimization per M1-M2 distance were realised. The vertical error bars have been determined by this procedure.

Unstable zones are delimited by the red dashed lines. It can be hard to determine unstable zone as there is still laser emission. However, the laser beam was for each time containing only superposed transversal modes with less than 19 % of the highest output power recorded. The intensity output power was also very unstable.

The experimental distances of M1 and M2 curved mirrors which corresponds to stable zones of the cavity are similar to the distances obtained with the numerical simulation (ABCD and Gaussian beam formalism) presented in chapter 4 (figure 4.14). The realisation of our home-made linear cavity has permitted to quantify the performance of the laser in a mode-locked regime in terms of CW and ML output power and stability along M1-M2 distance. In an experimental point of view, it has also allowed to verify the performance and stability of the optical components of the cavity (mirrors, crystal, output coupler).

The next step consists in adapting this linear cavity to a bidirectional mode locked laser. The main structure of the cavity was kept. One folding mirror and two prisms must be added as only one cavity passage per round-trip is realised by the pulses in the bidirectional configuration. The development of the ring cavity is detailed in the next section.

5.5 Bidirectional cavity

5.5.1 Introduction

As the state of the art low phase noise lasers operate at 100 MHz repetition rate (see chapter 3), thus it was decided to set the bidirectional laser frequency repetition around this value. The repetition rate is controlled by the effective length of the cavity. To have a frequency repetition of around 100 MHz, the cavity length must be set up at approximately $\frac{v_g}{f_{rep}} = 3$ meters. v_g is the group velocity of the pulses propagating in the laser cavity.
A diagram of a bidirectional ring laser cavity was given in figure 5.4b and a picture of the cavity is presented in figure 5.12. It is composed of an optical resonator of 5 highly reflective mirrors (99.8 % for M1 and M2, 99.9 % for the flat mirrors) and an output coupler (90 % reflection), a prism compressor composed of four SF10 prisms and a 10 mm Ti:sa crystal rod.

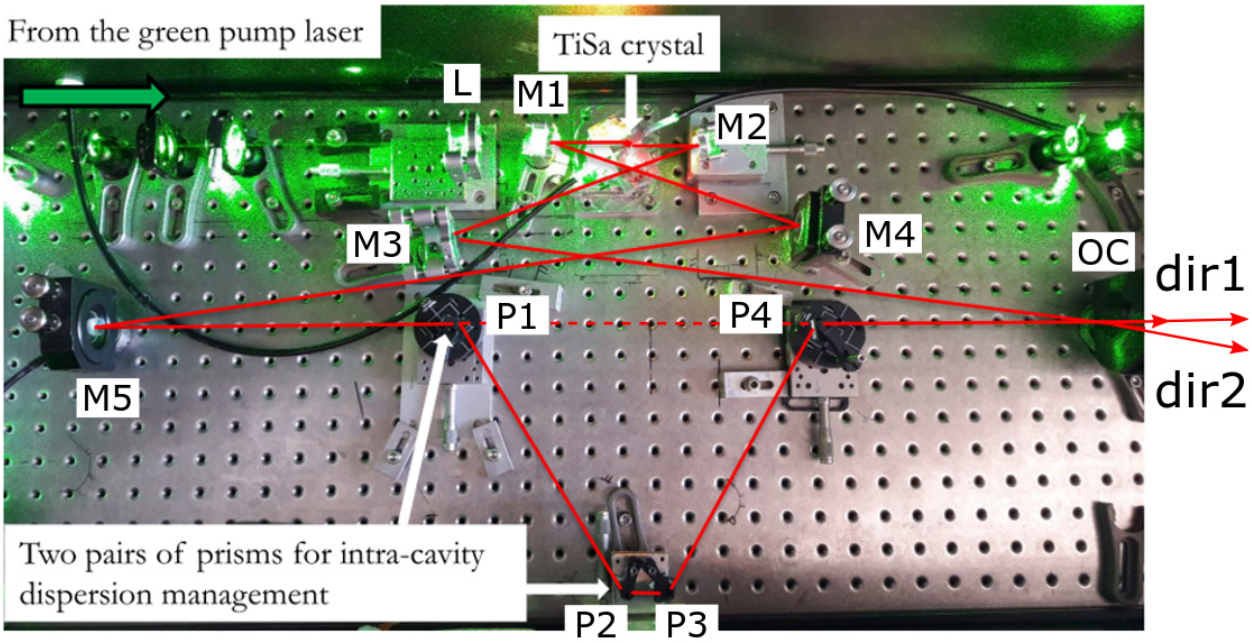

Figure 5.12: Picture of the bidirectional Ti:sa laser cavity. The laser cavity is composed of two curved mirrors (M1 and M2), three flat mirrors (M3 to M5), one output coupler (OC), four prisms (P1 to P4), and one focusing pump lens (L).

The linear cavity is readily converted to a bidirectional laser cavity. The curved mirrors M1,M2,

the crystal pump and lens positions are not modified. The mirrors M4 is moved, and the mirror M5 is added as presented in figure 5.12. The same procedure as for the linear cavity is used to generate CW laser. The only difference is that as lasing occurs in two directions, 4 fluorescent spots are observed after the output coupler. For sake of ease, it is better to realise an industrial drawing to know exactly where the laser is directed through the prisms. To not lose the optimised alignment of the cavity initially set up, a procedure of prism insertion was applied. P1 and P4 are inserted in the cavity at Brewster angle so that they cut the laser beam in half. After optimisation of the laser fluorescence through the prisms, the CW laser emission was propagating along two pathways : between M5 and OC (red dashed line in figure 5.12) and through the four prisms. Then, the prisms P1 and P4 were fully inserted so that the laser beam is close to their apexes. It is to note that the cavity stability is shifted because of the increase in cavity length. Setting the beam incidence angle on each prism at the Brewster angle is mandatory to minimize cavity losses. Once the stability zone has been roughly investigated and that the current position is identified, the CW output power can be optimized.

The objective of this bidirectional KLM cavity is to emit a mode locked laser in two directions with a tunable frequency repetition difference. The physical principle of this repetition frequency difference was developed in section 2.4.3. Experimentally, a slight intensity difference must exists to create a path-length difference in the crystal. This can be achieved by translating the crystal, the lens or by slightly misaligning the cavity. This aspect was demonstrated experimentally by Ideguchi et al. [229] and verified in our experiment.

5.5.2 Bidirectional ML generation procedure

In our work, the mode locking regime was always strong and relatively easy to start in the middle of the stability zone. As for the linear cavity, the output signal is monitored with a photodiode and a spectrometer. The mode-lock has often been started by hand with a fast translation of the prisms, even though a perturbation on one of the mirrors can also start it. Several teams have used these techniques to start the ML regime [229, 275]. Some teams even demonstrated self-starting mode-locked lasers [297]. Pelouch et al. [294], Kasper et al. [311] and Beddard et al. [312] obtained self starting ML by using a retro-injection strategy. Often, the ML regime was obtained when the alignment was not optimized for the CW output power. Difficulties to Mode-lock may come from micro-dusts sitting on the mirrors.

Experimentally, at first, the ML regime often occurs in one direction. The second direction ML was obtained by continually translating the prisms and misaligning slightly the cavity without loosing the ML regime in the first direction. When the two mode-locked directions are in a steady regime, Δf_{rep} can then be optimized. Ideguchi et al. [313] demonstrated that in a Ti:sa solid state bidirectional laser cavity Δf_{rep} could be shifted from 0 to 1 kHz by translating the crystal,

translating the pump lens or by cavity alignment [229]. We obtained experimentally a Δf_{rep} value from 0 to 450 Hz. These values were obtained by the optimisation of the cavity alignment, the translation of the prisms P2 and P3 and of the crystal position.
The phenomena of double or triple pulse emission regime can occur as shown in figure 5.13 for one of the directions of emission. This phenomenon is observable with a spectrometer when the time delay between the pulses is less than 10 ps. It is also observable on an oscilloscope when the time-delay between the pulses is higher than 2 ns rise-time of the oscilloscope. When this phenomenon occurs, it means that the intra-cavity power is higher than the multi-pulse threshold regime [314]. As a consequence the pump power must be lowered or the reflectivity of the output coupler must be reduced. A more detailed analysis on multi-pulse regime can be found in the study of Reynaud et al. [315].

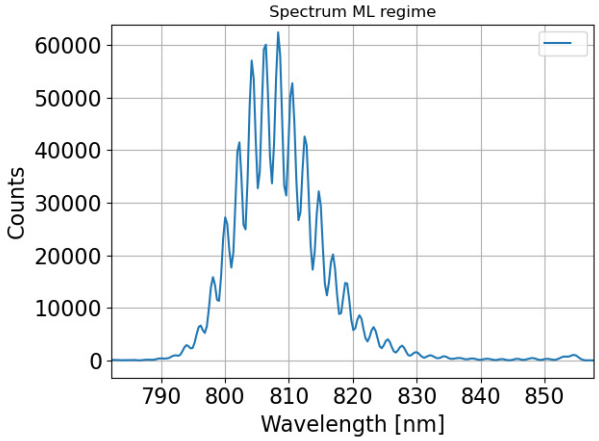

Figure 5.13: Observation of multi-pulse regime observed on the spectrum in direction 1. This is observable after the application of the Fourier transform on two pulses separated from less than 10 ps temporal delay. Above 10 ps, the oscillations on the spectrum are unresolved due to the 1 nm resolution of the spectrometer.

5.5.3 Characterisation of the bidirectional emission

In the main stable region (from M1-M2 distance of 107 to 110 mm), the output power emission was superior to 10 % ratio with the laser pump power (5.5 W). This corresponds to approximately 300 mW emitted from each arm. This output power could potentially be increased as it is suggested in figure 5.14. During the operation of mode-locked regime laser, the output power were close to a linear increase with the pump power with a factor of 194 mW per W of pump power. The limit of the pump power was reached before the limit of output power.

A total average of 600 mW at 800 nm is powerful enough to successfully convert the laser pulse trains to the UV range with doubling or tripling processes.

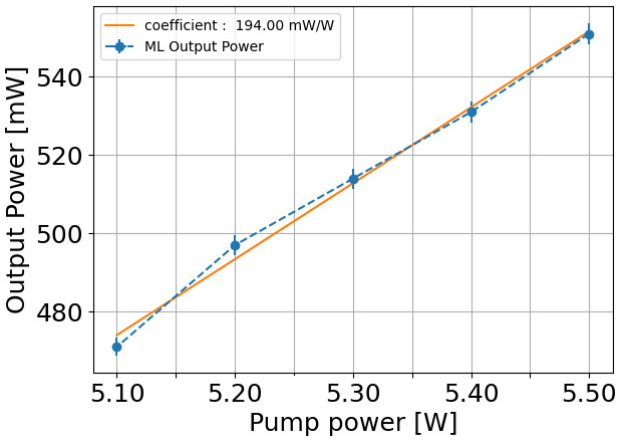

Figure 5.14: Evolution of the total bidirectional ML power as a function of the pump power. The linear curve indicates that potentially a higher output power in a mode-locked regime is reachable with higher pump power injected in the cavity.

The stability zone of the ring cavity in the CW and bidirectional ML (BML) was investigated. This is shown in figure 5.15 as the total laser output power as a function of the M1-M2 distance. We obtained bidirectional mode-locked regime, in the middle of the CW cavity stability zone. This phenomenon was also observed in the linear cavity configuration. This result is in agreement with the experimental results obtained by Mejia et al. in 1999 [274] for a ring bidirectional cavity, where they obtained mode locking regime near the center of the stability zone.

The spectrum obtained in the two directions are shown in figures 5.16 and in 5.17. Sometimes CW emission can be superposed to the BML spectrum and the two regimes can exist simultaneously. A way to recognize the CW emission, is to shift the whole spectrum by slowly translating the prisms and observe on the spectrum narrow straight lines that remains centred at the same wavelength despite the shifting. The spectrum position can be shifted by translating the P2 and P3 prisms. In all the spectra presented, only the ML regime was present.
The frequency repetition difference Δf_{rep} was experimentally shifted from 0 to 450 Hz. It was observed that the higher was the value of Δf_{rep}, the larger was the shift between the centre of each direction spectrum. At low value of Δf_{rep} (0 to 20 Hz), the spectra in the two directions have similar shape and width at modest resolution (+- 1nm) as shown in figure 5.16. When Δf_{rep} reached a value of several hundred, the spectrum center of direction 1 to direction 2 were separated. Also, the spectral width in one direction was systematically diminished, as shown in figure 5.17 ; this indicates longer pulse duration. This behaviour was observed in both directions. As a high value of Δf_{rep} is advantageous for high DCS SNR (see chapter 3) it also means a weak overlap between the two output spectra. Therefore a trade-off must be made to optimise the SNR of the spectrometer.

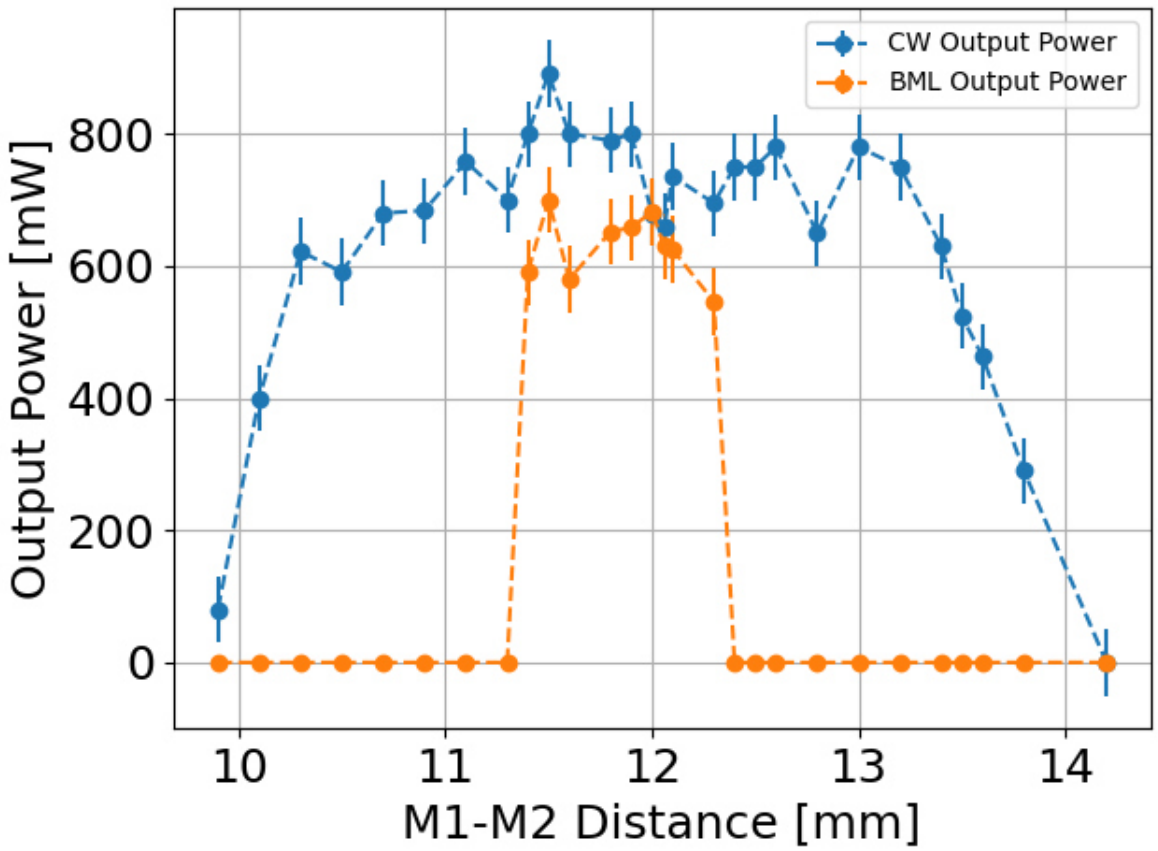

Figure 5.15: Stability zone of the ring cavity expressed as the output power as a function of the M1-M2 distance. The total output power corresponds to the sum of the two directions output powers. The values in the ML regime were considered as 0 when only one ML direction was obtained, or when the BML regime was not stable enough to remain. Pump power : 5.5 W.

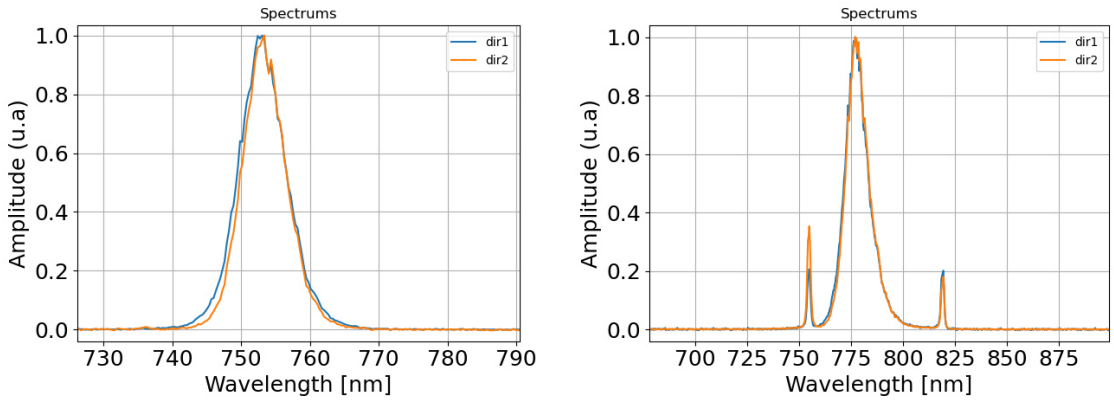

(a) (b)

Figure 5.16: Spectrum of the comb lasers in the two directions. Δf_{rep} was measured at 8 Hz in a) and 11 Hz in b). The output power in the two direction were 300 mW in a) and 350 mW in b). The pulse duration in the two directions were respectively 112(1) fs in case a) and 67(1) fs in case b). No quantitative relation between the spectrum amplitude and the output power can be made as it was dependant on the injection angle in the fiber. In the case b, the two narrow lines are part of the mode-locked spectrum curve.

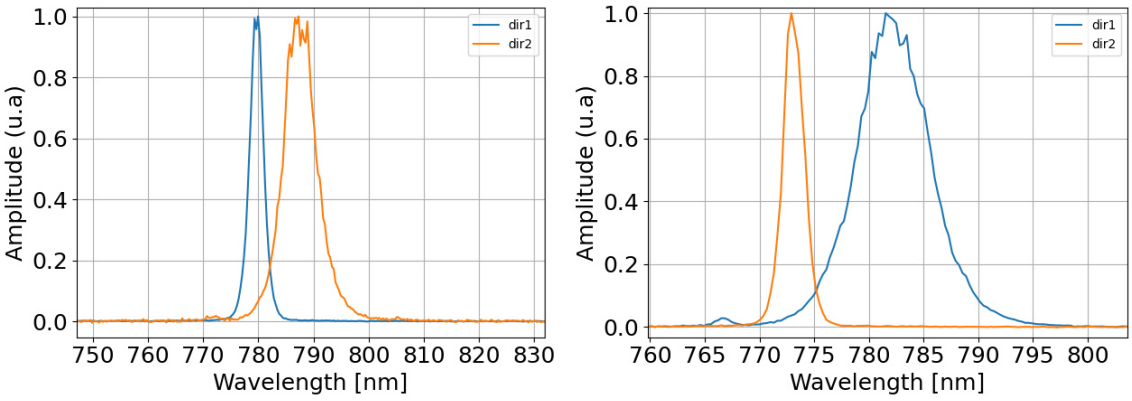

(a) (b)

Figure 5.17: Spectrum of the comb lasers in the two directions. Δf_{rep} was measured at 380 Hz in a) and 425 Hz in b). The output power in the two direction were 300 mW in a) and 350 mW in b). The pulse duration in the direction 1 and direction 2 were respectively 300(1) fs and 130(1) fs in case a) and 115(1) fs and 386(1) fs in case b). The spectrum amplitude peak shifts at high value of Δf_{rep}. The amplitude of the spectrum cannot be converted to output power.

5.6 Measure of the dual comb pulse duration

5.6.1 Description of the interferometric autocorrelator

As the duration of the pulses are in the femtosecond range, their duration is not measurable with an electronic device such as a photo-diode that has a typical rise time response in the nanosecond range up to several dozen of picoseconds. The interferometric autocorrelation method allows to measure the pulse duration in the femtosecond and attosecond range [316]. Compared to the intensity autocorrelation, this method is very sensitive to the pulse shape as it provides a higher contrasted pattern [317]. This is explained by the fact that the fourth power of the electric field amplitude is involved. Salin et al. [318] first demonstrated the possibility to record an interferometric autocorrelation figure of a 50 fs laser pulse duration from the second harmonic generation of a KDP crystal .
The setup of an interferometric auto-correlator is represented in figure 5.18. An interferometric autocorrelator is similar to a Michelson interferometer. The difference is that the recorded signal is obtained from the generation of the second harmonic of the recombined pulses.

The incident pulse is separated in two directions by a beam-splitter. A time delay variation is mechanically introduced along one of the optical paths. The two laser beams are then combined and focused into a non-linear crystal that is generating a second harmonic laser beam. In this configuration, when recombined, the two laser beams are propagating through the same light path. This creates a characteristic interference pattern recorded by the sensor camera. The interferometric figure shows fast oscillations rate of half the cycle of an optical wavelength. The intensity of the SHG laser beam is plotted as a function of the time delay. The maximum intensity of the interferometric signal is reached when the two pulses are coherently perfectly superposed. When the two pulses are far from each other, and don't overlap in the non-linear crystal, the sensor camera is recording the average intensity of the initial pulse. As the camera sensor is sensitive to the light intensity, the recorded interferometric autocorrelation signal corresponds to the integral of the sum of the combined electric fields. The mathematical expression is presented in equation 5.1.

$$I_{ac} = \int_{-\infty}^{+\infty} (E(t) + E(t+\tau))^4 dt \tag{5.1}$$

$E(t)$ is the electric field of the initial pulse and $E(t+\tau)$ the electric field of the pulse delayed by a time delay of τ. I_{ac} is the intensity corresponding to the second generation harmonic registered on the sensor.

One point on the autocorrelation figure corresponds to the superposition of one pulse with a second pulse time delayed by τ. Hence, it is possible, by scanning the time delay, to superpose the entire

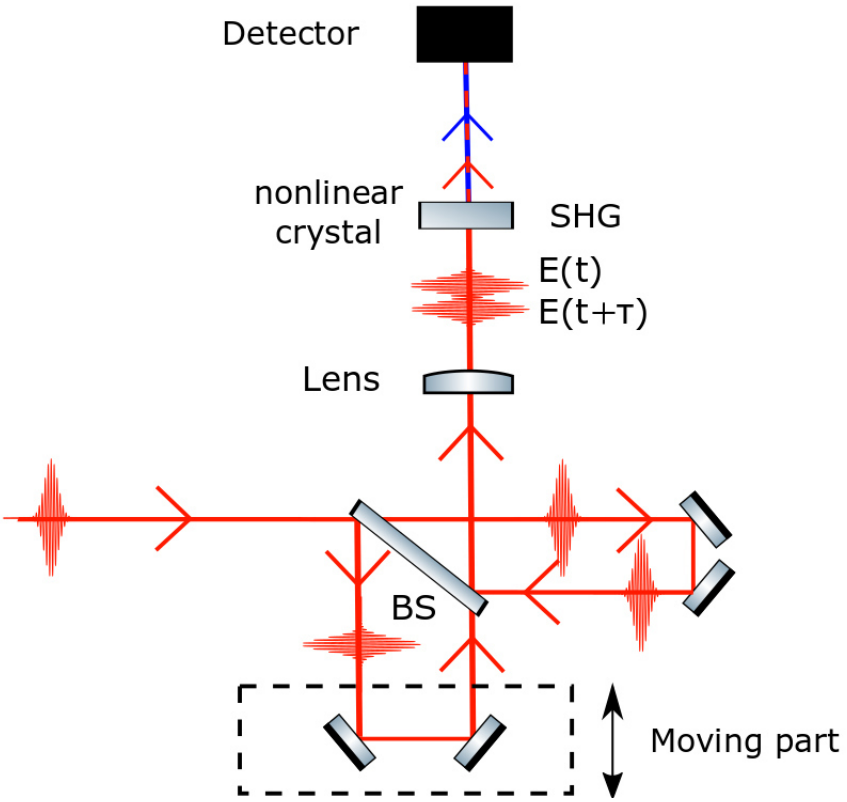

Figure 5.18: Interferometric autocorrelator schematic. The femtosecond pulses are separated by a beamsplitter and recombined after a time delayed is induced by a mechanical translation to one direction of pulses. The pulses are recombined and focused in a nonlinear crystal that generate a second harmonic (SHG) signal. The intensity of the signal is recorded on a CCD camera.

pulse with itself and thus to retrieve the entire autocorrelation figure. From this figure can be determined the duration of one single pulse emitted by the cavity. An example of the envelope of an autocorrelated signal that is low pass filtered is presented in figure 5.19.

5.6.2 Measure of the pulse duration of the dual comb laser

The instrument used for measuring the pulses duration is an industrial TPA ultrafast autocorrelator from Angewandte Physik und Elektronik (APE). The interferometric signal was fitted either with a Gaussian or with a secant hyperbolic function. The FHWM of the interferometric signal is noted $\tau_{autocorr}$. The pulse duration is obtained with the following relation : $\tau_{pulse} = 0.648 \times \tau_{autocorr}$ for a sech fit and $\tau_{pulse} = \frac{1}{\sqrt{2}} \times \tau_{autocorr}$ for a Gaussian fit. An example of the interferometric trace is presented in figure 5.19. A numerical low pass filter is applied to the interferometric signal, removing the fast oscillating fringes.

The prisms P2 et P3 were translated over 2 mm while the duration of the output spectrum in both directions were measured by the auto-correlator. As illustrated in figure 5.21, we observe that

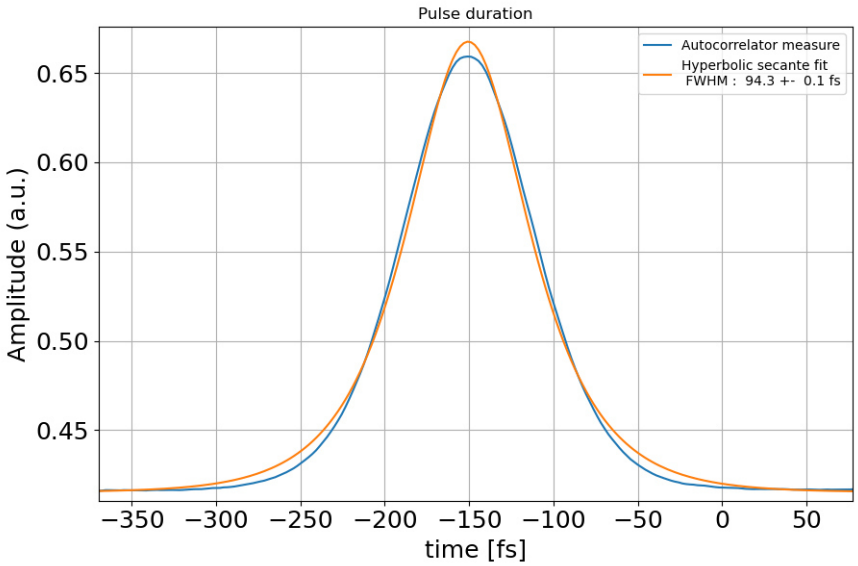

Figure 5.19: Envelope of the interferometric autocorrelation figure recorded with the interferometric autocorrelator (blue curve). The FWHM of an hyperbolic secant best fit (orange curve) permits to determine the duration of the pulse which was about 94.3 (1)fs. A numerical low pass filter is applied to the interferometric signal, removing the fast oscillating fringes. The FWHM of the filtered interferometric signal corresponds to the FWHM of the temporal envelop.

the pulse duration range from 70 to 110 fs. We also observe that the duration of the pulses from direction 2 is systematically higher than for pulses in direction 1. We also note that the duration of the pulses were continuously shifted during the translation of the prisms P2 and P3 over 2 mm from 70 to 110 fs. This is shown in figure 5.20. The duration of the pulses were continuously shifted without loosing the mode-locked regime operation. A minimum of pulse duration, for the two directions is observed between 6 and 6.50 mm. For the lower prism positions, the global GDD is positive (more insertion of prism material) which means that the higher frequencies contained in the pulse are slower than the lower frequencies. Past this minimum, for higher prism positions values, the global dispersion becomes negative (lower frequencies component is slower than the higher frequencies component). In almost all the cases, the duration of the pulses were higher in the direction 2. This observation is explained by the configuration of the laser cavity (figure 5.12). Indeed, in the direction 1, the laser pulses are temporally compressed by the prisms just before exiting the cavity whereas in the direction 2, positive dispersion is induced by the crystal and the propagation in the air before exiting the cavity. This is in agreement with similar results obtained by Curley et al. [319] where they obtained different pulse durations at the two opposite exit of a Ti:sa laser cavity.

It is possible to modify the emitted pulse duration by translating the prisms but also by translating the crystal, the curved mirrors or by modifying the cavity alignment. The available range of pulse

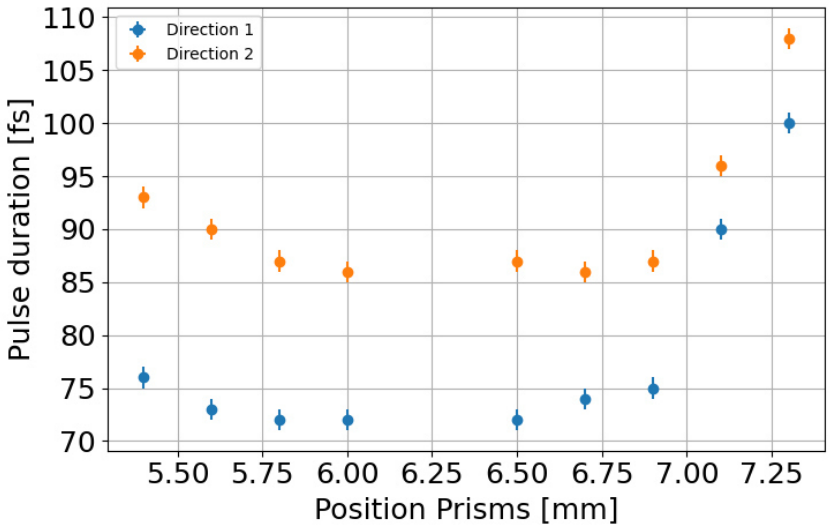

Figure 5.20: Evolution of the pulse duration as a function of the P2 and P3 prism position. The pulse duration were measured by means of an interferometric autocorrelator. The higher values of the prism positions corresponds to an increase of the negative dispersion induced (i.e withdrawal of the prisms).

duration emission was scanned. For each pulse duration measurements using the auto-correlator, the spectrum was recorded. The Fourier limit pulse duration obtained from the spectrum was then compared to the measured pulse duration. The spectrum width was obtained from the FWHM of a Gaussian fit. The Fourier Transform limit corresponds to a pulse with zero dispersion and no distortion. The Fourier transform limit is obtained from the spectrum using the following relation : $\Delta\nu \times \tau_{\text{pulse}} = 0.441$. $\Delta\nu$ corresponds to the FWHM of a Gaussian fit applied to the spectrum. The comparison of the duration of the pulse as a function with the Fourier limit pulse duration is presented in Figure 5.21. The lowest attainable duration time that was obtained from the dual comb laser source was 59 fs. A direct relation can be made between the pulse duration and the Fourier transform duration limit. The pulses durations from the direction 1 are close to the Fourier limit pulse duration (it is in the error bar range of the measured FT limit pulse duration). However, a measurement bias must exist as the pulses duration obtained from the auto-correlator appears systematically lower than the determined Fourier limit duration. Longer pulse duration are expected in the direction 2 during the measurement made of figure 5.20 as seen by the systematic pulse duration in the two directions presented in figure 5.21.

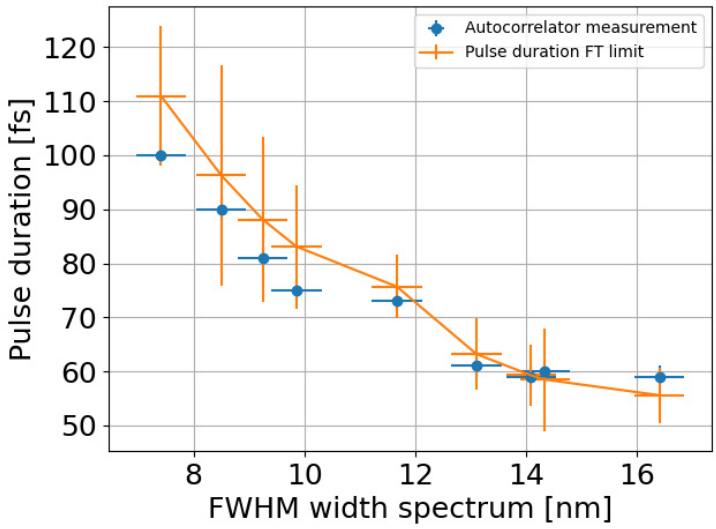

Figure 5.21: Evolution of the pulse duration as a function of the pulse duration limit obtained from the spectrum width. The pulse duration were measured by means of the interferometric autocorrelator TPA ultrafast autocorrelator (APE). The error on the pulse duration Fourier transform limit determine comes from the grating spectrometer resolution of 1 nm.

5.7 Conclusion

The realisation of a free-running KLM bidirectional cavity laser was detailed in this chapter. First, the stability of several optical tables in different rooms were assessed using a Michelson interferometer. Then the laser setup of the linear and ring cavities were presented. The pump alignment procedure, the CW and ML laser regime generation of the two cavities were then presented. The Kerr-lens mode-locking was obtained and the stability of the cavity was scanned for the CW and ML regime. The stability map in the CW and ML regime were plotted for the linear and ring cavities. In the four cases, the output power was superior or in the range of 10 % of the pump power. The procedure to realise the bidirectional cavity from the linear cavity was presented. The frequency repetition difference Δf_{rep} between the two pulse trains emitted was experimentally scanned from 0 to 450 Hz. The pulses duration was controlled by the position adjustment of the prisms, the crystal and the cavity alignment. The relative coherence of the two emitted radiations will be determined "a posteriori" via the Dual-comb spectrometer. We will show in the next and last chapter of this thesis that such a coherence has been observed over a time duration of at least 330 ms. The firsts spectroscopic results obtained from this single bidirectional cavity will be presented in the next chapter.

Chapter 6

Preliminary results using the DC spectrometer: Validation and perspectives

The first dual comb spectroscopic measurements using the home-made bidirectional ring cavity laser source are presented in this chapter. A FP etalon with known spectral characteristics and O_2 absorption spectra serve as reference for evaluating the DCS's performance, since O_2 presents a large absorption coefficient ($[O_2]\times\sigma_{O_2}$, with σ_{O_2} the absorption cross-section of O_2) at 760 nm spectrally close to the strongest emission from the Ti:sa laser source. Thus, the quantification of the relative coherence, the spectral resolution and the accuracy of the DCS method using our home-made laser source were assessed. The setup represented in figure 6.1 was designed to do this. The sample element represents either the Fabry-Perot etalon or the optical path in ambient air. For assessing O_2 transitions, the optical path is increased up to 7 meters before the photo-detector.

In all our measurements, the two pulse trains are co-propagating through the transmitting medium (symmetric geometry) which increases the signal to noise ratio (SNR) and contributes to further decrease the amplitude and phase noise induced by the turbulences of the atmosphere. The temporal trace of the interferogram is acquired using a Si photodetecteur connected to a trans-impedance amplifier (femto®model DHPCA-100 with a gain of 10^3 V/A, BW 80 MHz, AC). A low pass filter (Minicircuit; passband 48 MHz; loss 3 dB at 55 MHz) with a frequency cut of 48 MHz avoids possible aliasing effects from the down sampling of higher frequencies. The signal is digitalized by an A/D fast acquisition card (Model M4i.4450-X8-exp, 14 bit transient recorder, Bandwidth 1 GHz, voltage resolution 250 µV at +/-2V range). The DCS results presented in this chapter are the first measurements using our home-made laser source. All the spectra were obtained from

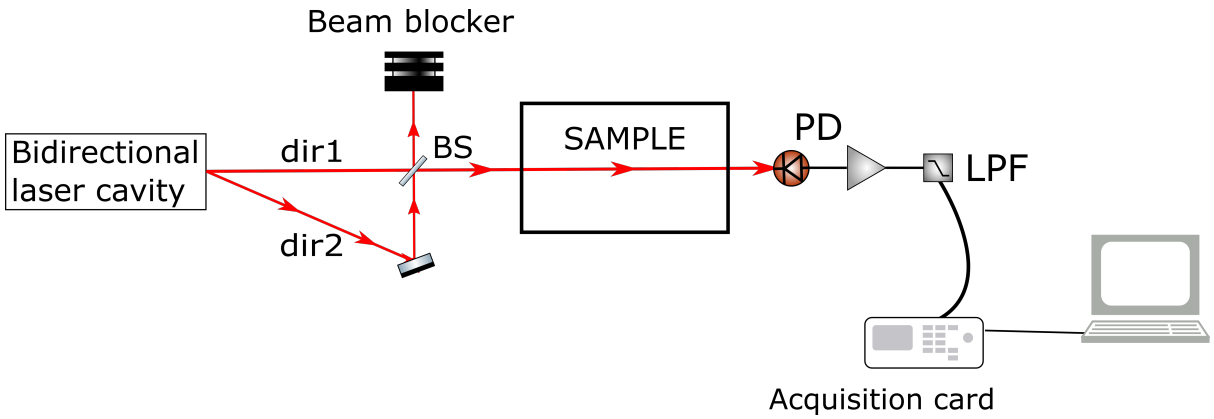

Figure 6.1: DCS experiment setup. The bidirectional laser cavity emitting in two directions are superposed by using a beam splitter (BS). The two lasers propagate through a transmitting element called sample before being recorded by a photo-detector (PD). LPF is an electronic low-pass filter.

the Fourier transform of non-averaged temporal traces and without the use of any post-processing protocol. In future work, averaging protocols will be used to increase the signal to noise ratio of the retrieved absorption transition lines amplitude.

In the first section is presented the spectral and temporal characterisation of the DCS using the home-made laser source. The determination of Δf_{CEO}, the precision on the parameters Δf_{rep} and f_{rep} and the relative coherence between the two combs are assessed. In the second section, a first spectroscopy experiment using the DCS laser source is demonstrated from the determination of the free spectral range (FSR) of a Fabry-Perot (FP) etalon. In section 6.3, the electronic and ro-vibrational absorption transitions of O_2 at 760 nm retrieved by DCS are presented. Detection and post-processing methods are presented as a perspective to improve the signal to noise ratio of the DCS method.

6.1 DCS spectrometer characterisation

First the interferogram is detected a few cm after the superposition of the two laser pulse trains. This corresponds to the setup shown in figure 6.1 without any sample. The two laser beams are precisely superposed on the beam-splitter and the photo-diode. The superposition of the two laser pulses on the photo-diode requires a precision of several µrad and a few µm in terms of angle and position respectively. Once the alignment has been achieved, series of interferograms can be detected.

Description of the temporal trace

The recorded temporal trace is presented in panel a) of figure 6.2.

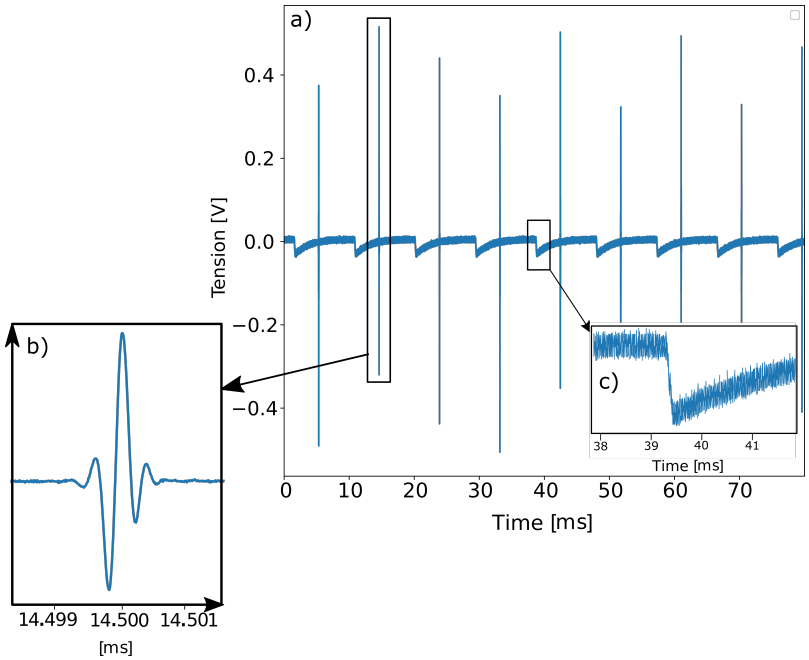

Figure 6.2: (a) DCS temporal trace (b) Zoom on a centerburst of one interferogram (c) Zoom on the base-line perturbation that reproduces periodically over one interferogram range of time. Sampling rate : 125 MHz

In the center of each interferogram can be observed centerbursts (zoom on the panel b)) which correspond to an overlap on the beam-splitter of the two pulses from direction 1 and direction 2 where the temporal delay between them ranges from 0 to approximately the duration of the laser pulses ($\sqrt{(}2) \times 100$ femtoseconds). From either part of these centerbusts, the nearly flat signal corresponds to a situation where the two pulses do not temporally overlap but "echoes" due to an absorbing element can eventually be seen. The base-line of the temporal trace reaches 0 V as the signal is recorded with the transimpedance amplifier in AC mode. We also observed a periodic perturbation on the base-line : it consists in a small but prompt decrease in the signal followed by an exponential decay-like recovery. A zoom of this phenomenon is showed in the panel c) in the figure 6.2. The temporal duration between the perturbation onset and the zero path delay (centerburst) agrees well with the time delay between the time when the pulses meet in the crystal and the time when they are superposed in the beam-splitter. This perturbation can be attributed to a gain depletion effect when both laser pulses overlap inside the Ti:Sa crystal. Further investigations are under-way to precisely quantify this observation.

Description of the RF spectra

RF spectra were obtained from the FFT applied over a truncated part of the temporal trace (figure 6.2). The FFT applied over one, two and nine interferograms of the temporal trace are represented in figures 6.3, 6.4 and figure 6.5 respectively. As developed in section 2.3.2, the spectral increment of the retrieved RF spectra is equal to the inverse of the truncated temporal window duration where the FFT was applied. The analysis of these spectra allows the evaluation of the relative coherence between the two combs.

The RF beat notes start to appear from the FFT applied over two full interferograms. To be clearly distinguished, the spectral increment must be lower than half of the RF spectral spacing (to have two points per beat note) corresponding to Δf_{rep} ($\approx$ 107 Hz) in the RF domain. In figure 6.4, the spectral increment is 62.5 Hz which is not sufficient to reproduces the RF beat notes. At nine interferograms, the beat notes are fully resolved and the spectral spacing Δf_{rep} can be clearly identified. A high relative coherence between the two laser combs is deduced from the retrieval of the beat notes in the RF spectrum from the FFT over a 9 interferogram (73 ms).

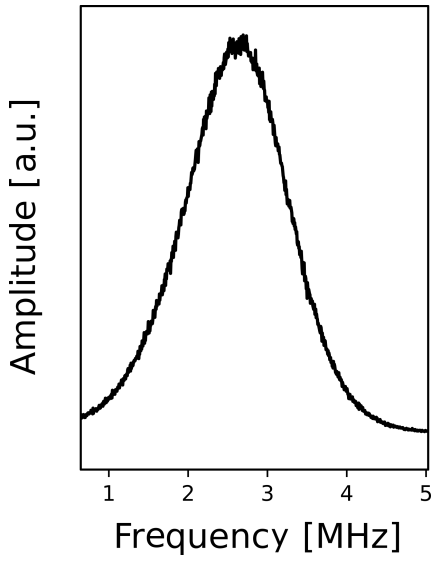

Figure 6.3: RF Spectrum obtained from the FFT applied on one truncated interferogram (represented in panel b of figure 6.2) over 150 µs (spectral increment of 6.6 kHz).

Spectral modulation can be observed on the spectrum represented in figure 6.5, this might be caused by f_{rep}, Δf_{rep} and Δf_{CEO} fluctuations.
It can be noted that the position of the spectrum in the RF domain between 0 and $f_{rep}/2$ depends on the values of f_{rep}, Δf_{rep} and Δf_{CEO} as explained in chapter 2.
As a results, to determine accurately the position of the spectrum in the optical domain from the RF spectrum, the values of f_{rep}, Δf_{rep} and Δf_{CEO} must be known. The equation given in equation 6.1 is used to rescale the RF spectrum towards the optical domain :

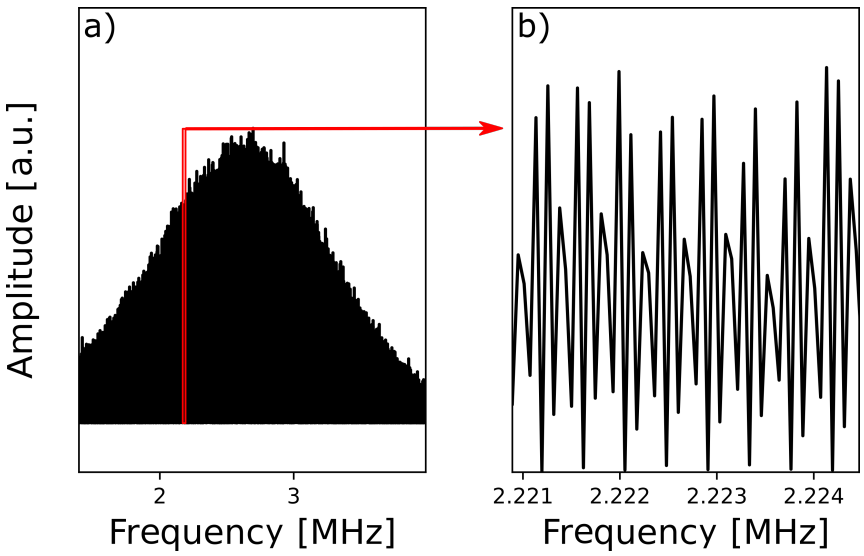

Figure 6.4: Panel a : RF Spectrum obtained from the FFT applied on two interferograms (of the figure 6.2 over 16 ms, spectral increment of 62.5 Hz). Panel b : Zoom over one part (red square) of the RF spectrum.

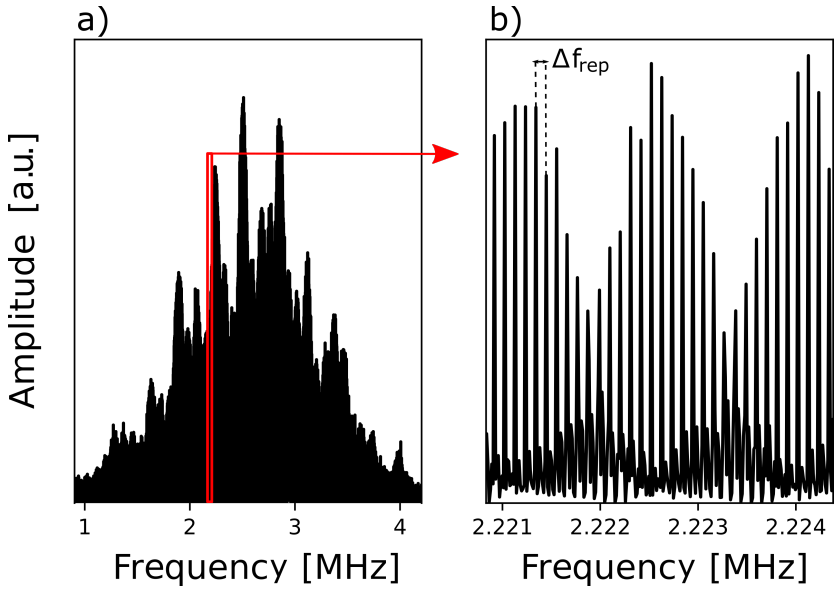

Figure 6.5: Panel a : RF Spectrum obtained from the FFT applied over nine interferograms corresponding to the figure 6.2) over 73 ms (spectral increment of 13.6 Hz). Panel b : Zoom over one part (red square) of the RF spectrum. The spectral spacing of Δf_{rep} (107 Hz) indicates that the beat notes are resolved.

$$\nu_{opt1} = k \times f_{rep} \times a \pm (\nu_{RF} - \Delta f_{CEO}) \times a + f_{CEO1} \tag{6.1}$$

This equation can be determined from the equation 2.18 or 2.20 (see chapter 2) combined with the comb equation $\nu_{\mathrm{opt1}} = \mathrm{mf_{rep1}} + \mathrm{f_{CEO1}}$ of laser 1. We will drop the subscript "1" in the following

for easier reading. ν_{opt} represents the optical frequencies, k represents an integer value (number of schema, see chapter 2), ν_{RF} are the RF frequencies, a is the scaling factor ($a = f_{rep}/\Delta_{rep}$) and f_{CEO1} is the carrier envelope offset frequency of the first comb laser.
First, the f_{rep} and Δf_{rep} values must be determined to rescale the RF spectrum towards the optical domain.

f_{rep} *and* Δf_{rep} ***determination***

The parameters f_{rep} and Δf_{rep} of the home-made laser can be accurately determined from the analysis of the full temporal window (panel a) of figure 6.2). This full temporal window corresponds to the retrieval of 9 successive interferograms which has a temporal duration of 73.718 ms. f_{rep} was measured using a 125 MHz bandwidth temporal trace, which provides a value at 10 Hz accuracy limited by acquisition memory depth. f_{rep} was determined at 118.2857(25) MHz. The determination of the optical frequencies is limited by the uncertainty of Δf_{rep} as we will show below. As a results, the determination of f_{rep} with a better uncertainty than 2.5 kHz is not necessary.

The value of Δf_{rep} was retrieved by two methods. The first method consists in measuring the temporal distance from the centerbursts which are separated by Δf_{rep}. The position of each interferogram is determined from the position of the Gaussian envelope maximum fitted to each centerburst as presented on figure 6.6. The positions of each centerburst of the nine interferograms are given in panel a) of figure 6.7. The standard deviation of the residuals with the interferogram center position linear fit (showed in panel b)) defines the uncertainty of Δf_{rep}. From this method, Δf_{rep} was determined to be 107.12 +- 0.03 Hz.

The second method to determine $\Delta \mathrm{f_{rep}}$ consists in determining the spectral spacing of the RF beat notes from the spectrum of the registered temporal trace (panel a) of figure 6.2). The corresponding RF spectrum obtained from a direct FFT without averaging is presented in panel b) of figure 6.5. A good stability of the laser source is demonstrated by the distinguished beat notes retrieved from the FFT applied over several dozen ms. A second Fourier transform is then applied to this spectrum to determine the value of Δf_{rep}. The result is presented in figure 6.8. The fluctuations of Δf_{rep} can be seen by the lower peaks on either sides of the central peak. Δf_{rep} was evaluated from the central peak position of the direct FFT applied on the spectrum at 107.12 (5) Hz. As showed by the figure 6.8, the two methods provide a similar result on the determination of Δf_{rep}. The scaling factor a (cf section 2.2) is thus determined to be $a = \frac{f_{rep}}{\Delta f_{rep}} = 1\ 104\ 235(110)$.

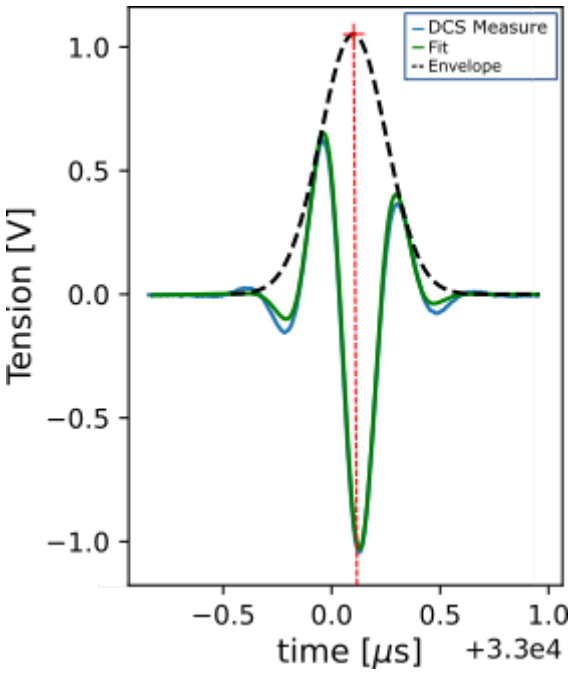

Figure 6.6: Representation of the Gaussian envelope of the centerburst of one interferogram (dashed black line). The summit represented by the red cross indicates the center position of the centerburst.

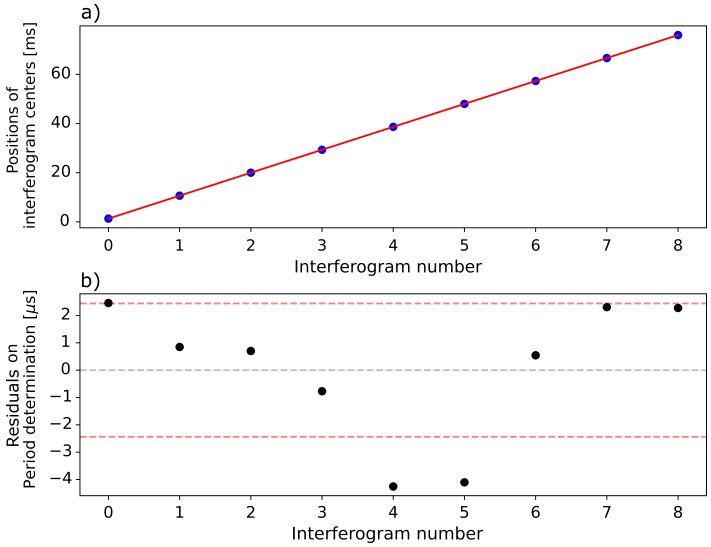

Figure 6.7: Determination of Δf_{rep} from the period between each centerbursts of the temporal trace presented in panel a) of figure 6.2. a) Positions of each interferogram center (blue dots) fitted with a linear function (red line). b) Residuals of each interferogram position with the linear fit. The standard deviation is indicated by the red dashed line (2.4 µs) and represents the uncertainty of the period.

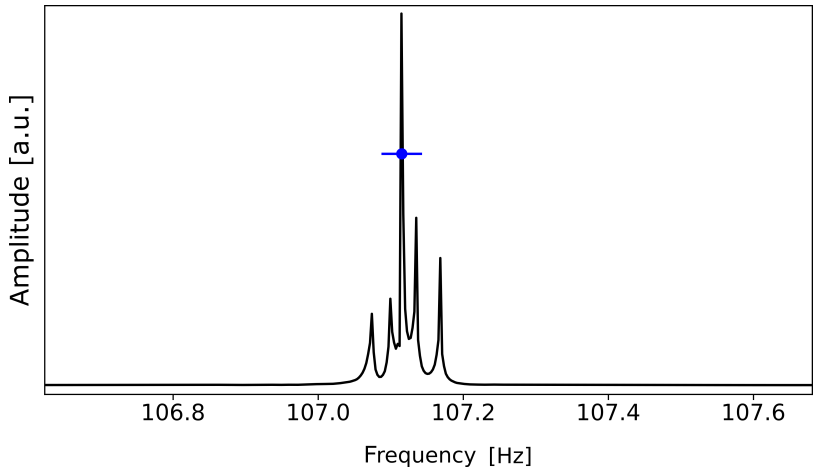

Figure 6.8: Fourier Transform applied to the spectrum of panel b) of figure 6.5 (FFT of nine IGMs). After FFT of the panel b) of figure 6.5, the x axis obtained is homogeneous to a time scale and its inverse is represented on the x axis to obtain the temporal frequency in Hz. The less intense peaks from either sides can be attributed to fluctuations of Δf_{rep}. The blue dot represents the Δf_{rep} value determined from the first method.

Retrieval of the laser emission envelop using DCS

The absolute value of Δf_{CEO} is not obtained from a direct measurement. Its value can be estimated from the rescaling of the DCS spectrum RF frequencies to the optical frequency domain when superposing the normalised DCS spectrum with the normalized product of the spectra of both trains of pulses measured with a grating spectrometer (see figure 6.9). The grating spectrometer (AvaSpec®, 0.9 nm spectral resolution) is placed at the position of the beam blocker of figure 6.1). The spectrum corresponding to each laser direction is recorded individually.

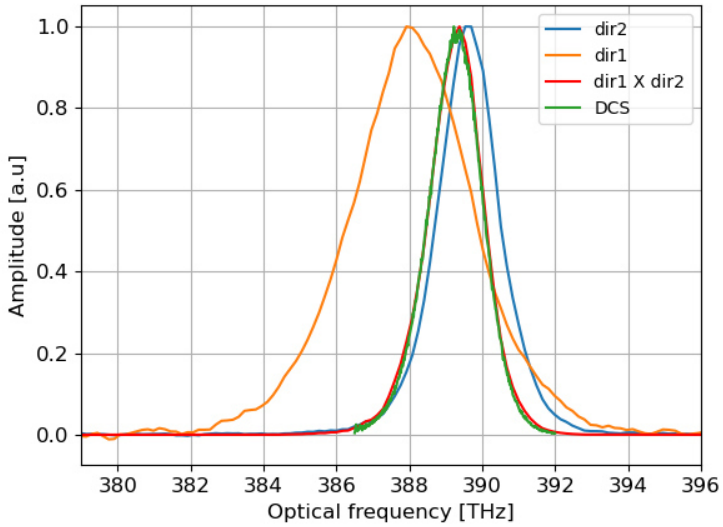

Figure 6.9: Normalized spectra of the two pulse trains directions measured with a grating spectrometer (direction 1 - orange trace and direction 2 - blue trace), of the multiplied spectrum (dir1 × dir2 - red trace) and of a spectrum obtained from FFT (green trace) applied on one truncated interferogram (see figure 6.3). The multiplied normalized spectrum (red trace) has a similar width and shape as the DCS spectrum. The central position of the green trace was adjusted using the free parameters Δf_{CEO} and k.

The carrier envelope offset frequency difference between the two lasers Δf_{CEO} was estimated to be 4.9(4) MHz (with $k = 3$) using the rescaling equation 6.1 and the superposition of the DCS spectrum with the spectrum retrieved from the grating spectrometer. This determination of Δf_{CEO} is limited by the resolution of the grating spectrometer (500 GHz at 800nm). This translates into a resolution in the RF domain of 500/a GHz ($\approx$ 450 kHz). The DCS spectrum width matches the spectrum obtained from the grating spectrometer very well, confirming the correct determination of the scaling factor a.

Discussion on the relative coherence

We were able to retrieve resolved RF beat comb notes from the FFT applied on a temporal trace over up to 330 ms of acquisition time without averaging. This measure was made without any active phase stabilisation. This demonstrates the high relative coherence between the two pulse trains over several hundred ms. The actual limitation of this duration is due to recording process that currently limits the maximal sample point at 5.10^7 which translates to a total duration of $5.10^7/f_{sample}$. Therefore, even longer temporal coherence is expected. It is worth mentioning that this relative coherence time of 330 ms is already larger than the existing state of the art free running Ti:sa laser sources (<100 µs [170, 229]). As a comparison, Coddington et al. [199] obtained 3 s of relative coherence time between the two lasers using an active stabilisation system where the combs are locked to a stable reference (see chapter 2). The relative coherence time of the DCS home-made laser beam will be further investigated to determine the exact mutual coherence limitation of the developed laser source.

6.2 Fabry-Perot spectroscopy

A DCS experiment was performed using a Fabry-Perot (FP) etalon as a sample. The experimental set-up is presented in figure 6.10. The geometry of the set-up corresponds to a symmetrical configuration where the two laser beams emitted from the laser sources are co-propagating through the FP etalon and are then focused on a photo-diode which records the interferogram.

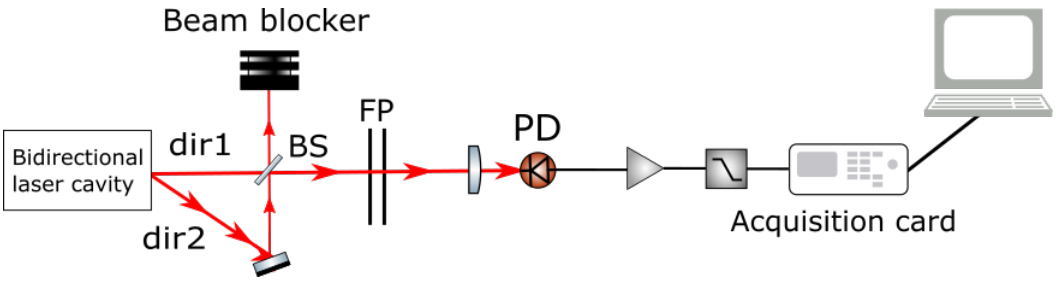

Figure 6.10: Experimental setup of a DCS applied on a Fabry-Perot etalon. BS, FP and PD stand for respectively Beam-Splitter, Fabry-Perot and Photo-Diode.

A 100 µs temporal trace recorded by the PD and centred in the centerburst of the truncated interferogram is presented in panel a) of figure 6.11. From either side of the centerburst can be observed similar but weaker features that are due to the extinction function of the FP, the so-called "echoes" in the temporal trace (see Chapter 2).

The FFT of this interferogram is represented in panel b). The frequency fringe pattern of the RF spectrum is due to the periodic constructive and destructive interferences created by the FP

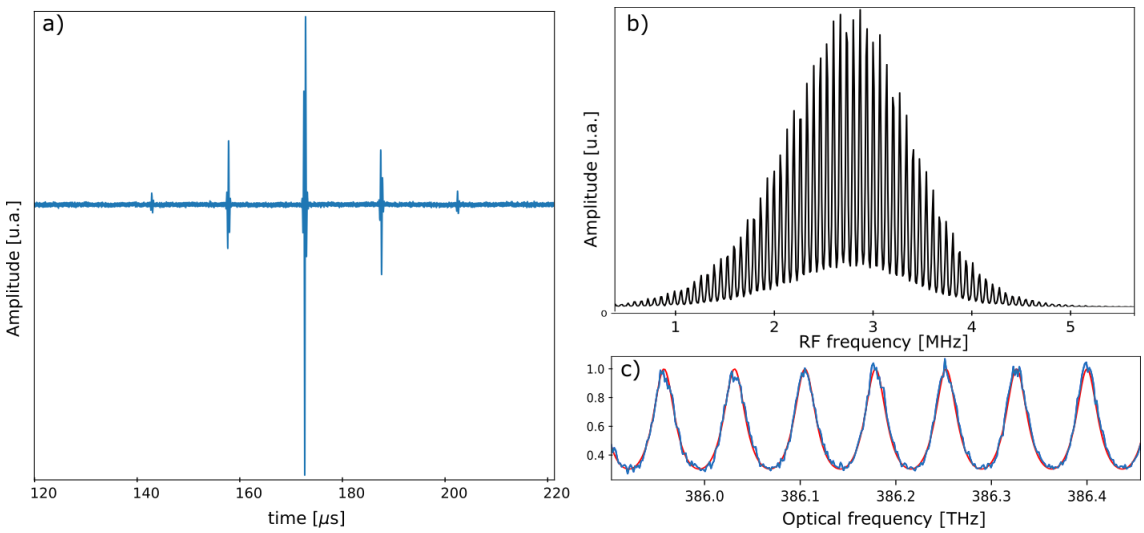

Figure 6.11: (a) Interferogram trace of 100 µs obtained in a symmetric geometry experiment with a Fabry-Perot etalon. (b) Spectrum obtained from the FFT of the interferogram trace. This figure corresponds to the expected convolution between the spectral laser intensity and the transmission of the Fabry-Perot. (c) Zoom of the spectrum (blue line) rescaled in the optical domain fitted with the simulated free spectral range transmission expression (red line) of the FP etalon. The expression is given in equation 6.2

etalon. The global shape of the spectrum corresponds to the theoretical simulation of a transmission spectrum of a Fabry-Perot multiplied by a Gaussian envelope spectrum of the pulse. Panel c) of figure 6.11 shows the measured transmission of the FP etalon in the optical domain fitted to a conventional theoretical expression of the FP etalon transmission T_e given in equation 6.2 after removal of the Gaussian envelope plus a baseline offset correction value [320]. The optical spectrum presented in panel c) of the figure was obtained from equation 6.1 as described in section 6.1 from the RF spectrum of panel b).

$$T_e(\nu) = \frac{1}{1 + F sin^2(\phi)} \tag{6.2}$$

Where $F = \frac{4R}{(1-R)^2}$ with R the reflectivity of the FP mirrors, $\phi = \frac{2\pi(\nu-\nu_0)}{\Delta\nu_{FSR}}$, ν is the laser frequency, ν_0 corresponds to a frequency offset, $\Delta\nu_{FSR}$ is the free spectral range. The fitting function (red trace) agrees well with the experimental data observed in panel b) of figure 6.11. The finesse is approximately 30% and the free spectral range of the FP etalon was estimated at 73.739(1) GHz from this fitting algorithm. The uncertainty (1 MHz) has been estimated from different choices in the fitting procedure (using different guess/starting values). Note that the FSR relative uncertainty (1.10^{-5}) obtained is one order of magnitude better than the relative uncertainty on the scaling factor a (1.10^{-4} and presented in section 6.1). This would indicate a better stability of Δf_{rep} on the timescale of a single interferogram.

The retrieved FSR value from the DCS experiment agrees within 2σ standard deviation with the FSR reported by the constructor 75(1) GHz. The exact value of the FSR depends on the position of a Piezo element that sets the distance and alignment between the mirrors and on the laser injection angle. A precise ($\approx$ 10 MHz precision) determination of the FP-FSR using another optical instrument is in progress to confirm the absolute value obtained from the DCS experiment. It is worth emphasizing that the developed laser source gave a highly precise determination of relative frequencies (1 MHz) in a very short acquisition time (100 µs) without implementing any active stabilization technique.

6.3 O_2 spectroscopy

Dual comb spectroscopy was performed using the home-made laser source to measure the concentration of a gas-phase absorber in an open-path environment. O_2 turns out to be the ideal molecule for this first molecular spectroscopic measurement. It is an abundant molecule in the ambient air ($\approx 5.10^{18}$molecules.cm^{-3}), and absorbs the light at 760 nm which lies within the Ti:sa fundamental range of emission. The positions of its absorption transitions are represented in figure 6.12. They were obtained from Hitran 2016 database [321].

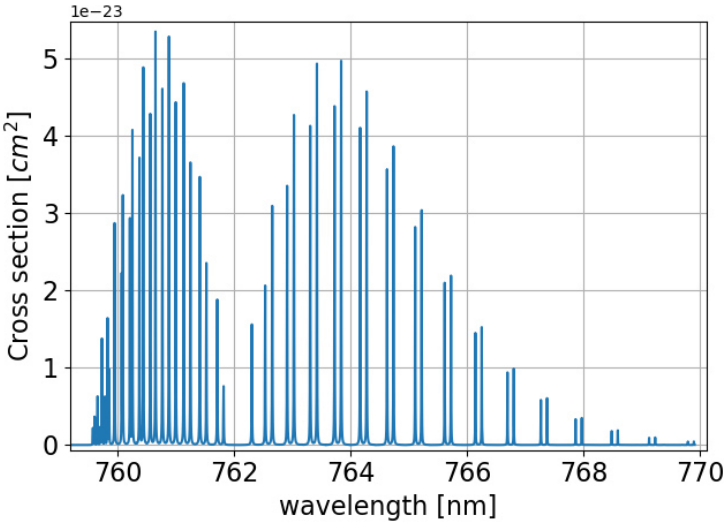

Figure 6.12: Absorption cross-sections in the O_2 A band, $b^1\sum_g^+ \leftarrow X^3\sum_g^-(0,0)$ between 758 and 769 nm. Data were taken from the Hitran database [321].

The set-up consists in a symmetrical geometry configuration where the two superposed pulse trains are propagating through an ambient indoor atmosphere before being focused on a photo-detector. The arrangement is represented in figure 6.13; the optical path length was set at 7 m.

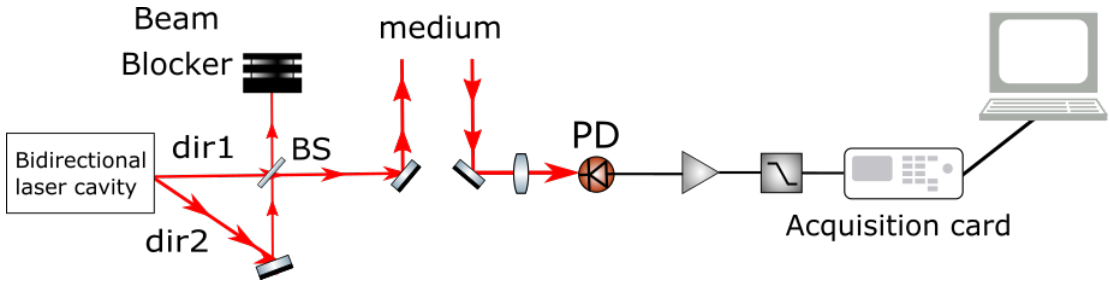

Figure 6.13: Schematic representation of the Dual-Comb Spectroscopy for detection of ambient indoor O_2. BS and PD indicate respectively beam-splitter and photo-diode.

The RF spectrum retrieved from the DCS measurement is presented in panel a) of figure 6.14. The spectrum was calculated from a FFT applied on a single interferogram truncated to 5,4 ms duration (Δf_{rep} = 20 Hz). This duration was chosen because a compromise was made between the spectral increment (185.2 Hz) and the spectral noise on the RF spectrum. The O_2 transition lines can be observed between 0.4 and 0.6 MHz in the RF spectrum. The strong peak at 0.26 MHz in the RF spectrum may be explained by electronic noise. Further investigations will be made to understand this narrow spectral peak.

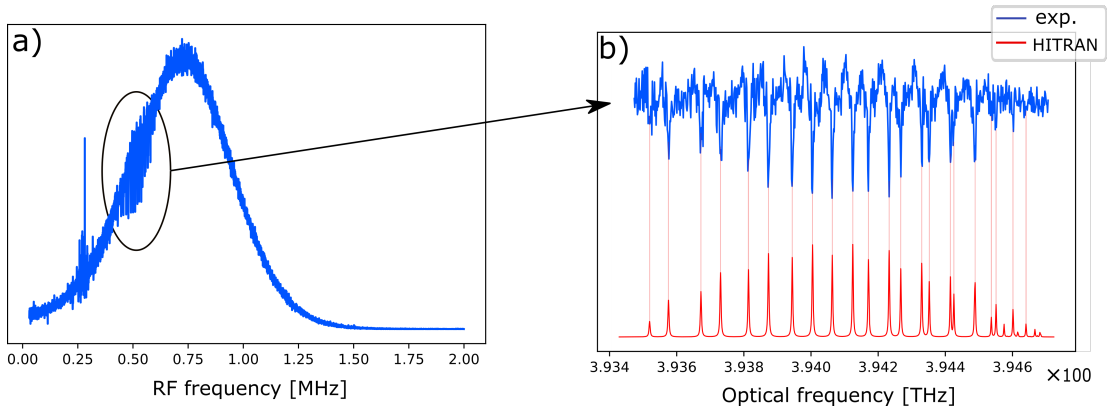

Figure 6.14: (a) DCS spectrum propagating through an optical path of approximately 7 m in air. The features observed on the left part of the spectrum are O_2 absorption lines. (b) Comparison of O_2 line positions measured with DCS (baseline removed) and reference values obtained from Hitran database.

Panel b) of figure 6.14 shows the differential spectrum of O_2 superposed with the calculated spectral absorption lines (determined from absorption cross-sections taken from the Hitran database). The differential spectrum corresponds to the spectrum of O_2 obtained from the retrieved DCS spectrum (panel a) of figure 6.14) after baseline removal using a Tchebychev polynomial function. The optical frequencies of the laser modes can be obtained with a precision of 500 GHz using the equation 6.1 (limited by the resolution of a grating spectrometer, see section 6.1). However, the high coherence over one truncated interferogram duration of the laser system allows far better

spectral calibration of the DCS RF spectrum using the well-known markers from O_2 absorption around 760 nm. A linear fit was used to calibrate spectrally the experimental DCS RF spectrum to the optical domain as illustrated in panel a) of figure 6.15. The assessed linear fit of equation $\nu_{\text{opt}} = 6.158.10^6 \times \text{f}_{\text{RF}} + 390.92$ THz provides secondary calibration for the DCS RF spectrum. As presented in the panel b) the residual standard deviation between the experimental frequency point and the linear fit is about 850 MHz. This frequency precision agrees with the resolution of the experiment which is taken from the inverse of the duration time of the temporal trace ($1/5.4\text{ms} \times \text{a} \approx 1\text{GHz}$). This demonstrates that an accurate absolute calibration of the optical frequencies from the RF frequencies is possible using a molecular reference.
We also determined that the relative absorption intensity of the transition lines agrees within 2.5% with their theoretical relative intensity.

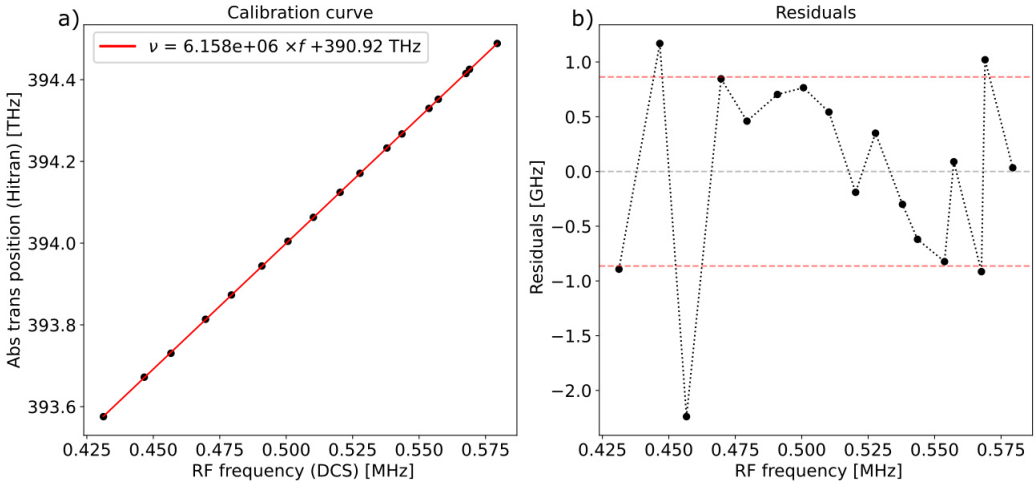

Figure 6.15: a) Linear calibration of the spectral absorption transition lines position frequencies retrieved from the DCS method by using the absorption cross-section obtained from Hitran database. The calibration linear fit equation was determined as $\nu_{\text{opt}} = 6.158.10^6 \times \text{f} + 390.92\text{THz}$ b) Residual of the position of the DCS as a function of the position given by the best calibration fit determined from panel a). The two horizontal red dashed lines represent the standard deviation of the residuals (0.86 GHz).

A signal to noise ratio of the retrieved transition lines of 6 is estimated. The concentration of O_2 averaged along the optical path was established using the Beer-Lambert law that takes as parameter the absorption cross-section obtained from the Hitran database. The result of the fitting algorithm gives O_2 mixing ratio of 0.24(5)% which agrees with the expected value around 0.21%. An uncertainty of 20 % on the average concentration of O_2 was estimated. This uncertainty level on the concentration is mainly due to an ill determined base-line level where oscillations higher than the statistical uncertainty of the base-line (determined without absorption) are observed (see b) of figure 6.14). The statistical noise is attributed to laser intensity fluctuations and consequent intensity noise due to Δf_{rep} and Δf_{CEO} fluctuations. The observed perturbation on the base-

line has not been attributed yet as these firsts results are preliminary and they will be further investigated in a near future.

6.4 Perspectives

To access molecular transition in ambient air in the UV range, it will be necessary to frequency double and triple the current home-made laser source. The options for doing this are presented below, but successful outcome clearly requires an improvement of at least one order of magnitude in the signal to noise ratio in the DCS spectrum observed at 760 nm (see section 3.3.2), either through improved detection strategies, or optimized post-processing.

UV generation

The generation of the laser pulses in the UV range and specifically at 308 nm, will allow the realisation of DCS to monitor UV absorbing molecules. First harmonic generation of UV laser was achieved using a Multiharmonic Generator (Model ATsG-O-800 Avesta project). It uses second harmonic generation (SHG) to obtain the doubled frequency (375-450 nm), and a sum frequency generation (SFG) process to obtain the tripled frequency (250-310 nm). A schematic of the multiple harmonic generation principle is given in figure 6.16.

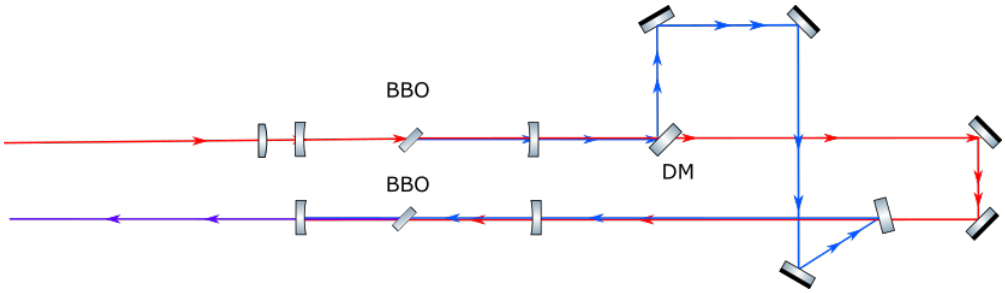

Figure 6.16: Harmonic generation system. Frequency doubling and tripling are achieved using two BBO crystals. The fundamental laser beam has a wavelength of 800 nm (red line), the doubled beam has a 400 nm (blue line) and the tripled laser beam is at 270 nm (purple line). A dichroic mirror (DM) is used after the generation of second harmonic to separate the fundamental and the SHG laser beams. These two radiations are then used to generate a laser radiation at 270 nm by sum frequency generation.

The tripling frequency (270 nm) from a fundamental laser beam (800 nm) is generated following two steps. The first step consists in the generation of a SHG by focusing the pulsed laser inside a BBO crystal. The BBO crystal is tilted to optimize the phase matching which maximise the SHG laser power. Then, in a second step, the fundamental and SHG laser radiations are used to generate a radiation with a frequency that corresponds to the sum of the fundamental and the

doubled laser frequencies. This is realised by SFG in a second BBO crystal. The phase matching is also optimized which maximise the output power of the 270 nm radiation.
125 mW of second harmonic generation laser at 400 nm was obtained from a fundamental laser beam injected at 800 nm, with 600 mW and approximately 100 fs pulse duration. This corresponds to a conversion rate of 21 % which is in agreement with the constructor values (20-25%). Third harmonic generation was obtained experimentally with a very low value (< 1 mW). More investigations are currently under progress to reach the constructor tripling efficiency performance (3-10%). These results represent our first steps towards UV-DCS.

Balanced detection

Balanced photo-detection consists of taking ratios or differences between correlated input signals, and amplifying the results eliminating the random noise and extracting small variations from the noise ground. The two detected signals are relatively phase shifted of π which allow their difference to highlights the signal and cancel the statistical fluctuation (due to noise). This results in an increase of the signal to noise ratio. Figure 6.17 illustrates the principle of balanced detection that will be set up in a near future in our set-up.

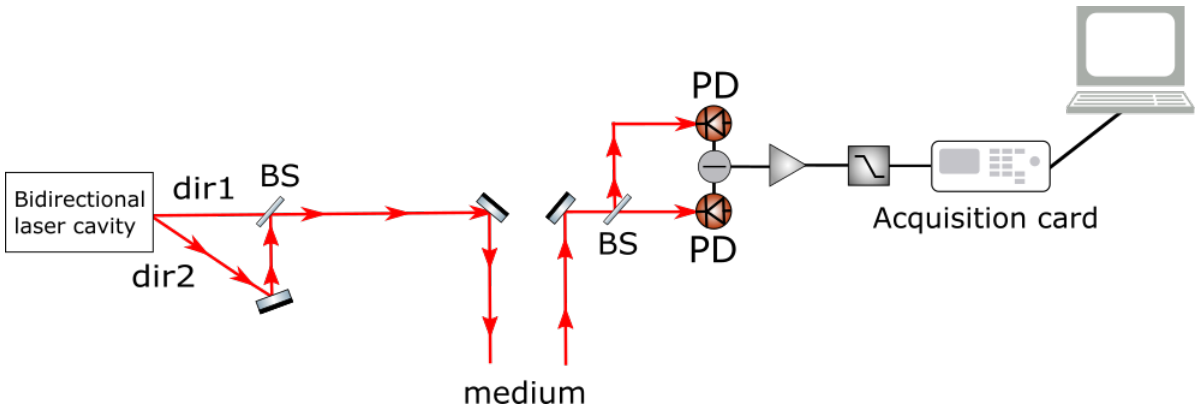

Figure 6.17: Schematic of a balanced detection. The two laser beams initially emitted from the bidirectional laser source are combined together and emitted towards the absorbing medium. Then, the signal is split towards two similar photo-detector. One of the two signals is phase-shifted of π. The difference applied on the two recorded signal removes the random fluctuations (due to statistical noise) while the signal is amplified by the trans-impedance amplifier, filtered and digitized.

As presented in chapter 3, Newbury et al. [237], show that the spectral relative intensity noise (RIN see 3.2.1) is reduced by a factor of 2 when using balanced detection. Truong et al. [322] used a similar method where two orthogonal polarised combs are detected on two PD which reduce the laser relative intensity noise of up to 4 dB higher than the detector shot noise limit.

Correction of fluctuations and averaging

The fluctuations on f_{rep}, Δf_{rep} and Δf_{CEO} (leading to timing fluctuations and carrier-envelope phase variation) limit the mutual coherence time between the two combs, which results in fine to a reduction of the spectral resolution and an increase of SNR. Methods such as real-time adaptative sampling method can be used to correct timing fluctuations and carrier-envelope phase variation. Once the temporal trace corrected, it is then possible to average the temporal trace using averaging coherent protocol to improve the signal to noise ratio of the DCS. These methods were presented in chapter 2.
Δf_{CEO} fluctuations can be corrected using for example Forman-Vanasse phase correction [323] by post-processing the interferograms with a phase correction algorithm. Fritsch et al. [226] demonstrated that the spectral SNR and spectral resolution could be significantly improved using this post-processing method for a dual comb spectroscopy measurement. Hebert et al. [221] developed a self-correction algorithm that extract and correct $\Delta \mathrm{f_{CEO}}$ and Δf_{rep} fluctuations. From this compensation, they could reach the spectral resolution limit (corresponding to the inverse of the temporal window ; initial spectral resolution 30 times larger) with a SNR of about 30 dB higher compared with initial spectrum.

6.5 Conclusion

In this section were presented the first DCS measurements using the home-made bidirectional Ti:sa laser source. First, the parameters $\mathrm{f_{rep}}, \Delta \mathrm{f_{rep}}$ and $\Delta \mathrm{f_{CEO}}$ of the dual comb were experimentally determined with an uncertainty of 2.5 kHz, 0.03 Hz and 400 kHz respectively. A high relative coherence between the free running pulse trains was observed along up to 330 ms of acquisition time which demonstrates a high stability of the laser source. The DCS method has allowed the retrieval of the free spectral range of a Fabry-Perot etalon with an accuracy of 1 MHz in 100 µs of acquisition time. The transition absorption lines of the ambient molecule O_2 was retrieved with a spectral resolution better than 1 GHz in 5,4 ms. The stability and the high relative coherence demonstrated by the laser radiation source seems highly promising for further spectroscopic measurements. The signal to noise ratio can be improved by using detecting method such as balanced detection, and by using post-process algorithm that compensates the fluctuations of DCS parameters.

General conclusions

The objective of this project was to realise a bidirectional TiSa laser cavity that is able to generate two pulse trains and measure atmospheric trace gases concentration in the UV range by dual-comb spectroscopy. First was assessed the feasibility of the UV-DCS in real atmospheric conditions, then a bidirectional mode-locked laser cavity was experimentally realised and the firsts dual-comb spectroscopic measurements were presented.

The first step of this project consisted in a numerical simulation work on the feasibility of the dual-comb spectroscopy in the UV range. Harmonic generation from a TiSa mode-locked laser cavity has been identified to be the current most adapted laser source to realise DCS in the UV. To be immune to the atmospheric turbulences, Δf_{rep} value was determined to be necessarily set higher than 130 Hz. The signal to noise ratio of UV-DCS was determined to be limited by the relative intensity noise of the laser source. Using this laser source, the DCS appeared to be highly relevant to monitor atmospheric gas of interest in the UV range : it is an in-situ remote sensing method, free of sampling retrieval, immune to atmospheric turbulences and according to our simulations it reaches similar sensitivity than the existing detection methods. UV-DCS is particularly competitive when a broad spectral range is necessary. Experimental DCS measurement in the UV should confirm that the propagation of a UV laser beam with the given average power is producing negligible radical OH in the optical path. This numerical study is preliminary to future experimental demonstrations of atmospheric trace gases remote detection using the UV-DCS.

Following this numerical study, the laser source was realised in our laboratory. First, the cavity design was investigated. The advantage of the generation of two laser beams from a single cavity is a high mutual coherence between the two pulse's trains which allows the design of a simpler configuration and a more compact instrument. The theoretical background of a mode-locked TiSa laser in a bidirectional configuration as well as the conditions needed to start the mode-locking regime were presented. A design of the laser cavity was realised to compensate for the loss of intra-cavity power that can be created by astigmatism or non-optimized Brewster angle of solid intra-cavity

transparent elements (crystal, prisms). A numerical study on the dispersion compensation created by a prism compressor allowed to optimise the prisms positions and therefore the net cavity dispersion needed to obtain a mode-locked regime. The stability of the laser cavities in a linear and a ring configuration were also numerically computed.

The experimental realisations of a linear and a ring laser cavity configuration allowed to verify experimentally the results on the cavity dispersion, the output power and the cavity stability obtained numerically. The measured output power of the mode-locked pulsed lasers was 700 mW which corresponds to a value higher than 10 % of the pump power. The output ML power available is currently limited by the pump power (5.5 W), but our experiments show that a higher ML output power is expected with a higher pump power. This is expected to provide enough power for generating 15 mW around 300 nm after a frequency tripling process. The Δf_{rep} value was obtained experimentally up to 450 Hz with pulses as short as 60 fs. Therefore the Δf_{rep} value is high enough to obtain immunity to noises induced by atmospheric turbulences. A high relative coherence between the two lasers was measured at 330 ms without the need for active phase stabilisation. This system shows a better coherence than the currently existing solid state dual-comb laser sources. This temporal coherence is expected to be longer as it is currently limited by the memory buffer of the acquisition card.

Dual-comb spectroscopy measurements were realised using our home-made laser source. Firsts DCS measurements were realised on a Fabry-Perot etalon and on the molecular ro-vibrational transitions at 760 nm of O_2. The free spectral range of a Fabry-Perot etalon was retrieved with an accuracy of 1 MHz in 100 µs of acquisition time. The FSR was thus estimated at 73.739(1) GHz. A comparison with another optical instrument such as CRDS will be realised in future as the value from the constructor may have varied from 75 +- 1 GHz depending on temperature. The Δf_{rep} was accurately retrieved with a value of 107.69(1) Hz from the analysis of nine interferograms which demonstrates the high relative stability between the two pulsed trains for a range of time in the order of 100 ms. The transition lines of O_2 at 760 nm were accurately retrieved with a spectral resolution inferior to 1 GHz in 5,4 ms. However, the high uncertainty on the retrieved concentration of O_2 can be improved. The signal to noise ratio of UV-DCS can be improved by using a balanced detection method or by compensating the Δf_{CEO} fluctuations using a post processing algorithm. The two laser beams were frequency tripled using a harmonic generation instrument. Even though about 125 mW was experimentally obtained at 400 nm by SHG, improvements of the frequency tripled generated power must be made to reach the 15 mW expected. These firsts results represent an important milestone towards the remote sensing of in-situ atmospheric trace gases in the UV using DCS.

Bibliography

[1] L. Connors, S. B. C. Péan, Y. C. N. Caud, L. Goldfarb, M. I. Gomis, M. Huang, K. Leitzell, E. Lonnoy, J. B. Matthews, T. K. Maycock, T. Waterfield, O. Yelekci, R. Yu, B. Zhou, [Masson-Delmotte, V., P. Zhai, and A. P. S], "Climate Change 2021: The Physical Science Basis. Contribution of Working Group I to the Sixth Assessment Report of the Intergovernmental Panel on Climate Change," *Cambridge University Press.*, August 2021. iii, iv, 1, 3

[2] G. B. Rieker, F. R. Giorgetta, W. C. Swann, J. Kofler, a. M. Zolot, L. C. Sinclair, E. Baumann, C. Cromer, G. Petron, C. Sweeney, P. P. Tans, I. Coddington, and N. R. Newbury, "Frequency-comb-based remote sensing of greenhouse gases over kilometer air paths," *Optica*, vol. 1, no. 5, pp. 290–298, 2014. iii, iv, 1, 15, 18, 20, 53, 54

[3] S. Coburn, C. B. Alden, R. Wright, K. Cossel, E. Baumann, G.-W. Truong, F. Giorgetta, C. Sweeney, N. R. Newbury, K. Prasad, I. Coddington, and G. B. Rieker, "Regional trace-gas source attribution using a field-deployed dual frequency comb spectrometer," *Optica*, vol. 5, pp. 320–327, Apr ts. iii, iv, 1, 19

[4] S. Galtier, C. Pivard, and P. Rairoux, "Towards DCS in the UV Spectral Range for Remote Sensing of Atmospheric Trace Gases," *Remote Sensing*, vol. 12, no. 20, 2020. iii, iv

[5] S. Manabe, K. Hasselmann, and G. Parisi, " The Nobel Prize in Physics 2021," 1

[6] S. Sterckx, I. Brown, A. Kääb, M. Krol, R. Morrow, P. Veefkind, K. F. Boersma, M. De Mazière, N. Fox, and P. Thorne, "Towards a European Cal/Val service for earth observation," *International Journal of Remote Sensing*, vol. 41, no. 12, pp. 4496–4511, 2020. 1, 9

[7] I. Coddington, N. Newbury, and W. Swann, "Dual-comb spectroscopy," *Optica*, vol. 3, pp. 414–426, Apr 2016. 1, 18, 35

[8] N. Picqué and T. W. Hänsch, "Frequency comb spectroscopy," *Nature Photonics*, vol. 13, p. 146–157, Feb 2019. 1, 18

[9] D. E. Heard and M. J. Pilling, "Measurement of OH and HO_2 in the Troposphere," *Chemical Reviews*, vol. 103, no. 12, pp. 5163–5198, 2003. PMID: 14664647. 1, 10

[10] U. Platt and J. Stutz, "Differential absorption spectroscopy," in *Differential Optical Absorption Spectroscopy, pages=135–174, year=2008, publisher=Springer.* 1, 5, 13, 14

[11] J. Li, M.-H. Wang, and Y.-S. Ho, "Trends in research on global climate change: A science citation index expanded-based analysis," *Global and Planetary Change*, vol. 77, no. 1-2, pp. 13–20, 2011. 1

[12] *The remote sensing of tropospheric composition from space, author=Burrows, John P and Platt, Ulrich and Borrell, Peter, year=2011, publisher=Springer Science & Business Media.* 1

[13] K. E. Trenberth, "Climate change caused by human activities is happening and it already has major consequences," *Journal of Energy & Natural Resources Law*, vol. 36, no. 4, pp. 463–481, 2018. 3

[14] K. E. Trenberth, "Framing the way to relate climate extremes to climate change," *Climatic change*, vol. 115, no. 2, pp. 283–290, 2012. 3

[15] S. Manabe, J. Smagorinsky, and R. F. Strickler, "Simulated climatology of a general circulation model with a hydrologic cycle," *Monthly Weather Review*, vol. 93, no. 12, pp. 769–798, 1965. 3

[16] K. E. Taylor, R. J. Stouffer, and G. A. Meehl, "An overview of CMIP5 and the experiment design," *Bulletin of the American meteorological Society*, vol. 93, no. 4, pp. 485–498, 2012. 3

[17] G. A. Meehl, W. M. Washington, J. M. Arblaster, A. Hu, H. Teng, J. E. Kay, A. Gettelman, D. M. Lawrence, B. M. Sanderson, and W. G. Strand, "Climate change projections in CESM1 (CAM5) compared to CCSM4," *Journal of Climate*, vol. 26, no. 17, pp. 6287–6308, 2013. 3

[18] M. L. Weitzman, "On modeling and interpreting the economics of catastrophic climate change," *The review of economics and statistics*, vol. 91, no. 1, pp. 1–19, 2009. 3

[19] S. C. Sherwood and M. Huber, "An adaptability limit to climate change due to heat stress," *Proceedings of the National Academy of Sciences*, vol. 107, no. 21, pp. 9552–9555, 2010. 3

[20] R. D. Manzanedo and P. Manning, "COVID-19: Lessons for the climate change emergency," *Science of The Total Environment*, vol. 742, p. 140563, 2020. 3

[21] Masson-Delmotte, P. Zhai, H.-O. Pörtner, D. Roberts, J. Skea, P. Shukla, A. Pirani, W. Moufouma-Okia, C. Péan, R. Pidcock, S. Connors, J. Matthews, Y. Chen, X. Zhou,

M. Gomis, E. Lonnoy, T. Maycock, M. Tignor, and T. W. (eds.), " Summary for Policymakers. Global Warming of 1.5°C. An IPCC Special Report on the impacts of global warming of 1.5°C above pre-industrial levels and related global greenhouse gas emission pathways, in the context of strengthening the global response to the threat of climate change, sustainable development, and efforts to eradicate poverty," 2018. 3

[22] H. Mayer, "Air pollution in cities," *Atmospheric environment*, vol. 33, no. 24-25, pp. 4029–4037, 1999. 4

[23] D. Mage, G. Ozolins, P. Peterson, A. Webster, R. Orthofer, V. Vandeweerd, and M. Gwynne, "Urban air pollution in megacities of the world," *Atmospheric environment*, vol. 30, no. 5, pp. 681–686, 1996. 4

[24] A. Baklanov, L. T. Molina, and M. Gauss, "Megacities, air quality and climate," *Atmospheric Environment*, vol. 126, pp. 235–249, 2016. 4

[25] G. P. Brasseur, J. T. Kiehl, J.-F. Müller, T. Schneider, C. Granier, X. Tie, and D. Hauglustaine, "Past and future changes in global tropospheric ozone: Impact on radiative forcing," *Geophysical Research Letters*, vol. 25, no. 20, pp. 3807–3810, 1998. 4

[26] O. R. Cooper, D. Parrish, J. Ziemke, N. Balashov, M. Cupeiro, I. Galbally, S. Gilge, L. Horowitz, N. Jensen, J.-F. Lamarque, *et al.*, "Global distribution and trends of tropospheric ozone: An observation-based reviewGlobal distribution and trends of tropospheric ozone," *Elementa: Science of the Anthropocene*, vol. 2, 2014. 4

[27] D. L. Mauzerall and X. Wang, "Protecting agricultural crops from the effects of tropospheric ozone exposure: reconciling science and standard setting in the United States, Europe, and Asia," *Annual Review of energy and the environment*, vol. 26, no. 1, pp. 237–268, 2001. 4

[28] K. Ito, S. F. De Leon, and M. Lippmann, "Associations between ozone and daily mortality: analysis and meta-analysis," *Epidemiology*, pp. 446–457, 2005. 4

[29] M. L. Bell, R. Goldberg, C. Hogrefe, P. L. Kinney, K. Knowlton, B. Lynn, J. Rosenthal, C. Rosenzweig, and J. A. Patz, "Climate change, ambient ozone, and health in 50 US cities," *Climatic Change*, vol. 82, no. 1, pp. 61–76, 2007. 4

[30] H. Desqueyroux, J.-C. Pujet, M. Prosper, Y. Le Moullec, and I. Momas, "Effects of air pollution on adults with chronic obstructive pulmonary disease," *Archives of Environmental Health: An International Journal*, vol. 57, no. 6, pp. 554–560, 2002. 4

[31] C. A. Pope III and D. W. Dockery, "Health effects of fine particulate air pollution: lines that connect," *Journal of the air & waste management association*, vol. 56, no. 6, pp. 709–742, 2006. 4

[32] L. CALDERon-GARCIDUEnas, W. Reed, R. R. Maronpot, C. Henriquez-Roldán, R. Delgado-Chavez, A. CALDERon-GARCIDUEnas, I. Dragustinovis, M. Franco-Lira, M. Aragón-Flores, A. C. Solt, *et al.*, "Brain inflammation and Alzheimer's-like pathology in individuals exposed to severe air pollution," *Toxicologic pathology*, vol. 32, no. 6, pp. 650–658, 2004. 4

[33] K. C. Bishop, J. D. Ketcham, and N. V. Kuminoff, "Hazed and confused: the effect of air pollution on dementia," tech. rep., National Bureau of Economic Research, 2018. 4

[34] R. Peters, N. Ee, J. Peters, A. Booth, I. Mudway, and K. J. Anstey, "Air pollution and dementia: a systematic review," *Journal of Alzheimer's Disease*, vol. 70, no. s1, pp. S145–S163, 2019. 4

[35] C. K. Chan and X. Yao, "Air pollution in mega cities in China," *Atmospheric environment*, vol. 42, no. 1, pp. 1–42, 2008. 4

[36] "Exposure to severe urban air pollution influences cognitive outcomes, brain volume and systemic inflammation in clinically healthy children, author=Calderón-Garcidueñas, Lilian and Engle, Randall and Mora-Tiscareño, Antonieta and Styner, Martin and Gómez-Garza, Gilberto and Zhu, Hongtu and Jewells, Valerie and Torres-Jardón, Ricardo and Romero, Lina and Monroy-Acosta, Maria E and others," *Brain and cognition*, vol. 77, no. 3, pp. 345–355, 2011. 4

[37] R. T. Burnett, S. Cakmak, and J. R. Brook, "The effect of the urban ambient air pollution mix on daily mortality rates in 11 Canadian cities," *Canadian journal of public health*, vol. 89, no. 3, pp. 152–156, 1998. 4

[38] A. S. Shuping Li, Jamie Matthews, "Atmospheric Hydroxyl Radical Production from Electronically Excited NO2 and H2O," *Science*, 2008. 5

[39] R. G. Prinn, "The Cleansing Capacity of the Atmosphere," *Annual Review of Environment and Resources*, vol. 28, no. 1, pp. 29–57, 2003. 5

[40] M. Saunois, A. R. Stavert, B. Poulter, P. Bousquet, J. G. Canadell, R. B. Jackson, P. A. Raymond, E. J. Dlugokencky, S. Houweling, P. K. Patra, *et al.*, "The global methane budget 2000–2017," *Earth System Science Data*, vol. 12, no. 3, pp. 1561–1623, 2020. 5

[41] K. M. Emmerson, N. Carslaw, D. Carslaw, J. D. Lee, G. McFiggans, W. J. Bloss, T. Gravestock, D. E. Heard, J. Hopkins, T. Ingham, *et al.*, "Free radical modelling studies during the UK TORCH Campaign in Summer 2003," *Atmospheric Chemistry and Physics*, vol. 7, no. 1, pp. 167–181, 2007. 5

[42] K. Lu, F. Rohrer, F. Holland, H. Fuchs, B. Bohn, T. Brauers, C. Chang, R. Häseler, M. Hu, K. Kita, *et al.*, "Observation and modelling of OH and HO_2 concentrations in the Pearl River Delta 2006: a missing OH source in a VOC rich atmosphere," *Atmospheric chemistry and physics*, vol. 12, no. 3, pp. 1541–1569, 2012. 5

[43] H. Levy, "Normal atmosphere: Large radical and formaldehyde concentrations predicted," *Science*, vol. 173, no. 3992, pp. 141–143, 1971. 5, 62

[44] J. Calvert, G. Yarwood, and A. Dunker, "An evaluation of the mechanism of nitrous acid formation in the urban atmosphere," *Research on Chemical Intermediates*, vol. 20, no. 3, pp. 463–502, 1994. 5

[45] M. Martinez, H. Harder, T. Kovacs, J. Simpas, J. Bassis, R. Lesher, W. Brune, G. Frost, E. Williams, C. Stroud, *et al.*, "OH and HO_2 concentrations, sources, and loss rates during the Southern Oxidants Study in Nashville, Tennessee, summer 1999," *Journal of Geophysical Research: Atmospheres*, vol. 108, no. D19, 2003. 5

[46] Y. F. Elshorbany, J. Kleffmann, A. Hofzumahaus, R. Kurtenbach, P. Wiesen, T. Brauers, B. Bohn, H.-P. Dorn, H. Fuchs, F. Holland, *et al.*, "HOx budgets during HOxComp: A case study of HOx chemistry under NOx-limited conditions," *Journal of Geophysical Research: Atmospheres*, vol. 117, no. D3, 2012. 5

[47] X. Ren, H. Harder, M. Martinez, R. L. Lesher, A. Oliger, J. B. Simpas, W. H. Brune, J. J. Schwab, K. L. Demerjian, Y. He, *et al.*, "OH and HO_2 chemistry in the urban atmosphere of New York City," *Atmospheric Environment*, vol. 37, no. 26, pp. 3639–3651, 2003. 5

[48] D. Tan, I. Faloona, J. Simpas, W. Brune, P. Shepson, T. Couch, A. Sumner, M. Carroll, T. Thornberry, E. Apel, *et al.*, "HO x budgets in a deciduous forest: Results from the PROPHET summer 1998 campaign," *Journal of Geophysical Research: Atmospheres*, vol. 106, no. D20, pp. 24407–24427, 2001. 5

[49] S. M. Griffith, R. Hansen, S. Dusanter, V. Michoud, J. Gilman, W. Kuster, P. Veres, M. Graus, J. de Gouw, J. Roberts, *et al.*, "Measurements of hydroxyl and hydroperoxy radicals during CalNex-LA: Model comparisons and radical budgets," *Journal of Geophysical Research: Atmospheres*, vol. 121, no. 8, pp. 4211–4232, 2016. 6

[50] A. Hofzumahaus, F. Rohrer, K. Lu, B. Bohn, T. Brauers, C.-C. Chang, H. Fuchs, F. Holland, K. Kita, Y. Kondo, *et al.*, "Amplified trace gas removal in the troposphere," *science*, vol. 324, no. 5935, pp. 1702–1704, 2009. 6

[51] F. Rohrer, K. Lu, A. Hofzumahaus, B. Bohn, T. Brauers, C.-C. Chang, H. Fuchs, R. Häseler, F. Holland, M. Hu, *et al.*, "Maximum efficiency in the hydroxyl-radical-based self-cleansing of the troposphere," *Nature Geoscience*, vol. 7, no. 8, pp. 559–563, 2014. 6

[52] M. Yousefi, P. F. Bernath, J. Hodges, and T. Masseron, "A new line list for the A2Σ+- X2Π electronic transition of OH," *Journal of Quantitative Spectroscopy and Radiative Transfer*, vol. 217, pp. 416–424, 2018. 7

[53] S. O. Danielache, C. Eskebjerg, M. S. Johnson, Y. Ueno, and N. Yoshida, "High-precision spectroscopy of 32s, 33s, and 34s sulfur dioxide: Ultraviolet absorption cross sections and isotope effects," *Journal of Geophysical Research: Atmospheres*, vol. 113, no. D17, 2008. 7

[54] A. C. Vandaele, P. C. Simon, J. M. Guilmot, M. Carleer, and R. Colin, "SO2 absorption cross section measurement in the UV using a Fourier transform spectrometer," *Journal of Geophysical Research: Atmospheres*, vol. 99, no. D12, pp. 25599–25605, 1994. 7

[55] H. Grosch, Z. Sárossy, H. Egsgaard, and A. Fateev, "Uv absorption cross-sections of phenol and naphthalene at temperatures up to 500°c," *Journal of Quantitative Spectroscopy and Radiative Transfer*, vol. 156, pp. 17–23, 2015. 7

[56] C. A. Smith, F. D. Pope, B. Cronin, C. B. Parkes, and A. J. Orr-Ewing, "Absorption cross sections of formaldehyde at wavelengths from 300 to 340 nm at 294 and 245 k," *The Journal of Physical Chemistry A*, vol. 110, no. 41, pp. 11645–11653, 2006. 7

[57] S. O. Danielache, C. Eskebjerg, M. S. Johnson, Y. Ueno, and N. Yoshida, "High-precision spectroscopy of 32S, 33S, and 34S sulfur dioxide: Ultraviolet absorption cross sections and isotope effects," *Journal of Geophysical Research: Atmospheres*, vol. 113, no. D17, 2008. 7

[58] A. Nölle, F. Pätzold, S. Pätzold, R. Meller, G. Moortgat, E. Röth, R. Ruhnke, and H. Keller-Rudek, "UV/Vis Spectra of Atmospheric Constituents version 1," *CD-ROM], ATMOS User Cent., Maintal, Germany*, 2001. 7

[59] A. Bongartz, J. Kames, U. Schurath, C. George, P. Mirabel, and J. Ponche, "Experimental determination of HONO mass accommodation coefficients using two different techniques," *Journal of atmospheric chemistry*, vol. 18, no. 2, pp. 149–169, 1994. 7

[60] K. Bogumil, J. Orphal, T. Homann, S. Voigt, P. Spietz, O. Fleischmann, A. Vogel, M. Hartmann, H. Kromminga, H. Bovensmann, *et al.*, "Measurements of molecular absorption spectra with the SCIAMACHY pre-flight model: instrument characterization and reference data for atmospheric remote-sensing in the 230–2380 nm region," *Journal of Photochemistry and Photobiology A: Chemistry*, vol. 157, no. 2-3, pp. 167–184, 2003. 7

[61] R. Cox, D. Sheppard, and M. Stevens, "Absorption coefficients and kinetics of the BrO radical using molecular modulation," *Journal of Photochemistry*, vol. 19, no. 3, pp. 189–207, 1982. 7

[62] A. Wahner, G. S. Tyndall, and A. Ravishankara, "Absorption cross sections for symmetric chlorine dioxide as a function of temperature in the wavelength range 240-480nm," *Journal of Physical Chemistry*, vol. 91, no. 11, pp. 2734–2738, 1987. 7

[63] A. Clarke and M. Radojevic, "Oxidation of SO2 in rainwater and its role in acid rain chemistry," *Atmospheric Environment (1967)*, vol. 21, no. 5, pp. 1115–1123, 1987. 6

[64] L. Yang, G. Zhou, B. Yu, and Z.-x. Wang, "Acid rain composition and its correlation analysis at Guangzhou," *Ecologic Science*, vol. 3, 2005. 6

[65] R. Yang and W. Chen, "Spatial correlation, influencing factors and environmental supervision on mechanism construction of atmospheric pollution: an empirical study on SO2 emissions in China," *Sustainability*, vol. 11, no. 6, p. 1742, 2019. 6

[66] F. S. Rowland, "Stratospheric ozone depletion," *Twenty Years of Ozone Decline*, pp. 23–66, 2009. 6

[67] S. Pattenden, G. Hoek, C. Braun-Fahrländer, F. Forastiere, A. Kosheleva, M. Neuberger, and T. Fletcher, "NO2 and children's respiratory symptoms in the PATY study," *Occupational and environmental medicine*, vol. 63, no. 12, pp. 828–835, 2006. 6

[68] M. Neuberger, D. Rabczenko, and H. Moshammer, "Extended effects of air pollution on cardiopulmonary mortality in Vienna," *Atmospheric Environment*, vol. 41, no. 38, pp. 8549–8556, 2007. 6

[69] H. Moshammer, M. Poteser, M. Kundi, K. Lemmerer, L. Weitensfelder, P. Wallner, and H.-P. Hutter, "Nitrogen-dioxide remains a valid air quality indicator," *International Journal of Environmental Research and Public Health*, vol. 17, no. 10, p. 3733, 2020. 6

[70] J. Heinrich, E. Thiering, P. Rzehak, U. Krämer, M. Hochadel, K. M. Rauchfuss, U. Gehring, and H.-E. Wichmann, "Long-term exposure to NO2 and PM10 and all-cause and cause-specific mortality in a prospective cohort of women," *Occupational and environmental medicine*, vol. 70, no. 3, pp. 179–186, 2013. 6

[71] D. Fahey, P. A. Newman, J. A. Pyle, B. Safari, M. P. Chipperfield, D. Karoly, D. E. Kinnison, M. Ko, M. Santee, and S. J. Doherty, "Scientific Assessment of Ozone Depletion: 2018, Global Ozone Research and Monitoring Project-Report No. 58," 2018. 7

[72] D. M. Wilmouth, R. J. Salawitch, and T. P. Canty, "Stratospheric ozone depletion and recovery," in *Green Chemistry, pages=177–209, year=2018, publisher=Elsevier.* 7

[73] S. Dejean, C. Raynaud, M. Meybeck, J.-P. Della Massa, and V. Simon, "Polycyclic aromatic hydrocarbons (PAHs) in atmospheric urban area: monitoring on various types of sites," *Environmental Monitoring and Assessment*, vol. 148, no. 1, pp. 27–37, 2009. 8

[74] I. Zdanevitch, S. Collet, M. Meyer, and J. Auvray, "Ambient air measurements related to traffic: evolution of VOCs over three years," in *2. Conference" Environment & transport" including the 15. Conference" Transport and air pollution", pages=201–206, year=2006, organization=INRETS. Arcueil*. 8

[75] W.-J. Lee, Y.-F. Wang, T.-C. Lin, Y.-Y. Chen, W.-C. Lin, C.-C. Ku, and J.-T. Cheng, "PAH characteristics in the ambient air of traffic-source," *Science of the Total Environment*, vol. 159, no. 2-3, pp. 185–200, 1995. 8

[76] G. Steineck, N. Plato, L. Alfredsson, and S. E. Norell, "Industry-related urothelial carcinogens: Application of a job-exposure matrix to census data," *American journal of industrial medicine*, vol. 16, no. 2, pp. 209–224, 1989. 8

[77] C.-E. Boström, P. Gerde, A. Hanberg, B. Jernström, C. Johansson, T. Kyrklund, A. Rannug, M. Törnqvist, K. Victorin, and R. Westerholm, "Cancer risk assessment, indicators, and guidelines for polycyclic aromatic hydrocarbons in the ambient air.," *Environmental health perspectives*, vol. 110, no. suppl 3, pp. 451–488, 2002. 8

[78] O. Wittmann, "Die nachträgliche Formaldehydabspaltung bei Spanplatten," *Holz als Roh-und Werkstoff*, vol. 20, no. 6, pp. 221–224, 1962. 8

[79] J. S. Gaffney and N. A. Marley, "The impacts of combustion emissions on air quality and climate–From coal to biofuels and beyond," *Atmospheric Environment*, vol. 43, no. 1, pp. 23–36, 2009. 8

[80] T. Salthammer, "Formaldehyde in the ambient atmosphere: from an indoor pollutant to an outdoor pollutant?," *Angewandte chemie international edition*, vol. 52, no. 12, pp. 3320–3327, 2013. 8

[81] M. Krzyzanowski, J. J. Quackenboss, and M. D. Lebowitz, "Chronic respiratory effects of indoor formaldehyde exposure," *Environmental research*, vol. 52, no. 2, pp. 117–125, 1990. 8

[82] K. H. Kilburn, R. Warshaw, and J. Thornton, "Pulmonary function in histology technicians compared with women from Michigan: effects of chronic low dose formaldehyde on a national sample of women.," *Occupational and Environmental Medicine*, vol. 46, no. 7, pp. 468–472, 1989. 8

[83] P. S. Burge, M. Harries, W. Lam, I. O'brien, and P. Patchett, "Occupational asthma due to formaldehyde.," *Thorax*, vol. 40, no. 4, pp. 255–260, 1985. 8

[84] G. W. Harris, W. P. Carter, A. M. Winer, J. N. Pitts, U. Platt, and D. Perner, "Observations of nitrous acid in the Los Angeles atmosphere and implications for predictions of ozone-precursor relationships," *Environmental science & technology*, vol. 16, no. 7, pp. 414–419, 1982. 8

[85] A. Sjoedin, "Studies of the diurnal variation of nitrous acid in urban air," *Environmental science & technology*, vol. 22, no. 9, pp. 1086–1089, 1988. 8

[86] R. M. Harrison, J. D. Peak, and G. M. Collins, "Tropospheric cycle of nitrous acid," *Journal of Geophysical Research: Atmospheres*, vol. 101, no. D9, pp. 14429–14439, 1996. 8

[87] F. Spataro and A. Ianniello, "Sources of atmospheric nitrous acid: State of the science, current research needs, and future prospects," *Journal of the Air & Waste Management Association*, vol. 64, no. 11, pp. 1232–1250, 2014. 8

[88] M. B. McElroy, R. J. Salawitch, S. C. Wofsy, and J. A. Logan, "Reductions of Antarctic ozone due to synergistic interactions of chlorine and bromine," *Nature*, vol. 321, no. 6072, pp. 759–762, 1986. 8

[89] L. Barrie, J. Bottenheim, R. Schnell, P. Crutzen, and R. Rasmussen, "Ozone destruction and photochemical reactions at polar sunrise in the lower Arctic atmosphere," *Nature*, vol. 334, no. 6178, pp. 138–141, 1988. 8

[90] U. Platt and T. Wagner, "Satellite mapping of enhanced BrO concentrations in the troposphere," *Nature*, vol. 395, no. 6701, pp. 486–490, 1998. 8

[91] S. Wang, S. M. McNamara, C. W. Moore, D. Obrist, A. Steffen, P. B. Shepson, R. M. Staebler, A. R. Raso, and K. A. Pratt, "Direct detection of atmospheric atomic bromine leading to mercury and ozone depletion," *Proceedings of the National Academy of Sciences*, vol. 116, no. 29, pp. 14479–14484, 2019. 8

[92] C. Camy-Peyret, "Balloon-borne infrared Fourier transform spectroscopy for measurements of atmospheric trace species," *Spectrochimica Acta Part A: Molecular and Biomolecular Spectroscopy*, vol. 51, no. 7, pp. 1143–1152, 1995. 9

[93] Y. Zhao and Z. Chen, "Application of Fourier transform infrared spectroscopy in the study of atmospheric heterogeneous processes," *Applied Spectroscopy Reviews*, vol. 45, no. 1, pp. 63–91, 2010. 9

[94] J. M. Plane and A. Saiz-Lopez, "UV-visible differential optical absorption spectroscopy (DOAS)," *Analytical techniques for atmospheric measurement*, pp. 147–188, 2006. 9

[95] E. Spinei, A. Cede, J. Herman, G. Mount, E. Eloranta, B. Morley, S. Baidar, B. Dix, I. Ortega, T. Koenig, *et al.*, "Ground-based direct-sun DOAS and airborne MAX-DOAS measurements of the collision-induced oxygen complex, O 2 O 2, absorption with significant pressure and temperature differences," *Atmospheric Measurement Techniques*, vol. 8, no. 2, pp. 793–809, 2015. 9

[96] H. Bovensmann, J. Burrows, M. Buchwitz, J. Frerick, S. Noël, V. Rozanov, K. Chance, and A. Goede, "SCIAMACHY: Mission objectives and measurement modes," *Journal of the atmospheric sciences*, vol. 56, no. 2, pp. 127–150, 1999. 9

[97] L. Mei, P. Guan, and Z. Kong, "Remote sensing of atmospheric NO 2 by employing the continuous-wave differential absorption lidar technique," *Optics express*, vol. 25, no. 20, pp. A953–A962, 2017. 9

[98] Q. Liu, Y. Chen, J. Wang, J. Huang, and S. Hu, "Measurement of atmospheric NO2 profile using three-wavelength dual-differential absorption lidar," in *LIDAR Imaging Detection and Target Recognition 2017, volume=10605, pages=106053L, year=2017, organization=International Society for Optics and Photonics*. 9

[99] R. Rossi, D. Di Giovanni, A. Malizia, and P. Gaudio, "Measurements of vehicle pollutants in a high-traffic urban area by a multiwavelength dial approach: Correlation between two different motor vehicle pollutants," *Atmosphere*, vol. 11, no. 4, p. 383, 2020. 9

[100] E. V. Browell, "Differential absorption lidar sensing of ozone," *Proceedings of the IEEE*, vol. 77, no. 3, pp. 419–432, 1989. 9

[101] L. Liu, J. Yang, J. Huang, K. Yin, S. Hu, *et al.*, "Study on the temporal and spatial distribution of atmospheric SO2 and NO2 in Huainan observed by Lidar," in *Fifth Conference on Frontiers in Optical Imaging Technology and Applications, volume=10832, pages=1083212, year=2018, organization=International Society for Optics and Photonics*. 9

[102] G. Megie, "Laser remote sensing: fundamentals and applications," 1985. 9

[103] Y. Matsumi, H. Shigemori, and K. Takahashi, "Laser-induced fluorescence instrument for measuring atmospheric SO2," *Atmospheric Environment*, vol. 39, no. 17, pp. 3177–3185, 2005. 9

[104] J. A. Thornton, P. J. Wooldridge, and R. C. Cohen, "Atmospheric NO2: In situ laser-induced fluorescence detection at parts per trillion mixing ratios," *Analytical Chemistry*, vol. 72, no. 3, pp. 528–539, 2000. 9

[105] B. Fawcett, A. Parkes, D. Shallcross, and A. Orr-Ewing, "Trace detection of methane using continuous wave cavity ring-down spectroscopy at 1.65 μm," *Physical Chemistry Chemical Physics*, vol. 4, no. 24, pp. 5960–5965, 2002. 9

[106] H. Dahnke, G. Von Basum, K. Kleinermanns, P. Hering, and M. Mürtz, "Rapid formaldehyde monitoring in ambient air by means of mid-infrared cavity leak-out spectroscopy," *Applied Physics B*, vol. 75, no. 2, pp. 311–316, 2002. 9

[107] A. O'Keefe and O. Lee, "Trace gas analysis by pulsed laser absorption spectroscopy," *American Laboratory*, vol. 21, no. 12, pp. 19–22, 1989. 9

[108] A. O'Keefe, J. Scherer, J. Paul, and R. Saykally, "Cavity-ringdown laser spectroscopy history, development, and applications," ACS Publications, 1999. 9

[109] P. Rairoux, B. Koch, D. Moller, G. Goritz, G. Warmbier, and A. Czyzewski, "Atmospheric traces monitoring applying Cavity Ring-Down Spectroscopy," *ENVIRONMENTAL SCIENCE AND POLLUTION RESEARCH*, pp. 68–71, 2002. 9

[110] R. Engeln, G. Berden, R. Peeters, and G. Meijer, "Cavity enhanced absorption and cavity enhanced magnetic rotation spectroscopy," *Review of scientific instruments*, vol. 69, no. 11, pp. 3763–3769, 1998. 9

[111] Z. Li, R. Hu, P. Xie, H. Wang, K. Lu, and D. Wang, "Intercomparison of in situ CRDS and CEAS for measurements of atmospheric N2O5 in Beijing, China," *Science of the Total Environment*, vol. 613, pp. 131–139, 2018. 9

[112] J. Duan, M. Qin, B. Ouyang, W. Fang, X. Li, K. Lu, K. Tang, S. Liang, F. Meng, Z. Hu, *et al.*, "Development of an incoherent broadband cavity-enhanced absorption spectrometer for in situ measurements of HONO and NO 2," *Atmospheric measurement techniques*, vol. 11, no. 7, pp. 4531–4543, 2018. 9

[113] N. Jordan, C. Z. Ye, S. Ghosh, R. A. Washenfelder, S. S. Brown, and H. D. Osthoff, "A broadband cavity-enhanced spectrometer for atmospheric trace gas measurements and Rayleigh scattering cross sections in the cyan region (470–540 nm)," *Atmospheric Measurement Techniques*, vol. 12, no. 2, pp. 1277–1293, 2019. 9

[114] H. Berresheim, T. Elste, C. Plass-Dülmer, F. Eiseleb, and D. Tannerb, "Chemical ionization mass spectrometer for long-term measurements of atmospheric OH and H2SO4," *International Journal of Mass Spectrometry*, vol. 202, no. 1-3, pp. 91–109, 2000. 9

[115] F. Arnold, R. Fabian, G. Henschen, and W. Joos, "Stratospheric trace gas analysis from ions: H2O and HNO3," *Planetary and Space Science*, vol. 28, no. 7, pp. 681–685, 1980. 9

[116] M. Hanke, J. Uecker, T. Reiner, and F. Arnold, "Atmospheric peroxy radicals: ROXMAS, a new mass-spectrometric methodology for speciated measurements of HO2 and RO2 and first results," *International Journal of Mass Spectrometry*, vol. 213, no. 2-3, pp. 91–99, 2002. 9

[117] F. Arnold and G. Henschen, "First mass analysis of stratospheric negative ions," *Nature*, vol. 275, no. 5680, pp. 521–522, 1978. 9

[118] L. G. Huey, "Measurement of trace atmospheric species by chemical ionization mass spectrometry: Speciation of reactive nitrogen and future directions," *Mass spectrometry reviews*, vol. 26, no. 2, pp. 166–184, 2007. 9

[119] D. H. Stedman, E. E. Daby, F. Stuhl, and H. Niki, "Analysis of ozone and nitric oxide by a chemiluminescent method in laboratory and atmospheric studies of photochemical smog," *Journal of the Air Pollution Control Association*, vol. 22, no. 4, pp. 260–263, 1972. 9

[120] B. Ridley and L. Howlett, "An instrument for nitric oxide measurements in the stratosphere," *Review of Scientific Instruments*, vol. 45, no. 6, pp. 742–746, 1974. 9

[121] D. Heard, *Analytical techniques for atmospheric measurement*. John Wiley & Sons, 2008. 10

[122] D. R. Blake, T.-Y. Chen, T. W. Smith Jr, C. J.-L. Wang, O. W. Wingenter, N. J. Blake, F. Rowland, and E. W. Mayer, "Three-dimensional distribution of nonmenthane hydrocarbons and halocarbons over the northwestern Pacific during the 1991 Pacific Exploratory Mission (PEM-West A)," *Journal of Geophysical Research: Atmospheres*, vol. 101, no. D1, pp. 1763–1778, 1996. 10

[123] R. Purvis, A. Lewis, R. Carney, J. McQuaid, S. Arnold, J. Methven, H. Barjat, K. Dewey, J. Kent, P. Monks, *et al.*, "Rapid uplift of nonmethane hydrocarbons in a cold front over central Europe," *Journal of Geophysical Research: Atmospheres*, vol. 108, no. D7, 2003. 10

[124] D. Helmig, "Air analysis by gas chromatography," *Journal of chromatography A*, vol. 843, no. 1-2, pp. 129–146, 1999. 10

[125] L. G. Huey, D. R. Hanson, and C. J. Howard, "Reactions of SF6-and I-with atmospheric trace gases," *The Journal of Physical Chemistry*, vol. 99, no. 14, pp. 5001–5008, 1995. 10

[126] D. Stone, L. K. Whalley, and D. E. Heard, "Tropospheric OH and HO_2 radicals: field measurements and model comparisons," *Chem. Soc. Rev.*, vol. 41, pp. 6348–6404, 2012. 10, 64

[127] H. Chen, R. Hu, P. Xie, X. Xing, L. Ling, Z. Li, F. Wang, Y. Wang, J. Liu, and W. Liu, "A hydroxyl radical detection system using gas expansion and fast gating laser-induced fluorescence techniques," *Journal of environmental sciences*, vol. 65, pp. 190–200, 2018. 11

[128] T. M. Hard, R. J. O'Brien, T. Cook, and G. Tsongas, "Interference suppression in HO fluorescence detection," *Applied optics*, vol. 18, no. 19, pp. 3216–3217, 1979. 10

[129] P. Stevens, J. Mather, and W. Brune, "Measurement of tropospheric OH and HO_2 by laser-induced fluorescence at low pressure," *Journal of Geophysical Research: Atmospheres*, vol. 99, no. D2, pp. 3543–3557, 1994. 10, 12, 15

[130] J. Luque and D. R. Crosley, "Transition probabilities in the A 2 Σ+- X 2 Π i electronic system of OH," *The Journal of chemical physics*, vol. 109, no. 2, pp. 439–448, 1998. 11

[131] R. Stimpfle and J. Anderson, "In-situ detection of OH in the lower stratosphere with a balloon borne high repetition rate laser system," *Geophysical research letters*, vol. 15, no. 13, pp. 1503–1506, 1988. 12

[132] R. Stimpfle, P. Wennberg, L. Lapson, and J. Anderson, "Simultaneous, in situ measurements of OH and HO_2 in the stratosphere," *Geophysical research letters*, vol. 17, no. 11, pp. 1905–1908, 1990. 12

[133] P. Wennberg, R. Cohen, N. Hazen, L. Lapson, N. Allen, T. Hanisco, J. Oliver, N. Lanham, J. Demusz, and J. Anderson, "Aircraft-borne, laser-induced fluorescence instrument for the in situ detection of hydroxyl and hydroperoxyl radicals," *Review of scientific instruments*, vol. 65, no. 6, pp. 1858–1876, 1994. 12

[134] M. R. Heal, D. Heard, M. Pilling, and B. Whitaker, "On the Development and Validation of FAGE for Local Measurement of Tropospheric OH and H02," *Journal of Atmospheric Sciences*, vol. 52, no. 19, pp. 3428–3441, 1995. 12

[135] D. Creasey, G. Evans, D. Heard, and J. Lee, "Measurements of OH and HO_2 concentrations in the Southern Ocean marine boundary layer," *Journal of Geophysical Research: Atmospheres*, vol. 108, no. D15, 2003. 12

[136] J. M. PS Stevens and W. Brune, "Measurement of tropospheric OH and HO_2 by laser-induced fluorescence at low pressure," *Journal of geophysical research*, vol. 99, no. D2, 1994. 12

[137] G. P. Smith and D. R. Crosley, "A photochemical model of ozone interference effects in laser detection of tropospheric OH," *Journal of Geophysical Research: Atmospheres*, vol. 95, no. D10, pp. 16427–16442, 1990. 12

[138] F. Holland, M. Hessling, and A. Hofzumahaus, "In situ measurement of tropospheric OH radicals by laser-induced fluorescence—a description of the KFA instrument," *Journal of Atmospheric Sciences*, vol. 52, no. 19, pp. 3393–3401, 1995. 12

[139] M. Rodgers, J. Bradshaw, S. Sandholm, S. KeSheng, and D. Davis, "A 2-λ laser-induced fluorescence field instrument for ground-based and airborne measurements of atmospheric OH," *Journal of Geophysical Research: Atmospheres*, vol. 90, no. D7, pp. 12819–12834, 1985. 12

[140] F. Winiberg, S. Smith, I. Bejan, C. Brumby, T. Ingham, T. Malkin, S. Orr, D. Heard, and P. Seakins, "Pressure-dependent calibration of the OH and HO_2 channels of a FAGE HO x instrument using the Highly Instrumented Reactor for Atmospheric Chemistry (HIRAC)," *Atmospheric Measurement Techniques*, vol. 8, no. 2, pp. 523–540, 2015. 12

[141] F. Eisele and D. Tanner, "Ion-assisted tropospheric OH measurements," *Journal of Geophysical Research: Atmospheres*, vol. 96, no. D5, pp. 9295–9308, 1991. 12, 15

[142] R. Mauldin III, F. Eisele, C. Cantrell, E. Kosciuch, B. Ridley, B. Lefer, D. Tanner, J. Nowak, G. Chen, L. Wang, *et al.*, "Measurements of OH aboard the NASA P-3 during PEM-Tropics B," *Journal of Geophysical Research: Atmospheres*, vol. 106, no. D23, pp. 32657–32666, 2001. 12

[143] R. Mauldin III, S. Madronich, S. Flocke, F. Eisele, G. Frost, and A. Prevot, "New insights on OH: Measurements around and in clouds," *Geophysical Research Letters*, vol. 24, no. 23, pp. 3033–3036, 1997. 12

[144] R. Mauldin III, G. Frost, G. Chen, D. Tanner, A. Prevot, D. Davis, and F. Eisele, "OH measurements during the First Aerosol Characterization Experiment (ACE 1): Observations and model comparisons," *Journal of Geophysical Research: Atmospheres*, vol. 103, no. D13, pp. 16713–16729, 1998. 12

[145] F. Eisele, R. Mauldin, D. Tanner, C. Cantrell, E. Kosciuch, J. Nowak, B. Brune, I. Faloona, D. Tan, D. Davis, *et al.*, "Relationship between OH measurements on two different NASA aircraft during PEM Tropics B," *Journal of Geophysical Research: Atmospheres*, vol. 106, no. D23, pp. 32683–32689, 2001. 12

[146] H. Fuchs, Z. Tan, A. Hofzumahaus, S. Broch, H.-P. Dorn, F. Holland, C. Künstler, S. Gomm, F. Rohrer, S. Schrade, *et al.*, "Investigation of potential interferences in the detection of atmospheric RO x radicals by laser-induced fluorescence under dark conditions," *Atmospheric measurement techniques*, vol. 9, no. 4, pp. 1431–1447, 2016. 12

[147] D. Perner, D. Ehhalt, H. Pätz, U. Platt, E. Röth, and A. Volz, "OH-radicals in the lower troposphere," *Geophysical Research Letters*, vol. 3, no. 8, pp. 466–468, 1976. 13

[148] W. Armerding, M. Spiekermann, and F. Comes, "OH multipass absorption: Absolute and in situ method for local monitoring of tropospheric hydroxyl radicals," *Journal of Geophysical Research: Atmospheres*, vol. 99, no. D1, pp. 1225–1239, 1994. 14

[149] W. Armerding, M. Spiekermann, J. Walter, and F. Comes, "MOAS: an absorption laser spectrometer for sensitive and local monitoring of tropospheric OH and other trace gases," *Journal of Atmospheric Sciences*, vol. 52, no. 19, pp. 3381–3393, 1995. 14

[150] T. Brauers, M. Hausmann, U. Brandenburger, and H.-P. Dorn, "Improvement of differential optical absorption spectroscopy with a multichannel scanning technique," *Applied optics*, vol. 34, no. 21, pp. 4472–4479, 1995. 14

[151] H.-P. Dorn, J. Callies, U. Platt, and D. Ehhalt, "Measurement of tropospheric OH concentrations by laser long-path absorption spectroscopy," *Tellus B: Chemical and Physical Meteorology*, vol. 40, no. 5, pp. 437–445, 1988. 14, 15

[152] H. Fuchs, H.-P. Dorn, M. Bachner, B. Bohn, T. Brauers, S. Gomm, A. Hofzumahaus, F. Holland, S. Nehr, F. Rohrer, *et al.*, "Comparison of OH concentration measurements by DOAS and LIF during SAPHIR chamber experiments at high OH reactivity and low NO concentration," *Atmospheric measurement techniques*, vol. 5, no. 7, pp. 1611–1626, 2012. 14, 15

[153] H.-P. Dorn, U. Brandenburger, T. Brauers, and M. Hausmann, "A new in situ laser long-path absorption instrument for the measurement of tropospheric OH radicals," *Journal of Atmospheric Sciences*, vol. 52, no. 19, pp. 3373–3380, 1995. 14

[154] A. Richter and J. Burrows, "Tropospheric NO2 from GOME measurements," *Advances in Space Research*, vol. 29, no. 11, pp. 1673–1683, 2002. 14

[155] J. P. Burrows, M. Weber, M. Buchwitz, V. Rozanov, A. Ladstätter-Weißenmayer, A. Richter, R. DeBeek, R. Hoogen, K. Bramstedt, K.-U. Eichmann, *et al.*, "The global ozone monitoring experiment (GOME): Mission concept and first scientific results," *Journal of the Atmospheric Sciences*, vol. 56, no. 2, pp. 151–175, 1999. 14

[156] A. Richter, F. Wittrock, M. Eisinger, and J. P. Burrows, "GOME observations of tropospheric BrO in northern hemispheric spring and summer 1997," *Geophysical Research Letters*, vol. 25, no. 14, pp. 2683–2686, 1998. 14

[157] S. Baidar, H. Oetjen, S. Coburn, B. Dix, I. Ortega, R. Sinreich, and R. Volkamer, "The CU Airborne MAX-DOAS instrument: Vertical profiling of aerosol extinction and trace gases," *Atmospheric Measurement Techniques*, vol. 6, no. 3, pp. 719–739, 2013. 15

[158] M. Hausmann, U. Brandenburger, T. Brauers, and H.-P. Dorn, "Detection of tropospheric OH radicals by long-path differential-optical-absorption spectroscopy: Experimental setup, accuracy, and precision," *Journal of Geophysical Research: Atmospheres*, vol. 102, no. D13, pp. 16011–16022, 1997. 15, 61

[159] W. Armerding, M. Spiekermann, J. Walter, and F. Comes, "Multipass optical absorption spectroscopy: a fast-scanning laser spectrometer for the in situ determination of atmospheric trace-gas components, in particular OH," *Applied optics*, vol. 35, no. 21, pp. 4206–4219, 1996. 15

[160] A. Novelli, B. Bohn, H.-P. Dorn, R. Häseler, A. Hofzumahaus, M. Kaminski, Z. Yu, X. Li, R. Tillmann, R. Wegener, *et al.*, "Investigation of OH Radical Regeneration from Isoprene Oxidation Across Different NO x Regimes in the Atmosphere Simulation Chamber SAPHIR," in *AGU Fall Meeting Abstracts, volume=2017, pages=A12A–04, year=2017*. 15

[161] A. Novelli, M. Kaminski, M. Rolletter, I.-H. Acir, B. Bohn, H.-P. Dorn, X. Li, A. Lutz, S. Nehr, F. Rohrer, *et al.*, "Evaluation of OH and HO_2 concentrations and their budgets during photooxidation of 2-methyl-3-butene-2-ol (MBO) in the atmospheric simulation chamber SAPHIR," *Atmospheric chemistry and physics*, vol. 18, no. 15, pp. 11409–11422, 2018. 15

[162] K. C. Cossel, E. M. Waxman, F. R. Giorgetta, M. Cermak, I. R. Coddington, D. Hesselius, S. Ruben, W. C. Swann, G.-W. Truong, G. B. Rieker, *et al.*, "Open-path dual-comb spectroscopy to an airborne retroreflector," *Optica*, vol. 4, no. 7, pp. 724–728, 2017. 15, 19

[163] S. Coburn, C. B. Alden, R. Wright, K. Cossel, E. Baumann, G.-W. Truong, F. Giorgetta, C. Sweeney, N. R. Newbury, K. Prasad, I. Coddington, and G. B. Rieker, "Regional trace-gas source attribution using a field-deployed dual frequency comb spectrometer," *Optica*, vol. 5, pp. 320–327, Apr 2018. 15

[164] T. R. Hayden, N. Malarich, D. Petrykowski, S. P. Nigam, J. D. Christopher, C. Lapointe, N. T. Wimer, P. E. Hamlington, and G. B. Rieker, "OH radical measurements in combustion environments using wavelength modulation spectroscopy and dual-frequency comb spectroscopy near 1491 nm," *Applied Physics B*, vol. 125, no. 12, pp. 1–14, 2019. 15, 18, 20

[165] A. A. Michelson, "ART. XXI.–The relative motion of the Earth and the Luminiferous ether," *American Journal of Science (1880-1910)*, vol. 22, no. 128, p. 120, 1881. 16

[166] J. A. d. H. Peter R.Griffiths, *Fourier Transform Infrared Spectrometry*. John Wiley and Sons, 2007. 16

[167] S. Okubo, K. Iwakuni, H. Inaba, K. Hosaka, A. Onae, H. Sasada, and F.-L. Hong, "Ultra-broadband dual-comb spectroscopy across 1.0–1.9 μm," *Applied Physics Express*, vol. 8, no. 8, p. 082402, 2015. 18

[168] G. Millot, S. Pitois, M. Yan, T. Hovhannisyan, A. Bendahmane, T. W. Hänsch, and N. Picqué, "Frequency-agile dual-comb spectroscopy," *Nature Photonics*, vol. 10, no. 1, pp. 27–30, 2016. 18, 39, 42

[169] S.-J. Lee, B. Widiyatmoko, M. Kourogi, and M. Ohtsu, "Ultrahigh Scanning Speed Optical Coherence Tomography Using Optical Frequency Comb Generators," *Japanese Journal of Applied Physics*, vol. 40, pp. L878–L880, aug 2001. 18

[170] F. Keilmann, C. Gohle, and R. Holzwarth, "Time-domain mid-infrared frequency-comb spectrometer, volume = 29, year = 2004," no. 13, pp. 1542–1544. 18, 132

[171] A. Schliesser, M. Brehm, F. Keilmann, and D. W. V. D. Weide, "Frequency-comb infrared spectrometer for rapid , remote chemical sensing," vol. 13, no. 22, pp. 310–312, 2005. 18

[172] A. M. Zolot, F. R. Giorgetta, E. Baumann, J. W. Nicholson, W. C. Swann, I. Coddington, and N. R. Newbury, "Direct-comb molecular spectroscopy with accurate, resolved comb teeth over 43 THz," *Optics letters*, vol. 37, no. 4, pp. 638–640, 2012. 18, 19

[173] T. Yasui, Y. Kabetani, E. Saneyoshi, S. Yokoyama, and T. Araki, "Terahertz frequency comb by multifrequency-heterodyning photoconductive detection for high-accuracy, high-resolution terahertz spectroscopy," *Applied Physics Letters*, vol. 88, no. 24, p. 241104, 2006. 18

[174] Z. Zhang, T. Gardiner, and D. T. Reid, "Mid-infrared dual-comb spectroscopy with an optical parametric oscillator," *Opt. Lett.*, vol. 38, pp. 3148–3150, Aug 2013. 18

[175] S. A. Meek, A. Hipke, G. Guelachvili, T. W. Hänsch, and N. Picqué, "Doppler-free Fourier transform spectroscopy," *Optics letters*, vol. 43, no. 1, pp. 162–165, 2018. 18

[176] E. M. Waxman, K. C. Cossel, F. Giorgetta, G.-W. Truong, W. C. Swann, I. Coddington, and N. R. Newbury, "Estimating vehicle carbon dioxide emissions from Boulder, Colorado, using horizontal path-integrated column measurements," *Atmospheric chemistry and physics*, vol. 19, no. 7, pp. 4177–4192, 2019. 19

[177] G. Ycas, F. R. Giorgetta, K. C. Cossel, E. M. Waxman, E. Baumann, N. R. Newbury, and I. Coddington, "Mid-infrared dual-comb spectroscopy of volatile organic compounds across long open-air paths," *Optica*, vol. 6, pp. 165–168, Feb 2019. 19

[178] R. A. Alvarez, S. W. Pacala, J. J. Winebrake, W. L. Chameides, and S. P. Hamburg, "Greater focus needed on methane leakage from natural gas infrastructure," *Proceedings of the National Academy of Sciences*, vol. 109, no. 17, pp. 6435–6440, 2012. 19

[179] L. C. Sinclair, I. Coddington, W. C. Swann, G. B. Rieker, A. Hati, K. Iwakuni, and N. R. Newbury, "Operation of an optically coherent frequency comb outside the metrology lab," *Optics Express*, vol. 22, no. 6, pp. 6996–7006, 2014. 19

[180] F. R. Giorgetta, G. B. Rieker, E. Baumann, W. C. Swann, L. C. Sinclair, J. Kofler, I. Coddington, and N. R. Newbury, "Broadband phase spectroscopy over turbulent air paths," *Physical review letters*, vol. 115, no. 10, p. 103901, 2015. 20

[181] R. Peeters, G. Berden, and G. Meijer, "Near-infrared cavity enhanced absorption spectroscopy of hot water and OH in an oven and in flames," *Applied Physics B*, vol. 73, no. 1, pp. 65–70, 2001. 20

[182] L. Rutkowski, A. C. Johansson, D. Valiev, A. Khodabakhsh, A. Tkacz, F. M. Schmidt, and A. Foltynowicz, "Detection of OH in an atmospheric flame at 1.5 um using optical frequency comb spectroscopy," *Photonics letters of Poland*, vol. 8, no. 4, pp. 110–112, 2016. 20

[183] S. Schiller, "Spectrometry with frequency combs," *Opt. Lett.*, vol. 27, pp. 766–768, May 2002. 23

[184] T. W. Hänsch, "Nobel lecture: passion for precision," *Reviews of Modern Physics*, vol. 78, no. 4, p. 1297, 2006. 23

[185] T. Udem, R. Holzwarth, and T. W. Hänsch, "Optical frequency metrology," *Nature*, vol. 416, no. 6877, pp. 233–237, 2002. 23

[186] "Measuring the α-particle charge radius with muonic helium-4 ions, author=Krauth, Julian J and Schuhmann, Karsten and Ahmed, Marwan Abdou and Amaro, Fernando D and Amaro, Pedro and Biraben, François and Chen, Tzu-Ling and Covita, Daniel S and Dax, Andreas J and Diepold, Marc and Luis M.P.Fernandes and Beatrice Franke and Sandrine Galtier and others, journal=Nature, volume=589, number=7843, pages=527–531, year=2021, publisher=Nature Publishing Group," 23

[187] M. T. Murphy, T. Udem, R. Holzwarth, A. Sizmann, L. Pasquini, C. Araujo-Hauck, H. Dekker, S. D'Odorico, M. Fischer, T. W. Hänsch, and A. Manescau, "High-precision wavelength calibration of astronomical spectrographs with laser frequency combs," *Monthly Notices of the Royal Astronomical Society*, vol. 380, pp. 839–847, 08 2007. 23

[188] V. Torres-Company and A. M. Weiner, "Optical frequency comb technology for ultra-broadband radio-frequency photonics," *Laser & Photonics Reviews*, vol. 8, no. 3, pp. 368–393, 2014. 23

[189] J. Eckstein, A. Ferguson, and T. Hänsch, "High-resolution two-photon spectroscopy with picosecond light pulses," *Physical Review Letters*, vol. 40, no. 13, p. 847, 1978. 23

[190] L. Nugent-Glandorf, T. Neely, F. Adler, A. J. Fleisher, K. C. Cossel, B. Bjork, T. Dinneen, J. Ye, and S. A. Diddams, "Mid-infrared virtually imaged phased array spectrometer for rapid and broadband trace gas detection," *Opt. Lett.*, vol. 37, pp. 3285–3287, Aug 2012. 23

[191] L. Rutkowski and J. Morville, "Broadband cavity-enhanced molecular spectra from Vernier filtering of a complete frequency comb," *Optics letters*, vol. 39, no. 23, pp. 6664–6667, 2014. 23

[192] J. Morgenweg, I. Barmes, and K. S. Eikema, "Ramsey-comb spectroscopy with intense ultrashort laser pulses," *Nature Physics*, vol. 10, no. 1, pp. 30–33, 2014. 23

[193] R. Salzer, "Peter R. Griffiths, James A. de Haseth: Fourier transform infrared spectrometry (2nd edn.)," *Analytical and Bioanalytical Chemistry*, vol. 391, no. 7, pp. 2379–2380, 2008. 23

[194] J. Ye and S. T. Cundiff, *Introduction*, pp. 12–53. Boston, MA: Springer US, 2005. 24

[195] R. K. Cole, A. S. Makowiecki, N. Hoghooghi, and G. B. Rieker, "Baseline-free quantitative absorption spectroscopy based on cepstral analysis," *Opt. Express*, vol. 27, pp. 37920–37939, Dec 2019. 26

[196] H. Harde, S. Keiding, and D. Grischkowsky, "THz commensurate echoes: Periodic rephasing of molecular transitions in free-induction decay," *Phys. Rev. Lett.*, vol. 66, pp. 1834–1837, Apr 1991. 26

[197] T. Ideguchi, A. Poisson, G. Guelachvili, N. Picqué, and T. W. Hänsch, "Adaptive real-time dual-comb spectroscopy," *Nature communications*, vol. 5, no. 1, pp. 1–8, 2014. 36, 37, 62

[198] I. Coddington, W. C. Swann, and N. R. Newbury, "Coherent multiheterodyne spectroscopy using stabilized optical frequency combs," *Physical Review Letters*, vol. 100, no. 1, p. 013902, 2008. 37

[199] I. Coddington, W. C. Swann, and N. R. Newbury, "Coherent dual-comb spectroscopy at high signal-to-noise ratio," *Phys. Rev. A*, vol. 82, p. 043817, Oct 2010. 37, 62, 132

[200] T. Ideguchi, a. Poisson, G. Guelachvili, T. W. Hänsch, and N. Picqué, "Adaptive dual-comb spectroscopy in the green region.," *Optics letters*, vol. 37, no. 23, pp. 4847–9, 2012. 37

[201] J. Roy, J.-D. Deschênes, S. Potvin, and J. Genest, "Continuous real-time correction and averaging for frequency comb interferometry," *Optics express*, vol. 20, no. 20, pp. 21932–21939, 2012. 37

[202] M. Cassinerio, A. Gambetta, N. Coluccelli, P. Laporta, and G. Galzerano, "Absolute dual-comb spectroscopy at 1.55 μ m by free-running Er: fiber lasers," *Applied Physics Letters*, vol. 104, no. 23, p. 231102, 2014. 37

[203] J.-D. Deschênes, P. Giaccari, and J. Genest, "Optical referencing technique with CW lasers as intermediate oscillators for continuous full delay range frequency comb interferometry," *Optics Express*, vol. 18, no. 22, pp. 23358–23370, 2010. 37

[204] K. Kieu and M. Mansuripur, "All-fiber bidirectional passively mode-locked ring laser," *Optics letters*, vol. 33, no. 1, pp. 64–66, 2008. 38

[205] S. Mehravar, R. A. Norwood, N. Peyghambarian, and K. Kieu, "Real-time dual-comb spectroscopy with a free-running bidirectionally mode-locked fiber laser," *Applied Physics Letters*, vol. 108, no. 23, p. 231104, 2016. 38, 42

[206] X. Zhao, G. Hu, B. Zhao, C. Li, Y. Pan, Y. Liu, T. Yasui, and Z. Zheng, "Picometer-resolution dual-comb spectroscopy with a free-running fiber laser," *Optics Express*, vol. 24, no. 19, pp. 21833–21845, 2016. 38, 42

[207] Y. Nakajima, Y. Hata, and K. Minoshima, "High-coherence ultra-broadband bidirectional dual-comb fiber laser," *Optics express*, vol. 27, no. 5, pp. 5931–5944, 2019. 38, 42

[208] Y. Qin, B. Cromey, O. Batjargal, and K. Kieu, "All-fiber single-cavity dual-comb for coherent anti-Stokes Raman scattering spectroscopy based on spectral focusing," *Optics letters*, vol. 46, no. 1, pp. 146–149, 2021. 38

[209] R. Liao, Y. Song, W. Liu, H. Shi, L. Chai, and M. Hu, "Dual-comb spectroscopy with a single free-running thulium-doped fiber laser," *Optics express*, vol. 26, no. 8, pp. 11046–11054, 2018. 38, 42

[210] R. Liao, Y. Song, L. Chai, and M. Hu, "Dual repetition-rate femtosecond pulses directly from a Tm-doped fiber laser," in *CLEO: Science and Innovations, pages=SM4L–5, year=2017, organization=Optical Society of America.* 38

[211] Y. Nakajima, Y. Hata, Y. Kusumi, K. Yoshii, and K. Minoshima, "Mid-Infrared Dual-Comb Fiber Laser from 3.2 to 4.4 μm," in *CLEO: Science and Innovations, pages=JW2E–15, year=2020, organization=Optical Society of America.* 39

[212] J. Fellinger, A. S. Mayer, G. Winkler, W. Grosinger, G.-W. Truong, S. Droste, C. Li, C. M. Heyl, I. Hartl, and O. H. Heckl, "Tunable dual-comb from an all-polarization-maintaining single-cavity dual-color Yb: fiber laser," *Optics express*, vol. 27, no. 20, pp. 28062–28074, 2019. 39, 42

[213] B. Willenberg, J. Pupeikis, L. M. Krüger, F. Koch, C. R. Phillips, and U. Keller, "Femtosecond dual-comb Yb:CaF2 laser from a single free-running polarization-multiplexed cavity for optical sampling applications," *Opt. Express*, vol. 28, pp. 30275–30288, Sep 2020. 39

[214] A. Parriaux, K. Hammani, and G. Millot, "Two-micron all-fibered dual-comb spectrometer based on electro-optic modulators and wavelength conversion," *Communications Physics*, vol. 1, no. 1, pp. 1–7, 2018. 39

[215] A. Schliesser, N. Picqué, and T. W. Hänsch, "Mid-infrared frequency combs," *Nature photonics*, vol. 6, no. 7, pp. 440–449, 2012. 39

[216] A. Parriaux, K. Hammani, and G. Millot, "Electro-optic frequency combs," *Adv. Opt. Photon.*, vol. 12, pp. 223–287, Mar 2020. 39

[217] R. Liao, H. Tian, W. Liu, R. Li, Y. Song, and M. Hu, "Dual-comb generation from a single laser source: principles and spectroscopic applications towards mid-IR—A review," *Journal of Physics: Photonics*, vol. 2, no. 4, p. 042006, 2020. 40

[218] M. Yu, Y. Okawachi, A. G. Griffith, N. Picqué, M. Lipson, and A. L. Gaeta, "Silicon-chip-based mid-infrared dual-comb spectroscopy," *Nature communications*, vol. 9, no. 1, pp. 1–6, 2018. 40

[219] C. Khurmi, N. B. Hébert, W. Q. Zhang, S. A. V., G. Chen, J. Genest, T. M. Monro, and D. G. Lancaster, "Ultrafast pulse generation in a mode-locked Erbium chip waveguide laser," *Opt. Express*, vol. 24, pp. 27177–27183, Nov 2016. 40

[220] N. B. Hébert, D. G. Lancaster, V. Michaud-Belleau, G. Y. Chen, and J. Genest, "Highly coherent free-running dual-comb chip platform," *Opt. Lett.*, vol. 43, pp. 1814–1817, Apr 2018. 40

[221] N. B. Hébert, J. Genest, J.-D. Deschênes, H. Bergeron, G. Y. Chen, C. Khurmi, and D. G. Lancaster, "Self-corrected chip-based dual-comb spectrometer," *Optics express*, vol. 25, no. 7, pp. 8168–8179, 2017. 40, 42, 139

[222] P. Guay, N. B. Hébert, V. Michaud-Belleau, D. G. Lancaster, and J. Genest, "Methane spectroscopy using a free-running chip-based dual-comb laser," *Optics letters*, vol. 44, no. 17, pp. 4375–4378, 2019. 40, 42

[223] S. M. Link, D. Maas, D. Waldburger, and U. Keller, "Dual-comb spectroscopy of water vapor with a free-running semiconductor disk laser," *Science*, vol. 356, no. 6343, pp. 1164–1168, 2017. 40, 42

[224] J. Nürnberg, C. G. E. Alfieri, Z. Chen, D. Waldburger, N. Picqué, and U. Keller, "An unstabilized femtosecond semiconductor laser for dual-comb spectroscopy of acetylene," *Opt. Express*, vol. 27, pp. 3190–3199, Feb 2019. 40, 42

[225] A. Gluth, Y. Wang, V. Petrov, J. Paajaste, S. Suomalainen, A. Härkönen, M. Guina, G. Steinmeyer, X. Mateos, S. Veronesi, M. Tonelli, J. Li, Y. Pan, J. Guo, and U. Griebner, "GaSb-based SESAM mode-locked Tm:YAG ceramic laser at 2 µm," *Opt. Express*, vol. 23, pp. 1361–1369, Jan 2015. 40

[226] K. Fritsch, J. Brons, M. Iandulskii, K. F. Mak, Z. Chen, N. Picqué, and O. Pronin, "Dual-comb thin-disk oscillator," *arXiv preprint arXiv:2004.10303*, 2020. 40, 42, 139

[227] N. Modsching, J. Drs, J. Fischer, S. Schilt, V. J. Wittwer, and T. Südmeyer, "Dual-Comb Thin-Disk Laser Oscillator Based on Polarization Splitting," in *CLEO: Science and Innovations, pages=SF3H–2, year=2020, organization=Optical Society of America.* 41

[228] C.-y. Wang, L. Chai, W. Zhang, and K. M. Yoo, "Pulse colliding in a self-mode-locked ring-cavity Ti: sapphire laser," *Applied optics*, vol. 37, no. 3, pp. 522–525, 1998. 41

[229] T. Ideguchi, T. Nakamura, Y. Kobayashi, and K. Goda, "Kerr-lens mode-locked bidirectional dual-comb ring laser for broadband dual-comb spectroscopy," *Optica*, vol. 3, pp. 748–753, Jul 2016. 41, 42, 43, 66, 96, 97, 112, 113, 132

[230] A. E. Akosman and M. Y. Sander, "Dual comb generation from a mode-locked fiber laser with orthogonally polarized interlaced pulses," *Optics express*, vol. 25, no. 16, pp. 18592–18602, 2017. 42

[231] J. Olson, Y. H. Ou, A. Azarm, and K. Kieu, "Bi-Directional Mode-Locked Thulium Fiber Laser as a Single-Cavity Dual-Comb Source," *IEEE Photonics Technology Letters*, vol. 30, no. 20, pp. 1772–1775, 2018. 42

[232] A. Parriaux, K. Hammani, and G. Millot, "Electro-optic dual-comb spectrometer in the thulium amplification band for gas sensing applications," *Optics letters*, vol. 44, no. 17, pp. 4335–4338, 2019. 42

[233] N. Modsching, J. Drs, P. Brochard, J. Fischer, S. Schilt, V. J. Wittwer, and T. Südmeyer, "High-power dual-comb thin-disk laser oscillator for fast high-resolution spectroscopy," *Optics Express*, vol. 29, no. 10, pp. 15104–15113, 2021. 42

[234] H. Haus and E. Ippen, "Group velocity of solitons," *Optics letters*, vol. 26, no. 21, pp. 1654–1656, 2001. 43

[235] M. Y. Sander, E. P. Ippen, and F. X. Kärtner, "Carrier-envelope phase dynamics of octave-spanning dispersion-managed Ti: sapphire lasers," *Optics express*, vol. 18, no. 5, pp. 4948–4960, 2010. 43

[236] U. Platt and J. Stutz, *Differential Optical Absorption Spectroscopy: Principles and Applications*. Physics of Earth and Space Environments, Springer Berlin Heidelberg, 2008. 46, 57

[237] N. R. Newbury, I. Coddington, and W. Swann, "Sensitivity of coherent dual-comb spectroscopy," *Opt. Express*, vol. 18, pp. 7929–7945, Apr 2010. 47, 48, 49, 52, 56, 57, 138

[238] R. R. Alfano, ed., *Supercontinuum Generation in Microstructure Fibers*, pp. 481–497. New York, NY: Springer New York, 2006. 50

[239] I. Coddington, W. C. Swann, and N. R. Newbury, "Coherent linear optical sampling at 15 bits of resolution," *Opt. Lett.*, vol. 34, pp. 2153–2155, Jul 2009. 50, 51, 52

[240] Y. Wang, J. Fonseca-Campos, W.-g. Liang, C.-Q. Xu, and I. Vargas-Baca, "Noise Analysis of Second-Harmonic Generation in Undoped and MgO-Doped Periodically Poled Lithium Niobate.," *Advances in OptoElectronics*, 2008. 50

[241] M. Tawfieq, A. K. Hansen, O. B. Jensen, D. Marti, B. Sumpf, and P. E. Andersen, "Intensity noise transfer through a diode-pumped titanium sapphire laser system," *IEEE Journal of Quantum Electronics*, vol. 54, no. 1, pp. 1–9, 2017. 50

[242] K. Moutzouris, F. Sotier, F. Adler, and A. Leitenstorfer, "Highly efficient second, third and fourth harmonic generation from a two-branch femtosecond erbium fiber source," *Opt. Express*, vol. 14, pp. 1905–1912, Mar 2006. 50

[243] O. Kuzucu, F. N. C. Wong, D. E. Zelmon, S. M. Hegde, T. D. Roberts, and P. Battle, "Generation of 250 mW narrowband pulsed ultraviolet light by frequency quadrupling of an amplified erbium-doped fiber laser," *Opt. Lett.*, vol. 32, pp. 1290–1292, May 2007. 50

[244] Carlson, David R., *Frequency Combs for Spectroscopy in the Vacuum Ultraviolet*. PhD thesis, The University of Arizona, Jan. 2016. 50

[245] V. Schuster, C. Liu, R. Klas, P. Dominguez, J. Rothhardt, J. Limpert, and B. Bernhardt, "Towards Dual Comb Spectroscopy in the Ultraviolet Spectral Region," *arXiv e-prints*, pp. arXiv–2006, 2020. 50

[246] R. Ell, U. Morgner, F. X. Kärtner, J. G. Fujimoto, E. P. Ippen, V. Scheuer, G. Angelow, T. Tschudi, M. J. Lederer, A. Boiko, and B. Luther-Davies, "Generation of 5-fs pulses and octave-spanning spectra directly from a Ti:sapphire laser," *Opt. Lett.*, vol. 26, pp. 373–375, Mar 2001. 51, 71

[247] L. Matos, D. Kleppner, O. Kuzucu, T. R. Schibli, J. Kim, E. P. Ippen, and F. X. Kaertner, "Direct frequency comb generation from an octave-spanning, prismless Ti:sapphire laser," *Opt. Lett.*, vol. 29, pp. 1683–1685, Jul 2004. 51

[248] A. Bartels, D. Heinecke, and S. A. Diddams, "Passively mode-locked 10 GHz femtosecond Ti:sapphire laser," *Opt. Lett.*, vol. 33, pp. 1905–1907, Aug 2008. 51

[249] S. Backus, M. T. Asaki, C. Shi, H. C. Kapteyn, and M. M. Murnane, "Intracavity frequency doubling in a Ti:sapphire laser: generation of 14-fs pulses at 416 nm," *Opt. Lett.*, vol. 19, pp. 399–401, Mar 1994. 51

[250] D. Steinbach, W. Hügel, and M. Wegener, "Generation and detection of blue 10.0-fs pulses," *J. Opt. Soc. Am. B*, vol. 15, pp. 1231–1234, Mar 1998. 51

[251] A. Fürbach, T. Le, C. Spielmann, and F. Krausz, "Generation of 8-fs pulses at 390 nm," *Applied Physics B*, Jun 2000. 51

[252] F. Rotermund and V. Petrov, "Generation of the fourth harmonic of a femtosecond Ti:sapphire laser," *Opt. Lett.*, vol. 23, pp. 1040–1042, Jul 1998. 51

[253] Q. Quraishi, S. A. Diddams, and L. Hollberg, "Optical phase-noise dynamics of Titanium:sapphire optical frequency combs," *Optics Communications*, vol. 320, pp. 84–87, 2014. 51

[254] D. V. Sutyrin, N. Poli, N. Beverini, and G. M. Tino, "Carrier-envelope offset frequency noise analysis in Ti:sapphire frequency combs," *Optical Engineering*, vol. 53, no. 12, pp. 1 – 5, 2014. 51, 52

[255] M. Tawfieq, A. K. Hansen, O. B. Jensen, D. Marti, B. Sumpf, and P. E. Andersen, "Intensity Noise Transfer Through a Diode-Pumped Titanium Sapphire Laser System," *IEEE Journal of Quantum Electronics*, vol. 54, no. 1, pp. 1–9, 2018. 52

[256] T. D. Mulder, R. P. Scott, and B. H. Kolner, "Amplitude and envelope phase noise of a modelocked laser predicted from its noise transfer function and the pump noise power spectrum," *Opt. Express*, vol. 16, pp. 14186–14191, Sep 2008. 52

[257] A. ISHIMARU, *Wave Propagation and Scattering in Random Media.* Academic Press, 1978. 53, 54

[258] W. Armerding, M. Spiekermann, J. Walter, and F. J. Comes, "Multipass optical absorption spectroscopy: a fast-scanning laser spectrometer for the in situ determination of atmospheric trace-gas components, in particular OH," *Appl. Opt.*, vol. 35, pp. 4206–4219, Jul 1996. 53, 61, 65

[259] H. Fuchs, H.-P. Dorn, M. Bachner, B. Bohn, T. Brauers, S. Gomm, A. Hofzumahaus, F. Holland, S. Nehr, F. Rohrer, R. Tillmann, and A. Wahner, "Comparison of OH concentration measurements by DOAS and LIF during SAPHIR chamber experiments at high OH reactivity and low NO concentration," *Atmospheric Measurement Techniques*, vol. 5, no. 7, pp. 1611–1626, 2012. 59, 61

[260] J. Stutz, H.-J. Oh, S. I. Whitlow, C. Anderson, J. E. Dibb, J. H. Flynn, B. Rappenglück, and B. Lefer, "Simultaneous DOAS and mist-chamber IC measurements of HONO in Houston, TX," *Atmospheric Environment*, vol. 44, no. 33, pp. 4090–4098, 2010. 61

[261] A. C. Vandaele and M. Carleer, "Development of Fourier transform spectrometry for UV–visible differential optical absorption spectroscopy measurements of tropospheric minor constituents," *Appl. Opt.*, vol. 38, pp. 2630–2639, Apr 1999. 61, 65

[262] G. Hönninger, H. Leser, O. Sebastián, and U. Platt, "Ground-based measurements of halogen oxides at the Hudson Bay by active longpath DOAS and passive MAX-DOAS," *Geophysical Research Letters*, vol. 31, no. 4, pp. 1–5, 2004. 61

[263] Hebestreit, Stutz, Rosen, Matveiv, Peleg, Luria, and Platt, "DOAS measurements of tropospheric bromine oxide in mid-latitudes," *Science*, vol. 283 5398, pp. 55–7, 1999. 61

[264] S. Davis, M. Abrams, and J. Brault, "Fourier Transform Spectrometry," 2001. 62

[265] G. Moortgat and A. Ravishankara, "Ozone depletion and related topics | photochemistry of ozone," pp. 370 – 379, 2015. 63

[266] E. J. Dunlea and A. R. Ravishankara, "Measurement of the rate coefficient for the reaction of o(1d) with h2o and re-evaluation of the atmospheric oh production rate," *Phys. Chem. Chem. Phys.*, vol. 6, pp. 3333–3340, 2004. 63, 64

[267] L. K. Whalley, D. Stone, B. Bandy, R. Dunmore, J. F. Hamilton, J. Hopkins, J. D. Lee, A. C. Lewis, and D. E. Heard, "Atmospheric OH reactivity in central London: observations, model predictions and estimates of in situ ozone production," *Atmospheric Chemistry and Physics*, vol. 16, no. 4, pp. 2109–2122, 2016. 64

[268] A. A.-R. Alpes, "Acces aux donnees de mesure." •, july 2019. *https* : *//www.atmo* − *auvergnerhonealpes.fr/donnees/acces* − *par* − *polluant*. 64

[269] F. Holland, U. Aschmutat, M. Hessling, A. Hofzumahaus, and D. Ehhalt, "Highly time resolved measurements of OH during POPCORN using laser-induced fluorescence spectroscopy," in *Atmospheric Measurements during POPCORN—Characterisation of the Photochemistry over a Rural Area*, pp. 205–225, Springer, 1998. 64

[270] T. Shirley, W. Brune, X. Ren, J. Mao, R. Lesher, B. Cardenas, R. Volkamer, L. Molina, M. J. Molina, B. Lamb, *et al.*, "Atmospheric oxidation in the Mexico city metropolitan area (MCMA) during April 2003," *Atmospheric Chemistry and Physics*, vol. 6, no. 9, pp. 2753–2765, 2006. 64

[271] J. Mao, X. Ren, S. Chen, W. Brune, Z. Chen, M. Martinez, H. Harder, B. Lefer, B. Rappenglück, J. Flynn, and M. Leuchner, "Atmospheric oxidation capacity in the summer of Houston 2006: Comparison with summer measurements in other metropolitan studies," *Atmospheric Environment*, vol. 44, pp. 4107–4115, 10 2010. 65

[272] S. Yefet and A. Pe'er, "A review of cavity design for Kerr lens mode-locked solid-state lasers," *Applied Sciences*, vol. 3, no. 4, pp. 694–724, 2013. 68, 80, 81

[273] W. R. Jean-Claude Diels, *Ultrashort Laser Pulse Phenomena*. Elsevier, 2006. 68, 69, 71, 78, 84, 101

[274] J. Garduno-Mejia, M. Mohebi, and N. Jamasbi, "Direction of propagation of the beam in a unidirectional Kerr lens mode locked Ti: Sapphire ring laser," *Optics communications*, vol. 171, no. 4-6, pp. 263–269, 1999. 68, 97, 114

[275] J. Garduno-Mejia, M. Mohebi, and N. Jamasbi, "The role of cavity design in a bi-directional Kerr lens mode locked ring Ti: Sapphire laser," *Optics communications*, vol. 207, no. 1-6, pp. 307–314, 2002. 68, 95, 112

[276] W. T. Silfvast, *Laser fundamentals*. Cambridge university press, 2004. 69

[277] H. A. Haus, J. G. Fujimoto, and E. P. Ippen, "Analytic theory of additive pulse and Kerr lens mode locking," *IEEE Journal of quantum electronics*, vol. 28, no. 10, pp. 2086–2096, 1992. 71

[278] O. Martinez, R. Fork, and J. P. Gordon, "Theory of passively mode-locked lasers including self-phase modulation and group-velocity dispersion," *Optics letters*, vol. 9, no. 5, pp. 156–158, 1984. 71

[279] F. Salin, P. Grangier, G. Roger, and A. Brun, "Observation of high-order solitons directly produced by a femtosecond ring laser," *Physical review letters*, vol. 56, no. 11, p. 1132, 1986. 71

[280] P. Curley, C. Spielmann, T. Brabec, F. Krausz, E. Wintner, and A. Schmidt, "Operation of a femtosecond Ti: sapphire solitary laser in the vicinity of zero group-delay dispersion," *Optics letters*, vol. 18, no. 1, pp. 54–56, 1993. 71

[281] M. T. Asaki, C.-P. Huang, D. Garvey, J. Zhou, H. C. Kapteyn, and M. M. Murnane, "Generation of 11-fs pulses from a self-mode-locked Ti: sapphire laser," *Optics letters*, vol. 18, no. 12, pp. 977–979, 1993. 71

[282] T. Brabec, C. Spielmann, and F. Krausz, "Mode locking in solitary lasers," *Optics letters*, vol. 16, no. 24, pp. 1961–1963, 1991. 72

[283] T. Brabec, C. Spielmann, and F. Krausz, "Limits of pulse shortening in solitary lasers," *Optics letters*, vol. 17, no. 10, pp. 748–750, 1992. 72

[284] A. Kasper and K.-J. Witte, "10-fs pulse generation from a unidirectional Kerr-lens mode-locked Ti: sapphire ring laser," *Optics letters*, vol. 21, no. 5, pp. 360–362, 1996. 72, 96

[285] Schott, "Optical Glass Data Sheet," tech. rep., Schott, https://refractiveindex.info/download/data/2017/schott_2017-01-20b.agf, 2017. 78, 83, 94

[286] D. Kuizenga and A. Siegman, "FM and AM mode locking of the homogeneous laser-Part I: Theory," *IEEE Journal of Quantum Electronics*, vol. 6, no. 11, pp. 694–708, 1970. 79

[287] D. Kuizenga and A. Siegman, "FM and AM mode locking of the homogeneous laser-Part II: Experimental results in a Nd: YAG laser with internal FM modulation," *IEEE Journal of Quantum Electronics*, vol. 6, no. 11, pp. 709–715, 1970. 79

[288] U. Keller, "Recent developments in compact ultrafast lasers," *nature*, vol. 424, no. 6950, pp. 831–838, 2003. 79

[289] V. Magni, G. Cerullo, S. De Silvestri, and A. Monguzzi, "Astigmatism in Gaussian-beam self-focusing and in resonators for Kerr-lens mode locking," *JOSA B*, vol. 12, no. 3, pp. 476–485, 1995. 79, 80

[290] G. Cerullo, S. De Silvestri, and V. Magni, "Self-starting Kerr-lens mode locking of a Ti: sapphire laser," *Optics letters*, vol. 19, no. 14, pp. 1040–1042, 1994. 79, 80

[291] J.-M. Shieh, F. Ganikhanov, K.-H. Lin, W.-F. Hsieh, and C.-L. Pan, "Completely self-starting picosecond and femtosecond Kerr-lens mode-locked Ti: sapphire laser," *JOSA B*, vol. 12, no. 5, pp. 945–949, 1995. 79

[292] F. Salin, J. Squier, and M. Piche, "Mode locking of Ti: Al 2 O 3 lasers and self-focusing: a Gaussian approximation," *Optics letters*, vol. 16, no. 21, pp. 1674–1676, 1991. 79

[293] A. Bartels, T. Dekorsy, and H. Kurz, "Femtosecond Ti: sapphire ring laser with a 2-GHz repetition rate and its application in time-resolved spectroscopy," *Optics letters*, vol. 24, no. 14, pp. 996–998, 1999. 79

[294] W. Pelouch, P. Powers, and C. Tang, "Self-starting mode-locked ring-cavity Ti: sapphire laser," *Optics letters*, vol. 17, no. 22, pp. 1581–1583, 1992. 79, 112

[295] T. Brabec, C. Spielmann, P. Curley, and F. Krausz, "Kerr lens mode locking," *Optics letters*, vol. 17, no. 18, pp. 1292–1294, 1992. 80

[296] K.-H. Lin, Y. Lai, and W.-F. Hsieh, "Simple analytical method of cavity design for astigmatism-compensated Kerr-lens mode-locked ring lasers and its applications," *JOSA B*, vol. 12, no. 3, pp. 468–475, 1995. 80

[297] G. Cerullo, S. De Silvestri, V. Magni, and L. Pallaro, "Resonators for Kerr-lens mode-locked femtosecond Ti: sapphire lasers," *Optics letters*, vol. 19, no. 11, pp. 807–809, 1994. 80, 112

[298] V. Magni, G. Cerullo, and S. De Silvestri, "Closed form Gaussian beam analysis of resonators containing a Kerr medium for femtosecond lasers," *Optics Communications*, vol. 101, no. 5-6, pp. 365–370, 1993. 80

[299] S. Yefet and A. Pe'er, "Mode locking with enhanced nonlinearity-a detailed study," *Optics express*, vol. 21, no. 16, pp. 19040–19046, 2013. 81

[300] A. Kowalevicz, T. Schibli, F. Kärtner, and J. Fujimoto, "Ultralow-threshold Kerr-lens mode-locked Ti: Al 2 O 3 laser," *Optics Letters*, vol. 27, no. 22, pp. 2037–2039, 2002. 81

[301] P. E. Ciddor, "Refractive index of air: new equations for the visible and near infrared," *Appl. Opt.*, vol. 35, pp. 1566–1573, Mar 1996. 83

[302] R. L. Kelly, "Program of the 1972 Annual Meeting of the Optical Society of America," *J. Opt. Soc. Am.*, vol. 62, pp. 1336–1336, Nov 1972. 83

[303] J.-P. Taché, "Ray matrices for tilted interfaces in laser resonators," *Applied optics*, vol. 26, no. 3, pp. 427–429, 1987. 85

[304] H. Kogelnik, E. Ippen, A. Dienes, and C. Shank, "Astigmatically compensated cavities for CW dye lasers," *IEEE Journal of Quantum Electronics*, vol. 8, no. 3, pp. 373–379, 1972. 85

[305] C. Ramirez-Guerra, J. A. Moreno-Larios, M. Rosete-Aguilar, and J. Garduno-Mejia, "Mode-coupling enhancement by pump astigmatism correction in a Ti: Sapphire femtosecond laser," *Applied optics*, vol. 55, no. 34, pp. 9889–9894, 2016. 86

[306] P. E. Ciddor, "Refractive index of air: new equations for the visible and near infrared," *Applied optics*, vol. 35, no. 9, pp. 1566–1573, 1996. 93

[307] M. J. Dodge, *"Refractive Index" in Handbook of Laser Science and Technology, Optical Materials: Part 2*, vol. Volume IV. CRC Press, Boca Raton, 1986. 93

[308] B. Lemoff and C. Barty, "Generation of high-peak-power 20-fs pulses from a regeneratively initiated, self-mode-locked Ti: sapphire laser," *Optics letters*, vol. 17, no. 19, pp. 1367–1369, 1992. 95

[309] A. Bartels and H. Kurz, "Generation of a broadband continuum by a Ti: sapphire femtosecond oscillator with a 1-GHz repetition rate," *Optics letters*, vol. 27, no. 20, pp. 1839–1841, 2002. 95

[310] C. Ramírez-Guerra, J. A. Moreno-Larios, M. Rosete-Aguilar, and J. Garduno-Mejia, "Mode-coupling enhancement by pump astigmatism correction in a Ti:Sapphire femtosecond laser," *Appl. Opt.*, vol. 55, pp. 9889–9894, Dec 2016. 102

[311] A. Kasper and K. J. Witte, "10-fs pulse generation from a unidirectional Kerr-lens mode-locked Ti:sapphire ring laser," *Opt. Lett.*, vol. 21, pp. 360–362, Mar 1996. 112

[312] T. Beddard, W. Sibbett, D. Reid, J. Garduno-Mejia, N. Jamasbi, and M. Mohebi, "High-average-power, 1-MW peak-power self-mode-locked Ti: sapphire oscillator," *Optics letters*, vol. 24, no. 3, pp. 163–165, 1999. 112

[313] T. Ideguchi, T. Nakamura, Y. Kobayashi, and K. Goda, "Kerr-lens mode-locked bidirectional dual-comb ring laser for broadband dual-comb spectroscopy, volume = 3, month = Jul, year = 2016, url = $http://www.osapublishing.org/optica/abstract.cfm?URI = optica-3-7-748$, doi = 10.1364/OPTICA.3.000748„" *Optica*, no. 7, pp. 748–753. 112

[314] S. Yefet and A. Pe'er, "A Review of Cavity Design for Kerr Lens Mode-Locked Solid-State Lasers," *Applied Sciences*, vol. 3, no. 4, pp. 694–724, 2013. 113

[315] F. Reynaud and F. Salin and A. Barthelemy, "Measurement of phase shifts introduced by nonlinear optical phenomena on subpicosecond pulses, volume = 14, month = Mar, year = 1989, url = http://ol.osa.org/abstract.cfm?URI=ol-14-5-275, doi = 10.1364/OL.14.000275„" *Opt. Lett.*, no. 5, pp. 275–277. 113

[316] Y. Nabekawa, T. Shimizu, T. Okino, K. Furusawa, H. Hasegawa, K. Yamanouchi, and K. Midorikawa, "Interferometric autocorrelation of an attosecond pulse train in the single-cycle regime," *Physical review letters*, vol. 97, no. 15, p. 153904, 2006. 117

[317] J.-C. Diels, E. Van Stryland, and D. Gold, "Investigation of the parameters affecting subpicosecond pulse durations in passively mode locked dye lasers," in *Picosecond Phenomena, pages=117–120, year=1978, publisher=Springer*. 117

[318] F. Salin, P. Georges, G. Le Saux, G. Roger, and A. Brun, "Autocorrélation interférométrique monocoup d'impulsions femtosecondes," *Revue de Physique Appliquée*, vol. 22, no. 12, pp. 1613–1618, 1987. 117

[319] P. Curley, C. Spielmann, T. Brabec, E. Wintner, and F. Krausz, "Periodic pulse evolution in solitary lasers," *JOSA B*, vol. 10, no. 6, pp. 1025–1028, 1993. 119

[320] A. Lipson, S. G. Lipson, and H. Lipson, *Optical physics*. Cambridge University Press, 2010. 133

[321] D. Robichaud, J. Hodges, P. Maslowski, L. Yeung, M. Okumura, C. Miller, and L. Brown, "High-accuracy transition frequencies for the O_2 A-band," *Journal of Molecular Spectroscopy*, vol. 251, pp. 27–37, 2008. 134

[322] "Accurate frequency referencing for fieldable dual-comb spectroscopy, author=Truong, Gar-Wing and Waxman, Eleanor M and Cossel, Kevin C and Baumann, Esther and Klose, Andrew and Giorgetta, Fabrizio R and Swann, William C and Newbury, Nathan R and Coddington, Ian, journal=Optics express, volume=24, number=26, pages=30495–30504, year=2016, publisher=Optical Society of America," 138

[323] M. L. Forman, W. H. Steel, and G. A. Vanasse, "Correction of asymmetric interferograms obtained in Fourier spectroscopy," *JOSA*, vol. 56, no. 1, pp. 59–63, 1966. 139

[324] R. W. Boyd, *Nonlinear optics*. Academic press, 2020. 173

[325] P. N. Butcher and D. Cotter, *The elements of nonlinear optics*. No. 9, Cambridge university press, 1990. 173

[326] T. Brabec and F. Krausz, "Nonlinear optical pulse propagation in the single-cycle regime," *Physical Review Letters*, vol. 78, no. 17, p. 3282, 1997. 174

Appendix

Kerr-lens Mode-locking description

As the laser beam propagates through the crystal, it induces a polarisation P due to the interaction between the material and the propagating electric field. The material induced polarisation term is given in equation 6.1.

$$P = \epsilon_0 \chi(\omega) E \tag{6.1}$$

ϵ_0 is the vacuum permittivity. The induced polarisation of the material directly depends on the nature of the crystal material parameters contained in the χ term that is the susceptibility of the material. E is the electric field of the laser propagating through the crystal. At high intensity, the polarisation of the material doesn't behave linearly with the amplitude of incident electromagnetic field. The term χ must be developed to the second and third order. To describe the Kerr effect, the third order of the dielectric susceptibility needs to be presented. The formalism developed is similar to the one developed the books of Boyd and of Butcher and Cotter [324, 325]. The equation 6.2 presents the total induced polarisation of the material that is caused by an initial electromagnetic wave E.

$$\begin{aligned} P(t) &= P^{(1)}(t) + P^{(2)}(t) + P^{(3)}(t) + ... \\ &= \epsilon_0 \chi^{(1)} E + \frac{\epsilon_0}{2!} \chi^{(2)} E^2 + \frac{\epsilon_0}{3!} \chi^{(3)} E^3 + ... \end{aligned} \tag{6.2}$$

The third order polarisation is developed in equation 6.3. It is reminded that the electric field $E(t)$ can be developed, using the complex values : $E(t) = \frac{\mathcal{E}(t)+\mathcal{E}^*(t)}{2}$

$$P^{(3)}(t) = \frac{\epsilon_0 \chi^{(3)}}{8} \Big(\mathcal{E}^3(t) + \mathcal{E}^{*3}(t) + 3(\mathcal{E}^2(t)\mathcal{E}^*(t) + \mathcal{E}(t)\mathcal{E}^{*2}(t)) \Big) \tag{6.3}$$

The red terms are responsible of the third harmonic generation, while the blue terms are responsible of the the Kerr effect. For the demonstration and to simplify, only the terms responsible of the Kerr effect and the polarisation term $\mathcal{P}$ as in equation 6.4 are kept.

$$\mathcal{P} = \frac{3\epsilon_0\chi^{(3)}}{4}\mathcal{E}^*(t)\mathcal{E}(t)^2 = \frac{3\epsilon_0\chi^{(3)}}{4}|\mathcal{E}(t)|^2\mathcal{E}(t) \tag{6.4}$$

$\mathcal{E}(t) = |\mathcal{E}|e^{i\phi(t)}$. The difference with the nonlinearity at second order is that the phase-matching is never cancelled, and as a result, the effects at third order will accumulate in long distance. Moreover, the third order effects is always present in any material, centro-symmetric or not. To present the Kerr effect, the laser beam propagation equation presented in 6.5 must be solved.

$$\Delta\vec{\mathcal{E}}(\vec{r},t) - \vec{\nabla}(\vec{\nabla}.\vec{\mathcal{E}}(\vec{r},t) - \frac{1}{c^2}\frac{\delta^2\vec{\mathcal{E}}}{\delta^2 t} = \frac{1}{\epsilon_0 c^2}\frac{\delta^2\vec{\mathcal{P}}}{\delta^2 t} \tag{6.5}$$

We pose : $\vec{\mathcal{E}}(\vec{r},t) = \mathcal{A}(\vec{r},t)e^{i(k_0 z-\omega_0 t)}$ Where $\mathcal{A}$ is the amplitude of the electric field, κ_0 is the wavenumber, ω_0 is the pulse rate of the central spectrum. z is the axis parallel to the propagation of the laser beam . After having replaced the complex electric field and polarisation in the equation 6.5, the relation 6.6 is obtained.

$$\frac{\delta\mathcal{A}}{\delta z} = \left(-i\frac{k_0''}{2}\frac{\delta^2}{\delta t^2} + \frac{k_0'''}{6}\frac{\delta^3}{\delta t^3} + \frac{i}{2k_0}\Delta_\perp \right)\mathcal{A}(\vec{r},t) + \frac{i\omega_0}{2\epsilon_0 n_0 c}\mathcal{P}(\vec{r},t+k_0' z)e^{i(\omega_0 t+\omega_0 k_0' z-k_0 z)} \tag{6.6}$$

k_0', k_0'' and k_0''' are respectively the first, second and third derivative of the wavenumber with the frequency. The range of approximation used to solve the equation are called Slowly-Evolving-Wave-Approximation (SEWA), [326].

- the paraxial approximation : fluctuation in the propagation direction are negligible compared to the transversal fluctuation of the electric field : $\Delta_\perp\mathcal{E} >> \frac{\delta^2\vec{\mathcal{E}}}{\delta^2 z}$
- the material is assumed isotropic

The red part represents the dispersion operator $\hat{D}$, while the blue part is the non-linear operator $\hat{N}$ and describes the impact of the non-linearity on the envelope of the light pulse. Therefore, it can be shortened as showed in equation 6.7.

$$\frac{\delta\mathcal{A}}{\delta z} = \hat{D}\mathcal{A}(\vec{r},t) + \hat{N}\mathcal{A}(\vec{r},t) \tag{6.7}$$

The dispersion and non-linear components of the equation can be treated separately. The solution of the Kerr effect can be found by solving the non-linear part of the equation. This solution is given in equation 6.8.

$$\hat{N}\mathcal{A}(\vec{r},t) = i\gamma|\mathcal{A}|^2\mathcal{A}(\vec{r},t) \tag{6.8}$$

With $\gamma = \frac{3\omega_0\chi^{(3)}}{8n_0c}$, where ω_0 is the central frequency of the envelope, $\chi^{(3)}$ is the third non-linear order of the dielectric susceptibility, n_0 is the refractive index of the material at the frequency ω_0, and c the light celerity.

In the case of our study, we consider $\chi^{(3)}$ real, which means that $|A(\vec{r},t)|^2 = |A(0,t)|^2$ is a constant. This allows us to write the solution of the propagation equation 6.8, which is given in equation 6.9 in terms of the electric field:

$$\mathcal{E}(z,t) = A(0,t)e^{i((k_0+\gamma|\mathcal{E}(z,t)|^2)z - w_0t))} \tag{6.9}$$

As we can write that $k_0 = \frac{n_0}{\omega_0}$, ans as the term $|\mathcal{E}(z,t)|^2 \propto I$, one can write the phase term of equation 6.9 as $:(n_0 + n_2I)\frac{w_0}{c}$. The phase term can be rewritten as the equation 6.10.

$$n(I) = n_0 + n_2 \times I \tag{6.10}$$

With $n_2 = \gamma \times \frac{2}{cn_0\epsilon_0} = \frac{3\omega_0\chi^{(3)}}{4n_0\epsilon_0c^2}$

The refractive index of the material is thus dependant on the intensity. The second order refractive index value of Ti:sa crystal is $3.10^{-20}\mathrm{m}^2.\mathrm{W}^{-1}$.